TESIS DE LA UNIVERSIDAD DE ZARAGOZA

2025 242

Nerea Novo Huerta

The human Apoptosis Inducing Factor family: from the molecular mechanism of the Apoptosis Inducing Factor and the Apoptosis Inducing Factor–Like to their functional and pathological significance

Director/es
Medina Trullenque, María Milagros
Ferreira Neila, Patricia

ISSN 2254-7606

Prensas de la Universidad Universidad Zaragoza

Universidad de Zaragoza
Servicio de Publicaciones

ISSN 2254-7606

Universidad Zaragoza
1542

Tesis Doctoral

THE HUMAN APOPTOSIS INDUCING FACTOR FAMILY: FROM THE MOLECULAR MECHANISM OF THE APOPTOSIS INDUCING FACTOR AND THE APOPTOSIS INDUCING FACTOR–LIKE TO THEIR FUNCTIONAL AND PATHOLOGICAL SIGNIFICANCE

Autor

Nerea Novo Huerta

Director/es

Medina Trullenque, María Milagros
Ferreira Neila, Patricia

UNIVERSIDAD DE ZARAGOZA
Escuela de Doctorado

Programa de Doctorado en Bioquímica y Biología Molecular

2023

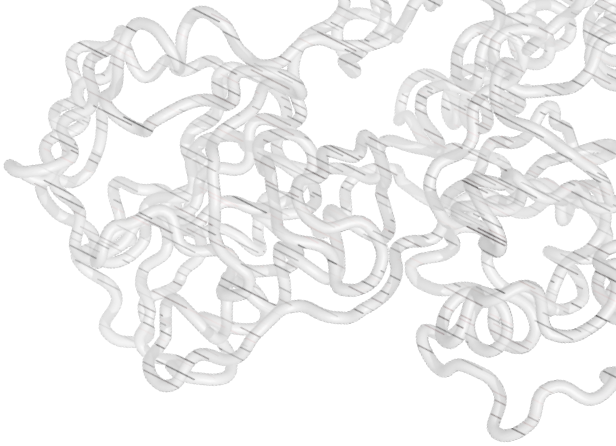

The human Apoptosis Inducing Factor family:

from the Molecular Mechanism of the Apoptosis Inducing Factor and the Apoptosis Inducing Factor-Like to their Functional and Pathological Significance

Tesis Doctoral

Nerea Novo Huerta

Universidad de Zaragoza

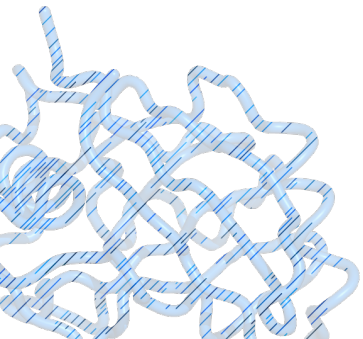

UNIVERSIDAD DE ZARAGOZA

FACULTAD DE CIENCIAS

Universidad Zaragoza

DEPARTAMENTO DE BIOQUÍMICA Y BIOLOGÍA MOLECULAR Y CELULAR

TESIS DOCTORAL

The human Apoptosis Inducing Factor family: from the molecular mechanism of the Apoptosis Inducing Factor and the Apoptosis Inducing Factor–Like to their functional and pathological significance

Memoria presentada por NEREA NOVO HUERTA,

Graduada en Biotecnología, para optar al grado de

Doctora por la Universidad de Zaragoza

Mayo 2023

A mis directoras,

Por haberme dado esta oportunidad, haberme acompañado en el camino, y haber apoyado mi desarrollo como investigadora.

Por los consejos y las enseñanzas.

A todas las personas que han pasado por el laboratorio, incluyendo a "los de enfrente" y "a los del otro lado", y a los que nos consideran sólo "compañeros/as"…

A todos aquellos que ya se han ido, a Sandra y a Silvia y en especial a Ernesto, por ser mi "papá del laboratorio", por enseñarme prácticamente todo lo que sé, por su paciencia y su dedicación, por ayudarme con todas mis preguntas y cuestiones aún a día de hoy.

Al que está a punto de terminar también, Tony, por su buena voluntad y su humor, por las risas que nos echábamos cada día, y por los traguitos disimulados de Limoncello de su nonna.

A los que se quedan, a Patricia, Andrea, Olga y Maribel, por ser mis primeros "pollitos" (algunas más que otras), y a Diego, Miguel y Víctor, por hacer del laboratorio un lugar en el que se podía estar, un lugar en el que trabajar con ganas, en el que divertirse y reírse, en el que cotillear y compartir. Por hacer divertidos hasta los días más pesados y por alegrar hasta los días más oscuros.

Por las risas y las confidencias.

Al profesorado y personal del departamento,

En especial a nuestras increíbles técnicos, Manoli, Fina y Esther, por todo su trabajo y esfuerzo, por su diligencia y rapidez solucionando cualquier problema, y a Marta Fajés, por su infinita asistencia con toda la horrible burocracia.

Por el apoyo y la ayuda.

A los patos,

Por los buenos ratos que hemos pasado olvidando las responsabilidades y obligaciones. Por los días de cervecitas y juegos, los días de tardeo en las terrazas, y los días de simplemente contarnos la vida. Por todos los buenos recuerdos, pasados, presentes y futuros.

Por la empatía y la compresión.

A mi familia,

A mis padres Carmen y Antonio, por su interés cándido en el bienestar de mis "bichitos", por aguantar e incluso fomentar mis clases magistrales en proteínas y ADN y esas cosas biológicas, y por estar siempre ahí cuando más lo necesitaba, animándome, apoyándome, y ayudándome a seguir.

A mis hermanos Borja y Leire, por su humor –a veces cuestionable– y su apoyo férreo.

Por el amor y el ánimo.

A Javi,

Por su dedicación inquebrantable a este curioso proyecto que es mi vida. Por ayudarme a superar los momentos más duros, por reírse conmigo en los momentos más divertidos, por ofuscarse más que yo en los momentos más injustos. Por preocuparse por mí, por ayudarme a ser feliz y por su fe inestimable.

Por estar siempre a mi lado y ayudarme a crecer en cada momento.

A todas las personas que me han acompañado en este viaje

"Around here, however, we don't

look backwards for very long.

We **keep moving forward**, opening up new doors and

doing new things, because we're curious...

and curiosity keeps leading us down new paths."

Walt Disney

INDEX

INDEX OF FIGURES AND TABLES

1. The Apoptosis–Inducing Factor Family

3. Experimental Procedures

4. Beyond a Platform Protein for the Assembly of the Degradosome

5. A Portray of Two Recently–Discovered Pathological Mutations of AIF

6. W483 IN THE APOPTOSIS INDUCING FACTOR

7. The Apoptosis Inducing Factor–Like

ABBREVIATIONS

4R–NADD	[4R–^{2}H]–NADD
4S–NADD	[4S–^{2}H]–NADD
ΔG	free Gibbs energy variation
ΔH	enthalpy variation
ΔS	entropy variation
ΔT_m	melting temperature variation
$\Delta \Psi_m$	mitochondrial transmembrane potential
aa	amino acid
Abs	absorbance
AFM	atomic force microscopy
AIF	apoptosis inducing factor
$AIF_{\Delta 77}$	AIF truncated from amino acid 1 to 77 (soluble mitochondrial form)
$AIF_{\Delta 101}$	AIF truncated from amino acid 1 to 101 (apoptotic form)
AIFL	AIF–like
$AIFL_{\Delta 64}$	AIFL truncated from amino acid 1 to 64 (complete form without unstructured N–terminus)
$AIFL_{65-168}$	AIFL with amino acids 65 to 168 (Rieske domain)
$AIFL_{\Delta 195}$	AIFL truncated from amino acid 1 to 195 (oxidoreductase and C–terminal domains)
AIFM1	apoptosis–inducing factor mitochondrion–associated 1
AIFM2	apoptosis–inducing factor mitochondrion–associated 2
AIFM3	apoptosis–inducing factor mitochondrion–associated 3
AMID	AIF–homologous mitochondrion associated inducer of death
^{app}MW	apparent molecular weight
APS	ammonium persulfate
BN–PAGE	blue native polyacrylamide gel electrophoresis
BS^3	bis(sulfosuccinimidyl)suberate

CD	circular dichroism
cDNA	coding DNA
CHCHD4	coiled–coil–helix–coiled–coil–helix domain containing 4
CMTX4	X–linked Charcot–Marie–Tooth disease type 4 (a.k.a. Cowchock syndrome)
CN–PAGE	clear native polyacrylamide gel electrophoresis
COXPD6	combined oxidative phosphorylation deficiency 6
C_p	heat capacity
CTC	charge transfer complex
CV	column volume
CypA	cyclophilin A
Da	Dalton (atomic mass unit)
DCPIP	2,6–dichlorophenolindophenol
DIN	DNA integrity number
DFNX5	deafness, X–linked 5 (a.k.a. auditory neuropathy, X–linked 1, with peripheral sensory neuropathy)
DNA	deoxyribonucleic acid
DNAse	deoxyribonuclease
dsDNA	double–stranded DNA
DT	deuterium ($^2_1$H) transfer
DTT	dithiothreitol
EDTA	ethylene diamine tetra acetic acid
EMSA	electrophoretic–mobility–shift assay
ESRT	endosomal sorting complexes required for transport
ESP	electrostatic surface potential
ESPRIT	expression of soluble proteins by random incremental truncation
ETC	electron transfer chain

et al.	and others
EtBr	ethidium bromide
FAD	flavin adenine nucleotide (oxidized)
$FADH^{\bullet}$	neutral flavin adenine nucleotide semiquinone
$FAD^{\bullet-}$	anionic flavin adenine nucleotide semiquinone
$FADH_2$	flavin adenine nucleotide (reduced)
Fe–S	iron–sulphur
FSP1	ferroptosis suppressor protein 1
gDNA	genomic DNA
H2AX	histone 2AX
Hsp70	heat shock 70–kDa protein
HT	hydride (^1_1H) transfer
IMM	inner mitochondrial membrane
IMS	intermembrane space
isc	iron–sulphur cluster
IPTG	isopropyl β–d–1–thiogalactopyranoside
ITC	isothermal titration calorimetry
K_a	association constant
k_{cat}	catalytic constant
K_d	dissociation constant
KIE	kinetic isotope effect
K_M	affinity constant
k_{obs}	observed constant
Kpi	potassium phosphate
LB	Luria–Bertani
MD	molecular dynamics

MEG3	maternally expressed 3 long non–coding RNA
MIM	mitochondrial inner membrane
miRNA	microRNA
MLS	mitochondrial localization sequence
MNNG	methylnitronitrosoguanidine
MW	molecular weight
N	binding stoichiometry
NAD^+	nicotinamide adenine dinucleotide (oxidized)
NADH	nicotinamide adenine dinucleotide (reduced)
NDE	external NADH dehydrogenase
NDI	internal NADH dehydrogenase
NDI1	rotenone–insensitive NADH–ubiquinone oxidoreductase
OD	optical density
O/N	overnight
ox	oxidized
OVA	ovalbumin
OXPHOS	oxidative phosphorylation
PAGE	polyacrylamide gel electrophoresis
PARP–1	poly [ADP–ribose] polymerase 1
PBS	phosphate buffered saline
PCD	programmed cell death
PDB	protein data bank
PP	PreScission Plus protease
PRG3	p53–responsive gene 3
Primary KIE	1° KIE
PTM	post–translational modification

PVDF	polyvinylidene difluoride
rd	reduced
RMSD	root–mean–square deviation
RMSF	root–mean–square fluctuation
RNA	ribonucleic acid
ROS	reactive oxygen species
rpm	revolutions per minute
RT	room temperature
SDS	sodium dodecyl sulfate
SEC	size exclusion chromatography
Secondary KIE	2° KIE
SEMDHL	X–linked spondyloepimetaphyseal dysplasia with hypo myelinating leukodystrophy
SF	stopped flow
ssDNA	single–stranded DNA
TBS(–T)	Tris buffered saline (with Tween)
TEMED	tetramethylethylenediamine
Thb	thrombin protease
T_m	Melting temperature
UV	ultraviolet
Vis	visible
WB	western blot
WT	wild–type

1. The Apoptosis Inducing Factor Family

Moonlighting proteins in the crosstalk between mitochondria and nuclei

Multicellular living organisations prioritise the overall development, reproduction and survival of the organism in detrition of any individual cellular consideration. Therefore, some biomolecules can be found performing functions that might be considered contradictory at first glance, but that are in fact essential to maintain cellular homeostasis. The proteins constituting the Apoptosis Inducing Factor (AIF) family are a clear example of such molecules, as they happen to be *moonlight* proteins that play a significant part in the critical decision *cell life or cell death* (Jeffery, 2014).

In *Homo sapiens*, this family is made up of three distinctive proteins that share three characteristics: mitochondrial localization in healthy cells, the presence of FAD– and NADH–dependent domains involved in an oxidoreductase function that is not well understood yet, and an apoptosis–inducing activity. All three proteins partake in the pool of more than 80 flavoproteins performing a multiplicity of functions in the human body, most of them being involved in oxido–reduction processes in the primary metabolism (Lienhart *et al.*, 2013). However, apart from these common characteristics the three human AIF proteins possess specific structural and functional features that envision for them distinctive mechanisms and physiological roles.

1.1. Phylogenetic Relationships in the AIF Family

The three members of the human AIF family are known as:

- The apoptosis inducing factor mitochondrion–associated 1 protein or apoptosis inducing factor, usually referred to as AIFM1 or simply AIF (UniProtKB – O95831 (AIFM1_HUMAN), gene – *aifm1*, located in the Xq26.1 cytogenetic locus)
- The apoptosis inducing factor mitochondrion–associated 2 protein, AIF–homologous mitochondrion–associated inducer of death or p53–responsive gene 3, known as AIFM2, AMID or PRG3, respectively (UniProtKB – Q9BRQ8 (FSP1_HUMAN), gene – *aifm2*, 10q22.1)
- The apoptosis inducing factor mitochondrion–associated 3 protein or apoptosis inducing factor–like, known as AIFM3 or AIFL (UniProtKB – Q96NN9 (AIFM3_HUMAN), gene – *aifm3*, 22q11.21)

As has been noted before, human AIFs share a flavin–dependent oxidoreductase domain (namely Pyr_redox_2 domain, Pfam ID PF07992) (*Fig. 1.1*) that envisages for

them a powerful role in oxidative respiration (Klim *et al.*, 2018). AIF and AIFL share 27% sequence identity in this domain, which decreases below 19% when comparing either of them to AMID (Xie *et al.*, 2005). In addition to the Pyr_redox_2 domain, AIF also holds a pro–apoptotic C–terminal domain (AIF_C, PF14721), while AIFL has an N–terminal Rieske domain (PF00355) and a reductase C–terminal domain (Reductase_C, PF14759). Such Rieske domains are often found in the mitochondrion electron transport chain (ETC) and in non–heme iron–dependent oxygenases, while Reductase_C domains are involved in the dimerization of putidaredoxin reductase and in the interaction of ferredoxin reductase with Rieske ferredoxins.

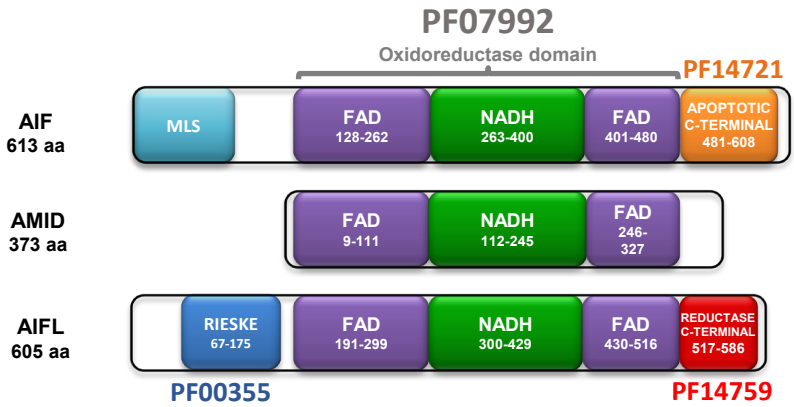

Figure 1.1. Predicted domains in the human AIF family. Scheme of domains and their overlapping in AIF, AMID and AIFL. The bipartite FAD–binding, NADH–binding, apoptotic C–terminal, Rieske and reductase C–terminal protein domains are respectively shown in violet, green, orange, blue and red, and the corresponding Pfam domain codes are specified. The region containing the mitochondrial localization signal (MLS) in AIF is shown in light blue. Residues comprising each domain are indicated.

Furthermore, sequence and phylogenetic analyses demonstrate significant homology among AIFs and NADH–oxidoreductases all the way from bacteria to mammalian species. In particular, AIF proteins are closely related to internal NADH dehydrogenases (NDI) of the rotenone–insensitive NADH–ubiquinone oxidoreductase type (NDI1), enzymes of mitochondrial inner membrane (MIM) localization that regulate NAD^+/H homeostasis, contribute to the ETC activity and are also apoptotic induction factors (Nguyen *et al.*, 2020).

Remarkably, chronology of evolution predicts a clear separation of AIF/AIFL from AMID/NDI1 (*Fig. 1.2*) (Elvitigala *et al.*, 2015; Klim *et al.*, 2018).

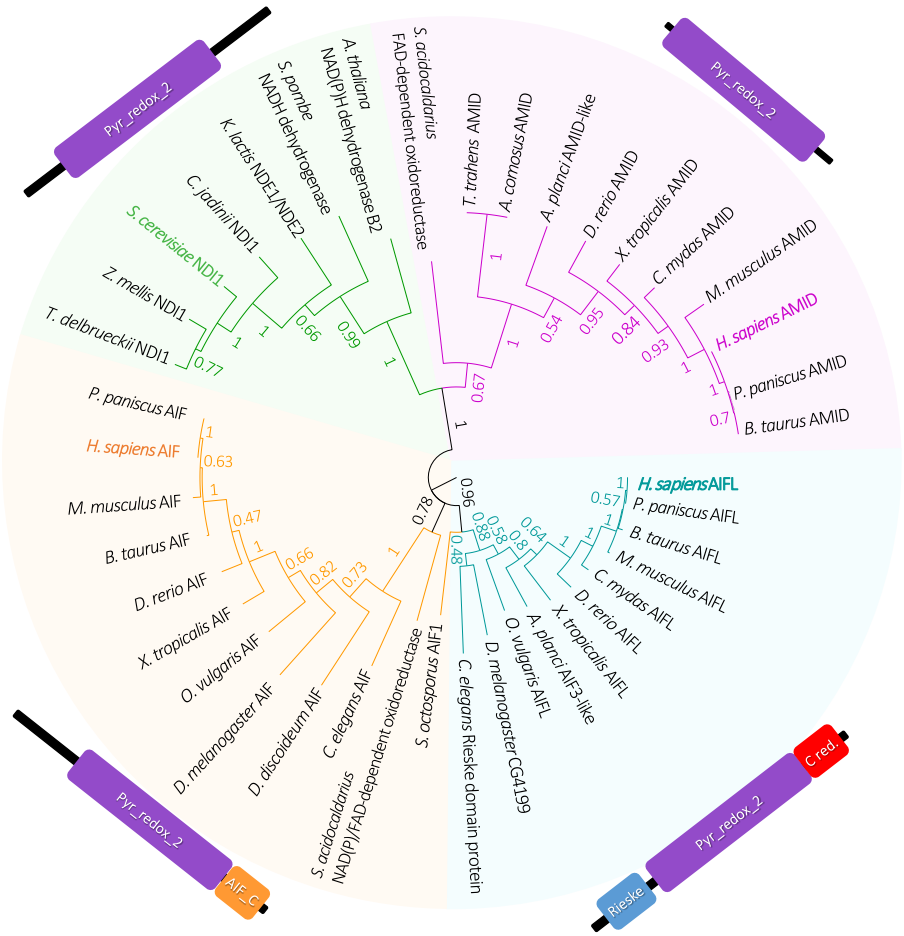

Figure 1.2. Phylogenetic tree of the AIF family and the NDI1 orthologue. Target sequences for *H. sapiens* AIF, AMID and AIFL and *Saccharomyces cerevisiae* NDI1 were obtained from the NCBI database, with references NP_004199.1, NP_001185625.1, NP_653305.1 and QHB10619.1 respectively. An individual protein BLAST alignment (https://blast.ncbi.nlm.nih.gov) was performed for each target sequence, and 10 sequences in the 30% to 99% identity range were selected for each one. All target and selected sequences were then globally aligned using the MUSCLE algorithm in the MEGA–X software (https://www.megasoftware.net) and a Maximum Likelihood tree was constructed. The Bootstrap method was used to test the tree, performing 500 replications. Bootstrap values are indicated beside each node. The Jones–Taylor–Thornton substitution model was chosen to construct the tree, setting the rates among sites as uniform. Tree inference was carried out through the Nearest–Neighbour–Interchange method. AIF, AMID, AIFL and NDI1 homologues appear highlighted in orange, purple, blue and green respectively. A simplified scheme showing the characteristic domains of each target protein appears beside each group of homologues, maintaining the colour code from figure 1.1.

The AIF/AIFL phylogenetic branch contains an AIF sub–branch with protein sequences from various ancient eukaryotic taxonomic clades, while the AMID and NDI1 sub–branches contain both eubacterial proteins and sequences from the five major ancient eukaryotic groups (Klim *et al.*, 2018; Li *et al.*, 2006). Such information predicts a eubacterial origin for AIFs and indicates divergence of AIF, AMID, AIFL and NDI1 sequences occurring before the divergence of eukaryotes (*Fig. 1.2*) (Klim *et al.*, 2018). This is further supported by domain architecture, since both eukaryotic and eubacterial AIF proteins contain the AIF_C domain (PF14721), while AIFL proteins contain the Rieske domain (PF00355) at its N–terminus.

1.2. Structural Features in the AIF Family

1.2.1. AIF's crystal structures

3D crystal structures within the human AIF family have only been reported for AIF (Ferreira *et al.*, 2014; Ye *et al.*, 2002), with structures also available for its homologous in *Mus musculus* (mAIF) (Mate *et al.*, 2002; Sevrioukova *et al.*, 2009). In these two species, AIF structures reveal similar organizations in the oxidised (AIF_{ox}) and in the reduced states (AIF_{rd}, in complex with the NAD^+ product and formed upon NADH oxidation), and lack the first approximately 127 residues (Ferreira *et al.*, 2014; Sevrioukova *et al.*, 2009). Homology modelling allows to predict a putative folding of this N–terminal region, not seen in crystal structures, that is compatible with its insertion mode in the MIM (*Fig. 1.3*).

1.2.1.1. Main structural motifs and environment of the FAD cofactor

AIF_{ox} folds into three structural domains, of which two constitute the oxidoreductase Pyr_redox_2 Pfam motif. This motif is formed by a discontinuous FAD–binding domain (aa 130–262 and 401–480 in AIF) and a NAD(P)H–binding domain (aa 263–400 in AIF), both of which are characterised by the classical Rossmann fold topology (*Fig. 1.3*). In agreement with the presence of this Pyr_redox_2 motif, AIF proteins are reduced by NAD(P)H (being NADH the preferred substrate) with hydride transfer (HT) from the coenzyme producing full reduction of the FAD cofactor, the concomitant formation of an exceptionally air–stable $FADH^-$:NAD^+ charge transfer complex (CTC) and the dimerization of the protein (Ferreira *et al.*, 2014; Miramar *et*

al., 2001; Sevrioukova *et al.*, 2009). The third AIF domain (aa 481–613 in AIF) constitutes the apoptotic AIF_C Pfam motif, which folds into five antiparallel β–strands followed by two α–helices.

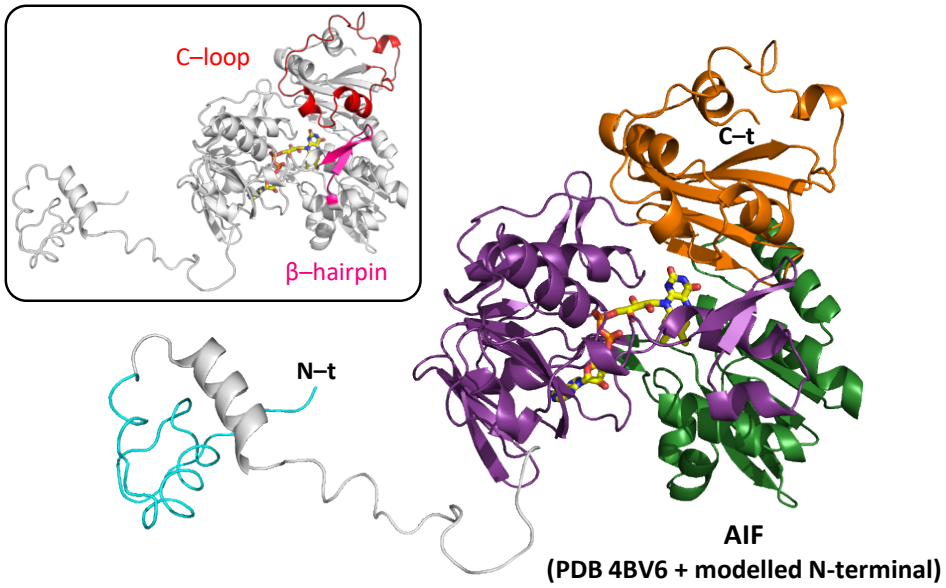

Figure 1.3. Structural features of AIF. Crystal structure of AIF (PDB 4BV6) with the N–terminal region modelled by homology modelling using the RaptorX server (http://raptorx.uchicago.edu/) and the protein sequence as input. The structure was prepared on PyMOL (Delano, 2002) and is shown as cartoon, with the FAD cofactor represented as sticks CPK coloured in yellow. Domain colours as in figure 1.1. The inset shows the same structure with the C–loop (509–560) and β–hairpin (190–202) highlighted in red and pink.

The isoalloxazine ring of the FAD cofactor is stabilised at the interface of the three domains, being partially accessible from the solvent, while the adenine, pyrophosphate and ribityl moieties reside in the FAD–binding domain. The AIF_C terminal motif is considered the pro–apoptotic domain, and it contains a potentially flexible region (aa 509–560 in AIF, known as regulatory C–loop) that occludes access to the redox active site. The regulatory C–loop, together with the 190–202 β–hairpin, constitute the two specific insertions of mammalian AIFs (Ferreira *et al.*, 2014). This region contains a Pro–rich motif (aa 544–554 in AIF), that is a potential recognition and interaction site for partners implicated in the regulation of different cellular processes, as well as a PEST–sequence (aa 529–560 in AIF) typically involved in protein–protein interactions. These regions can modulate calpain proteolytic activity, acting as a proteolytic signal via proteasomal degradation (Mate *et al.*, 2002).

1.2.1.2. Structural features of NADH binding

The crystal structure of NADH–reduced AIF confirmed formation and stability of $FADH^-$:NAD^+ CTC homodimers, as well as the presence of two sites for coenzyme binding per protein protomer (namely $NADH_A$ and $NADH_B$). This finding lead to the structure being baptized as AIF_{rd}:2NADH CTC (*Fig. 1.4* and figure 3 in Ferreira *et al.*, 2014).

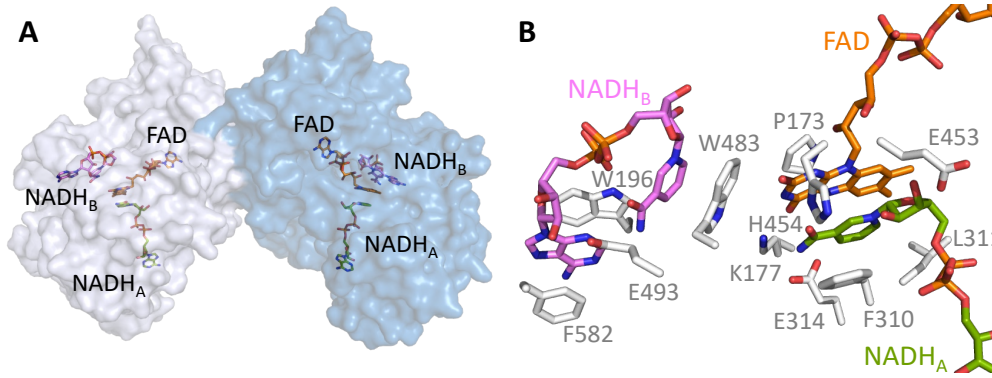

Figure 1.4. Structure of the AIF_{rd}:2NADH dimer and its binding sites. (**A**) Surface representation of the AIF_{rd}:2NADH dimer from its crystal structure (PDB 4BUR). Chain A is shown in white and chain B in sky blue. The cofactor and coenzymes are labelled and represented as sticks CPK coloured in orange for the FAD, in green for $NADH_A$ and in violet for $NADH_B$. (**B**) FAD and NADH binding sites, highlighting key residues involved in the network of H–bonds and hydrophobic stacking interactions. The cofactor and coenzymes are labelled and represented as in A. Key residues are also labelled and represented as sticks, CPK coloured in white.

The dimeric organization is stabilised by several H–bonds and salt bridges, creating an interface that involves residues 439–453 (Ferreira *et al.*, 2014; Sevrioukova *et al.*, 2009). The $NADH_A$ molecule, also known as *catalytic* NADH, shows an extended conformation with its nicotinamide stacking between the *re*–face of the FAD flavin and the F310 rings (*Fig. 1.4B* and figure 4 in Ferreira *et al.*, 2014). Its binding is stabilised through a H–bond network (involving G308, F310, L311, E314, E336, G399, E453, H454 and W483), with the side chains of K177, F310 and H454 shifting to allocate the $NADH_A$ nicotinamide portion (Ferreira *et al.*, 2014). Mutational analyses indicated that P173, K177 and E314 modulate active site conformation, flavin properties and affinity for NADH, while F310 and H454 create a compact active site essential for NADH binding, CTC stabilisation and strong NAD^+ affinity for the reduced state of the protein. $NADH_B$ binds at the *si*–face of the flavin, with W483

stacking at one side with its nicotinamide ring and at the other with the flavin ring, and W196, E493 and F582 also contributing to its binding (Ferreira *et al.*, 2014; Romero–Tamayo *et al.*, 2021; Villanueva *et al.*, 2015). Recent mutational analyses have also demonstrated that W196 modulates AIF's low efficiency as an oxidoreductase, assisting in the configuration of a noncompetent geometry for HT in its active site as well as boosting NAD^+ affinity to potentiate CTC stabilization (Romero–Tamayo *et al.*, 2021).

Transformation of AIF_{ox} into AIF_{rd}:2NADH induces conformational changes in the β–hairpin and in the C–loop, as well as in the dimerization interface (*Fig. 1.5* and figure 5 in Ferreira *et al.*, 2014). The C–loop in AIF_{ox} shows its 517–533 moiety folded into two short α–helices (517–524 and 529–533) that, together with W483, decrease solvent accessibility to the flavin active site and are stabilised by interactions with side–chains of the 190–202 β–hairpin, particularly R201 (Villanueva *et al.*, 2019). These two short helices become disordered in AIF_{rd}:2NADH, being their position occupied by $NADH_B$, while access of its nicotinamide to the flavin ring remains blocked by W483. This second coenzyme molecule is envisaged to allosterically regulate some protein functions (Brosey *et al.*, 2016; Ferreira *et al.*, 2014; Ferreira *et al.*, 2018; Sorrentino *et al.*, 2015).

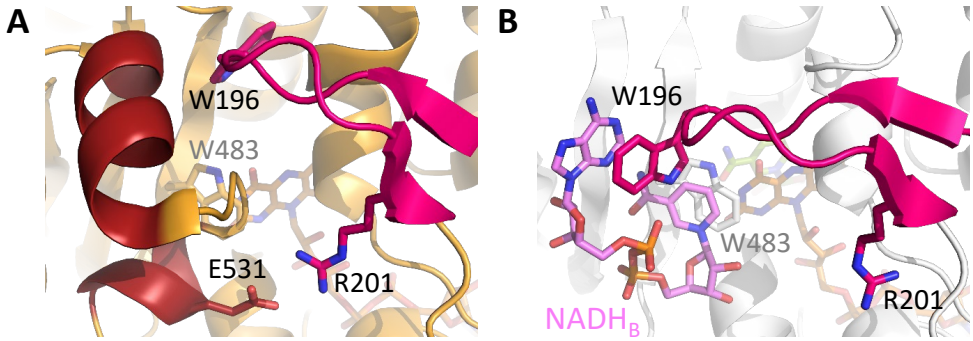

Figure 1.5. Conformational changes in AIF after NADH–induced dimerization. Cartoon representation of (**A**) AIF_{ox} and (**B**) AIF_{rd}:2NADH (PDB 4BV6 and 4BUR respectively) CPK coloured in light orange and white respectively. Key residues are labelled and represented as sticks. The cofactor and coenzymes are represented as in figure 1.4. The 190–202 β–hairpin and the 517–533 C–loop moiety (folded in A into two short α–helices, comprising residues 517–524 and 529–533 respectively, and disordered in B) are CPK coloured in red and pink.

1.2.2. Homology modelling of AMID and AIFL

Although 3D structures have not been solved yet for either AMID or AIFL in any species, homology modelling has been employed to fill this gap (*Fig. 1.6*). AMID has been modelled using as template the structure of a type II NADH:quinone oxidoreductase, a respiratory enzyme found in the ETC of many species with the exception of mammals. Conversely, two templates were required to generate the AIFL model: its Rieske moiety was modelled from the corresponding domain of a dioxygenase, while a ferredoxin reductase was employed for its Pyr_redox_2 and Reductase_C domains.

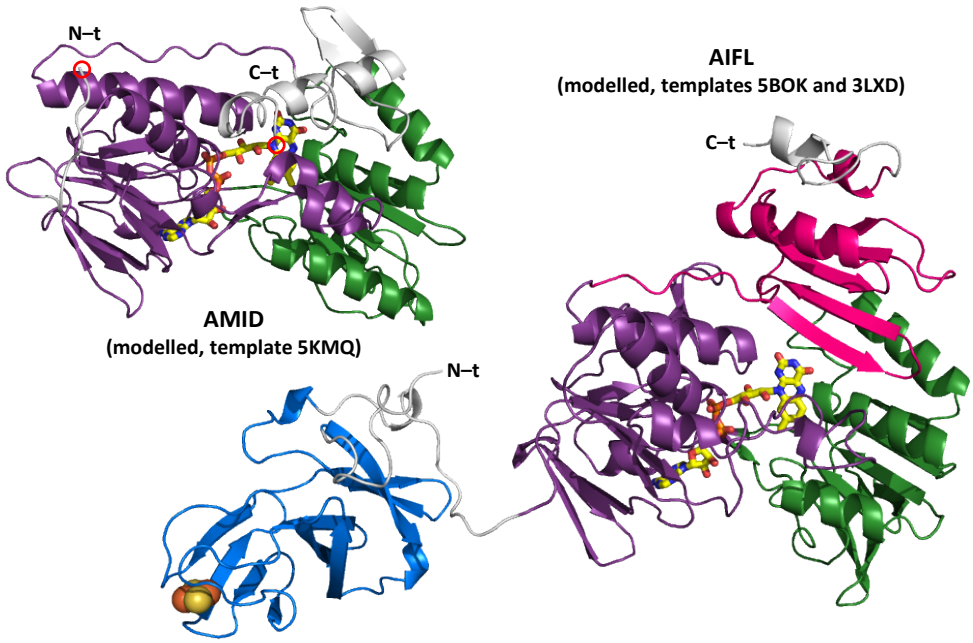

Figure 1.6. Structural models of AMID and AIFL. Models were generated by homology modelling using the RaptorX server (http://raptorx.uchicago.edu/) and the protein sequence as input. Templates were selected based on sequence identities to the target sequence. AMID was modelled using as template a variant of *Caldalkalibacillus thermarum* type II NADH dehydrogenase (PDB 5KMQ, 21% SeqID). AIFL required the use of two templates, the ferredoxin component of the 3–nitrotoluene dioxygenase from *Diaphorobacter* sp. strain DS2 (PDB 5BOK, 17% SeqID) for its Rieske domain and ferredoxin reductase ArR from *Novosphingobium aromaticivorans* (PDB 3LXD, 26% SeqID) for its Pyr_redox_2 and Reductase_C domains. Structures were prepared on PyMOL (Delano, 2002) and are shown as cartoon, with the FAD cofactor represented as sticks CPK coloured in yellow and the Fe–S cluster as spheres. Domain colours as in figure 1.1.

The FAD–binding and NAD(P)H–binding domains of the AMID and AIFL models predicted a similar overall folding topology to AIF, with the isoalloxazine moiety of the FAD cofactor sitting between domains in much the same manner.

1.2.3. Sequence conservation in the AIF family

Plotting sequence conservation of each protein among species on top of their 3D models showed highly conserved cores for AIF and AIFL at the FAD and NADH binding sites (*Fig. 1.7*). Even though the C–terminal domain of AIF is significantly conserved, this is not the case for its C–loop, in agreement with it being an insertion compared to structurally–related proteins. Conservation in the Rieske domain of AIFL concentrates around the iron–sulphur (Fe–S) cluster, while the Reductase_C domain shows particular conservation in regions pointing to the protein redox sites.

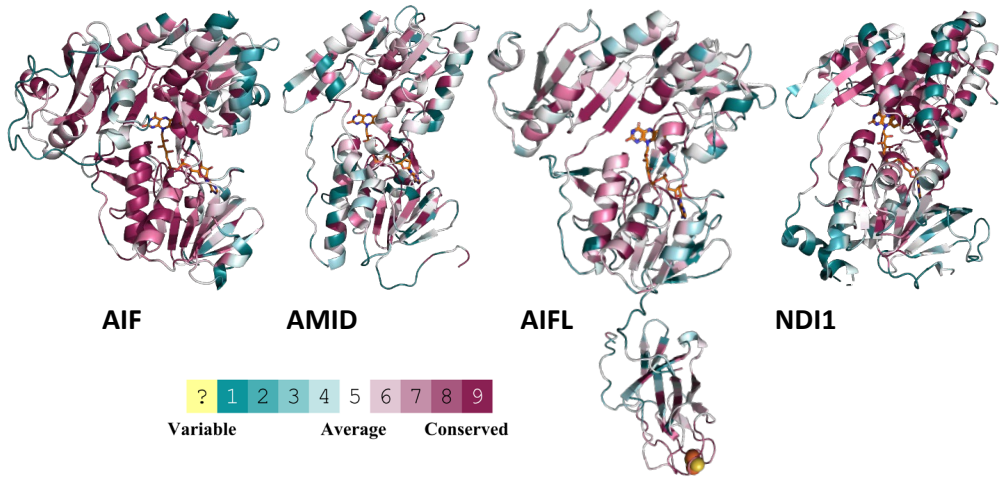

Figure 1.7. Overall residue conservation in the human AIF family and yeast orthologue NDI1. Conservation was calculated by the ConSurf server (https://consurf.tau.ac.il) and figures were subsequently prepared using PyMOL. For AIF and NDI1 available crystal structures were used as input (PDB 4BV6 and 4G9K respectively). For AMID and AIFL the protein sequence was provided in FASTA format (NP_001185625.1 and NP_653305.1 respectively) and the server generated the structural models using MODELLER (https://salilab.org/modeller/). The ConSurf server automatically selected the homologues and made a multiple sequence alignment for each target. Structures are shown as cartoon coloured according to conservation score (from deep teal, less conserved, to deep maroon, most conserved), with the FAD cofactor represented as sticks CPK coloured in orange and the Fe–S cluster as spheres.

Upon a closer look to the redox site of these models, high identity of residues shaping the cavities for the isoalloxazine ring of the FAD and the nicotinamide of $NADH_A$ can be observed (*Fig. 1.8*). Specifically, E314 in AIF, a residue identified as key to set up the holo–enzyme active site conformation (Villanueva *et al.*, 2015), is exceptionally conserved throughout all family members, broadcasting its critical role. Furthermore, most residues in the AIF active site are highly conserved, not only among AIF enzymes but also in the AIFL ones (*Fig. 1.8A, C*), hinting to a similar NADH oxidizing function. The active sites of AMID and NDI1 are in general more variable, with the latter exhibiting a more conserved site among species than the former (*Fig. 1.8B, D*).

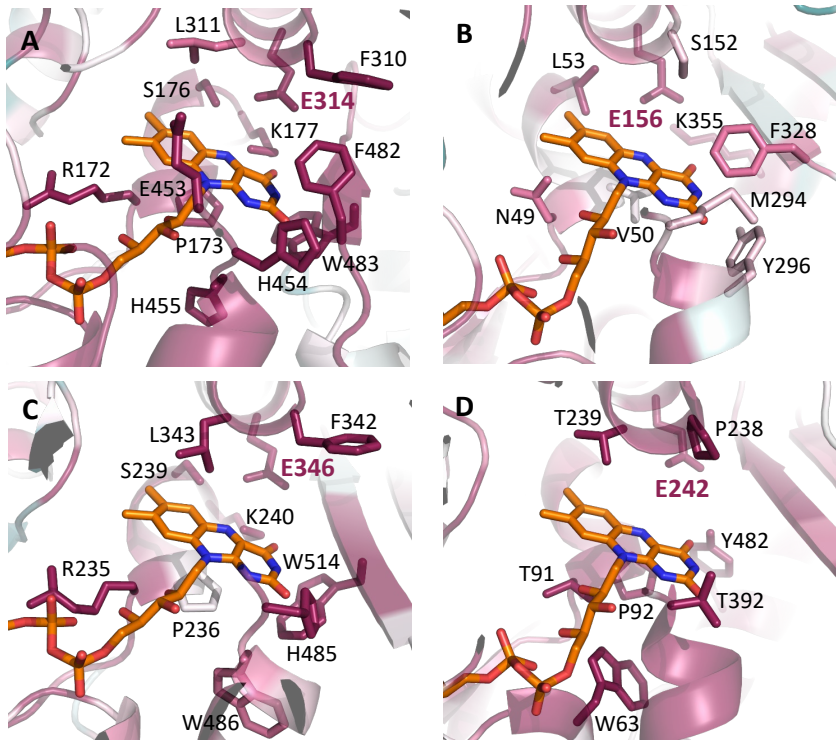

Figure 1.8. Residue conservation around the FAD cofactor in the human AIF family and yeast orthologue NDI1. Residue conservation score around the N5 of the FAD cofactor in (**A**) AIF, (**B**) AMID, (**C**) AIFL and (**D**) NDI1 respectively. Conservation was calculated and figures were prepared as in figure 1.7. A glutamate residue (E314 in AIF) is highly conserved throughout all structures, reinstating its essential role in the cofactor's redox environment. Other identical residues can be found between the structures, particularly in the case of AIF and AIFL.

Electrostatic surface potential (ESP) analyses of the proteins show localized patches with either positive or negative charges distributed on the protein surfaces (*Fig. 1.9*),

suggesting they might be involved in the modulation of biomolecular interactions, catalytic rates and mid–point reduction potentials (E_m) in a pH–dependent manner (Zhou *et al.*, 2018). AIF, AMID and AIFL contain therefore homologous domains as well as specific domains, indicating that they share both pro–death and pro–life traits. Nonetheless, the precise roles of their apoptogenic, oxidoreductase and Rieske domains remain far from being fully explored or, in some cases, even known.

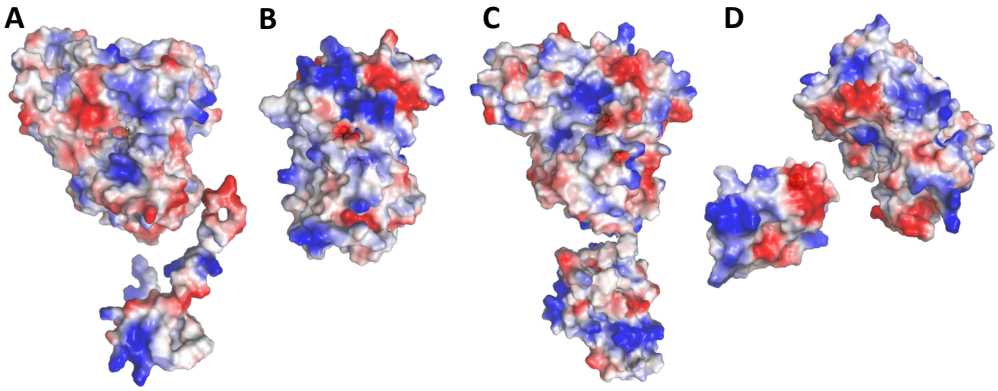

Figure 1.9. ESP in the human AIF family. ESP of (**A**) AIF, (**B**) AMID, (**C**) AIFL and (**D**) a docking pose coupling the Rieske and oxidoreductase domains of AIFL. Net positive charges are coloured blue, negative charges red, and neutral ones white. Structures are represented with surface transparency set to 20%, the FAD cofactor as sticks CPK coloured in orange and the Fe–S cluster as spheres. Panels A, B and C correspond to the structures of figures 1.3 and 1.6, while panel D was generated by the ClusPro server (https://cluspro.bu.edu/) through the docking of the oxidoreductase (receptor) and Rieske (ligand) domains of AIFL. PDB files of each domain were used as the only input, each extracted from the complete AIFL model in figure 1.6. Docking structures were evaluated based on shape complementarity, electrostatic interactions and desolvation contributions, after which only the 10 lowest-energy structures were provided as output. Structure D reflects the possibility of an electrostatic attraction between the Rieske domain (with a net negative charge at the interface) and the oxidoreductase domain (with a net positive charge at the interface) of AIFL, which could promote their hypothetical interaction.

All three proteins are synthesized in the cytosol but localize in the mitochondrial intermembrane space (IMS) in healthy cells, presumably anchored to the MIM (Nguyen *et al.*, 2020; Xie *et al.*, 2005). However, only AIF presents a canonical bipartite mitochondrial localization sequence (MLS) in its N–terminus (aa 1–37 and 63–89), although the N–terminus of AMID and the Rieske domain of AIFL are still thought to contribute to their mitochondrial localization.

1.3. The AIF Family in Cell Death

Since most of the main apoptotic factors were already encoded in the proto–mitochondrion and have eubacterial origin, the mitochondrial programmed cell death (PCD) machinery can be considered to be an ancient adaptation that has evolved to its current form. Taken together, AIF, AMID and AIFL are homologous proteins that localize to the mitochondria of healthy cells and that share pro–death activity within the apoptosis intrinsic pathway. However, different domains appear to hold said activity in each of these three proteins, indicating that the mechanisms of PCD activation could also be diverse and still far from fully understood (Kaczanowski 2016). Moreover, discrepancies can be found among the literature in regards to these cell death roles (Bilyy *et al.*, 2008; Elvitigala *et al.*, 2015; Gong *et al.*, 2007; Kojima *et al.*, 2015; Lu *et al.*, 2016; Miriyala *et al.*, 2016; Xie *et al.*, 2005), which may suggest compensatory activity of the members of the AIF family in different *in vivo* situations.

1.3.1. The pro–death activity of AIF

AIF gives name to the family, being the best characterised member at the molecular, biochemical and cellular levels. It was first described as a caspase–independent apoptosis effector that translocates from mitochondria to the nucleus following pro–apoptotic stimuli, where it has been shown to act as a mediator of necrotic poly (ADP–ribose) polymerase (PARP)–1–dependent cell death (parthanatos) (Alano *et al.*, 2010; Modjtahedi *et al.*, 2006; Modjtahedi *et al.*, 2015; Susin *et al.*, 1999). In healthy cells, AIF is synthesised in the cytosol and immediately sent to the mitochondria thanks to its N–terminal MLS (*Fig. 1.10*). The first portion of the bipartite MLS is proteolytically truncated once in the IMS, generating the $AIF_{\Delta 54}$ mature mitochondrial isoform that uses the transmembrane region (aa 67–83) of the second MLS to anchor to the MIM (Modjtahedi *et al.*, 2006; Otera *et al.*, 2005; Robinson and Lemire, 1996). However, after an apoptotic insult, the $AIF_{\Delta 54}$ mitochondrial isoform is cleaved, producing the $AIF_{\Delta 101}$ soluble pro–apoptotic form, which can subsequently travel from the IMS into the cytosol. The regulatory mechanism by which AIF is released is still not understood, but it might be modulated by its structural reorganization due to depletion of NADH coenzyme levels during PARP–1 hyperactivation (Alano *et al.*, 2010).

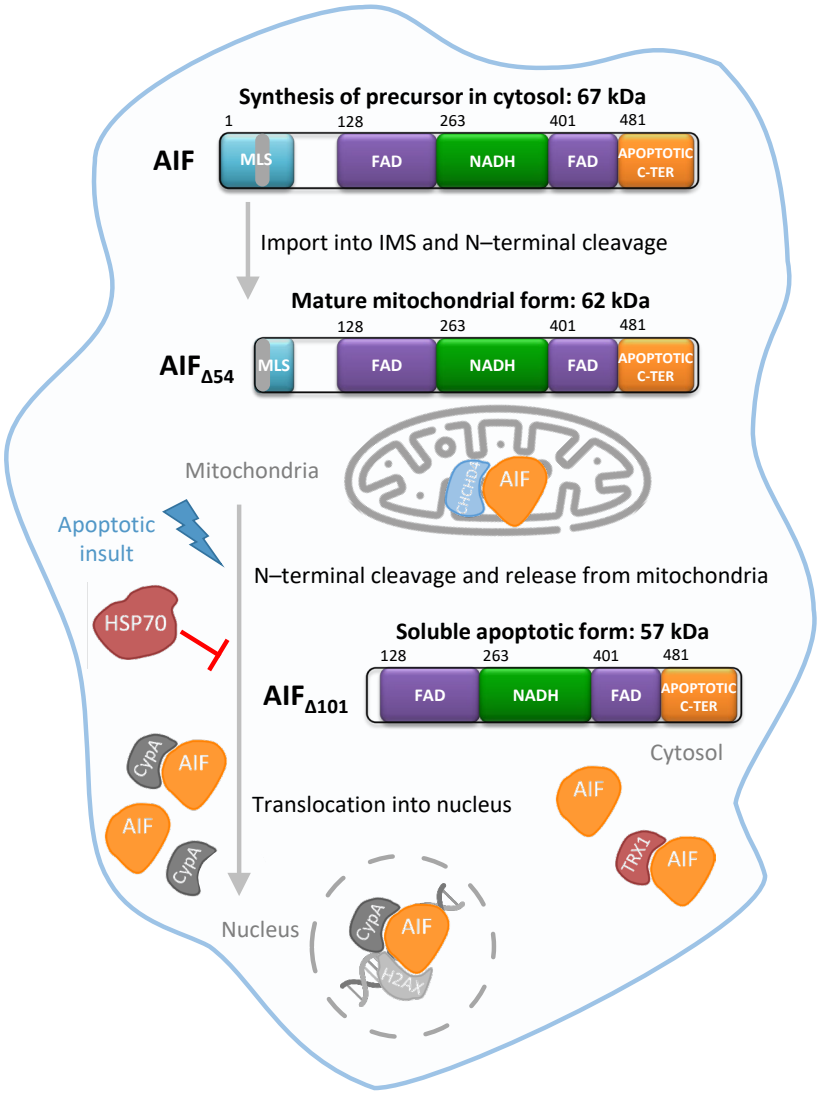

Figure 1.10. AIF processing, subcellular localization and partners. AIF is synthesised by cytoplasmic ribosomes and subsequently imported into the mitochondrial IMS. There, the first portion of its N–terminal MLS is cleaved to generate its mature mitochondrial form, which is anchored to the MIM through the transmembrane region of its remaining MLS. Thanks to its interaction with partner CHCHD4, AIF can then perform its pro–life function. However, upon an apoptotic insult, AIF is cleaved again and subsequently released from the mitochondria. In the cytosol, it can interact with HSP70 or with CypA in antagonistic manners. Its interaction with reduced TRX1 further inhibits its apoptotic activity, promoting interaction with HSP70. If the AIF:CypA complex is favoured, the proteins are co–translocated to the nucleus (alternatively, they could be translocated separately), where they interact with H2AX to form the degradosome. This complex can bind DNA, inducing its degradation.

$AIF_{\Delta 101}$ can interact in the cytosol with heat shock 70–kDa protein (HSP70) or with endonuclease cyclophilin A (CypA) in antagonistic and redox–controlled manners that further regulate its subcellular localization (Choudhury *et al.*, 2011; Gurbuxani *et al.*, 2003). The interaction of $AIF_{\Delta 101}$ with reduced thioredoxin TRX1 in the cytosol regulates its redox status, promoting its interaction with the cell death regulator HSP70 and its retention in this compartment (Ravagnan *et al.*, 2001), which, as a consequence, attenuates its lethal action (Shelar *et al.*, 2015) and induces cellular survival (Choudhury *et al.*, 2011; Gurbuxani *et al.*, 2003; Ravagnan *et al.*, 2001).

On the contrary, under pro–apoptotic oxidative stress conditions, TRX1 becomes oxidised and the cytosolic TRX1:AIF complex dissociates, favouring the potential formation of the AIF:CypA complex instead and the nuclear co–translocation of these two proteins (Cande *et al.*, 2004; Farina *et al.*, 2017; Shelar *et al.*, 2015; Zhu *et al.*, 2007). Alternatively, AIF and CypA may translocate into the nucleus separately and interact once there, before or after recruiting histone H2AX. This network of interactions ultimately leads to the assembly of the AIF–mediated DNA degradation complex, AIF:CypA:H2AX, known as *degradosome* (Artus *et al.*, 2010). This complex can bind DNA and promote its degradation into 20– to 50–kb fragments, consequently inducing chromatin condensation and cell disassembly (Cande *et al.*, 2004; Farina *et al.*, 2017; Susin *et al.*, 1999; Zhu *et al.*, 2007).

However, the molecular mechanisms by which the degradosome is formed, as well as by which it acts as a death effector, are not well understood yet, with many details of the exact role of AIF in PCD in different cell types still lacking.

1.3.2. The pro–death activity of AMID

Similar to AIF, AMID is activated in response to lethal signals and toxicological stress, and translocates from mitochondria to the nucleus to bind DNA, promoting caspase–independent nuclear apoptosis by chromatin condensation and large–scale DNA fragmentation (Bilyy *et al.*, 2008; Gong *et al.*, 2007; Lu *et al.*, 2016; Miriyala *et al.*, 2016). Heterologous expression of AMID and its truncated domains revealed that this protein induces caspase–independent apoptosis through its C–terminus, suggesting that its oxidoreductase activity might be dispensable for some of its cell death functions (Li *et al.*, 2006; Ohiro *et al.*, 2002; Ohyama *et al.*, 2015; Wu *et al.*, 2002).

AMID binds DNA, both in its holo and apo forms, but lacks apparent DNA sequence specificity, as is the case for AIF. A major protein conformational change is proposed upon formation of the AMID:DNA complex, while the presence of the nicotinamide coenzyme has a deleterious effect on DNA binding. On its side, DNA binding suppresses the enzyme's redox activity (Gong *et al.*, 2007; Marshall *et al.*, 2005). This antagonism in the binding of these two ligands suggests a clear mechanistic connection between coenzyme and DNA binding, redox activity and apoptotic function for AMID.

In this context, it has been suggested that the interaction of AMID with foreign DNA (from a bacterial or viral infection, or because of a leakage from the mitochondria during apoptosis) might contribute to the onset of cell death by lessening survival cell signalling (Gong *et al.*, 2007). The *aifm2* gene was initially recognized as a p53 target gene whose expression was induced in human colon cancer cells undergoing p53–dependent apoptosis. Expression of *aifm2* was reported as upregulated by the p53 tumour suppressor protein (whose inactivation is observed in a large number of human cancers) as well as by genotoxins, but downregulated in tumours. These observations initially pointed to AMID being involved in the p53–induced downstream effects such as growth arrest or apoptosis, becoming a potential tumour suppressor gene (Horikoshi *et al.*, 1999; Ohiro *et al.*, 2002; Wu *et al.*, 2004).

However, more recent studies suggest that AMID does not play any critical, non–redundant role for normal development and p53–mediated tumour suppression (di Salvo *et al.*, 2017; Mei *et al.*, 2006). In fact, *aifm2* knockdown studies in a mouse erythroleukemia cell line did not produce apparent difference in cell death regarding control cells, but envisaged a potential function in cell differentiation (Kojima *et al.*, 2015). Little is known yet regarding the diverse functions that AMID might support in cell death and differentiation, and further studies will be required to clarify its relevance under diverse physiological situations.

1.3.3. The pro–death activity of AIFL

Contrary to AIF and AMID, AIFL does not translocate to the nucleus and it is the only family member that induces caspase–dependent apoptosis (caspase–3 activation) (Xie *et al.*, 2005). AIFL induces apoptosis via mitochondrial depolarization (either increasing membrane permeability or being released itself from the mitochondria under special situations) mediated by cytochrome c release and caspase–3 activation.

HEK293 cells transfected with full–length AIFL or its Rieske domain, but not with the oxidoreductase domain, produced apoptosis. Thus, the AIFL Rieske domain may both induce apoptosis and promote protein mitochondrial localization.

Nevertheless, the manner in which AIFL affects mitochondrial permeability, as well as if this protein might interact with other proteins during apoptosis initiation and execution, remain unknown (Xie *et al.*, 2005). In this later point, a recent bioinformatics study suggests that AIFL might interact with protein tyrosine phosphatase nonreceptor–type12, which facilitates cellular detachment by acting on an unidentified substrate and activating caspase–3, and contributes to control ephrin type–A receptor 3 phosphorylation and ephrin–induced cytoskeletal remodelling (Sun *et al.*, 2011; Zheng *et al.*, 2019). Here, it is also worth to mention that expressional modulation of the AIFL homologue from disk abalone (*Haliotis discus discus*) is induced by different chemicals, which might also envisage, at least in this species, a putative significance for its PCD activity in host innate immune responses against microbial invasions (Elvitigala *et al.*, 2015). As is the case for AMID, all the diverse functions that AIFL might aid in PCD, as well as its molecular mechanisms, are still incredibly far from being known.

1.4. The Mitochondrial Pro–Life Role of the AIF Family

1.4.1. The pro–life activity of AIF

Many apoptotic factors, such as the members of the AIF family, happen to have non–apoptotic functions as well (Kaczanowski, 2016). AIF in particular is synthesised in the cytoplasm of multiple organs and reaches its native conformation in their mitochondria, where it exerts a vital function in cell bioenergetics (Ferreira *et al.*, 2014; Modjtahedi *et al.*, 2015).

AIF regulates OXPHOS and energy homeostasis by assisting biogenesis and/or stabilisation of multi–subunit respiratory chain complexes, through its interaction with the human chaperone coiled–coil–helix–coiled–coil–helix domain containing 4 protein (CHCHD4) (*Fig. 1.11*) (Ferreira *et al.*, 2018; Hangen *et al.*, 2015; Modjtahedi *et al.*, 2015; Modjtahedi *et al.*, 2016). AIF controls the import and proper localisation of CHCHD4, which in turn is in charge of the mitochondrial import and oxidative folding of certain subunits of the respiratory complexes and assembly factors

(Erdogan *et al.*, 2018). In particular, a recent study in HEK293 cells lacking AIF demonstrated that, while expression levels of CHCHD4 remained stable, the protein was unable to efficiently interact or mediate the import of its substrates. This effect was especially suffered by NDUFS5, a subunit of complex I, which accumulated in the cytosol and was degraded, leading to a critical stall in complex I assembly (Salscheider *et al.*, 2022). As a consequence, defects in AIF give rise to major dysfunctions in OXPHOS, secondary to the deficiency of CHCHD4, causing severe neurodegenerative illnesses (Meyer *et al.*, 2015; Modjtahedi *et al.*, 2016).

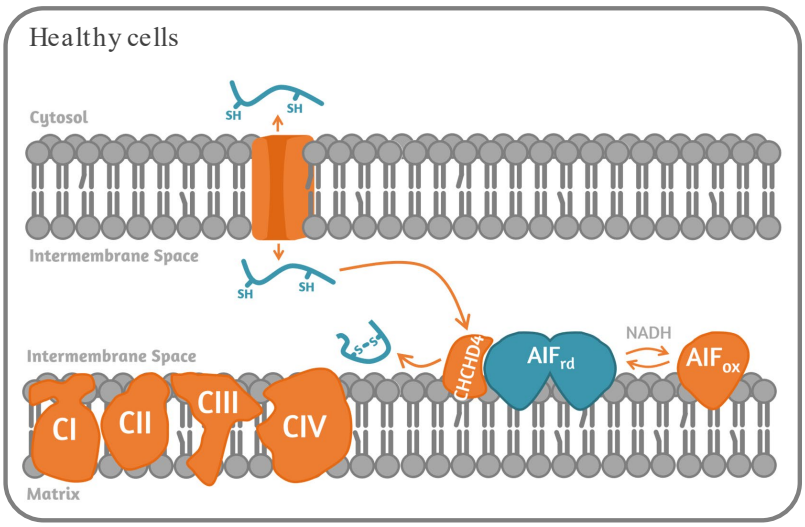

Figure 1.11. Schematic representation of AIF's pro–life role in mitochondria. The mature mitochondrial isoform of AIF is found anchored to the MIM, in an equilibrium between its oxidised and reduced forms that depends on the concentration of NADH. In its reduced form, AIF can interact with partner CHCHD4, aiding the import and folding of some of the proteins that make up the respiratory chain complexes.

However, the molecular bases that regulate this redox–dependent interaction remain yet largely unknown. Similarly, *in vivo* electron acceptors of the AIF oxidoreductase activity have not been described up to date, but it is suggested that its interaction with other molecules might be modulated by its redox NADH–dependent monomer–dimer transition (Ferreira *et al.*, 2014). Moreover, the binding of the second coenzyme molecule, $NADH_B$, is proposed to allosterically regulate the monomer–dimer transition, additionally attributing to AIF a function as a sensor of the mitochondrial redox state (Brosey *et al.*, 2016; Ferreira *et al.*, 2014; Ferreira *et al.*, 2018; Sorrentino *et al.*, 2015).

A recent study using a novel AIF–deficient mouse model has also confirmed that its deficiency destabilises mitochondrial ETC and induces supercomplex disorganization, mitochondrial transmembrane potential loss, and high generation of mitochondrial reactive oxygen species (ROS) (Delavallée *et al.*, 2020). This model shows AIF as a key factor regulating cell differentiation and fate, possibly through its key roles in controlling the mitochondrial OXPHOS/metabolism.

1.4.2. The pro–life activity of AMID

Contrary to AIF, AMID is a lipid–droplet–associated NADH oxidase specific to brown adipose tissue, where it is induced by cold exposure and diet (Nguyen *et al.*, 2020). In these tissues, AMID associates with the outer side of the MIM, increasing mitochondrial activity to regenerate cytosolic NAD^+ for robust glycolysis and to support the ETC for thermogenesis.

As a consequence, the NADH oxidase activity of AMID is a requirement for its effect on glycolysis and the subsequent glucose oxidation to maximize thermogenesis, functioning, once translocated to the mitochondria, as a mammalian external NADH dehydrogenase (NDE) (similar to yeast NDE1). In fact, this activity was also proven after reconstitution of bacterial or mitochondrial membranes with either AIF or AMID, as both displayed NADH oxidation and were able to support NADH–linked proton pumping activities in the host membranes almost as efficiently as NDE1 (Elguindy and Nakamaru–Ogiso, 2015). The *in vitro* evaluation of the biochemical and enzymological properties of AMID further confirmed its NAD(P)H oxidase activity, being able to catalyse the NAD(P)H–dependent reduction of cytochrome *c* and other electron acceptors (including molecular oxygen).

It has also been determined that, unlike AIF or AIFL, AMID has a 6–hydroxy–FAD cofactor instead of an FAD and favours NADPH binding over NADH (Marshall *et al.*, 2005; Wu *et al.*, 2002). The latter studies have also demonstrated a regulation of the AMID NAD(P)H oxidase activity by the binding of exogenous DNAs, and point to an opportunity to regulate the production of ROS through the control of its oxidoreductase activity.

Finally, a new role has recently been identified for AMID as an endogenous suppressor of glutathione–independent ferroptosis, a non–apoptotic form of regulated necrosis triggered by activation of iron–dependent oxidative stress pathways (Dai *et al.*, 2020). In this mechanism, the oxidoreductase activity of AMID regenerates ubiquinone to

ubiquinol, which traps lipid peroxyl radicals to prevent peroxidative damage of lipids. For this reason, AMID has been baptized ferroptosis suppressor protein 1 (FSP1) (Doll *et al.*, 2019).

1.4.3. The pro–life activity of AIFL

The ubiquitous expression of AIFL and its primary localization in the MIM envisages a housekeeping non–apoptogenic function in mitochondria. Even though the oxidoreductase domain of AIFL is expected to play a role in such functions, these are far from being clarified as of date (Xie *et al.*, 2005).

Contrary to AIF or AMID, where the final electron acceptor is not known, the Rieske [2Fe–2S] cluster could play such a role in AIFL, as well as scavenging free radicals to promote cell survival. Thus, AIFL might contribute to maintenance of complex I of the ETC, but the molecular mechanisms of its mitochondrial targeting need extensive investigation. AIFL has also been identified as N–myristoylated, a feature that is shared by many proteins playing key roles in regulating cellular structure and function and that is also found in many disease–related proteins (Takamitsu *et al.*, 2015). A recent study in human kidney development actually found AIFL to be of significant importance in energy production in nephrogenesis and tubular maturation, promoting cell survival (Lozic *et al.*, 2021).

Transcripts lacking the oxidoreductase domain of AIFL (produced by intron retention) have been described in human and in medaka (Japanese rice fish) (Murata *et al.*, 2011; Xie *et al.*, 2005). Studies in the latter envisage a tissue–specific function for the short Rieske transcript and full–length AIFL. In this organism, AIFL is particularly abundant in the brain, suggesting it functions as a radical scavenger for proper development and maintenance of the nervous system. On its self, the short Rieske transcript induces changes in mitochondria morphology and growth arrest and, contrary to full–length AIFL, is prone to localize in the nucleus (Murata *et al.*, 2011).

Altogether, diverse physiological functions seem to be predicted for the flavin dependent oxidoreductase domain of the members of the AIF family, many of which, particularly in the cases of AMID and AIFL, must still be thoroughly researched.

1.5. The AIF Family in Health and Disease

Members of the AIF family support different functions in cell physiology, metabolism and bioenergetics, which also contribute to stress–induced or pathological cell death. Therefore, enhancement or impairment of the capacities of these proteins under different scenarios can be the cause of different phenotypes or pathologies.

In addition, the *aifm1*, *aifm2* and *aifm3* genes happen to be targets of various microRNAs (miRNA). These molecules are small non–coding RNAs that, in general, negatively regulate the expression of target genes and can be packaged into exosomes to modulate cellular response of recipients (Grimson *et al.*, 2007). The DIANA–TarBase v8, a reference database devoted to the indexing of experimentally supported miRNA targets, identifies *aifm1*, *aifm2* and *aifm3* as targets of up to 11, 10 and 4 miRNAs respectively (*Annex I*) (Karagkouni *et al.*, 2018). Searches in prediction databases, such as the miRDB database (Chen and Wang, 2020), increase these numbers considerably. Therefore, as many other components of apoptosis–related signalling pathways, the three AIF proteins as well as their corresponding genes and mRNAs, can also be envisaged as therapeutic targets and biomarkers.

1.5.1. AIF in health and disease

For one, AIF is able to exert a cell–killing effect via caspase–independent apoptosis in cancer cells, increasing sensitivity to chemotherapy and being the releasing target of several cytotoxic drugs that cause apoptosis (Lee *et al.*, 2006; Millan and Huerta, 2009; Yu *et al.*, 2006). However, its NADH oxidase activity can also play a contributory role to the growth and aggressiveness of a variety of cancer types and tumour metastases, including colorectal, prostate, and pancreatic cancers (Jeong *et al.*, 2006; Lewis *et al.*, 2012; Scott *et al.*, 2016; Urbano *et al.*, 2005). This redox activity regulates metabolism but can also increase ROS levels and promote oxidative damage (Scott *et al.*, 2018). Furthermore, AIF overexpression has also been shown to aggravate hypoxic–ischemic brain injury in neonatal mice (Li *et al.*, 2020).

The *aifm1* gene is additionally the target of several miRNAs involved in the regulation of multiple cellular processes (including protein phosphorylation, cell fate commitment, heart rate and myotube differentiation, cardiac muscle hypertrophy and contraction, gene silencing, necrotic cell death, cell population proliferation and cytokine production, among others) (*Annex I*). The action of some of these miRNAs

is specifically related to hematologic and uterine cervical neoplasms as well as to B–cell chronic lymphocytic leukaemia.

On top of that, AIF is particularly pertaining to a significant number of rare mitochondrial diseases that course with severe neurodegeneration in patients of different ages, specifically resulting in acute paediatric mitochondriopathies and tumour metastases caused by over 25 point mutations in its gene (*Fig. 1.12*) (Ardissone *et al.*, 2015; Bano and Prehn, 2018; Berger *et al.*, 2011; Bogdanova–Mihaylova *et al.*, 2019; Diodato *et al.*, 2016; Ghezzi *et al.*, 2010; Heimer *et al.*, 2018; Kettwig *et al.*, 2015; Miyake *et al.*, 2017; Morton *et al.*, 2017; Pandolfo *et al.*, 2020; Rinaldi *et al.*, 2012; Sancho *et al.*, 2017; Zong *et al.*, 2015).

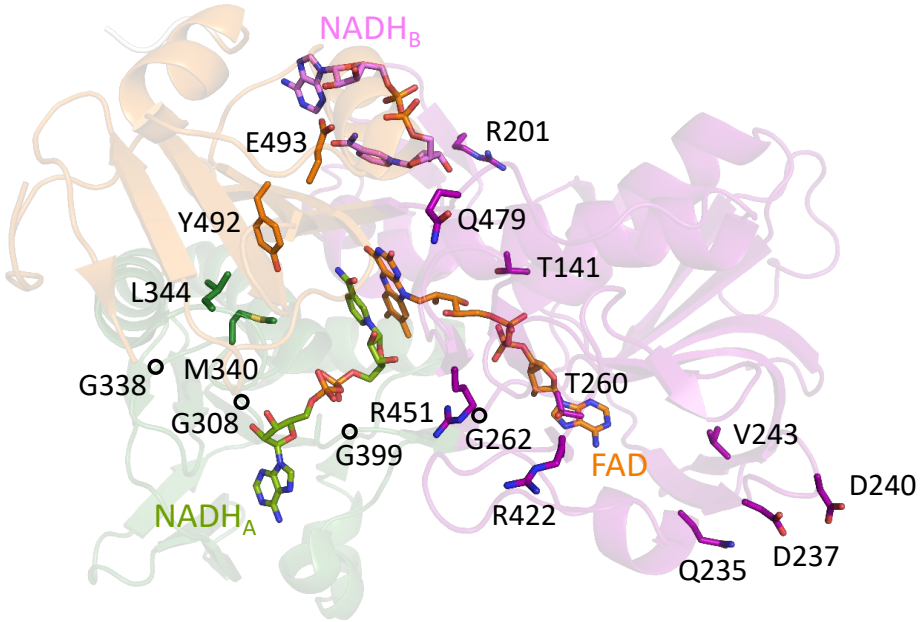

Figure 1.12. Localization of several key pathological mutations in human AIF. The structure of AIF (PDB 4BUR) is represented in cartoon with the FAD–binding, NADH–binding and C–terminal domains CPK coloured in green, purple and orange respectively. The cofactor and coenzymes are labelled, represented as sticks and CPK coloured in orange, green and violet. Key pathological residues are labelled and represented with their side chains as sticks. Residues in FAD–binding domain: T141, R201, V243, Q235, D237, D240, T260, G262, R422, R451 and Q479. Residues in NADH–binding domain: G308, G338, M340, G399 and L344. Residues in C–terminal domain: Y492 and E493.

Some of these mutations are:

- Mutations T141I, G262S, M340T, G399S and E493V, which cause the Cowchock syndrome (CMTX4, MIM #310490), a hereditary peripheral neuropathy associated with deafness and cognitive decline.
- Mutations ΔR201, V243L, G308E, G338E and Q479R, which cause combined oxidative phosphorylation deficiency 6 (COXPD6, MIM #300816), a severe encephalomyopathy associated with abnormal psychomotor development and variable deficiency in OXPHOS complexes.
- Mutations Q235V, D237G/V and the synonymous D240D replacement, which cause X–linked spondyloepimetaphyseal dysplasia with hypo myelinating leukodystrophy (SEMDHL, MIM #300232), resulting in a progressive neurodegeneration of the central and peripheral nervous systems.
- Mutations T260A, L344F, R422Q, R422W and R451Q, which cause hereditary X–linked sensory neuropathy coursing with deafness (DFNX5, MIM #300614).
- Mutation Y492H, which has also been identified in patients with mitochondrial pathologies but has not been associated with any particular pathology to date.

The treatment of patients with these hereditary mutations is a great challenge, as they present a heterogeneous group of phenotypes with a wide spectrum of severity in both symptoms and pathologies. Furthermore, the molecular characterization of some of the mutations associated with the Cowchock syndrome or COXPD6 shows a low genotype–phenotype correlation, clinical manifestations associated with low levels of AIF cell expression, incorrect protein folding and reduced conformational stability.

In this regard, AIF is part of the up to two thirds (nearly 60) of flavin–dependent human proteins associated with disorders caused by allelic variants (Lienhart *et al.*, 2013). Clarifying the molecular and functional implications of these mutations is a challenge that will be critical to provide proper genetic counselling in patients suffering these disorders. Recent observations linking mitochondrial signals and metabolism regulated by AIF to cell development and fate, also point to the mitochondrial AIF–mediated OXPHOS/metabolism as an emerging target in the development of new therapeutic approaches for diseases related to mitochondrial OXPHOS alteration/dysfunction (Delavallée *et al.*, 2020).

1.5.2. AMID in health and disease

AMID has been reported as a potential biomarker, since *aifm2* expression is downregulated in most human tumours but upregulated as a consequence of induced toxicity (i.e. cadmium disulphide or bean radiation therapy) (Hsiao *et al.*, 2013; Mei *et al.*, 2006; Miriyala *et al.*, 2016; Paesano *et al.*, 2016; Tao *et al.*, 2015; Wu *et al.*, 2004). In this context, toxicological stress induced in human lung cancer cells courses with *aifm2* upregulation and enhancement of apoptosis, which has been shown to contribute to the synergistic pro–apoptotic cytotoxic effect of some drugs (Lu *et al.*, 2016).

Furthermore, *aifm2* is a target of several microRNAs (*Annex I*) (Bazhabayi *et al.*, 2021; Fan *et al.*, 2017; Wang *et al.*, 2022). One such case is microRNA–214 (miR–214), a direct target itself of the maternally expressed 3 long non–coding RNA–MEG3 tumour suppressor, which results in *aifm2* expression being downregulated by miR–214 but increased by MEG3 in certain situations (Fan *et al.*, 2017). This has taken to the proposal of the MEG3–miR–214–AMID pathway regulating the growth of T–cell lymphoblastic lymphoma, playing as well a role in apoptotic cell death induced by over accumulation of the nuclear adiponectin hormone (Cho *et al.*, 2019). *aifm2* is also a direct target of miRNA–3622b–3p, which is upregulated in human prostate cancer (Wang *et al.*, 2022), and of miRNA–1228, in HER–2–positive breast cancer (Bazhabayi *et al.*, 2021), both of whose oncogenic function in tumour progression and metastasis is based on their interaction with AMID. Hence, current studies point to this protein as a potential prognosis marker and/or target for the treatment of such pathologies.

On the other hand, pharmacological targeting of AMID suggests that its coenzyme Q10–NAD(P)H pathway cooperates to suppress phospholipid peroxidation and ferroptosis (Doll *et al.*, 2019). The AMID–dependent recruitment of endosomal sorting complexes required for transport (ESCRT)–III in the plasma membrane seems to be responsible for ferroptosis resistance during tumour therapy with sorafenib, through the activation of a membrane repair mechanism that regulates membrane budding and fission (Dai *et al.*, 2020). AMID is also thought to play a potential role in human obesity and type 2 diabetes, exhibiting multiple single nucleotide polymorphisms associated with waist–hip ratio, body mass index, and fasting glucose–level–related insulin resistance (Dupuis *et al.*, 2010).

Finally, recent studies propose that *aifm2* may promote tumour growth by enhancing aerobic glycolysis (Nguyen *et al.*, 2020). Overexpression of AMID in skeletal muscle also appears to greatly potentiate exercise capacity by boosting the glycolytic rate, through an increase of the NAD^+/NADH ratio (Nguyen *et al.*, 2022). Other AMID potential functions in human health might be suggested from the study of homologues in different organisms, as for example the involvement in chronological aging reported for the yeast homologue NDI1 (Li *et al.*, 2006).

1.5.3. AIFL in health and disease

The *aifm3* gene has also been identified as a direct target of several miRNAs (*Annex I*). In particular, *aifm3* mRNA levels decrease upon upregulation of miR–210 (both exogenous and exosomal), a miRNA related to proliferation and enhanced radio sensitivity in hypoxic human hepatoma cells (Cheng *et al.*, 2020). In this line, it has also been proposed that neoplastic phenotypes in gastric organoids can be promoted by oesophageal adenocarcinoma–derived extracellular vesicle miRNAs via apoptosis suppression, which is in turn mediated by *aifm3* inhibition by miR–210 (Ke *et al.*, 2017). Considering the link of the *aifm3*/p53 signalling pathway to myocardial infarction, the potential use of miR–210 rich exosomes might attenuate AIFL apoptotic activity in post–infarction cardiac tissues, posing as a potential future cell therapy to explore for the treatment of ischemic heart diseases. The *aifm3* mRNA has been further involved in a network of competing endogenous RNAs closely related with bladder urothelial carcinoma pathogenesis, and identified as an independent prognostic factor for overall survival (Wang *et al.*, 2019; Zhu *et al.*, 2018).

Noticeably, despite AIFL being expressed in various tissues, so far it has only been reported as aberrantly expressed in a few cancers. Some of these are cholangiocarcinoma and breast cancer, where its higher expression levels are significantly associated with several tumour features, shorter overall survival and disease–free survival (Chua–on *et al.*, 2022; Zheng *et al.*, 2019). High AIFL expression in breast cancers has been linked to several signalling pathways, including oestrogen response, peroxisome, oxidative phosphorylation, DNA repair, p53 pathway and Wnt/β–catenin pathway signalling, among others, suggesting it might contribute to maintain cellular metabolism in tumour cells as well as in ROS pathways to regulate cancer development. In cholangiocarcinoma, AIFL plays a significant role in tumour cell motility, demonstrating particularly high expression levels in lymph node

metastasis. Furthermore, AIFL has also been found to be overexpressed in medullary thyroid cancer, with a considerable copy number gain (Araujo *et al.*, 2021). These observations have suggested AIFL as a potential target molecule for chemotherapy, as well as a novel prognostic biomarker assisting survival prediction in clinical practice.

Finally, the *aifm3* gene has been identified as one of the nine genes between low copy repeats LCR22A to LCR22D of chromosome 22q11.2, which are susceptible of nested atypical duplications reported as possible risk factors for neurodevelopmental phenotypes, particularly for autism spectrum disorder, speech and language delay, and behavioural abnormalities (Woodward *et al.*, 2019).

1.6. Art State Summary and Perspectives

In the last two decades, a significant increase in the potential functions of the AIF family in mammalian cells has been observed, being by far AIF the most deeply characterized member. Even so, all the diverse functions that each one of these proteins supports in both cell survival and cell death situations, as well as under pathological conditions, are still regretfully far from being understood or even known.

The information available on the AMID and AIFL family members is much scarcer than that of AIF, despite them sharing homologous domains that provide them with similar pro–cell death and pro–life traits. This fact indicates, however, that each of these proteins may aid remarkably diverse cellular processes and functions, through the potential use of variations in their unknown mechanisms of action. The picture emerging from the current knowledge of the AIF family indicates that intracellular levels of their transcripts, as well as of metabolites related to their activities (such as $NADH/^{+}$, ROS or Fe–S clusters), regulate signalling and transcription machineries in the crosstalk of mitochondria with the cytoplasm and the nucleus. The AIF family thus contributes to the dynamic and complex network of intracellular signalling pathways that maintain cell homeostasis by connecting the metabolome and proteome networks of these three cellular compartments.

Finally, considering the number and diversity of effects of the transcripts for the members of the AIF family in pathological situations, clarifying their molecular and functional mechanisms is critical to test and to exploit their potential as biomarkers, anti–tumour targets or therapeutic targets in mitochondrial related dysfunctions.

2. OBJECTIVES

The main goal of this PhD thesis is to deepen our understanding on the pro–life and pro–death functions of human AIF, particularly referred to its remarkably inefficient NADH oxidase activity and its ability to induce caspase–independent apoptosis respectively, as well as to better establish how these roles may be compromised by pathological variants. To achieve this general aim, we have proposed the following partial objectives:

1. Contribute to the description of the assembly of the DNA–degradosome through the analysis of the separate and simultaneous molecular interactions among AIF, its protein nuclear partners endonuclease CypA and histone H2AX, and the dsDNA.
2. Characterise the *in vitro* nuclease activity of human AIF, as well as the motifs in which it resides.
3. Assess the effect of pathological mutations T141I and M340T of human AIF on the protein's structural and functional properties, as well as on its interaction network.
4. Analyze the role of residue W483, located at the active site in close proximity with the FAD cofactor, in the NADH oxidase activity of human AIF.

Furthermore, we hoped to shed some light into the severely uncharacterized human AIFL protein. To do so, we proposed the following additional objective:

1. Evaluate differing overexpression procedures for human AIFL in *E. coli* to obtain its soluble, holoprotein form.

3. EXPERIMENTAL PROCEDURES

Additional procedures, not undertaken by the PhD candidate but relevant to the thesis, are enumerated and described at the end of this chapter.

3.1. Biological Material

The following bacterial strains of *Escherichia coli* and culture media were used for heterologous protein overexpression and/or plasmid conservation and isolation.

3.1.1. *E. coli* strains

Plasmid conservation and overexpression for its subsequent storage was always performed in the *E. coli* strain DH5α, while heterologous protein expression was carried out in different strains. Transformed strains were stored over time at –80 °C with 20% glycerol, while plasmid preparations were conserved at –20 °C.

Bacterial strains are described below in alphabetical order.

- C41 (DE3). The C41 (DE3) strain derives from the BL21 (DE3) strain, specifically constructed for high–level expression of recombinant proteins. It presents the following genotype: F^- *ompT* *hsdS*$_B$(r_B-, m_B-) *gal dcm* (DE3) (*Thermo Fisher Scientific*). As a lysogen of λDE3, the strain carries a chromosomal copy of the T7 RNA polymerase gene under control of the lacUV5 promoter, enabling inducible protein expression with isopropyl β–D–1–thiogalactopyranoside (IPTG). It also contains at least one uncharacterized mutation phenotypically selected to confer tolerance to toxic proteins (https://openwetware.org/wiki/E._coli_genotypes).
- **DH5α**. The DH5α strain was designed to maximize transformation efficiency, making it the go–to strain for cloning procedures (Hanahan, 1985; Taylor *et al.*, 1993). Its genotype is: F^- φ80*lac*ZΔM15 Δ(*lac*ZYA–*arg*F)U169 *rec*A1 *end*A1 *hsd*R17(r_K^-, m_K^+) *pho*A *sup*E44 λ^- *thi*–1 *gyr*A96 *rel*A1 (*Thermo Fisher Scientific*). The *rec*A1 mutation warrants high insert stability, *end*A hinders plasmid degradation and *lac*ZΔM15 enables blue/white color screening.

3.1.2. Culture media

Bacteria were grown in solution or on plates using the following culture media:

- Luria–Bertani (LB) broth: 10 g/L tryptone, 10 g/L NaCl and 5 g/L yeast extract.
- 2xYT broth: 16 g/L tryptone, 5 g/L NaCl and 10 g/L yeast extract.

- LB–agar: 10 g/L tryptone, 10 g/L NaCl, 5 g/L yeast extract and 20 g/L agar.

3.1.3. DNA samples

In order to evaluate the interaction of AIF and its protein partners with double–stranded DNA (dsDNA), the oligonucleotide had to be commercially synthetized as single strands (ss, forward ($ssDNA_{fw}$) and reverse ($ssDNA_{rv}$)) and subsequently hybridized. The following desalting–purified 15–bp ssDNA were obtained from *Integrated DNA Technologies*:

Forward: 5'– GGT TAG TTA TGC GCG –3'

Reverse: 5'– CGC GCA TAA CTA ACC –3'

Stocks of ssDNA were dissolved in sterile distilled water to 0.5 mM, mixed in an equimolar ratio and subsequently annealed using a Stratagene Mx3005P (*Agilent Technologies*) qPCR real–time thermocycler. The thermal annealing profile consisted of four steps: (1) equilibration at 25 °C for 30 s, (2) heating ramp to 99 °C, (3) equilibration at 99 °C for 60 s and (4) cooling down to 25 °C at a rate of 1 °C per 180 s (3 h in total). Final dsDNA concentration was calculated using equation 3.1.

$$\frac{1}{[\mathrm{dsDNA}]} = \frac{1}{[\mathrm{ssDNA_{fw}}]} + \frac{1}{[\mathrm{ssDNA_{rv}}]} \quad \text{(Eq. 3.1)}$$

where dsDNA is the double–stranded DNA, and $\mathrm{ssDNA_{fw}}$ and $\mathrm{ssDNA_{rv}}$ the forward and reverse single–stranded DNA respectively.

3.2. Expression constructs and Cell Transformation

Coding DNA (cDNA) constructs for the soluble mitochondrial and apoptotic forms of wild–type (WT) human AIF ($AIF_{\Delta 77}$ and $AIF_{\Delta 101}$ respectively) and the different truncated forms of human AIFL ($AIFL_{\Delta 64}$, $AIFL_{65-168}$ and $AIFL_{\Delta 195}$) were commercially synthetized and subsequently cloned into a pET28a(+) expression vector (*Fig. 3.1*) with a cleavable N– or C–terminal His_6–tag (*GenScript*). Plasmids encoding the different AIF variants studied in this work were obtained by site–directed mutagenesis on the pET28a(+)–$AIF_{\Delta 101}$ or –$AIF_{\Delta 77}$ vectors (*GenScript*), depending on the form of interest. cDNA constructs for AIF's protein partners CHCHD4, CypA and H2AX were previously synthetized in the same manner (Romero–Tamayo, 2022).

Competent *E. coli* C41 (DE3) cells were transformed with each commercial construct for protein production, as were competent *E. coli* DH5α cells for vector conservation. Transformed C41 (DE3) cells containing the pRISC expression construct were kindly provided by the group of Eduardo Ciccarelli (the vector being originally designed and synthetized by Nakamura *et al.*, 1999). More information on the pRISC expression vector is provided in chapter 7.

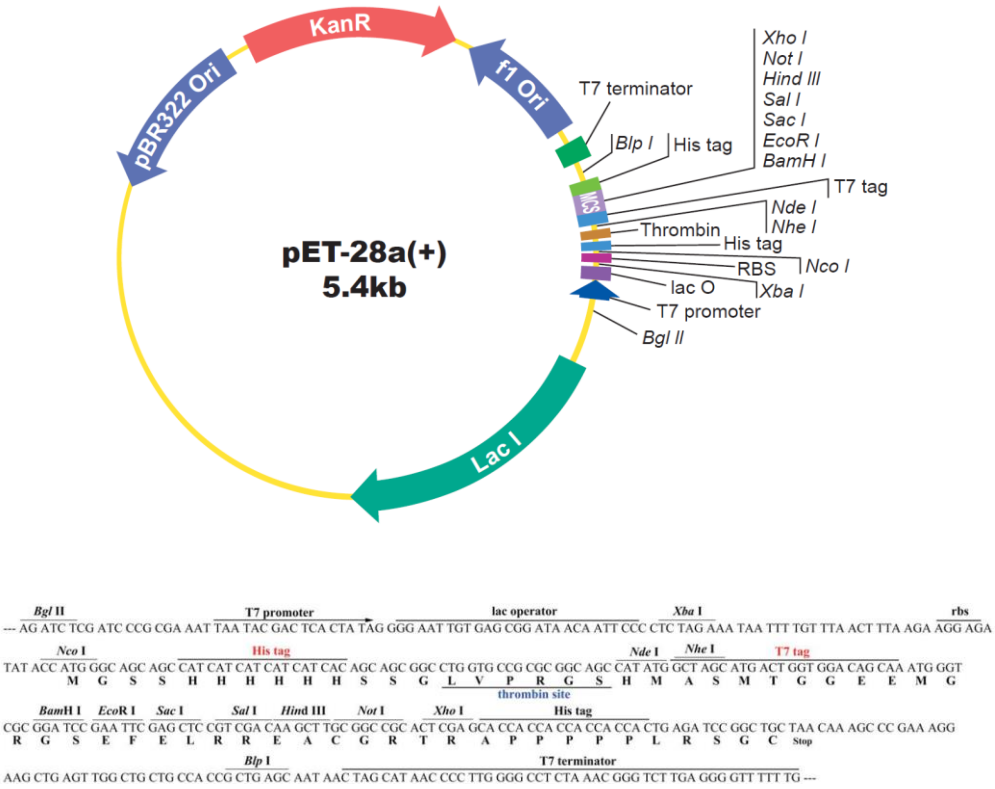

Figure 3.1. Map and sequence of the pET28a(+) expression vector. The pET28a(+) vector is designed for heterologous protein expression in *E. coli* (DE3) strains. It carries a gene that confers resistance to kanamycin and a strong bacteriophage T7 promoter (IPTG–inducible) after which target genes may be cloned. Unique sites are shown in the map. Depending on where the target gene is cloned, it may be expressed as a fusion protein with a cleavable N– or C–terminal His_6–tag. Figure from *GenScript*.

3.2.1. Protein expression constructs

The various constructs employed for protein expression in this work are listed below. All constructs here indicated were synthetized by *GenScript*. All proteins were designed to carry a cleavable N– or C–terminal His_6–tag in order to facilitate their purification. A legend with the elements present in the constructs is provided (*Table 3.1*).

Table 3.1. Color–coded elements of the constructs.

Element	Start	Spacer	His_6–tag	Thrombin protease (Thb) recognition site	PreScission Plus protease (PP) recognition site	cDNA	Stop

- pET28a(+)–$AIF_{\Delta 77}$

cDNA of the $AIF_{\Delta 77}$ protein (*aifm1*, apoptosis–inducing factor mitochondrion–associated 1 [*Homo sapiens*], Gene ID: 9131, with Δ1–77 deletion (soluble mitochondrial form)) cloned into the *Nco*I/*Nde*I restriction sites of a pET28a(+) vector with a cleavable C–terminal His_6–tag and recognition site for Thb.

ATGGTGGGCGCCGGCGCCTACGCCTACAAGACCATGAAGGAGGACGAGAAGAGGTACAACGAGAGGATC
AGCGGCCTGGGCCTGACCCCCGAGCAGAAGCAGAAGAAGGCCGCCCTGAGCGCCAGCGAGGGCGAGGAG
GTGCCCCAGGACAAGGCCCCCAGCCACGTGCCCTTCCTGCTGATCGGCGGCGGCACCGCCGCCTTCGCC
GCCGCCAGGAGCATCAGGGCCAGGGACCCCGGCGCCAGGGTGCTGATCGTGAGCGAGGACCCCGAGCTG
CCCTACATGAGGCCCCCCCTGAGCAAGGAGCTGTGGTTCAGCGACGACCCCAACGTGACCAAGACCCTG
AGGTTCAAGCAGTGGAACGGCAAGGAGAGGAGCATCTACTTCCAGCCCCCCAGCTTCTACGTGAGCGCC
CAGGACCTGCCCCACATCGAGAACGGCGGCGTGGCCGTGCTGACCGGCAAGAAGGTGGTGCAGCTGGAC
GTGAGGGACAACATGGTGAAGCTGAACGACGGCAGCCAGATCACCTACGAGAAGTGCCTGATCGCCACC
GGCGGCACCCCCAGGAGCCTGAGCGCCATCGACAGGGCCGGCGCCGAGGTGAAGAGCAGGACCACCCTG
TTCAGGAAGATCGGCGACTTCAGGAGCCTGGAGAAGATCAGCAGGGAGGTGAAGAGCATCACCATCATC
GGCGGCGGCTTCCTGGGCAGCGAGCTGGCCTGCGCCCTGGGCAGGAAGGCCAGGGCCCTGGGCACCGAG
GTGATCCAGCTGTTCCCCGAGAAGGGCAACATGGGCAAGATCCTGCCCGAGTACCTGAGCAACTGGACC
ATGGAGAAGGTGAGGAGGGAGGGCGTGAAGGTGATGCCCAACGCCATCGTGCAGAGCGTGGGCGTGAGC
AGCGGCAAGCTGCTGATCAAGCTGAAGGACGGCAGGAAGGTGGAGACCGACCACATCGTGGCCGCCGTG
GGCCTGGAGCCCAACGTGGAGCTGGCCAAGACCGGCGGCCTGGAGATCGACAGCGACTTCGGCGGCTTC
AGGGTGAACGCCGAGCTGCAGGCCAGGAGCAACATCTGGGTGGCCGGCGACGCCGCCTGCTTCTACGAC
ATCAAGCTGGGCAGGAGGAGGGTGGAGCACCACGACCACGCCGTGGTGAGCGGCAGGCTGGCCGGCGAG
AACATGACCGGCGCCGCCAAGCCCTACTGGCACCAGAGCATGTTCTGGAGCGACCTGGGCCCCGACGTG
GGCTACGAGGCCATCGGCCTGGTGGACAGCAGCCTGCCCACCGTGGGCGTGTTCGCCAAGGCCACCGCC
CAGGACAACCCCAAGAGCGCCACCGAGCAGAGCGGCACCGGCATCAGGAGCGAGAGCGAGACCGAGAGC
GAGGCCAGCGAGATCACCATCCCCCCCAGCACCCCCGCCGTGCCCCAGGCCCCCGTGCAGGGCGAGGAC
TACGGCAAGGGCGTGATCTTCTACCTGAGGGACAAGGTGGTGGTGGGCATCGTGCTGTGGAACATCTTC
AACAGGATGCCCATCGCCAGGAAGATCATCAAGGACGGCGAGCAGCACGAGGACCTGAACGAGGTGGCC
AAGCTGTTCAACATCCACGAGGACGGCAGTTCTCTGGTGCCCAGGGGCAGCGGCAGTTCTCACCACCAC
CACCACCACGGCAGTTCTTGA

Resulting $AIF_{\Delta 77}$–Thb–His_6 fusion protein.

MVGAGAYAYKTMKEDEKRYNERISGLGLTPEQKQKKAALSASEGEEVPQDKAPSHVPFLLIGGGTAAFA
AARSIRARDPGARVLIVSEDPELPYMRPPLSKELWFSDDPNVTKTLRFKQWNGKERSIYFQPPSFYVSA
QDLPHIENGGVAVLTGKKVVQLDVRDNMVKLNDGSQITYEKCLIATGGTPRSLSAIDRAGAEVKSRTTL
FRKIGDFRSLEKISREVKSITIIGGGFLGSELACALGRKARALGTEVIQLFPEKGNMGKILPEYLSNWT
MEKVRREGVKVMPNAIVQSVGVSSGKLLIKLKDGRKVETDHIVAAVGLEPNVELAKTGGLEIDSDFGGF
RVNAELQARSNIWVAGDAACFYDIKLGRRRVEHHDHAVVSGRLAGENMTGAAKPYWHQSMFWSDLGPDV
GYEAIGLVDSSLPTVGVFAKATAQDNPKSATEQSGTGIRSESETESEASEITIPPSTPAVPQAPVQGED
YGKGVIFYLRDKVVVGIVLWNIFNRMPIARKIIKDGEQHEDLNEVAKLFNIHEDGSSLVPRGSGSSHHH
HHHGSS*

- pET28a(+)–$AIF_{\Delta 101}$

cDNA of the $AIF_{\Delta 101}$ protein (*aifm1*, apoptosis–inducing factor mitochondrion–associated 1 [*Homo sapiens*], Gene ID: 9131, with Δ1–101 deletion (apoptotic form)) cloned into the *Nde*I/*Not*I restriction sites of a pET28a(+) vector with a cleavable N–terminal His_6–tag and recognition site for Thb.

ATGGGCAGCAGCCATCATCATCATCATCACAGCAGCGGCCTGGTGCCGCGCGGCAGCCATATGGGGCTG
ACACCAGAACAGAAACAGAAAAAGGCCGCGTTATCTGCTTCAGAAGGAGAGGAAGTTCCTCAAGACAAG
GCGCCAAGTCATGTTCCTTTCCTGCTAATTGGTGGAGGCACAGCTGCTTTTGCTGCAGCCAGATCCATC
CGGGCTCGGGATCCTGGGGCCAGGGTACTGATTGTATCTGAAGATCCTGAGCTGCCGTACATGCGACCT
CCTCTTTCAAAAGAACTGTGGTTTTCAGATGACCCAAATGTCACAAAGACACTGCGATTCAAACAGTGG
AATGGAAAAGAGAGAAGCATATATTTCCAGCCACCTTCTTTCTATGTCTCTGCTCAGGACCTGCCTCAT
ATTGAGAATGGTGGTGTGGCTGTCCTCACTGGGAAGAAGGTAGTACAGCTGGATGTGAGAGACAACATG
GTGAAACTTAATGATGGCTCTCAAATAACCTATGAAAAGTGCTTGATTGCAACAGGAGGTACTCCAAGA
AGTCTGTCTGCCATTGATAGGGCTGGAGCAGAGGTGAAGAGTAGAACAACGCTTTTCAGAAAGATTGGA
GACTTTAGAAGCTTGGAGAAGATTTCACGGGAAGTCAAATCAATTACGATTATCGGTGGGGGCTTCCTT
GGTAGCGAACTGGCCTGTGCTCTTGGCAGAAAGGCTCGAGCCTTGGGCACAGAAGTGATTCAACTCTTC
CCCGAGAAAGGAAATATGGGAAAGATCCTCCCCGAATACCTCAGCAACTGGACCATGGAAAAAGTCAGA
CGAGAGGGGGTTAAGGTGATGCCCAATGCTATTGTGCAATCCGTTGGAGTCAGCAGTGGCAAGTTACTT
ATCAAGCTGAAAGACGGCAGGAAGGTAGAAACTGACCACATAGTGGCAGCTGTGGGCCTGGAGCCCAAT
GTTGAGTTGGCCAAGACTGGTGGCCTGGAAATAGACTCAGATTTTGGTGGCTTCCGGGTAAATGCAGAG
CTACAAGCACGCTCTAACATCTGGGTGGCAGGAGATGCTGCATGCTTCTACGATATAAAGTTGGGAAGG
AGGCGGGTAGAGCACCATGATCACGCTGTTGTGAGTGGAAGATTGGCTGGAGAAAATATGACTGGAGCT
GCTAAGCCGTACTGGCATCAGTCAATGTTCTGGAGTGATTTGGGCCCCGATGTTGGCTATGAAGCTATT
GGTCTTGTGGACAGTAGTTTGCCCACAGTTGGTGTTTTTGCAAAAGCAACTGCACAAGACAACCCCAAA
TCTGCCACAGAGCAGTCAGGAACTGGTATCCGATCAGAGAGTGAGACAGAGTCCGAGGCCTCAGAAATT
ACTATTCCTCCCAGCACCCCGGCAGTTCCACAGGCTCCCGTCCAGGGGGAGGACTACGGCAAAGGTGTC
ATCTTCTACCTCAGGGACAAAGTGGTCGTGGGGATTGTGCTATGGAACATCTTTAACCGAATGCCAATA
GCAAGGAAGATCATTAAGGACGGTGAGCAGCATGAAGATCTCAATGAAGTAGCCAAACTATTCAACATT
CATGAAGACTGA

Resulting His_6–Thb–$AIF_{\Delta 101}$ fusion protein.

MGSSHHHHHHSSGLVPRGSHMGLTPEQKQKKAALSASEGEEVPQDKAPSHVPFLLIGGGTAAFAAARSI
RARDPGARVLIVSEDPELPYMRPPLSKELWFSDDPNVTKTLRFKQWNGKERSIYFQPPSFYVSAQDLPH
IENGGVAVLTGKKVVQLDVRDNMVKLNDGSQITYEKCLIATGGTPRSLSAIDRAGAEVKSRTTLFRKIG
DFRSLEKISREVKSITIIGGGFLGSELACALGRKARALGTEVIQLFPEKGNMGKILPEYLSNWTMEKVR
REGVKVMPNAIVQSVGVSSGKLLIKLKDGRKVETDHIVAAVGLEPNVELAKTGGLEIDSDFGGFRVNAE
LQARSNIWVAGDAACFYDIKLGRRRVEHHDHAVVSGRLAGENMTGAAKPYWHQSMFWSDLGPDVGYEAI
GLVDSSLPTVGVFAKATAQDNPKSATEQSGTGIRSESETESEASEITIPPSTPAVPQAPVQGEDYGKGV
IFYLRDKVVVGIVLWNIFNRMPIARKIIKDGEQHEDLNEVAKLFNIHED*

- pET28a(+)–AIF variants

Variants of $AIF_{\Delta 101}$ and $AIF_{\Delta 77}$ (*Table 3.2*) were synthetized through site–directed mutagenesis of the pET28a(+)–$AIF_{\Delta 101}$ or –$AIF_{\Delta 77}$ vector, respectively, at *GenScript*. All variants were synthetized in both the apoptotic and mitochondrial forms excepting Y443A, K446A, R449A, R450A, R451A, H454S, D489A/K518A, K518A/E522A and K510A/K518A, which were solely synthetized in the apoptotic form. Amino acid and nucleotide positions are given with regard to the complete sequence of human AIF.

Table 3.2. Summary of the AIF variants produced in this work. Mutations are indicated for protein (p.) and DNA (c.) sequence. Modified nucleotides appear in red. All sequences are displayed in the 5'–3' sense.

Mutation		Native DNA sequence	Variant DNA sequence
p.Thr141Ile	c.422C>T	GGC ACA GCT	GGC ATA GCT
p.Met340Thr	c.1019T>C	AAT ATG GGA	AAT ACG GGA
p.Tyr443Ala	c.1327T>G c.1328A>C	TTC TAT GAT	TTC GCT GAT
p.Lys446Ala	c.1336A>G c.1337A>C	ATT AAA CTG	ATT GCA CTG
p.Arg449Ala	c.1345C>G c.1346G>C	GGC CGT CGT	GGC GCT CGT
p.Arg450Ala	c.1348C>G c.1349G>C	CGT CGT CGT	CGT GCT CGT
p.Arg451Ala	c.1351C>G c.1352G>C	CGT CGT GTG	CGT GCT GTG
p.His454Ser	c.1362C>T c.1363A>C	GAG CAC CAC	GAG TCC CAC
p.Trp483Gly	c.1447T>G	TTC TGG AGC	TTC GGG AGC
p.Trp483Leu	c.1448G>T	TTC TGG AGC	TTC TTG AGC
p.Trp483Tyr	c.1448G>A c.1449G>C	TTC TGG AGC	TTC TAC AGC
p.Asp489Ala	c.1466A>C	CCG GAT GTT	CCG GCT GTT
p.Lys518Ala	c.1552A>G c.1553A>C	CCG AAG AGC	CCG GCG AGC
p.Lys518Ala	c.1552A>G c.1553A>C	CCG AAG AGC	CCG GCG AGC
p.Glu522Ala	c.1565A>C	ACC GAG CAA	ACC GCG CAA
p.Lys510Ala	c.1528A>G c.1529A>C	GCG AAA GCG	GCG GCA GCG
p.Lys518Ala	c.1552A>G c.1553A>C	CCG AAG AGC	CCG GCG AGC

- pET28a(+)–AIFL$_{\Delta 64}$

cDNA of the AIFL$_{\Delta 64}$ protein (*aifm3*, apoptosis–inducing factor mitochondrion–associated 3 [*Homo sapiens*], Gene ID: 150209, with 1–64 deletion (complete form without unstructured N–terminus)) cloned into the *Nco*I/*Nde*I restriction sites of a pET28a(+) vector with a cleavable C–terminal His$_6$–tag and recognition site for PP.

ATGGGCCAGGATTGCGTGGAGGCTGCTGTCTGCCACGTCAAGGACCTCGAGAATGGCCAGATGCGGGAA
GTGGAGCTGGGCTGGGGGAAGGTGTTGCTGGTGAAGGACAATGGGGAGTTCCACGCCCTGGGCCATAAG
TGTCCGCACTACGGCGCACCCCTGGTGAAAGGCGTTCTGTCCCGTGGTCGGGTGCGCTGCCCCTGGCAC
GGCGCCTGCTTCAACATCAGCACTGGGGACCTGGAGGACTTCCCTGGCCTGGACAGTCTACACAAGTTC
CAGGTGAAGATTGAGAAGGAGAAGGTGTACGTCCGGGCCAGCAAGCAGGCCCTACAGCTGCAGCGAAGG
ACCAAGGTGATGGCCAAGTGTATCTCTCCAAGTGCTGGGTACAGCAGTAGCACCAATGTGCTCATTGTG
GGTGCAGGTGCAGCTGGCCTGGTGTGTGCAGAGACACTGCGGCAGGAGGGCTTCTCCGACCGGATCGTC
CTGTGCACGCTAGACCGGCACCTTCCCTACGACCGTCCCAAGCTCAGCAAGTCCCTGGACACACAGCCT
GAGCAGCTGGCCCTGAGGCCCAAGGAGTTTTTCCGAGCCTATGGCATCGAGGTGCTCACCGAGGCTCAG
GTGGTCACAGTGGACGTGAGAACTAAGAAGGTCGTGTTCAAGGATGGCTTCAAGCTGGAGTACAGCAAG
CTGCTGCTGGCACCAGGGAGCAGCCCCAAGACTCTGAGCTGCAAAGGCAAAGAAGTGGAGAACGTGTTC
ACTATCCGGACGCCAGAGGATGCCAATCGCGTGGTGAGGCTGGCCCGAGGCCGCAACGTGGTCGTCGTG
GGAGCCGGCTTCCTGGGGATGGAGGTGGCCGCTTACCTGACGGAGAAGGCCCACTCTGTGTCTGTGGTG
GAGCTGGAGGAGACGCCCTTCAGGAGGTTCCTGGGGGAGCGCGTGGGTCGTGCCCTCATGAAGATGTTT
GAGAACAACCGGGTGAAGTTCTACATGCAGACGGAGGTGTCTGAGCTGCGGGGCCAGGAGGGAAAGCTG
AAGGAGGTTGTGCTGAAGAGCAGCAAGGTCGTGCGGGCTGACGTCTGCGTGGTGGGCATTGGTGCAGTG
CCCGCCACAGGCTTCCTGAGGCAAAGCGGCATCGGTTTGGATTCCCGAGGCTTCATCCCTGTCAACAAG
ATGATGCAGACCAATGTCCCAGGCGTGTTTGCAGCTGGCGATGCTGTCACCTTCCCCCTTGCCTGGAGG
AACAACCGCAAAGTGAACATTCCACATTGGCAGATGGCTCATGCTCAGGGGCGCGTGGCAGCCCAGAAC
ATGTTGGCGCAGGAGGCGGAGATGAGCACTGTGCCCTACCTCTGGACCGCCATGTTTGGCAAGAGCCTG
CGCTACGCGGGCTACGGAGAAGGCTTCGACGACGTCATCATCCAGGGGGATCTGGAGGAGCTGAAGTTT
GTGGCTTTTTACACTAAAGGCGACGAGGTGATCGCCGTGGCCAGCATGAACTACGATCCCATTGTGTCC
AAGGTCGCTGAGGTGCTGGCCTCAGGCCGTGCCATCCGGAAGCGGGAGGTGGAGCTGTTTGTGCTGCAC
AGCAAGACTGGCGACATGTCCTGGCTTACGGGGAAAGGATCCGGCAGTTCTCTAGAAGTATTATTCCAG
GGGCCGGGCAGTTCACATCATCATCATCATCATGGCAGTTCTTGA

Resulting AIFL$_{\Delta 64}$–PP–His$_6$ fusion protein.

MGQDCVEAAVCHVKDLENGQMREVELGWGKVLLVKDNGEFHALGHKCPHYGAPLVKGVLSRGRVRCPWH
GACFNISTGDLEDFPGLDSLHKFQVKIEKEKVYVRASKQALQLQRRTKVMAKCISPSAGYSSSTNVLIV
GAGAAGLVCAETLRQEGFSDRIVLCTLDRHLPYDRPKLSKSLDTQPEQLALRPKEFFRAYGIEVLTEAQ
VVTVDVRTKKVVFKDGFKLEYSKLLLAPGSSPKTLSCKGKEVENVFTIRTPEDANRVVRLARGRNVVVV
GAGFLGMEVAAYLTEKAHSVSVVELEETPFRRFLGERVGRALMKMFENNRVKFYMQTEVSELRGQEGKL
KEVVLKSSKVVRADVCVVGIGAVPATGFLRQSGIGLDSRGFIPVNKMMQTNVPGVFAAGDAVTFPLAWR
NNRKVNIPHWQMAHAQGRVAAQNMLAQEAEMSTVPYLWTAMFGKSLRYAGYGEGFDDVIIQGDLEELKF
VAFYTKGDEVIAVASMNYDPIVSKVAEVLASGRAIRKREVELFVLHSKTGDMSWLTGKGSGSSLEVLFQ
GPGSSHHHHHHGSS*

- pET28a(+)–AIFL$_{\Delta 195}$

cDNA of the AIFL$_{\Delta 195}$ protein (*aifm3*, apoptosis–inducing factor mitochondrion–associated 3 [*Homo sapiens*], Gene ID: 150209, with 1–195 deletion (oxidoreductase and reductase C–

terminal domains)) cloned into the *Nco*I/*Nde*I restriction sites of a pET28a(+) vector with a cleavable C–terminal His_6–tag and recognition site for PP.

ATGGGCACCAATGTGCTCATTGTGGGTGCAGGTGCAGCTGGCCTGGTGTGTGCAGAGACACTGCGGCAG
GAGGGCTTCTCCGACCGGATCGTCCTGTGCACGCTAGACCGGCACCTTCCCTACGACCGTCCCAAGCTC
AGCAAGTCCCTGGACACACAGCCTGAGCAGCTGGCCCTGAGGCCCAAGGAGTTTTTCCGAGCCTATGGC
ATCGAGGTGCTCACCGAGGCTCAGGTGGTCACAGTGGACGTGAGAACTAAGAAGGTCGTGTTCAAGGAT
GGCTTCAAGCTGGAGTACAGCAAGCTGCTGCTGGCACCAGGGAGCAGCCCCAAGACTCTGAGCTGCAAA
GGCAAAGAAGTGGAGAACGTGTTCACTATCCGGACGCCAGAGGATGCCAATCGCGTGGTGAGGCTGGCC
CGAGGCCGCAACGTGGTCGTCGTGGGAGCCGGCTTCCTGGGGATGGAGGTGGCCGCTTACCTGACGGAG
AAGGCCCACTCTGTGTCTGTGGTGGAGCTGGAGGAGACGCCCTTCAGGAGGTTCCTGGGGGAGCGCGTG
GGTCGTGCCCTCATGAAGATGTTTGAGAACAACCGGGTGAAGTTCTACATGCAGACGGAGGTGTCTGAG
CTGCGGGGCCAGGAGGGAAAGCTGAAGGAGGTTGTGCTGAAGAGCAGCAAGGTCGTGCGGGCTGACGTC
TGCGTGGTGGGCATTGGTGCAGTGCCCGCCACAGGCTTCCTGAGGCAAAGCGGCATCGGTTTGGATTCC
CGAGGCTTCATCCCTGTCAACAAGATGATGCAGACCAATGTCCCAGGCGTGTTTGCAGCTGGCGATGCT
GTCACCTTCCCCCTTGCCTGGAGGAACAACCGCAAAGTGAACATTCCACATTGGCAGATGGCTCATGCT
CAGGGGCGCGTGGCAGCCCAGAACATGTTGGCGCAGGAGGCGGAGATGAGCACTGTGCCCTACCTCTGG
ACCGCCATGTTTGGCAAGAGCCTGCGCTACGCGGGCTACGGAGAAGGCTTCGACGACGTCATCATCCAG
GGGGATCTGGAGGAGCTGAAGTTTGTGGCTTTTTACACTAAAGGCGACGAGGTGATCGCCGTGGCCAGC
ATGAACTACGATCCCATTGTGTCCAAGGTCGCTGAGGTGCTGGCCTCAGGCCGTGCCATCCGGAAGCGG
GAGGTGGAGCTGTTTGTGCTGCACAGCAAGACTGGCGACATGTCCTGGCTTACGGGGAAAGGATCCGGC
AGTTCTCTAGAAGTATTATTCCAGGGGCCGGGCAGTTCACATCATCATCATCATCATGGCAGTTCTTGA

Resulting $AIFL_{\Delta 195}$–PP–His_6 fusion protein.

MGTNVLIVGAGAAGLVCAETLRQEGFSDRIVLCTLDRHLPYDRPKLSKSLDTQPEQLALRPKEFFRAYG
IEVLTEAQVVTVDVRTKKVVFKDGFKLEYSKLLLAPGSSPKTLSCKGKEVENVFTIRTPEDANRVVRLA
RGRNVVVVGAGFLGMEVAAYLTEKAHSVSVVELEETPFRRFLGERVGRALMKMFENNRVKFYMQTEVSE
LRGQEGKLKEVVLKSSKVVRADVCVVGIGAVPATGFLRQSGIGLDSRGFIPVNKMMQTNVPGVFAAGDA
VTFPLAWRNNRKVNIPHWQMAHAQGRVAAQNMLAQEAEMSTVPYLWTAMFGKSLRYAGYGEGFDDVIIQ
GDLEELKFVAFYTKGDEVIAVASMNYDPIVSKVAEVLASGRAIRKREVELFVLHSKTGDMSWLTGKGSG
SSLEVLFQGPGSSHHHHHHGSS*

- pET28a(+)–$AIFL_{65–168}$

cDNA of the $AIFL_{65–168}$ protein (*aifm3*, apoptosis–inducing factor mitochondrion–associated 3 [*Homo sapiens*], Gene ID: 150209, with amino acids 65 to 168 (Rieske domain)) cloned into the *Nco*I/*Nde*I restriction sites of a pET28a(+) vector with a cleavable N–terminal His_6–tag and recognition site for PP.

ATGGGCAGTTCTCATCATCATCATCATCATGGCAGTTCACTAGAAGTATTATTCCAGGGGCCGGGCAGT
TCTCAGGATTGCGTGGAGGCTGCTGTCTGCCACGTCAAGGACCTCGAGAATGGCCAGATGCGGGAAGTG
GAGCTGGGCTGGGGGAAGGTGTTGCTGGTGAAGGACAATGGGGAGTTCCACGCCCTGGGCCATAAGTGT
CCGCACTACGGCGCACCCCTGGTGAAAGGCGTTCTGTCCCGTGGTCGGGTGCGCTGCCCCTGGCACGGC
GCCTGCTTCAACATCAGCACTGGGGACCTGGAGGACTTCCCTGGCCTGGACAGTCTACACAAGTTCCAG
GTGAAGATTGAGAAGGAGAAGGTGTACGTCCGGGCCAGCTGA

Resulting His_6–PP–$AIFL_{65–168}$ fusion protein.

MGSSHHHHHHGSSLEVLFQGPGSSQDCVEAAVCHVKDLENGQMREVELGWGKVLLVKDNGEFHALGHKC
PHYGAPLVKGVLSRGRVRCPWHGACFNISTGDLEDFPGLDSLHKFQVKIEKEKVYVRAS*

- pET28a(+)–CHCHD4

cDNA of the CHCHD4 protein (*chchd4*, coiled–coil–helix–coiled–coil–helix domain containing 4 [*Homo sapiens*], Gene ID: 131474) cloned into the *Nde*I/*Not*I restriction sites of a pET28a(+) vector with a cleavable N–terminal His_6–tag and recognition site for Thb.

```
ATGGGCAGTTCTCATCATCATCATCATCATGGCAGTTCACTGGTGCCCAGGGGCAGCGGCAGTTCTATG
AGCTACTGCAGGCAGGAGGGCAAGGACAGGATCATCTTCGTGACCAAGGAGGACCACGAGACCCCCAGC
AGCGCCGAGCTGGTGGCCGACGACCCCAACGACCCCTACGAGGAGCACGGCCTGATCCTGCCCAACGGC
AACATCAACTGGAACTGCCCCTGCCTGGGCGGCATGGCCAGCGGCCCCTGCGGCGAGCAGTTCAAGAGC
GCCTTCAGCTGCTTCCACTACAGCACCGAGGAGATCAAGGGCAGCGACTGCGTGGACCAGTTCAGGGCC
ATGCAGGAGTGCATGCAGAAGTACCCCGACCTGTACCCCCAGGAGGACGAGGACGAGGAGGAGGAGAGG
GAGAAGAAGCCCGCCGAGCAGGCCGAGGAGACCGCCCCCATCGAGGCCACCGCCACCAAGGAGGAGGAG
GGCAGCAGCTGA
```

Resulting His_6–Thb–CHCHD4 fusion protein.

```
MGSSHHHHHHGSSLVPRGSGSSMSYCRQEGKDRIIFVTKEDHETPSSAELVADDPNDPYEEHGLILPNG
NINWNCPCLGGMASGPCGEQFKSAFSCFHYSTEEIKGSDCVDQFRAMQECMQKYPDLYPQEDEDEEEER
EKKPAEQAEETAPIEATATKEEEGSS*
```

- pET28a(+)–CypA

cDNA of the CypA protein (*ppia*, peptidyl prolyl isomerase A [*Homo sapiens*], Gene ID: 5478) cloned into the *Nde*I/*Not*I restriction sites of a pET28a(+) vector with a cleavable N–terminal His_6–tag and recognition site for Thb.

```
ATGGGCAGTTCTCATCATCATCATCATCATGGCAGTTCACTGGTGCCCAGGGGCAGCGGCAGTTCTATG
GTGAACCCCACCGTGTTCTTCGACATCGCCGTGGACGGCGAGCCCCTGGGCAGGGTGAGCTTCGAGCTG
TTCGCCGACAAGGTGCCCAAGACCGCCGAGAACTTCAGGGCCCTGAGCACCGGCGAGAAGGGCTTCGGC
TACAAGGGCAGCTGCTTCCACAGGATCATCCCCGGCTTCATGTGCCAGGGCGGCGACTTCACCAGGCAC
AACGGCACCGGCGGCAAGAGCATCTACGGCGAGAAGTTCGAGGACGAGAACTTCATCCTGAAGCACACC
GGCCCCGGCATCCTGAGCATGGCCAACGCCGGCCCCAACACCAACGGCAGCCAGTTCTTCATCTGCACC
GCCAAGACCGAGTGGCTGGACGGCAAGCACGTGGTGTTCGGCAAGGTGAAGGAGGGCATGAACATCGTG
GAGGCCATGGAGAGGTTCGGCAGCAGGAACGGCAAGACCAGCAAGAAGATCACCATCGCCGACTGCGGC
CAGCTGGAGTGA
```

Resulting His_6–Thb–CypA fusion protein.

```
MGSSHHHHHHGSSLVPRGSGSSMVNPTVFFDIAVDGEPLGRVSFELFADKVPKTAENFRALSTGEKGFG
YKGSCFHRIIPGFMCQGGDFTRHNGTGGKSIYGEKFEDENFILKHTGPGILSMANAGPNTNGSQFFICT
AKTEWLDGKHVVFGKVKEGMNIVEAMERFGSRNGKTSKKITIADCGQLE*
```

- pET28a(+)–H2AX

cDNA of the H2AX protein (*h2afx*, H2A histone family member X [*Homo sapiens*], Gene ID: 3014) cloned into the *Nco*I/*Nde*I restriction sites of a pET28a(+) vector with a cleavable N–terminal His_6–tag and recognition site for PP.

```
ATGGGCAGTTCTCATCATCATCATCATCATGGCAGTTCACTAGAAGTATTATTCCAGGGGCCGGGCAGT
TCTATGAGCGGCAGGGGCAAGACCGGCGGCAAGGCCAGGGCCAAGGCCAAGAGCAGGAGCAGCAGGGCC
GGCCTGCAGTTCCCCGTGGGCAGGGTGCACAGGCTGCTGAGGAAGGGCCACTACGCCGAGAGGGTGGGC
GCCGGCGCCCCCGTGTACCTGGCCGCCGTGCTGGAGTACCTGACCGCCGAGATCCTGGAGCTGGCCGGC
AACGCCGCCAGGGACAACAAGAAGACCAGGATCATCCCCAGGCACCTGCAGCTGGCCATCAGGAACGAC
```

GAGGAGCTGAACAAGCTGCTGGGCGGCGTGACCATCGCCCAGGGCGGCGTGCTGCCCAACATCCAGGCC
GTGCTGCTGCCCAAGAAGACCAGCGCCACCGTGGGCCCCAAGGCCCCCAGCGGCGGCAAGAAGGCCACC
CAGGCCAGCCAGGAGTACTGA

Resulting His_6–PP–H2AX fusion protein.

MGSSHHHHHHGSSLEVLFQGPGSSMSGRGKTGGKARAKAKSRSSRAGLQFPVGRVHRLLRKGHYAERVG
AGAPVYLAAVLEYLTAEILELAGNAARDNKKTRIIPRHLQLAIRNDEELNKLLGGVTIAQGGVLPNIQA
VLLPKKTSATVGPKAPSGGKKATQASQEY*

A brief summary of all the expression constructs used in this work is shown below (*Table 3.3*).

Table 3.3. Summary of protein expression constructs employed in this study.

Construct name	Protein	His_6–tag site	Cloning sites	Protease	GenBank code
pET28a(+)–$AIF_{\Delta 101}$*	$AIF_{\Delta 101}$	N–ter	*Nde*I/*Not*I	Thb	9131
pET28a(+)–$AIF_{\Delta 77}$*	$AIF_{\Delta 77}$	C–ter	*Nco*I/*Nde*I	Thb	9131
pET28a(+)–$AIFL_{\Delta 64}$	$AIFL_{\Delta 64}$	C–ter	*Nco*I/*Nde*I	PP	150209
pET28a(+)–$AIFL_{\Delta 195}$	$AIFL_{\Delta 195}$	C–ter	*Nco*I/*Nde*I	PP	150209
pET28a(+)–$AIFL_{65-168}$	$AIFL_{65-168}$	N–ter	*Nco*I/*Nde*I	PP	150209
pET28a(+)–CHCHD4*	CHCHD4	N–ter	*Nde*I/*Not*I	Thb	131474
pET28a(+)–CypA*	CypA	N–ter	*Nde*I/*Not*I	Thb	5478
pET28a(+)–H2AX*	H2AX	N–ter	*Nco*I/*Nde*I	PP	3014

* Generated in previous work (Romero–Tamayo, 2022).

3.2.2. Preparation and transformation of competent *E. coli*

Transformation is the natural process by which a cell uptakes foreign DNA from its surroundings through the cell membrane. For this to occur favorably bacteria must be in a state known as *competence*, which may be artificially induced in a laboratory through temporary membrane permeabilization (Johnston *et al*., 2014).

Transformation of competent bacteria with an expression vector of interest enables target protein production.

In this work, a chemical method was used to make competent *E. coli* C41 (DE3) and DH5α cells through repeated exposure to various solutions of divalent cations (Sambrook and Russell, 2006). Since starting cultures are antibiotic sensitive, aseptic conditions had to be kept along the whole process. Consequently, all materials and buffers were either sterilized in an autoclave or filtered with Millipore™ 0.22 μm sterile filters. Frozen starting cultures were scraped, spread in a LB–agar plate and grown overnight (O/N). A single colony was picked and transferred into 10 mL of LB broth medium in a 50 mL tube, where it was incubated at 37 °C with 180 revolutions per minute (rpm) agitation O/N. The next day, 200 mL of fresh LB medium in a 500 mL bottle were inoculated with 5 mL of the preinoculum and incubated at 37 °C and 180 rpm until the optical density at 600 nm (OD_{600nm}) reached 0.35–0.45. At that point, culture growth was stopped by immersion on ice for 20 min. The inoculum was maintained at 4 °C from that moment on. Cells were recovered by centrifugation for 15 min at 4,000 rpm and 4 °C in a JA–25.50 rotor using an Avanti J25 (*Beckman Coulter*) centrifuge. The supernatant was discarded and the pellet was resuspended in 40 mL of ice–cold buffer 1 (100 mM $CaCl_2$, 70 mM $MgCl_2$, 40 mM NaAc pH 5.5). After another round of centrifugation under the same conditions, the resulting pellet was resuspended in 4 mL of buffer 2 (100 mM $CaCl_2$, 15% glycerol) and subsequently dispensed in 200 μL aliquots. Competent cell aliquots were frozen by immersion in liquid nitrogen to ensure their transformation capacity and stored at –80 °C.

Competent cell transformation (*Fig. 3.2*) was performed with the pertaining expression vectors when required. Aliquots were thawed in an ice bath, after which 100 μL of competent cells were transferred to sterile microcentrifuge tubes. Then, 100 ng of plasmid were added and the contents were gently mixed. The whole procedure was followed in parallel with a negative control, adding the equivalent volume of sterile water. After 15 minutes of incubation on ice, a heat shock was performed for exactly 50 s at 42 °C to trigger membrane permeabilization. Tubes were hurriedly transferred back to ice for another 2 min, after which 1 mL of LB medium was added. Cells were then incubated at 37 °C and 220 rpm for 1 h 30 min, allowing them to recover and begin expressing the antibiotic resistance marker encoded in the plasmid. An appropriate volume of transformed bacteria (50, 100 or 200 μL per 90 mm plate) was transferred onto LB–agar plates with antibiotic and homogeneously distributed. The plates were stored at room temperature (RT) until the liquid had been absorbed,

after which they were inverted and incubated O/N at 37 °C. Transformed colonies were expected to appear after 12–16 hours (Sambrook and Russell, 2006).

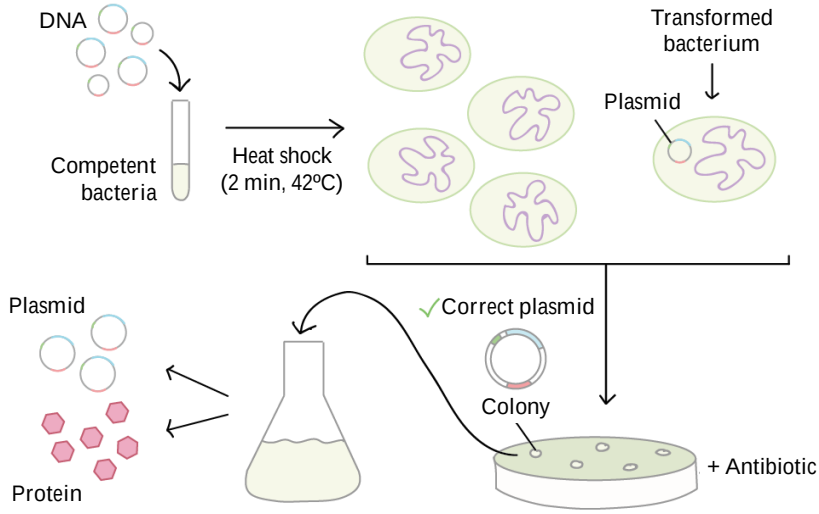

Figure 3.2. Chemically–competent cell transformation through the heat–shock method. Bacteria are mixed with the DNA of interest and exposed to a heat shock, after which a minority of cells may incorporate the genetic material. After incubation in a LB–agar plate with antibiotic, transformed colonies can be selected and subsequently grown. Overexpressed plasmid or protein can be purified afterwards depending on the characteristics of the strain that was transformed. Figure from ya–webdesign.com.

3.2.3. Plasmid purification

A transformed colony was picked and transferred into 5 mL of LB medium with antibiotic in a 50 mL tube, where it was incubated at 37 °C and 180 rpm O/N. Plasmid purification was performed by the alkaline lysis method with the GenElute Plasmid Miniprep kit (*Sigma–Aldrich*) following manufacturer instructions. Briefly, cells were harvested, resuspended in the appropriate buffer and lysed. The mixture was neutralized after up to 5 min and centrifuged to precipitate cell debris, proteins and chromosomal DNA. Then, a DNA–binding column was prepared and the lysate was loaded into it. The column was washed and dried, after which the purified plasmid could be finally eluted.

3.3. Protein Production and Purification

3.3.1. Evaluation of target proteins' expression

Expression of target proteins on transformed *E. coli* cells was initially evaluated through small–scale production in order to optimize growth and induction conditions.

Several colonies containing the expression vector of interest were separately inoculated into 5 mL of LB medium (unless otherwise stated) with antibiotic (LB^{ab}) in 50 mL tubes. Preinoculi were incubated at 37 °C and 180 rpm O/N, after which 100 μL of each were used to inoculate 10 mL of fresh LB^{ab} in 50 mL tubes. Inoculi were subsequently grown at 37 °C and 180 rpm until the desired OD_{600nm} was reached.

At that point, target protein expression was induced by adding IPTG to the optimal final concentration. When deemed necessary, additional supplements were also added. Induced cultures were subsequently incubated at the desired temperature and agitation during the estimated optimal time (O/N unless otherwise stated), after which cells were harvested by centrifugation at 12,000 rpm for 5 min in a 5427R Eppendorf centrifuge at 4 °C. Resulting pellets were resuspended in 1 mL of 50 mM Tris/HCl, pH 8.0, and transferred to 1 mL tubes that were kept in an ice–bath for the following steps.

Cells were lysed with an Up200S (*Hielscher*) ultrasonic equipment for 3–5 cycles of 30 s with an amplitude of 80% and 0.5 s pulses, leaving 30 s of rest in-between cycles. Lysed cultures were centrifuged once more under the same conditions in order to separate the insoluble fraction (cell debris, membranes, precipitated or aggregated protein, chromosomal DNA, etc.) from the soluble one (soluble proteins, sugars, nucleic acids, etc.). Supernatant and pellet samples from each culture were analyzed using 12–20% (depending on the size of the target protein) polyacrylamide denaturing electrophoresis to assess protein expression. Colonies showing the highest soluble protein expression were stored in 500 μL aliquots with 20% glycerol at –80 °C until required.

Optimized growth and induction conditions for each target protein, such as medium, OD_{600nm}, IPTG concentration, induction conditions (temperature, agitation and duration) or supplements are summarized in table 3.4.

Table 3.4. Summary of the optimized growth and induction conditions for each target protein.

Protein	Medium	AB	OD_{600nm}	IPTG (mM)	Induction conditions	Supplements
$AIF_{\Delta 101}$ & variants	LB	Kan	0.8–1.0	1.0	25 °C 100 rpm O/N	RF
$AIF_{\Delta 77}$ & variants	2xYT	Kan	0.5	0.5	37 °C 180 rpm O/N	RF
$AIFL_{\Delta 64}$	LB	Kan	0.8–1.0	0.5	18 °C 100 rpm O/N	Iron chelates, cysteine and RF
$AIFL_{\Delta 195}$	LB	Kan	0.8–1.0	0.5	18 °C 100 rpm O/N	Iron chelates, cysteine and RF
$AIFL_{65-168}$	LB	Kan	0.8–1.0	0.5	18 °C 100 rpm O/N	Iron chelates, cysteine and RF
pRISC + $AIFL_{\Delta 64}$	LB	Kan + Tet	0.8–1.0	0.5	25 °C 100 rpm O/N	Iron chelates, cysteine and RF
CHCHD4	LB	Kan	0.5	1.0	37 °C 180 rpm 3 h	None
CypA	LB	Kan	0.5	0.5	37 °C 180 rpm 3 h	None
H2AX	LB	Kan	0.6	1.0	37 °C 180 rpm 3 h	None

AB stands for antibiotic, Kan for kanamycin (30 μg/mL), Tet for tetracycline (15 μg/mL) and RF for riboflavin. Supplements were added to the following final concentrations: riboflavin (8 μg/mL), ammonium ferric citrate (2 mM), iron sulphate heptahydrate (1 mM) and cysteine (1 mM).

3.3.2. Medium–scale expression of target proteins

Once production conditions had been optimized, target protein expression was taken to medium–scale. Frozen colonies selected for their high expression were slightly thawed on an ice–bath, after which 100 μL were used to inoculate 500 mL of LB^{ab} in a 1 L bottle. Preinoculi were incubated at 37 °C and 180 rpm O/N. The next day, 50 mL were inoculated into 10 Erlenmeyer flasks of 2 L containing 1 L of fresh LB^{ab} each

(unless otherwise stated). The medium was additionally supplemented when deemed necessary (*Table 3.4*). Inoculi were incubated and subsequently induced in the pertaining optimum conditions (*Table 3.4*). Afterwards, cells were harvested by centrifugation at 9.000 rpm for 10 min in a JA–10 rotor in an Avanti J–25 centrifuge (*Beckman Coulter*) at 4 °C. The supernatant was discarded and the pellet was stored at –20 °C.

3.3.3. Purification of target proteins

Target protein purification was facilitated by the presence of a His_6–tag in all cases. Hence, purification protocols were almost identical, excepting working buffers. Target proteins were initially purified with a Ni^{2+} affinity chromatography gel specifically binding the His_6–tag. A summary of the buffers used for the binding, elution and dialysis of each target protein is shown below (*Table 3.5*). When considered necessary, an additional purification step was performed subsequently by means of size exclusion chromatography. H2AX was purified following a slightly differing protocol, as is described in section 3.3.3.2, due to its high degree of impurity carryover.

Table 3.5. Summary of the buffers used for the binding (buffer A), elution (buffer B) and posterior dialysis of each target protein during affinity chromatography. Kpi stands for potassium phosphate.

Protein	Binding buffer (A)	Elution buffer (B)	Dialysis buffer
AIF & variants	50 mM Kpi, pH 7.4, 0.4 M KCl 4 mM Imidazole	50 mM Kpi, pH 7.4, 1 M Imidazole	50 mM Kpi, pH 7.4, 150 mM NaCl
CHCHD4	50 mM Kpi, pH 7.0, 150 mM NaCl	50 mM Kpi, pH 7.0, 150 mM NaCl, 1 M Imidazole	50 mM Kpi, pH 7.0, 150 mM NaCl, 10 mM DTT *
CypA	50 mM Tris/HCl, pH 8.0, 1 mM NaCl	50 mM Tris/HCl, pH 8.0, 1 mM NaCl, 1 M Imidazole, 10% Glycerol	50 mM Kpi, pH 7.4, 150 mM NaCl
H2AX	50 mM Kpi, pH 7.4, 150 mM NaCl	50 mM Kpi, pH 7.4, 150 mM NaCl, 1 M Imidazole	50 mM Kpi, pH 7.4, 150 mM NaCl

* The CHCHD4 dialysis buffer contained 10 mM DTT to ensure a reducing environment.

3.3.3.1. Preparation of raw cell extracts

Cell pellets were transferred to a glass container of 250 mL inside an ice–bath and resuspended in ~100 mL of 50 mM Tris/HCl, pH 8.0, with half a pill of Complete™ Protease Inhibitor Cocktail (*Roche*) per 10 L of culture. Then, cells were lysed by sonication using an UP200S Ultrasonic equipment (*Hielscher*), for 10–12 cycles of 30 s with 30 s of rest in–between, an amplitude of 80% and 0.5 s pulses. The lysate was centrifuged for 1 h at 9,000 rpm in a JA–10 rotor in an Avanti J–25 centrifuge (*Beckman Coulter*) at 4 °C to remove insoluble debris. The supernatant was collected, transferred to a new Beckman bottle and centrifuged once more for 30 min under the same conditions. The resulting raw extract was transferred to a new bottle.

3.3.3.2. Affinity chromatography purification

Target proteins were initially –and seldom solely– purified in an Immobilized Metal ion Affinity Chromatography (IMAC) Sepharose 6 Fast Flow gel (*Cytiva*) previously activated with nickel (Ni^{2+}) (*Fig. 3.3*). The imidazole side chains of a His–tag can establish irreversible bonds with several divalent metal ions (such as Ni^{2+}, cobalt (Co^{2+}) or zinc (Zn^{2+})), amongst which Ni^{2+} is the one that shows both the highest affinity and selectivity. The IMAC Sepharose 6 Fast Flow gel (*Cytiva*) is specifically designed for the binding of His_6–tag proteins and exhibits, furthermore, low non–specific interaction with contaminating proteins. Bound target proteins may be eluted with high concentrations of imidazole, a competitive molecule which displaces their interaction with the activated matrix to allow their recovery.

All buffers in contact with the matrix were previously thoroughly filtered and degasified. For preparation, the Ni^{2+} resin was first washed with 10 column volumes (CV) of distilled water to remove the ethanol used for storage. Then, it was activated with 1 CV of $NiSO_4$ 0.1 M and subsequently washed with another 10 CV of distilled water to remove excess nickel. Finally, it was equilibrated in 10 CV of 50 mM Tris/HCl, pH 8.0.

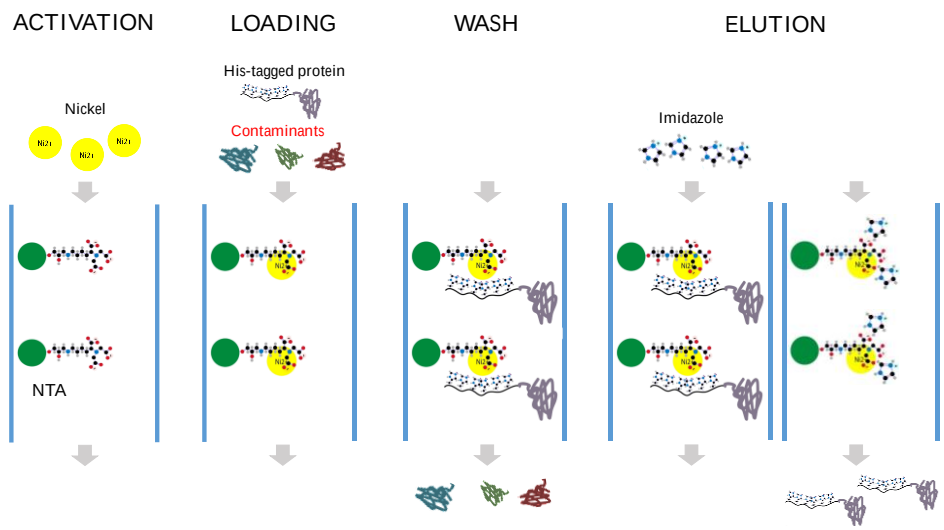

Figure 3.3. Scheme of the affinity chromatography purification of target proteins with a His_6–tag. The affinity chromatography gel is first charged with Ni^{2+}, after which the sample can be loaded. His–tagged proteins bond to the activated matrix (with NTA acting as the chelating ligand), while contaminant proteins are eluted with a subsequent wash. Bound proteins can finally be eluted with a high concentration of imidazole.

The raw cell extract was incubated with the equilibrated Ni^{2+} resin in a bidirectional orbital rocker for 1 h at 4 °C, after which the mixture was loaded and packed into a glass column with the aid of a syringe. 0.4 M KCl and 4 mM imidazole were additionally added to hinder unspecific binding. 5 CV of buffer A (*Table 3.5*) were used to wash the column. Then, bound proteins were eluted with a linear imidazole gradient from 40 to 500 mM of buffer B (*Table 3.5*), with a flow rate of 4 mL/min, and collected in 5 mL fractions at 4 °C using an ÄKTAprime system (*Cytiva*). Fractions containing the target protein were combined, concentrated and dialyzed O/N against the appropriate dialysis buffer (*Table 3.5*) to remove imidazole traces.

The Ni^{2+} resin was regenerated by washing with 5 CV of 1 M imidazole followed by 5 CV of 1 M NaCl and 10 CV of distilled water. For long–term storage, the resin was washed with 5 CV of 20% ethanol and kept at 4 °C.

H2AX purification

For H2AX purification, the cell lysate was centrifuged to remove debris and subsequently mixed with Ni^{2+} IMAC Sepharose 6 Fast Flow gel (*Cytiva*) equilibrated in Tris/HCl 50 mM, pH 8 supplemented with 0.4 M KCl and 4 mM imidazole. This

mixture was incubated on a bidirectional rocker for 45 min at 4 °C, and then packed into an empty column. All subsequent steps were performed at 4 °C in 50 mM potassium phosphate (Kpi), pH 7.4, 150 mM NaCl. The matrix was washed with 200 mM imidazole to discard contaminants, after which impure H2AX was eluted with 1 M of imidazole. Fractions were pooled and subsequently loaded to a PD–10 column (*Cytiva*) to remove the imidazole content, filtered and loaded into a 1–mL HisTrap™ High Performance column (*Cytiva*). The matrix was then washed with 350 mM imidazole and pure H2AX was finally eluted with 1 M imidazole. Fractions were pooled and the imidazole content was removed in a PD–10 column as before.

3.3.3.3. Size exclusion chromatography purification

Size exclusion chromatography (SEC) separates molecules according to their size as they pass through a porous matrix composed of unreactive spherical particles (a.k.a. beads). Molecules from the sample can penetrate the pores to varying degrees based on their size, resulting in a differential elution. Larger molecules are unable to enter the pores and so they elute first; while smaller molecules are "entertained" passing through the pores, consequently eluting last (*Fig. 3.4*).

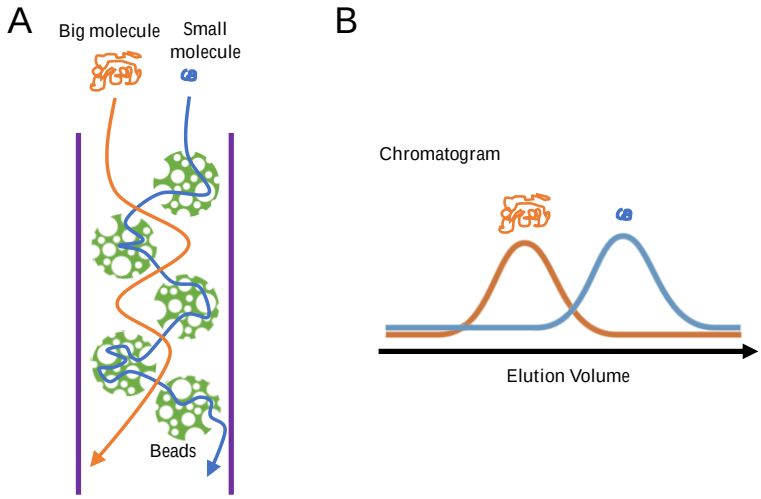

Figure 3.4. Schematic representation of a SEC column (A) and chromatogram (B) of the elution profile. Big particles (orange) cannot diffuse into the pores, taking the shortest path and consequently going through the column faster than smaller ones. This is translated in the chromatogram as a lower elution volume. Small particles (blue) are able to penetrate the pores, taking a longer path and hence eluting much later.

A HiPrep 26/60 Sephacryl™ S–200 High Resolution SEC column (*Cytiva*) attached to an ÄKTAprime system (*Cytiva*) was used to purify target proteins to homogeneity when deemed necessary. Samples up to 10 mL were filtered with Millipore™ 0.22 μm sterile filters and subsequently loaded and eluted with a flow of 1 mL/min in the same buffer in which they had been previously dialyzed (*Table 3.5*). Target proteins were collected in 4 mL fractions at 4 °C, combined, concentrated and stored at –80 °C. Previous to sample loading, the SEC resin was washed with 1.5 CV of distilled water and equilibrated in 1 CV of the appropriate buffer. After its use, traces of sample and buffer were washed away with 1.5 CV of distilled water, and the resin was stored in 1 CV of 20% ethanol with overpressure. All buffers were previously thoroughly filtered and degasified. For column calibration, an LMW (Low Molecular Weight) calibration kit containing six proteins in the 6.4–160 kDa range was used (*Cytiva*).

3.3.3.4. Removal of the His_6–tag

While target protein purification was indeed facilitated by the presence of the His_6–tag, in some instances it was deemed necessary to remove said tag. In order to do so, the purified protein of interest was treated with the pertaining protease (be that Thb or PP, *Table 3.3*) and subsequently loaded onto a Ni^{2+} activated HiTrap Chelating HP column (*Cytiva*). Columns were previously activated following the instructions provided by the manufacturer.

Typically, 1 mL of protein containing 0.2 U of protease was loaded onto the column and subsequently incubated, first for 1 hour at RT and then overnight at 4 °C. The following day, the target protein was eluted with the working buffer of interest (usually the dialysis buffer, *Table 3.5*). The remaining non–digested protein was retained in the column and could thereafter be eluted with buffer B (*Table 3.5*) and dialyzed.

3.4. Biochemical and Biophysical Characterization

3.4.1. Target protein identification

As a preliminary step to ensure that levels of protein expression were adequate, and in order to ascertain the purity of a protein sample after purification, target proteins were identified through polyacrylamide gel electrophoresis. When imperative (i.e., for significantly impure samples), a western blot (WB) was additionally performed.

3.4.1.1. Polyacrylamide gel electrophoresis

Polyacrylamide gel electrophoresis (PAGE) is an analytical technique that allows proteins to be separated according to their differential motility in an electric field. PAGE can be performed under non–denaturing conditions, separating proteins based on their hydrodynamic charge and size, or under denaturing conditions (i.e., through the addition of the anionic detergent sodium dodecyl sulphate, SDS), separating proteins based only on their size (Laemmli, 1970). In denaturing PAGE (SDS–PAGE), the SDS molecule binds proteins non–specifically, covering their intrinsic charge and providing them of a similar charge–to–mass ratio. Therefore, when the protein–SDS complex migrates through an SDS–PAGE it separates according solely to its size. By comparison with known molecular weight (MW) markers, the MW of target proteins can be determined. On the other hand, through the use of clear native PAGE (CN–PAGE), whole protein complexes or assemblies (formed by more than one subunit or protein) can be resolved. In this way, the MW of native proteins and assemblies can be determined, allowing the identification of significant protein–protein interactions.

Gels were prepared in a Mini–PROTEAN Tetra Cell (*Bio–Rad*) system following the recipes in table 3.6, with a resolution ranging from 12% to 20% of polyacrylamide depending on the protein of interest. Glasses were thoroughly cleaned with water and ethanol and subsequently assembled following manufacturer instructions (*Fig. 3.5*).

In the first place, the running gel was prepared, adding the APS and TEMED last, and the solution mixture was slowly poured between the assembled glasses. The mixture was immediately covered with isopropanol to smooth its surface and allowed to polymerize. Thereafter, the isopropanol was removed and the space between the glasses was carefully washed with distilled water and subsequently dried with a small piece of paper. The stacking gel was prepared and immediately poured over the running gel. Then, a comb was inserted between both glasses avoiding the formation of bubbles and the gel was allowed to polymerize.

Once all gel cassettes were assembled, each one was placed into the clamping frame facing either another cassette or the buffer dam and the system was hermetically locked as in figure 3.5E. The frame was filled with electrophoresis buffer (25 mM Tris/HCl, pH 8.8, 0.2 M glycine, 12.5% SDS for SDS–PAGE gels; or cathode buffer (5 mM tricine, 7.5 mM imidazole, pH 7.0; supplemented with 0.02% dodecyl maltoside and 0.05% deoxycholate) inside the sandwich and anode buffer (25 mM imidazole/HCl, pH 7.0) in the bucket for CN–PAGE gels) and the comb was

withdrawn from each gel. Samples were mixed with 5x loading buffer (50 mM Tris/HCl, pH 8.0, 50 mM EDTA, 12.5% SDS, 25% BME, 35% glycerol, 0.1% bromophenol blue for SDS–PAGE gels; 100 mM Tris/HCl, pH 8.0, 10% glycerol, 0.006% phenol red for CN–PAGE gels) up to a maximum volume of 20 µL, boiled for 5 min at 100 °C (in the case of SDS–PAGE gels) and subsequently loaded.

Table 3.6. Solution mixtures for PAGE gel preparation. Quantities are specified for approximately two gels. APS stands for ammonium persulfate, TEMED for tetramethylethylenediamine.

Reagents	SDS–PAGE				CN–PAGE	
	Running gel			Stacking gel	Running gel	Stacking gel
	12%	15%	20%	4%	12%	4%
Distilled H_2O	4.3 mL	3.6 mL	2.3 mL	3.6 mL	2.6 mL	2.6 mL
Acrylamide 30%	3.0 mL	3.7 mL	5 mL	666 µL	4 mL	666 µL
Buffer	2.5 mL	2.5 mL	2.5 mL	625 µL	3.3 mL	1.7 mL
SDS 20%	50 µL	50 µL	50 µL	25 µL	–	-
APS 10% *	100 µL	100 µL	100 µL	50 µL	100 µL	50 µL
TEMED *	10 µL	10 µL	10 µL	5 µL	10 µL	5 µL

* Added last. Buffer: Tris 1.5 M, pH 8.8., for SDS–PAGE running gel; Tris 1 M, pH 6.8, for SDS–PAGE stacking gel; 50 mM Bis–Tris, 1.5 M aminocaproic acid, pH 7, for CN–PAGE gels.

Up to 5 µL of PageRuler Plus Prestained Protein Ladder (*Thermo Fisher Scientific*) MW marker were also loaded onto at least one well of each gel. At this point, the tank was filled with electrophoresis buffer, the lid was placed and the system was connected to the power supply. The amperage was set to 20 mA/gel until the sample front reached the running gel, after which it was increased to 40 mA/gel. The run carried on until the sample front reached the end of the gel. Then, each gel was withdrawn from its cassette and glasses, and subsequently put in a container with staining solution (0.5 g Coomassie Brilliant Blue R–250, 45% methanol, 10% acetic acid, 2% glycerol) until the protein bands became visible. Thereafter, the staining solution was discarded and the gels were submerged in de–staining solution (25% methanol, 10% acetic acid, 2% glycerol) which was periodically replaced with fresh solution until the excess colorant was completely removed.

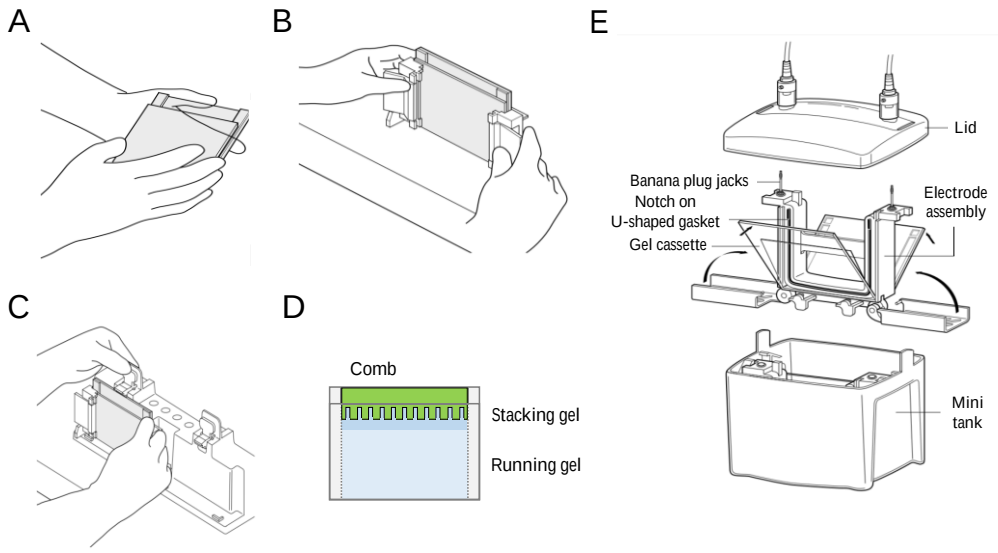

Figure 3.5. Schematic PAGE gel preparation and assembly of the vertical electrophoresis system. (A–C) Glasses were assembled following manufacturer instructions with the notch towards the inside. (D) Running and stacking gels were prepared and subsequently poured into the assembled glasses one on top of the other, allowing the former to polymerize in between. A comb was inserted before polymerization of the latter to create the wells. (E) Gel cassettes were placed in the clamping frame with the short plate facing inward, locked in place with both lateral arms and subsequently introduced in the tank. The tank was filled with electrophoresis buffer, the lid was placed over it and the system was connected to the power supply. Panels A–C and E are taken from the Mini–PROTEAN Tetra Cell (*Bio–Rad*) instruction manual.

3.4.1.2. Western blot

WB is a renowned technique widely used for the specific identification of target proteins within a complex protein mixture. Once the sample has been separated by gel electrophoresis, proteins are transferred to a solid support and the target can subsequently be marked with the appropriate primary and secondary antibodies (Mahmood and Yang, 2012). In this work, WB was performed when target protein identification was otherwise uncertain.

Protein bands from electrophoretic gels were transferred to a polyvinylidene difluoride (PVDF) membrane using a Mini Trans–Blot Cell (*Bio–Rad*) system. The membrane was initially activated with methanol for 5 s, rinsed with water and equilibrated in ice–cold transfer buffer (48 mM Tris/HCl, pH 8.0, 39 mM glycine, 1.6 mM SDS, 20% methanol) for at least 10 min. Thereafter, the gel sandwich was

assembled following manufacturer instructions (*Fig. 3.6A*). Fiber pads, filter papers and the gel were also previously equilibrated in transfer buffer. The sandwich was firmly locked, placed in the module and introduced in the tank, together with the frozen cooling unit and a stir bar (*Fig. 3.6B*). Then, the tank was filled with transfer buffer, the lid was put over it and the system was connected to the power supply.

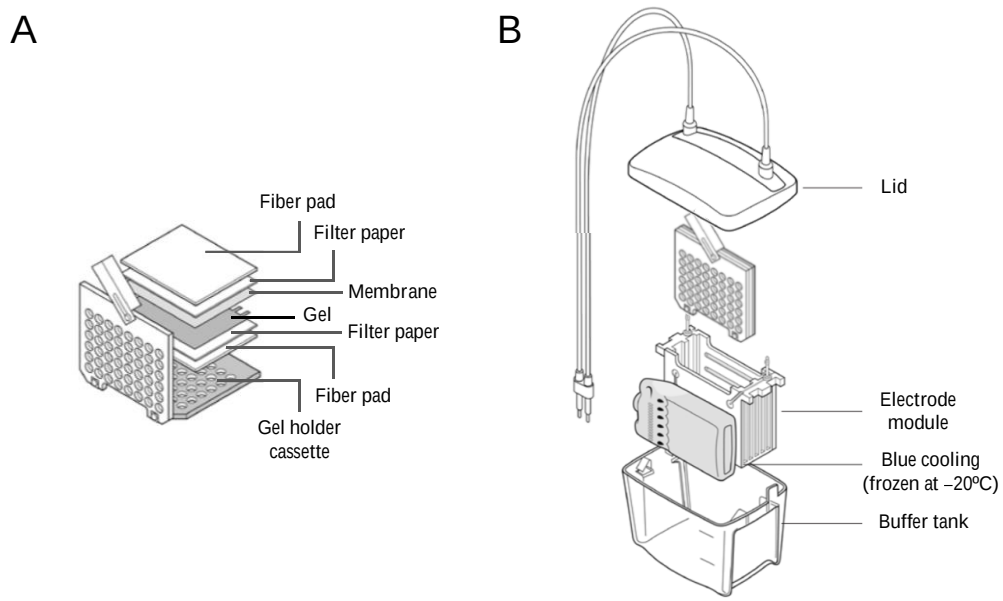

Figure 3.6. Scheme of gel sandwich and transference system assembly. (A) The activated membrane is placed directly on top of the electrophoretic gel, being enclosed on both sides by two pieces of filter paper and two fiber pads previously equilibrated in transfer buffer. (B) The sandwich is locked and introduced in the electrode module, which is in turn placed inside the buffer tank. A frozen cooling unit and a stir bar are added and the tank is filled with transfer buffer. Finally, the lid is put on top and the system can be connected to a power supply. Figure from the Mini Trans–Blot Cell (*Bio–Rad*) instruction manual.

Electrotransference took place for 1 h at 100 V and 4 °C. After this, the sandwich was taken apart and the membrane was put in a plastic container with distilled water, where it was rinsed for 10 min. The water was discarded and the membrane was blocked in TBS–T (Tris Buffered Saline: 50 mM Tris/HCl, pH 7.5, 150 mM NaCl; 0.1% v/v Tween–20) with 5% of milk either for 1 h at RT or O/N at 4 °C with constant agitation.

Once the membrane had been blocked, the solution was discarded and the membrane was washed for 5 min three consecutive times with fresh TBS–T until all milk traces

were removed. At that point, the membrane was incubated with the primary antibody (mouse anti–His–tag, *GenScript*; or rabbit anti–hAIF, *Sigma*) for either 1 h at RT or O/N at 4 °C with constant agitation. Then, the membrane was washed three more times and incubated with the secondary antibody (goat anti–mouse IgG, *GenScript*; or goat anti–rabbit IgG, *Invitrogen*), conjugated with radish peroxidase, for 1 h at RT. Both antibodies were diluted in TBS–T to the suitable concentration (1:10,000 or 1:20,000 for the primary antibodies, and 1:1,000 or 1:6,000 for the secondary) with 0.1% of milk. The membrane was washed three last times to remove any excess antibody and incubated for 1 min with chemiluminescent Pierce™ ECL Western Blotting Substrates (*Thermo Fisher Scientific*). The detection reagents, luminol and peroxide, react with radish peroxidase producing chemiluminescence which can be immediately detected. Target protein bands were developed using the Amersham™ Imager 600 (*Cytiva*) automated WB processor.

Membranes may be reused after the procedure. Attached proteins and antibodies can be removed by immersing the membrane in stripping solution (1 M Tris/HCl, pH 6.7, 100 mM BME, 2% SDS) and incubating at 58 °C for 30 min. After three consecutive washes of 10 min with distilled water at RT the membrane is ready to be used again.

3.4.2. Chemical crosslinking

Quaternary assemblies and protein interaction partners were identified by SDS–PAGE after having been stabilized with the bis(sulfoccinimidyl) suberate (BS^3) crosslinker (*Thermo Fisher Scientific*). BS^3 is a homobifunctional amine–to–amine crosslinking agent that is water–soluble and membrane impermeable. It contains an *N*–hydroxysulfosuccinimide ester at each end which reacts with primary amines (such as that of the side chain of lysine residues or protein N–termini) to form stable amide bonds (*Thermo Fisher Scientific*).

Samples were incubated for 1 h at RT with 100–fold excess of BS^3, after which the reaction was stopped with quenching buffer 10x (0.5 M Tris/HCl, pH 8.0) for 15 min. Then, solutions were boiled for 5 min at 100 °C, mixed with SDS–PAGE loading buffer and loaded onto a polyacrylamide gel of the pertaining resolution depending on the target. Quaternary assemblies and protein interaction partners were subsequently identified by gel electrophoresis as in section 3.4.1.1. For the evaluation of the oligomerization of AIF variants, samples were prepared in the absence and presence of 100–fold excess NADH.

3.4.3. Molecular weight determination

Target proteins and their association states (such as quaternary assemblies and other complexes) were further evaluated through the determination of their apparent MW (^{app}MW) by size exclusion chromatography. Samples were prepared according to each experiment and SEC was performed as described in section 3.3.3.3, but with a smaller column of higher resolution (Superdex^{TM} 200 10/300 GL, *Cytiva*). Volumes were accordingly adjusted. The oligomerization of AIF variants was evaluated both in the absence and presence of 100–fold excess NADH. To determine the ^{app}MW of target proteins and their association states, a calibration curve had to be produced. The SEC column was calibrated as in section 3.3.3.3, and the relative mobility (K_{av}) of each protein within the calibration kit was calculated using equation 3.2. The K_{av} values obtained for the calibration proteins were represented against the logarithm of their MWs, yielding a calibration curve. This could subsequently be used to extrapolate the ^{app}MW of target proteins and their association states, having previously calculated their K_{av} values through their elution volumes with equation 3.2.

$$K_{av} = \frac{V_e - V_o}{V_c - V_o} \quad \text{(Eq. 3.2)}$$

where V_e is the protein elution volume, V_c the geometric column volume and V_o the column void volume.

3.4.4. Agarose gel electrophoresis

Agarose gel electrophoresis is an analytical technique akin to PAGE but with a lower resolving power, that is typically used to identify medium– to large–sized DNA or RNA molecules (traditionally 100 bp to 25 kb) due to its greater range of separation. As nucleotides are intrinsically negatively charged, the mobility of any DNA or RNA molecule directly correlates with its size (and consequently with its length, if the molecule is linearized). The DNA or RNA molecule may be bound to a protein or even a complex before being loaded, allowing for the study of protein–nucleic acid interactions through an effect known as *mobility shift* (see section 3.4.4.1). The presence of secondary structures such as DNA supercoiling (which may occur in plasmids) can also affect the rate of migration (*Bio–Rad*). In this work, ethidium bromide (EtBr, a fluorescent dye that can be excited with UV light) was employed to aid the visualization of dsDNA, as it is able to intercalate between its base pairs.

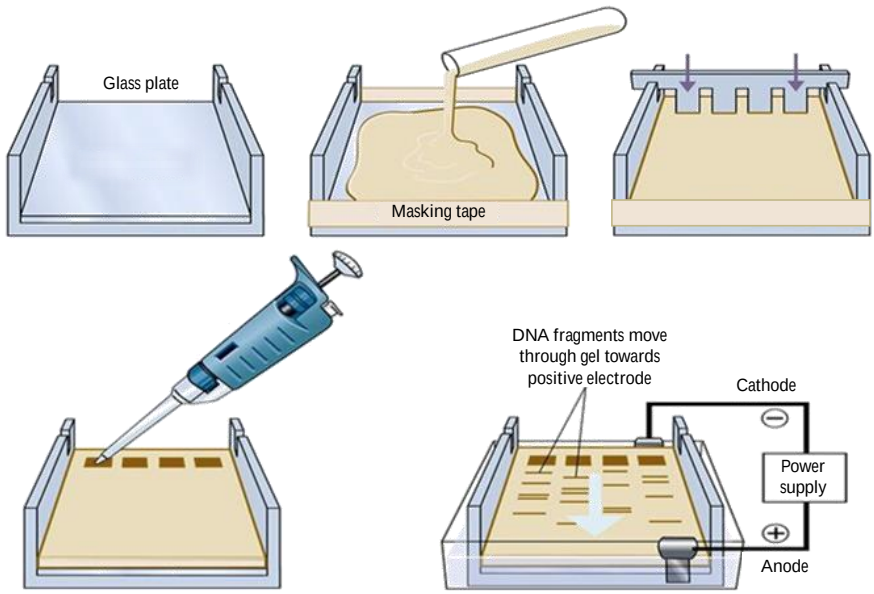

Figure 3.7. Schematic agarose gel preparation and assembly of the horizontal electrophoresis system. A glass plate is sealed on both sides with masking tape, after which the agarose solution is poured and the comb is added. To prepare the agarose solution, solid agarose is previously mixed with the chosen electrophoretic buffer and boiled until it becomes a homogeneous mixture, then allowed to cool and subsequently mixed with EtBr. Once the agarose gel has polymerized, the masking tape and the comb are taken off. Then, the gel plate can be immersed in the electrophoretic buffer within the gel tank, the samples loaded into the wells and the tank connected to the power supply. Gels are typically run for 1 hour at 90 V, although conditions vary depending on the size of the molecule of interest. Figure partly modified from https://microbiologynotes.org/gel-electrophoresis-types-principles-instrumentation-and-applications.

Unlike PAGE, agarose gel electrophoresis is performed in horizontal gel tanks. To prepare a standard gel (*Fig. 3.7*), solid agarose was mixed with 50 mL of the buffer of interest (typically TBE: 90 mM Tris–borate, pH 8.0, 2 mM EDTA; or TAE: 40 mM Tris–acetate, pH 8.0, 1 mM EDTA) in a concentration of 0.4 to 2%, depending on the size of the molecule to be separated (the lower the percentage of agarose, the wider the pores). The mixture was subsequently boiled until it became homogeneous, then it was allowed to cool to ~50 °C and the EtBr was added.

Once this was done, the agarose solution could be poured into a glass plate previously sealed with masking tape. A comb was added to form the wells and the gel was allowed to polymerize. Afterwards, the masking tape was taken off and the glass plate with the

agarose gel inside was immersed in the electrophoretic buffer in the gel tank. Samples were subsequently mixed with 6x DNA loading dye (*Thermo Fisher Scientific*) and loaded onto the wells. Then, the gel tank could be connected to the power supply. Typically, 1–2% agarose gels were run for 1 hour at 90 V at RT, and 0.4–0.7% gels were run for 4 hours at 60 V in an ice–bath.

Once the run had finished, the agarose gel was taken out of the glass plate and carefully set on the tray of a ChemiDoc™ XRS+ System transilluminator (*Bio–Rad*) for visualization of the resulting DNA bands. Images were visualized and analyzed using the Quantity One software (*Bio–Rad*).

3.4.4.1. Electrophoretic–mobility–shift assay

Electrophoretic–mobility–shift assays (EMSA) were carried out by mixing 500 ng of GeneRuler 100 bp dsDNA ladder (*Thermo Scientific*) with 6 µg of AIF, which were then incubated for 30 min at 25 °C in 50 mM of Kpi, pH 7.4. Samples were subsequently mixed with 2 µL of 6x DNA loading dye (*Thermo Fisher Scientific*), resolved by electrophoresis in 2% agarose gels and visualized by EtBr staining.

Results were processed with a ChemiDoc™ XRS+ System transilluminator (*Bio–Rad*), using the Quantity One software.

3.4.4.2. Nuclease activity assay

Nuclease activity assays were performed by mixing 250 ng of a double–stranded supercoiled pET–28a(+) plasmid or 500 ng of genomic dsDNA (gDNA) as substrate with 250 ng of purified $AIF_{\Delta 101}$ (or 1 IU of DNase) in 20 mM Tris, pH 8.0 in a final volume of 10 µL, with 0.1 mM $CaCl_2$ and 1mM $MgCl_2$ unless otherwise stated.

Samples were typically incubated for 1 min at 37 °C, after which they were mixed with 6x DNA loading dye (*Thermo Fisher Scientific*) and subsequently incubated for 10 min at 65 °C. Samples were then loaded onto a 1% or 0.7% agarose gel with EtBr and run for 1 or 4 hours at 90 or 60 V depending on whether they contained plasmid or genomic DNA. For the 4–hour long runs, gel chambers were immersed in an ice–bath to maintain a stable temperature.

Human or mouse genomic DNA was extracted from HeLa or MEF cells, respectively, by means of a QIAamp DNA kit (*Qiagen*). To determine the influence on nuclease

activity of the $AIF_{\Delta 101}$ interaction with physiological partners, protein mixtures were pre–incubated for 15 min at 25 °C prior to mixing with dsDNA.

Genomic DNA integrity assays were performed on the 2200 TapeStation microfluidic platform (Genomic ScreenTape device, *Agilent Technologies*) using a genomic ladder and following the manufacturer's instructions, by the SAI (Servicio de Atención a la Investigación, Unizar). Integrities were quantified using DNA Integrity Numbers (DINs) in a scale of 1 to 10 (from very degraded DNA to highly intact DNA).

Densitometry was employed to quantitate DNA degradation from the solution nuclease assays. Agarose gels stained with ethidium bromide were scanned with a Gel Doc EQ (*Bio–Rad*) system and subsequently quantitated using the Quantity One (*Bio–Rad*) software. To calculate the percentage of non–degraded DNA, the area comprising each peak was delimited and the intensity of signal within it was measured.

Background noise was calculated likewise, delimiting an area of identical dimensions in the same well but with no peak, and subsequently subtracted from the samples' and control's signals' intensity. The measured intensity of the control (DNA without nuclease) was considered to be 100%. To determine the relative rate of DNA degradation, the estimated amount of degraded DNA (ng) was divided by the time of degradation (seconds) and the amount of AIF (ng).

3.4.5. Spectroscopic characterization

Several spectroscopic techniques were employed for the functional and structural characterization of target proteins in this study. Ultraviolet/Visible (UV/Vis) absorption spectra were routinely recorded to check protein integrity and determine its concentration, as well as to calculate experimental molar extinction coefficients (ε). Circular dichroism (CD) and fluorescence spectra were used to evaluate structural features such as secondary structure or cofactor environment. Thermal denaturation curves were also recorded through CD and fluorescence, providing information on overall protein stability and cofactor release.

3.4.5.1. UV/Visible absorption spectroscopy

UV/Vis absorption spectroscopy is a conventional technique used to measure the attenuation of a beam of light as it passes through a solution. This attenuation is a result of the absorption properties of some functional groups within molecules, which

are known as *chromophores*. In the case of UV/Vis absorption spectroscopy, the measurement takes place within a specific range of light wavelength (200 to 800 nm) and can later be represented as absorption (in arbitrary units, AU) against wavelength (λ).

Using the Beer–Lambert law (*Eq. 3.3*) we can calculate the concentration of a sample from its absorption spectrum, and even determine its purity through the comparison with standard spectra. UV/Vis absorption spectra were routinely recorded in a Cary 100 Bio (*Agilent Technologies*) spectrophotometer to determine target protein integrity and concentration, using 1 cm light path cuvettes and a scan speed of 600 nm/min.

$$A_\lambda = \varepsilon_\lambda \cdot c \cdot l \quad \text{(Eq. 3.3)}$$

where A_λ is the absorption at a particular wavelength λ, ε_λ the molar extinction coefficient at that wavelength ($M^{-1}\ cm^{-1}$), c the sample concentration (M), and l the light path length (cm).

In some instances, target protein ε values had to be experimentally determined. Absorption spectra (A_{prot}) were recorded as triplicates, after which the samples were boiled for 5 min at 100 °C and centrifuged for 3 min at 12,000 rpm to pellet the denatured proteins. Then, spectra were recorded of the supernatants, containing the now–free cofactor (A_{cof}). With the observed absorption spectra before and after denaturation, target protein ε values could be calculated using equation 3.4. Free cofactor ε values were taken from the literature ($\varepsilon_{FAD,451} = 11.3\ mM^{-1}\ cm^{-1}$, Aliverti *et al.*, 1999).

$$\frac{A_{cof,\lambda}}{A_{prot,\lambda}} = \frac{\varepsilon_{cof,\lambda}}{\varepsilon_{prot,\lambda}} \quad \text{(Eq. 3.4)}$$

where A_λ is the absorption of the cofactor (cof) or protein (prot) at a particular λ, and ε_λ the molar extinction coefficient of the cofactor (cof) or protein (prot) at that particular λ.

A summary of the ε values of the target proteins studied in this work is shown in table 3.7.

Table 3.7. Summary of the ε values at the wavelength of interest of the various proteins used in this study. For target flavoproteins, λ of interest correspond to the maximum absorbance at the band I of the flavin.

Protein	Form	λ of interest (nm)	ε ($mM^{-1}·cm^{-1}$)
WT	$AIF_{\Delta 101}$	452	13.7[a]
WT	$AIF_{\Delta 77}$		13.6[b]
T141I	$AIF_{\Delta 101}$	452	12.6[a]
	$AIF_{\Delta 77}$		13.4[a]
M340T	$AIF_{\Delta 101}$	452	12.3[a]
	$AIF_{\Delta 77}$		16.7[a]
W483G	$AIF_{\Delta 101}$	451	12.8[b]
	$AIF_{\Delta 77}$		12.1[b]
W483L	$AIF_{\Delta 101}$	451	11.9[b]
	$AIF_{\Delta 77}$		12.2[b]
W483Y	$AIF_{\Delta 101}$	451	13.4[b]
	$AIF_{\Delta 77}$		13.6[b]
CHCHD4	–	280	13.3[c]
CypA	–	280	8.7[c]
H2AX	–	280	6.0[c]

[a] Data calculated in this work. [b] Data calculated in our lab. [c] Theoretical data calculated with the ProtParam tool (ExPASy Bioinformatic Resource Portal, https://web.expasy.org/protparam/). For variants Y443A, K446A, R449A, R450A, R451A, H454S, D489/K518A, K518A/E522A and K510A/K518A the ε was estimated to be equal to the WT.

3.4.5.2. Circular dichroism spectroscopy

CD spectroscopy is a prominent technique that measures the differential absorption of left– and right–handed circularly polarized light by an optically active chiral molecule (such as the α–carbons of a polypeptide chain). It is generally used to rapidly determine overall secondary structure (*Fig. 3.8*) and stability of recombinant proteins, as well as to analyze the possible effects of a mutation on these features (Greenfield, 2006).

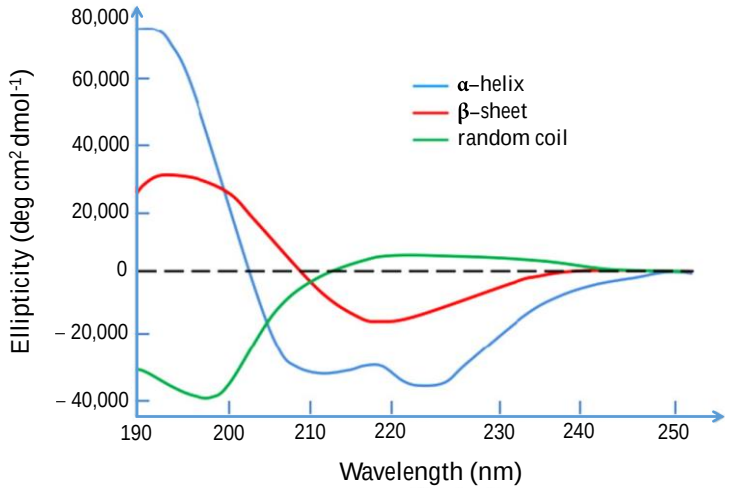

Figure 3.8. Characteristic CD spectra of the three basic secondary structures of a protein. CD spectra of hypothetical polypeptides composed solely of α–helixes (blue), β–sheets (red) or random coils (green) are roughly represented, being easily differentiable. Figure slightly modified from Wei *et al*., 2014.

As the polarized light is differentially absorbed by the sample it becomes *elliptically* polarized, an effect which can be reported as the *degree of ellipticity* (θ). This parameter can be corrected for concentration to *molar ellipticity* ($[\theta]$) regarding the whole protein (*Eq. 3.5*), and even further to *mean residue ellipticity* ($[\theta_{mr}]$) when referred to individual residues (*Eq. 3.6*) (*Applied Photophysics Ltd.*). θ_{mr} can be particularly useful, as it allows comparison of secondary structure content between proteins which may differ greatly in MW.

CD spectra were recorded in a thermostated Chirascan (*Applied Photophysics Ltd.*) spectrometer at 25 °C in 50 mM Kpi, pH 7.4, 21 mM NaCl (150 mM ionic strength), both in the Far–UV (190–260 nm) and near–UV/Vis range (260–700 nm). Measurements in the Far–UV range provided information regarding secondary structure elements (*Fig. 3.8, Eq. 3.6*), while Near–UV/Vis unveiled the overall environment of aromatic residues and cofactors (*Eq. 3.5*). Assays were performed in 0.1 cm path length cuvettes (*Hellma*) with 1 µM of protein for Far–UV CD, and in 1 cm path length cuvettes (*Hellma*) with 20 µM of protein for Near–UV/Vis CD. All spectra were baseline–corrected by subtracting the buffer signal. Oxygen was purged from the spectrometer before data recording through a nitrogen flow.

$$[\theta] = 100 * \frac{\theta}{c * l} \quad \text{(Eq. 3.5)}$$

$$[\theta_{mr}] = \frac{MW/(N-1) * \theta}{10 * c * l} \quad \text{(Eq. 3.6)}$$

where $[\theta]$ is the molar ellipticity (deg cm^2 dmol^{-1}), $[\theta_{mr}]$ the mean residue ellipticity (deg cm^2 dmol^{-1}), θ the observed ellipticity (deg), c the sample concentration (M), l the path length (cm), MW the molecular weight of the target protein (g mol^{-1}), and N the number of amino acids of the target protein.

3.4.5.3. Fluorescence spectroscopy

Fluorescence spectroscopy is a highly sensitive technique used to analyze structural features of a sample based on its fluorescent properties. A beam of light is emitted which can excite the electrons of certain molecules, causing them to emit light in exchange. Part of the energy is absorbed by the electron as it jumps from its ground state to an excited state, leading to the emission spectrum *shifting* towards longer wavelengths than the excitation spectrum (*Fig. 3.9*).

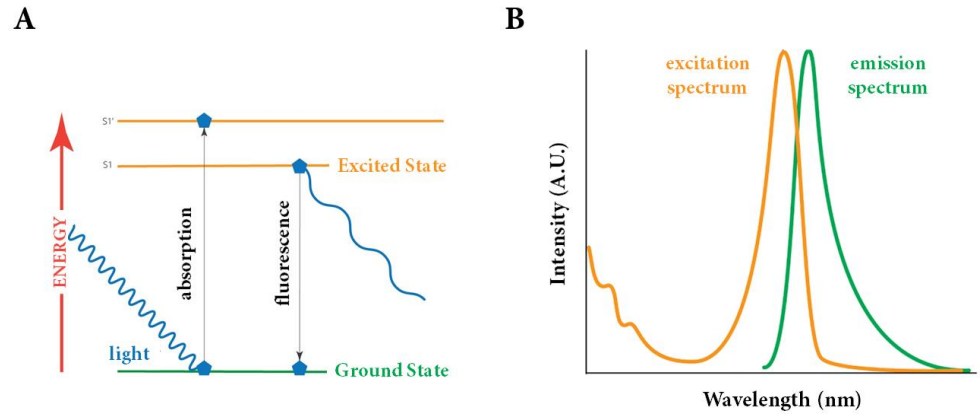

Figure 3.9. Schematic behavior of a fluorescent electron and resulting fluorescent spectra. (A) Emitted light is absorbed by the electron, allowing it to jump from the ground state (green) to the excited state (orange). Unable to linger there, the electron ends up dropping back to the ground state, emitting light. (B) Electron excitation yields an excitation spectrum (orange) that can be reported by fluorescent spectroscopy, while energy release as the electron returns to the ground state is reflected as an emission spectrum (green). Part of the original energy is lost in the process, causing emission spectra to *shift* to longer wavelengths. Figures slightly modified from *World Precision Instruments*.

Proteins display intrinsic fluorescence driven by the presence of aromatic residues (tryptophan, tyrosine and/or phenylalanine) in their sequence. Each aromatic residue presents a slightly differing behavior, but tryptophans stand out with the strongest signal. Since signal intensity is significantly influenced by the residues' environment, phenomena such as protein unfolding can be monitored with fluorescence spectroscopy. Some prosthetic groups (i.e., flavin cofactors) also present fluorescence, although it tends to be mostly quenched by the environment. Consequently, active site structural and dynamical features can be monitored too through changes in cofactor fluorescence signal.

Fluorescence spectra were recorded in a thermostated Cary Eclipse (*Agilent Technologies*) fluorescence spectrophotometer at 25 °C, in 50 mM Kpi, pH 7.4, 21 mM NaCl (150 mM ionic strength). Protein intrinsic fluorescence emission was measured from 300 to 400 nm upon excitation at 280 nm, while flavin fluorescence emission was measured from 480 to 600 nm after excitation at 450 nm. All measurements were performed in a 1 cm path length quartz cuvette (*Hellma*).

3.4.6. Thermal denaturation

Thermal denaturation curves were monitored by fluorescence emission of the flavin cofactor (if applicable) as well as with far–UV and near–UV/Vis CD, from 10 °C to 90 °C with scan rates of 1.5 °C/min and 1 °C/min respectively. The temperature was continuously monitored with a temperature probe and controlled by a Peltier unit. For AIF and its variants, assays were performed both in the absence and presence of 100–fold excess NADH.

Protein concentrations, wavelengths and pathlengths were 2 μM, 530 nm (excitation at 450 nm) and 1 cm for flavin fluorescence; 1 μM, 210 nm and 1 mm in far–UV CD (220 nm with NADH); and 20 μM, 300 nm and 1 cm in near–UV/Vis CD (420 nm and 600 nm with NADH).

Experimental data sets were analyzed individually as one–transition processes (two–state process, native ↔ unfolded, N ↔ U) or two–transition processes (three–state process, native ↔ intermediate ↔ unfolded, N ↔ I ↔ U) according to the unfolding model in equation 3.7 and subsequently following equations 3.8 and 3.9 respectively.

$$\Delta G_i = \Delta H_i \left(1 - \frac{1}{T_{mi}}\right) + \Delta C_{Pi} \left(T - T_{mi} - T \ln \frac{T}{T_{mi}}\right) \quad \text{(Eq. 3.7)}$$

where ΔG_i is the Gibbs free energy of an unfolding transition i at a given temperature T, ΔH_i the van't Hoff enthalpy for that transition i, ΔC_{Pi} the heat capacity change for that transition i, and T_{mi} the mid–point temperature of transition i.

$$S_{obs} = \frac{S_N + m_N T + (S_U + m_U T) e^{-(\Delta G/RT)}}{1 + e^{-(\Delta G/RT)}} \quad \text{(Eq. 3.8)}$$

$$S_{obs} = \frac{S_N + m_N T + (S_I + m_I T)\, e^{-(\Delta G_1/RT)} + (S_U + m_U T) e^{-((\Delta G_1 + \Delta G_2)/RT)}}{1 + e^{-(\Delta G_1/RT)} + e^{-((\Delta G_1 + \Delta G_2)/RT)}} \quad \text{(Eq. 3.9)}$$

where S_{obs} is the observed signal at a given temperature T; S_N, S_I and S_U the intrinsic signals of the native, intermediate and unfolded protein conformational states; m_N, m_I and m_U the slopes of the baselines before the first transition, between the first and the second transitions, and after the second, respectively; ΔG, ΔG_1 and ΔG_2 the Gibbs free energies associated to each transition (Eq. 3.7); and R the ideal gas constant.

3.4.7. Isothermal titration calorimetry

Isothermal titration calorimetry (ITC) is a powerful technique to quantitatively characterize intermolecular interactions based on the heat that is released (exothermic interactions) or absorbed (endothermic interactions) after binding (Velázquez–Campoy *et al*., 2004). The core of the ITC system is the calorimeter: it presents two cells, the reference and the sample, whose temperatures are continuously being monitored and kept equal (*Fig. 3.10*). The reference cell is filled with water, while the sample cell contains the target (typically a protein). The ligand, be it an organic molecule or another protein, is contained in a syringe which repeatedly injects a fixed volume into the sample cell, resting in between so the system can reach equilibrium.

If an interaction takes place in the sample cell after a ligand injection, a slight temperature variation is produced. As soon as the calorimeter senses this alteration, the thermal power supplied to the sample cell is adjusted in order to maintain both cells at the same temperature. Consequently, ligand injections can be represented as a sequence of heat peaks (*Fig. 3.10*), where the area of each peak directly relates to the heat exchanged after each binding and, in turn, to the amount of intermolecular complex formed. Injections are consecutively repeated until the sample is completely saturated with ligand and no more heat variations can be detected.

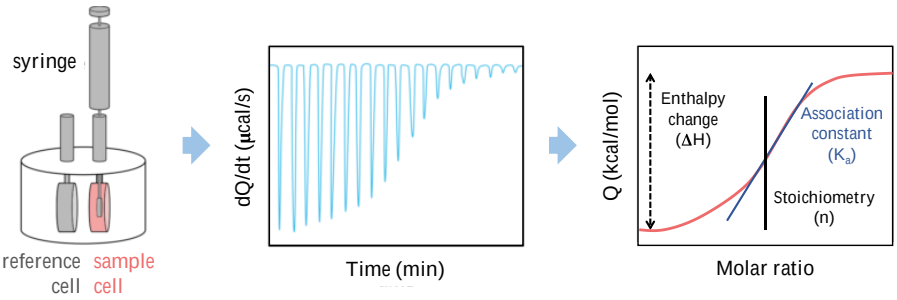

Figure 3.10. Schematic calorimeter of an ITC system and representative thermograms. The sample (typically the target protein) is placed in the sample cell, while the reference cell is filled with water (left). The ligand is consecutively injected in the sample cell with the syringe, leaving a set time between each injection for the reaction to reach an equilibrium. A temperature variation is generated with each interaction, causing the calorimeter to have to adjust the thermal power administered to the sample cell. This is reflected as a series of heat peaks over time (middle). The heat that is released (exothermic reaction) or absorbed (endothermic reaction) can be derived (right) and subsequently fitted to estimate the thermodynamic parameters of the interaction reaction. Figure slightly modified from 2bind.

In this work, a thermostated MicroCal Auto–iTC200 (*Cytiva*) system was employed to evaluate protein–protein and protein–ligand binding at 15 °C (excepting CypA and CHCHD4 assays, which were performed at 25 °C) in 50 mM Kpi, pH 7.4. Unless otherwise stated, the sample cell contained 10 µM of one of the interaction partners (usually the target protein), while the syringe was filled with 100–150 µM of the other interaction partner. Samples and buffers were previously degasified for 5 min in a vacuum machine and subsequently pipetted to 96–well plates. A sequence of 2 µL injections of titrating solution every 150 s was typically programmed, with a stirring speed of 750 rpm. The equipment was automatically cleaned before and after each assay.

The heat (Q) associated to each injection was calculated by integration of the calorimetric signal, represented against the [Ligand]/[Protein] molar fraction and subsequently fitted to the appropriate ligand binding site model, typically one site (1:1 ligand:protein stoichiometry), in the Origin 7.0 (*Origin Lab*) program. The association constant (K_a), enthalpy change (ΔH) and binding stoichiometry (n) were estimated from this fit. Thereafter, the dissociation constant (K_d), entropy ($-T\Delta S$) and free Gibbs energy change (ΔG) of the binding could be determined from basic thermodynamic relations (*Eq. 3.10–12*).

$$K_d = \frac{1}{K_a} \quad \text{(Eq. 3.10)} \qquad \Delta G = -R * T * \ln(K_d) \quad \text{(Eq. 3.11)}$$

$$\Delta G = \Delta H - T * \Delta S \quad \text{(Eq. 3.12)}$$

where K_a and K_d are the association and dissociation constants (M) respectively; ΔG, ΔH and ΔS the free Gibbs energy, enthalpy and entropy changes (kcal/mol); R the universal gas constant ($1.987 \cdot 10^{-3}$ kcal mol^{-1} K^{-1}); and T the temperature (K). Measurement errors were respectively ±30% and ±0.5 kcal/mol for binding constants (K_a, K_d) and thermodynamic parameters (ΔG, ΔH, ΔS).

3.4.7.1. Determination of cooperativity

Cooperativity is a phenomenon which takes place when the binding of a ligand to a protein influences, either favorably or unfavorably, the simultaneous binding of another ligand to that same molecule (Velázquez–Campoy *et al*., 2006). This can be expressed as the cooperation coefficient (α), which relates the apparent association constant (K_a^{app}) of ligand B with the concentration of ligand A (*Eq. 3.13*). In order to perform such assays, one of the ligands (ligand A) is previously added to a solution of $10\ \mu M$ of the target protein, and the mixture is put in the sample cell. The syringe is then filled with 100–$150\ \mu M$ of the second ligand (ligand B), which is used to titrate the complex of protein and ligand A. This procedure is repeated at different concentrations of ligand A. Assay conditions were as previously described.

$$K_a^{app,\,B} = K_a^B * \frac{1 + \alpha * K_a^A * [A]}{1 + K_a^A * [A]} \quad \text{(Eq. 3.13)}$$

where $K_a^{app,B}$ is the apparent association constant of ligand B, K_a^A and K_a^B the association constants of ligands A and B respectively, α the cooperation coefficient and $[A]$ the concentration of ligand A.

3.5. Protein Kinetics Study

3.5.1. Steady–state kinetics

3.5.1.1. Diaphorase activity

Certain flavoenzymes possess the ability to catalyze the transfer of electrons from reduced di– and tri–phosphopyridine nucleotides to artificial electron acceptors (typically dyes) (*Worthington Enzyme Manual*), a phenomenon known as *diaphorase activity*. In this work, the diaphorase activity of AIF was evaluated using 2,6–dichlorophenolindophenol (DCPIP) as the electron acceptor in the presence of NADH (*Fig. 3.11*).

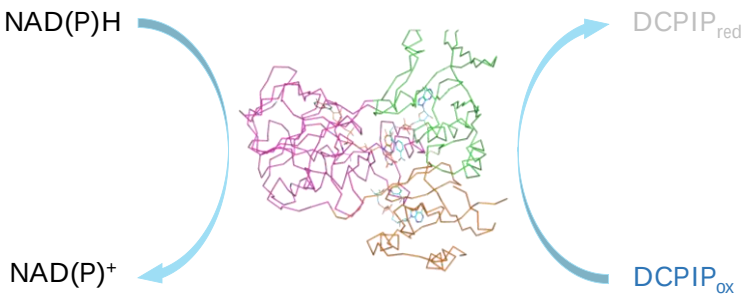

Figure 3.11. Schematic diaphorase activity of AIF with DCPIP as the electron acceptor and NAD(P)H as the electron donor. The crystal structure of AIF (PDB 4BV6) is depicted in ribbon, with each domain colored differently (FAD–binding in purple, NADH–binding in green, and C–terminal in orange). Oxidized DCPIP presents a blue color due to its absorbance at 620 nm, which is lacking in the reduced form.

The diaphorase activity of apoptotic and mitochondrial AIF and its variants was analyzed in a Cary 100 Bio (*Agilent Technologies*) spectrophotometer at 25 °C in 50 mM Kpi, pH 7.4, following the reduction of DCPIP at 620 nm for 1 min. Oxidized DCPIP presents a peak of absorbance at 620 nm with a ε_{620nm} of 21 $mM^{-1}cm^{-1}$, while its reduced form lacks any absorbance at this wavelength. Consequently, its reduction can be reliably monitored by the decrease in absorbance at 620 nm. Assays were performed with final concentrations of ~100 nM of protein, 95 μM of DCPIP and 0.02–10 mM of NADH. Reaction samples and references were prepared as indicated in table 3.8.

Table 3.8. Volumes used for reaction samples, references and blanks to evaluate diaphorase activity. AIF and DCPIP stocks were prepared at an initial concentration of $10\ \mu M$ and 1.9 mM respectively. NADH stocks, at an initial concentration of 2 times the final concentration.

Reagent	Sample cuvette (µL)	Reference cuvette (µL)	Blank cuvette (µL)
AIF	10	–	–
DCPIP	50	50	25
NADH	500	500	–
Buffer	440	450	975

Experimental data were fitted using linear regression to determine the initial velocity (v_0) at each concentration of NADH (*Eq. 3.14*). Assays were performed in quadruplicate. The contribution of the NADH background reaction with DCPIP was also calculated using the reference and subsequently subtracted from the samples' values. Then, initial velocities were represented against the concentration of substrate and, if a saturation profile was observed, the curve was fitted to the Michaelis–Menten equation to determine the kinetic constants (the turnover number, k_{cat}, and the Michaelis–Menten constant, K_M) (*Eq. 3.15*).

$$v_0 = \frac{\Delta A_{620nm} / \varepsilon_{620nm}}{t} \quad \text{(Eq. 3.14)}$$

where v_0 is the initial velocity of the reaction during linear dependency (s^{-1}), A_{620nm} and ε_{620nm} the absorbance signal and molar extinction coefficient ($M^{-1}\ cm^{-1}$) at 620 nm of the DCPIP, and t the time (s).

$$\frac{v_0}{e} = \frac{k_{cat} * [NADH]}{K_M + [NADH]} \quad \text{(Eq. 3.15)}$$

where v_0 is the initial velocity of the reaction (s^{-1}), e the enzyme concentration (M), k_{cat} the turnover number (s^{-1}), K_M the Michaelis–Menten constant (M), and [NADH] the concentration of NADH (M).

3.5.1.2. Charge transfer complex stability

The HT event in AIF takes place upon the formation of a CTC between the FAD cofactor and the NADH coenzyme. The stability of the CTC against reoxidation by molecular oxygen can be determined monitoring the decay in absorbance at 700 nm (characteristic maximum of the CTC) and subsequent rise at 450 nm (characteristic

maximum of the oxidized flavin) with a spectrophotometer. The time at which the fraction of CTC is equal to 0.5 is known as *CTC half–life* and serves as a viable indicator of CTC stability. In order to determine this parameter, 20 µM AIF samples were first fully reduced with a 1.5–fold excess of NADH in 50 mM Kpi, pH 7.4, at 25 °C. Absorbance spectra were then recorded in a Cary 100 Bio (*Agilent Technologies*) spectrophotometer from 400 nm to 800 nm every few minutes (every 30–45 s at the start, up to 15 min intervals as the CTC disappeared). Finally, the observed values of absorbance at 450 nm and 700 nm were normalized using equation 3.16 and subsequently represented as a function of time.

$$\text{Fraction} = 1 - \frac{\Delta A_{max} - \Delta A_t}{\Delta A_{max}} \quad \text{(Eq. 3.16)}$$

where ΔA_{max} is the difference between the minimum and maximum absorbance at 700 nm (for CTC disappearance) or 450 nm (for flavin reoxidation), and ΔA_t is the difference between each value of absorbance at a time t and the minimum absorbance at that wavelength.

3.5.2. Transient–state kinetics

Transient–state kinetics pertain the formation and consumption of enzyme–substrate intermediates during the time since the substrate(s) and enzyme are mixed until the steady state is reached. The transient state usually lasts milliseconds, with fast individual processes (i.e., ligand binding/dissociation, complex formation, electron/hydride transfer…) occurring over that timescale. With stopped–flow (SF) spectrophotometry, amongst other techniques, these critical biochemical processes may be observed and quantitatively analyzed.

A SF instrument is a rapid mixing device used to measure the kinetics of significantly fast reactions in solution. The process begins with the activation of the stop piston, which empties the contents of the stop syringe up to a fixed volume. Then the substrate(s) and enzyme, contained in two independent drive syringes, are forced by the drive piston to simultaneously enter the mixing chamber up to the volume that has been previously liberated from the stop syringe. After a few milliseconds of dead time (0.3–2 ms typically), the observation cell is filled with the substrate–enzyme mixture and the previous contents are displaced to the stop syringe, triggering the measuring device and effectively stopping the flow. The observation cell is subsequently illuminated with a light source and the selected optical property can be measured with the adequate detector (i.e., absorption, fluorescence …) (*Fig. 3.12*).

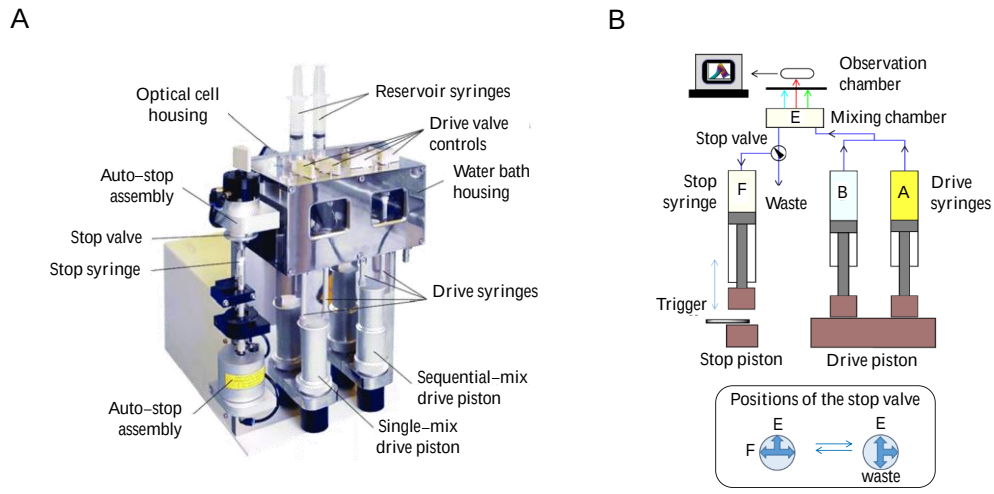

Figure 3.12. Sampling handling unit (SHU) of a SF spectrometer and schematic components diagram. (A) The SHU is shown in the sequential mixing configuration (four drive syringes), but it may be equipped with just two (standard single–mix system). Components are indicated. Figure from *Applied Photophysics Ltd.*, model SX17.MV. (B) The SF instrument presents two to four drive syringes (A and B, containing the solutions to be mixed) and one stop syringe. The drive piston simultaneously forces the solutions into the mixing chamber, where they stay for a couple of milliseconds until they are sent to the observation chamber. The previous contents are displaced and subsequently collected in the stop syringe, pushing the trigger that activates the measurement device. The stop valve, with two possible positions, guarantees that the displaced contents from the observation chamber are collected in the stop syringe while the previous contents from said syringe are sent in turn to the waste. Figure from Ferreira and Medina, 2021.

An SX17.MV (*Applied Photophysics Ltd.*) SF spectrofluorometer interfaced with the Pro–Data SX software was employed to evaluate the fast kinetics of AIF reduction with the NADH coenzyme using a photodiode array detector.

3.5.2.1. AIF reduction with NADH

To evaluate the reaction of reduction of AIF and its variants with the NADH coenzyme, ~20 µM of protein and increasing concentrations (0.04–20 mM) of NADH were placed in two separate drive syringes and subsequently mixed in equal volumes. Changes in absorbance were measured over different timescales in the 400–850 nm spectral range with a photodiode array detector. Assays were performed in air–

saturated 50 mM Kpi, pH 7.4, at 25 °C, in at least triplicate for each concentration and timescale.

Observed rates (k_{obs}) were determined by global analysis and numerical integration methods using the Pro–Kinetics I software (*Applied Photophysics Ltd.*). In general, fitting to a single–step model (A → B) best described the overall reaction at all assayed NADH concentrations. Average k_{obs} values were represented against the concentration of NADH and subsequently fitted to equation 3.17 using the Origin 8.0 software (*Origin Lab*). This equation describes the formation of the enzyme:substrate complex prior to the HT event (*Fig. 3.13*).

$$AIF_{ox} + NADH \underset{k_{off}}{\overset{k_{on}}{\rightleftharpoons}} AIF_{ox}{:}NADH \xrightarrow{k_{HT}} \boxed{AIF_{rd}{:}NAD^{+}}$$

Charge Transfer Complex

Figure 3.13. Formation of the AIF_{rd}:NAD^+ complex upon reduction of the FAD cofactor by the NADH coenzyme. The interaction between FAD and NADH leads to the formation of what is known as the CTC, a special conformation in which HT may occur. The constant that describes this complete process is k_{obs}, while the reverse reaction is defined by k_{rev} (which is practically zero). k_{obs} may be calculated from constants k_{on}, k_{off}, and k_{HT} as indicated in equation 3.17.

$$k_{obs} = \frac{k_{HT} * [\mathrm{NADH}]}{\mathrm{K_d^{NADH}} + [\mathrm{NADH}]} + k_{rev} \quad \text{(Eq. 3.17)}$$

where $\mathrm{k_{obs}}$ is the observed rate constant of the reaction (s^{-1}), $\mathrm{k_{HT}}$ the limiting rate constant of the HT from NADH to the FAD of AIF ($s^{-1}\ M^{-1}$), $\mathrm{K_d^{NADH}}$ the AIF_{rd}:NAD^+ dissociation constant (M) as calculated by k_{off}/k_{on}, [NADH] the concentration of NADH (M), and $\mathrm{k_{rev}}$ the rate constant of the reverse reaction (of negligible value) (s^{-1}).

3.5.2.2. Kinetic Isotope Effect

According to the transition state theory (Evans and Polanyi, 1935; Eyring, 1935), the rate (k) of a reaction can be empirically represented by the Arrhenius equation (*Eq. 3.18*), where A refers to the frequency of collisions between the particles involved in the reaction and the exponential term corresponds to the fraction of said collisions that actually have an equal or higher energy than the activation energy (E_a). By measuring the rate of a reaction at different temperatures, linearizing the function (*Eq. 3.19*) and plotting it (*Fig. 3.14*), it is possible to determine the values of the Arrhenius frequency factor and the E_a.

$$k = A * e^{-E_a/RT} \quad \text{(Eq. 3.18)}$$

$$\ln(k) = \ln(A) - \frac{1}{T} * \frac{E_a}{R} \quad \text{(Eq. 3.19)}$$

where A is the frequency of collisions factor, E_a the activation energy of the reaction (kcal/mol), R the gas constant ($1.987 \cdot 10^{-3}$ kcal mol^{-1} K^{-1}) and T the temperature (K).

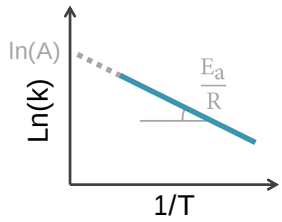

Figure 3.14. Representation of the logarithm of the Arrhenius equation. Expressing the Arrhenius equation as its logarithm causes the linearization of the function into equation 3.19, where $\frac{E_a}{R}$ is the slope and $\ln(A)$ the intercept. This enables the determination of the frequency factor (A) and the activation energy (E_a) through a simple linear regression fit.

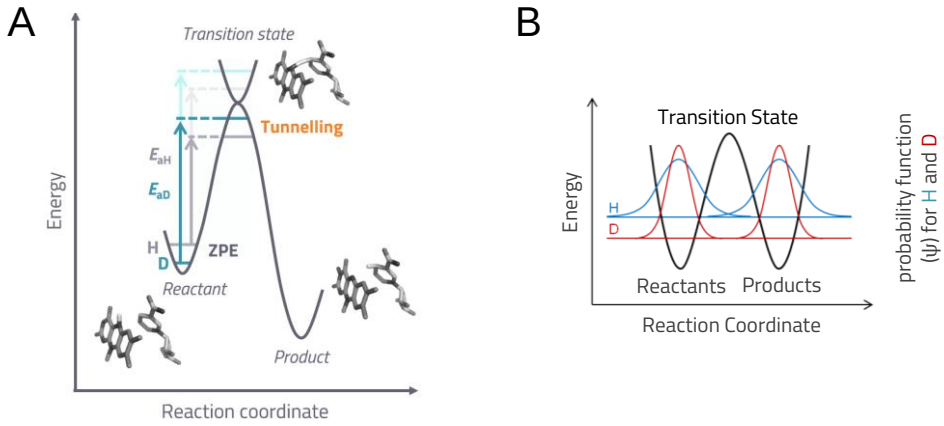

Figure 3.15. Diagrams of the energetic landscape of a chemical reaction reflecting the tunnelling effect (A) or the atoms' probability function (B). Particles may cross energy barriers without having reached the theoretical E_a through the quantum phenomenon of tunnelling. The probability of this occurrence is directly proportional to the mass of the particle. Heavier particles present lower ZPEs, which results in more localized probability functions and consequently in the requirement of a greater energetic input. H, stands for hydrogen. D, deuterium. E_a, energy of activation. ZPE, zero potential energy.

However, the Arrhenius equation is still essentially empirical; nowadays, it is common knowledge that particles are in fact capable of crossing energy barriers without reaching the activation energy through a quantum phenomenon known as *tunnelling* (Knapp and Klinman, 2002; Nagel and Klinman, 2006) (*Fig. 3.15A*).

The probability of said phenomenon is directly proportional to the mass of the particle in question, and is furthermore influenced by the dynamics of the active site. This is due to the fact that heavier particles present lower vibrational frequencies, which results in them having lower zero potential energies (ZPEs) and more localized probability functions (*Fig. 3.15B*). Consequently, heavier particles typically require a greater energetic input to reach the transition state than lighter ones.

Quantum tunnelling is, however, not the only phenomenon that influences the rate of a chemical reaction; in fact, current HT models incorporate as well a phenomenon of a different nature that is known as *protein dynamics* (Knapp and Klinman, 2002; Nagel and Klinman, 2006).

There are two types of protein dynamics that need to be considered. In the first place, there are *pre–organization* dynamics (*Fig. 3.16A*). These consist on a conformational sampling that takes place in regions far from the active site, in the range of nano to picoseconds. Secondly, and in this case more importantly, there are *reorganization* dynamics (*Fig. 3.16B*). These dynamics are ultrafast fluctuations of the heavy atoms that are present within the active site of the enzyme, which occur in the pico to femtosecond range.

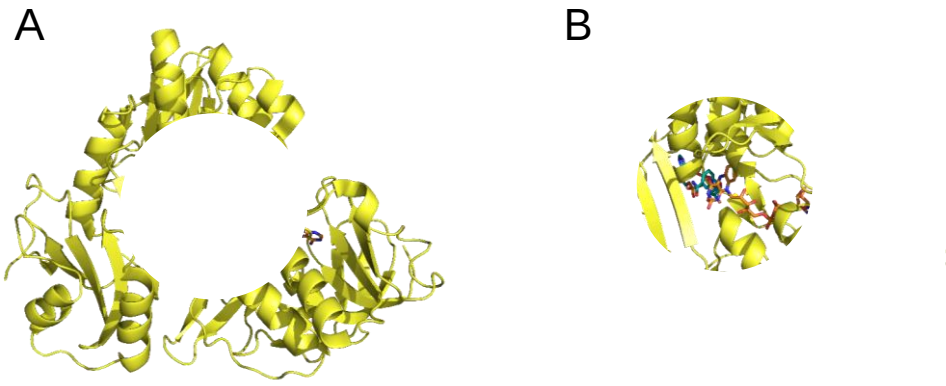

Figure 3.16. Reach of the two types of protein dynamics influencing the tunnelling effect. Pre–organization dynamics (A) affect regions far from the active site (ns to ps), while reorganization dynamics (B) take place within the active site (ps to fs).

Reorganization dynamics can be further classified into two subtypes. On the one hand, there are *passive* reorganization dynamics (*Fig. 3.17A*), also known as environmental, which are typically found in the active site of native enzymes. These have been optimized through evolution so that the distance between the donor and the acceptor is optimal, and as a consequence there is a point in the reaction coordinate where the hydrogen wave functions overlap, allowing tunnelling to take place.

However, not all active sites offer this warranty. In some active sites, usually from mutant proteins, the donor and acceptor are not naturally found at an optimal distance. For those cases, there are *active* reorganization dynamics (*Fig. 3.17B*), also known as gating, which require a sampling of the donor–acceptor's distance in search for the point at which both wave functions overlap. The contribution of these different types of reorganization dynamics can be evaluated through a phenomenon known as the *Kinetic Isotope Effect* (KIE).

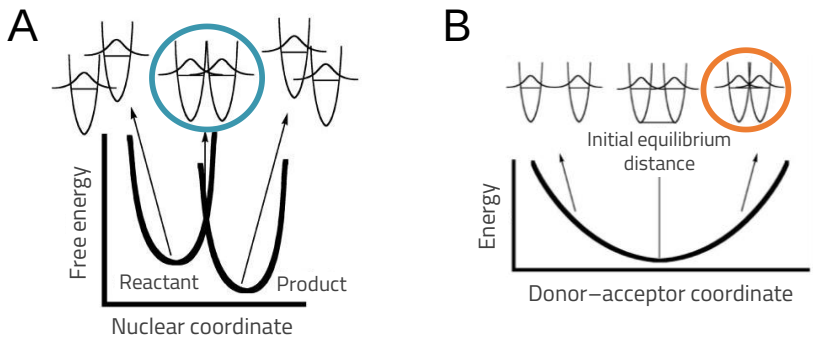

Figure 3.17. Energetic landscapes of passive and active reorganization dynamics. (A) In the native active site (passive dynamics), the donor and acceptor are naturally found at the optimal distance for HT, leading to the overlap of the hydrogen wave functions. (B) In the altered active site (active dynamics), the donor–acceptor distance has to be previously sampled in search for the point where the wave functions overlap.

The KIE is defined as the change in the rate of a reaction that is observed as a consequence of the replacement of an atom in the reactant molecule with one of its isotopes (Sánchez, 2013). It is expressed as the ratio of the rate constants of the reactions that involve the light (k_L) and the heavy (k_H) isotopologues (*Eq. 3.20*), where each rate is defined by its Arrhenius equation and can subsequently be linearized likewise (*Eq. 3.21*). The most widely studied substitution is that of a hydrogen atom

(H, $^{1}_{1}H$) with a deuterium one (D, $^{2}_{1}H$), as the latter presents one more neutron than the former and is consequently twice as heavy in mass (resulting in a much greater KIE than other isotope pairs).

$$KIE_{LH} = \frac{k_L}{k_H} \quad \text{(Eq. 3.20)}$$

where k_L is the observed rate constant of the reaction involving the light isotope (s^{-1}) and k_H that of the heavy isotope (s^{-1}).

$$\ln(KIE) = \ln\left(\frac{A_L}{A_H}\right) - \frac{1}{T} * \frac{\Delta E_a}{R} \quad \text{(Eq. 3.21)}$$

where A_L is the frequency factor of the light isotope, A_H that of the heavy isotope, T the temperature (K), E_a the activation energy of the reaction (kcal/mol) and R the gas constant ($1.987 \cdot 10^{-3}$ kcal mol^{-1} K^{-1}).

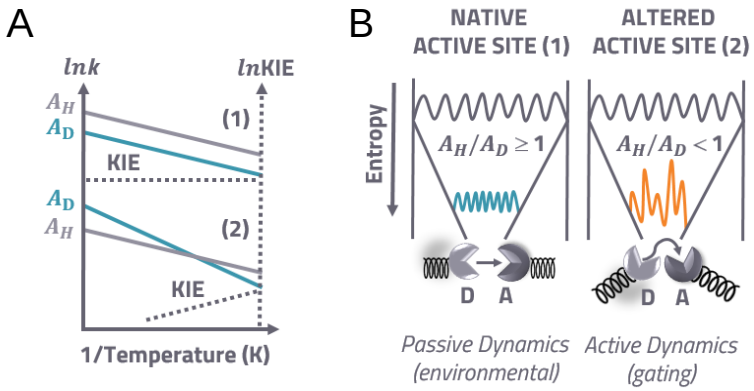

Figure 3.18. Study of passive or active reorganization dynamics through the KIE. (A) Progression of the rate constant (solid lines) and the KIE (dotted lines) along a temperature ramp, for the hydrogen (in grey) – deuterium (in blue) isotope pair. In mutant proteins with an altered active site, the KIE is typically temperature–dependent. (B) Schematic representation of a native active site, characterized by passive dynamics (the donor and acceptor are naturally found at the optimal distance for HT), and an altered active site (active dynamics), where there is a need to sample the distance between the donor and the acceptor. H, stands for hydrogen. D, deuterium. A, frequency factor. *k*, rate constant. KIE, kinetic isotope effect.

If the bond to the isotopic substituent is formed or broken during the reaction, it is known as *primary* KIE (1° KIE), and it can provide crucial information on the

structure and dynamics of the transition state (*Fig. 3.18*). Otherwise, it is known as *secondary* KIE (2° KIE), and it is typically of a considerably lower magnitude.

KIEs may appear as temperature–dependent in mutant proteins with an altered active site (Knapp and Klinman, 2002) (*Fig. 3.18*). This is due to the fact that, at lower temperatures when the environment's energetic input is low, the tunnelling effect becomes limiting. If the active site is not in the optimal conformation for the HT to take place, the need to sample the donor–acceptor distance will turn into a significant disadvantage, boosting the effect of the isotopic substitution on the rate.

In order to analyze the primary and secondary KIEs of AIF and its variants W483G, W483L and W483Y, 15 µM of protein and 2 mM of NADH (or its isotopologues [4S–^{2}H]–NADD (4S–NADD) or [4R–^{2}H]–NADD (4R–NADD)) were placed in two separate drive syringes and subsequently mixed in equal volumes. Changes in absorbance were measured over different timescales in the 400–850 nm spectral range with a photodiode array detector. Assays were performed in air–saturated 50 mM Kpi, pH 7.4, over a temperature ramp (typically from 5 °C to 35 °C, with a step of 5 °C), in at least triplicate for each temperature. k_{obs} values were determined by global analysis and numerical integration methods using the Pro–Kinetics I software (*Applied Photophysics Ltd.*), as in section 3.5.2.1. Relevant parameters (A, E_a and KIE) were derived from equations 3.19 and 3.20.

3.5.3. Mid–point reduction potential

The mid–point reduction potential (a.k.a. redox potential, E_m) is a measure of the thermodynamic tendency of a redox center to accept (higher E_m) or donate (lower E_m) electrons. The E_m of AIF and its variants was determined through the xanthine oxidase method.

The xanthine oxidase method (*Fig. 3.19*) makes use of a reference or indicator dye of known E_m to determine the E_m of a redox center of interest (Christgen *et al.*, 2019; Maklashina and Cecchini, 2020). Under anaerobic conditions, changes in the absorbance spectrum can be easily monitored, allowing the quantification of the oxidized and reduced redox species throughout the reaction (*Eq. 3.22*). By plotting the log of the oxidized/reduced concentrations of the redox center versus the dye along time (*Eq. 3.23*), the E_m of the former can be calculated (*Eq. 3.24*).

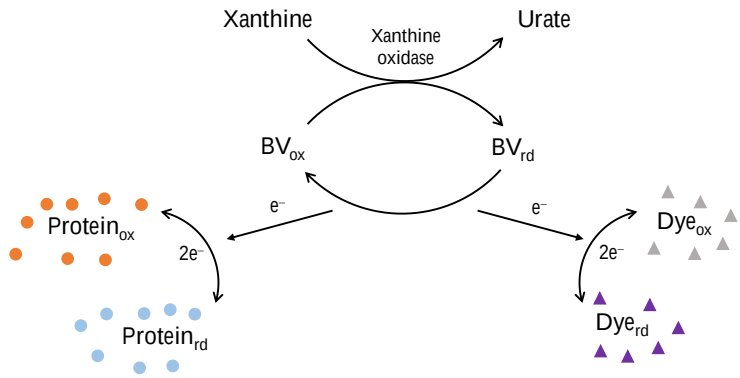

Figure 3.19. Schematic representation of the xanthine oxidase method. The protein of interest (presenting a redox center, such as a flavin cofactor) is mixed, under anaerobic conditions, with an indicator dye of known redox potential, xanthine oxidase (XOX) and its substrate, xanthine. The xanthine/XOX system provides a slow continuous reduction of the dye and the flavin of the protein through their mutual interaction with benzyl viologen (BV), warrantying rapid equilibration of reducing equivalents. This allows slow changes in the equilibrium of the reduced and oxidized forms of both molecules to take place until they are completely reduced.

10 µM of protein were mixed with 500 µM of xanthine, 2 µM of benzyl viologen and 5 µM of dye. The latter was chosen according to the estimated E_m of the protein, within a ±30 mV range. In this work, employed dyes were: benzyl viologen (E_m = –350 mV), safranin (–289 mV) or anthraquinone (–225 mV). 10 mM of glucose and 10 U/mL of glucose oxidase (GOX) were also added to the mixture to eliminate any traces of oxygen. On a separate tube, 0.002 U/mL of xanthine oxidase were prepared. Assays were performed at 25 °C in 50 mM Kpi, pH 7.4, under anaerobic conditions (obtained by several cycles of vacuum application and bubbling with O_2–free argon) in a homemade airtight spectrophotometer cuvette. The protein and xanthine oxidase samples were mixed only upon having achieved anaerobiosis, after which spectra were recorded every 3-5 min for up to 2 hours in a Cary 100 Bio spectrophotometer (*Agilent Technologies*). The ratios of oxidized/reduced dye and oxidized/reduced protein at different time points were calculated from these data following equation 3.22.

$$\frac{\mathrm{Ox}}{\mathrm{Red}} = \frac{\mathrm{A} - \mathrm{A_{min}}}{\mathrm{A_{max}} - \mathrm{A}} \qquad \text{(Eq. 3.22)}$$

where Ox/Red is the ratio of oxidized/reduced substance, A the absorbance at a given time point, A_{min} the substance's minimum absorbance and A_{max} the substance's maximum absorbance.

The log(ox/red) of the protein was then plotted versus that of the dye and subsequently fitted to linear equation 3.23.

$$\log\left(\frac{\mathrm{Ox(protein)}}{\mathrm{Red(protein)}}\right) = \frac{\mathrm{n(protein)}}{\mathrm{n(dye)}} * \log\left(\frac{\mathrm{Ox(dye)}}{\mathrm{Red(dye)}}\right) - \log\left(E_{m(protein)} - E_{m(dye)}\right) * \frac{nF}{2.3\ RT}$$

(Eq. 3.23)

where Ox/Red is the ratio of oxidized/reduced substance calculated by equation 3.22, n the number of transferred electrons, E_m the mid–point reduction potential, F the Faraday constant, R the ideal gas constant and T the temperature.

Finally, upon rearrangement of equation 3.23 the E_m of the flavoprotein was calculated from the known value of that of the dye using equation 3.24.

$$E_{m(protein)} = E_{m(dye)} - y * \frac{2.3\ RT}{nF} \qquad \text{(Eq. 3.24)}$$

where E_m is the mid–point reduction potential, y the y–intercept value, R the ideal gas constant, T the temperature, n the number of transferred electrons and F the Faraday constant.

3.6. Software and Computational tools

The GenBank database was used for the search of gene and protein sequences (http://www.ncbi.nlm.nih.gov/genbank/). Multiple sequence alignments and phylogenetic trees were performed using the MEGA-X software (https://www.megasoftware.net). The ProtParam tool on ExPASy (https://web.expasy.org/protparam/) was employed in some instances to determine protein theoretical parameters. Conservation scores were calculated by the ConSurf server (Ashkenazy *et al.*, 2016) using solely as input the sequence of the protein of interest.

To create sequence logos, the amino acid sequence of each of the three proteins of the human AIF superfamily were separately downloaded from the GenBank database of NCBI (references NP_004199.1, NP_001185625.1 and NP_653305.1 for AIF, AMID and AIFL, respectively). An individual protein BLAST alignment (https://blast.ncbi.nlm.nih.gov) was subsequently performed for each target sequence using default parameters, and the first 500 sequences were selected. Each target was then globally aligned with its selected sequences using the ClustalW algorithm in the

MEGA-X software (https://www.megasoftware.net) and a WebLogo was constructed with the resulting alignment (https://weblogo.berkeley.edu/logo.cgi).

Data were analyzed, fitted and shown in figures using the Origin software (*Origin Lab*). The PyMol software (DeLano, 2002) was used to analyze and visualize structural data, as well as to produce structural figures.

3.7. Additional Experimental Procedures

Several techniques that appear on this thesis were not performed by the PhD candidate herself, but rather by the helpful hands of different collaborators. Said techniques are described below, as well as the specific conditions in which they were employed.

3.7.1. Additional electrophoresis techniques

CN gradient and two–dimensional denaturing electrophoresis (2D SDS–PAGE) were performed by PhD. Silvia Romero–Tamayo during the development of her PhD thesis, under the direction of PhD. Milagros Medina and PhD. Patricia Ferreira.

CN–PAGE (followed in some instances by 2D–SDS–PAGE) was carried out after SEC to evaluate the formation of oligomers in samples containing $AIF_{\Delta 101}$ and its protein partners CypA and H2AX.

3.7.1.1. CN gradient electrophoresis

The use of polyacrylamide gels with an increasing gradient of acrylamide concentration (and consequently a decreasing gradient of pore size) offers in some instances an advantage over the classical acrylamide gels of fixed concentration (Romero–Tamayo, 2022). Proteins migrate until they reach a limiting pore size that hinders further progress, leading to their effective separation according to hydrodynamic size and shape. Consequently, molecules with close MW values are more easily resolved in a gradient gel, enabling the visualization and identification of quaternary assemblies formed by more than one protein or subunit (particularly when one component of the assembly is significantly bigger than the other).

CN-PAGE gradient gels were prepared the day prior to their use, following the recipe on table 3.9 and using 1.5 mm spacers. A peristaltic pump set at 3 mL/min was employed to mix the gradient gel (*Fig. 3.20*). Once in the cassette, the top of the gel was covered with isopropanol to smooth its surface and the gel was allowed to polymerize. Subsequently, the isopropanol was removed and the gel was washed with distilled water to get rid of any traces. Finally, the gel was covered in buffer, protected with plastic film and stored at 4 °C.

Table 3.9. Solution mixtures for CN–PAGE gel preparation. Quantities are specified for the preparation of approximately one gel. APS stands for ammonium persulfate, TEMED for tetramethylethylenediamine.

Reagents	Resolving gel		Stacking gel
	4%	20%	
Distilled H_2O	2.93 mL	0.33 mL	1.75 mL
Acrylamide mixture	0.40 mL	1.33 mL	0.25 mL
Buffer	1.66 mL	1.11 mL	1.00 mL
Glycerol	–	0.56 mL	–
APS 20% *	20 µL	12 µL	12 µL
TEMED *	4 µL	3 µL	3 µL

* Added right before pouring the solutions in the gradient maker. Acrylamide mixture: acrylamide:bisacrylamide (48:1.5). Buffer: 50 mM Bis–Tris, 1.5 M aminocaproic acid, pH 7.0.

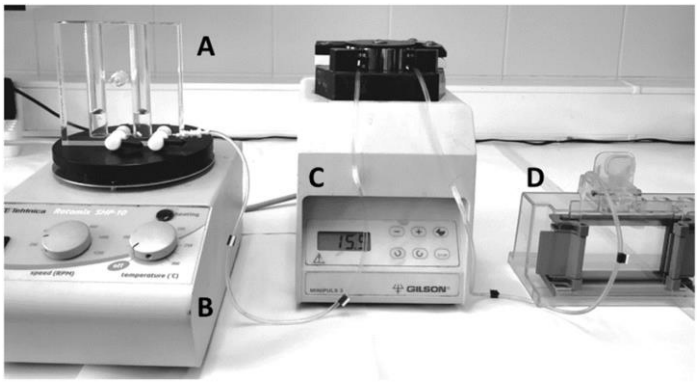

Figure 3.20. Assembly for CN gradient gel preparation. The 4% gel was poured in the left chamber of the mixer (A), while the 20% was poured in the right. Both chambers contained magnetic stirrers (B) to ensure an even solution and were connected from left to right, with the latter leading to the peristaltic pump (C). After turning on the peristaltic pump, the valve leading to the right chamber was opened, allowing the 20% solution to travel 1 cm from the tube. At this point, the valve to the left chamber was opened, allowing the 4% solution to travel into the right chamber and subsequently creating the gradient solution while filling the gel cassette (D). Figure from Romero–Tamayo, 2022.

Half an hour before running the electrophoresis, the stacking gel was prepared (*table 3.9*) and poured, the comb was added and the gel was left to polymerize. Afterwards, the comb was removed and the wells were cleaned with buffer to eliminate any leftover unpolymerized acrylamide. In order to facilitate loading, well positions were marked. The space between the gel and the buffer dam was filled with cold cathode buffer (50 mM tricine, 7.5 mM imidazole, pH 7.0; supplemented with 0.02% dodecyl maltoside and 0.05% deoxycholate), and the bucket with cold anode buffer (25 mM imidazole/HCl, pH 7.0). The electrophoresis was first run at 80 V and 4 °C for 25–30 min, and then the amperage was set to 12 mA/gel and the voltage limited to 300 V until the sample front reached the bottom of the gel (~120 min in total).

Once finished, gels were electroblotted onto Hybond-P PVDF membranes (*Amersham*) and then probed with the primary antibody against AIF (1:20,000 rabbit anti–hAIF, *Sigma*). Detection of immunoreactive proteins was performed using an HRP-conjugated secondary antibody (1:6,000 goat anti–rabbit IgG, *Invitrogen*). Signals were detected using the EZ-ECL Chemiluminescence Detection kit from HRP (*Pierce*™), and immunoblot images were obtained in an automated WB processor Amersham™ Imager 600 (*Cytiva*).

3.7.1.2. Two–dimensional denaturing electrophoresis

2D SDS–PAGE gives rise to the possibility of separating a mixture of proteins according to two different properties (one for each dimension), such as size and charge (*Fig. 3.21*).

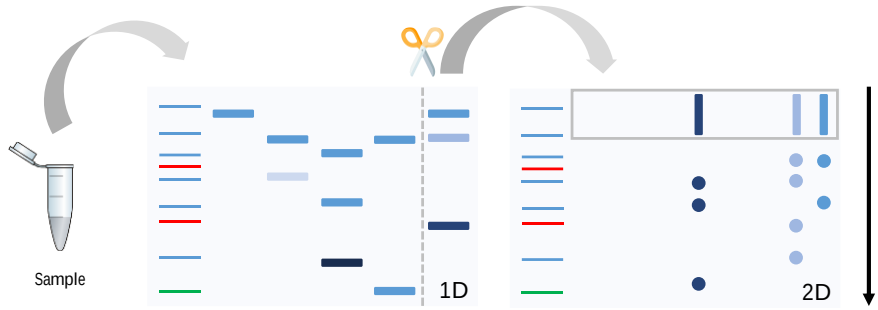

Figure 3.21. Schematic workflow of a 2D SDS–PAGE. In the first dimension (1D) gel, proteins are separated across an electrophoretic lane according to one property (i.e., their isoelectric point). Once the run is finished, the lane of interest is cut and loaded onto the second dimension (2D) gel, where they are further separated according to another property (i.e., their molecular weight) in a 90° angle. The lane on the left of each gel represents the marker.

Initially, a 1D electrophoresis was run to separate the proteins along an electrophoretic lane, typically according to their isoelectric point (first dimension). Once the run was finished, the lane was cut and stacked onto a second gel. As the 2D electrophoresis was run, the proteins of the lane began separating across the second dimension (in a 90° direction from the first) typically according to their molecular weight. As it is considerably unlikely that two molecules will behave in an identical way regarding two distinct properties, complexes and assemblies can be more effectively separated in 2D electrophoresis than in 1D electrophoresis.

In this work, 2D electrophoresis was employed to identify the different proteins that form the degradosome, using commercial BN–PAGE™ 3–12% Bis–Tris gels (*Thermo Fisher Scientific*) with 1 mm width and the CN buffers (see section 3.7.1.1). Once the 1D electrophoresis was done, the first-dimension lane was cut out from the gel and incubated for 1 hour at 25 °C in 1% SDS and 1% β-mercaptoethanol. The supernatant was then run in a 15% 2D SDS-PAGE gel of 1.5 mm (*Table 3.10*) at 4 °C and 30 V for 25–30 min, after which the voltage was set in the 80-120 V range until the dye reached the bottom of the gel.

Table 3.10. Solution mixtures for the 2D gel in 2D SDS–PAGE. Quantities are specified for the preparation of approximately one gel. APS stands for ammonium persulfate, TEMED for tetramethylethylenediamine.

Reagents	Resolving gel 15%	Stacking gel 4%
Distilled H_2O	4.4 mL	1.4 mL
Acrylamide mixture	3.6 mL	0.6 mL
Buffer	4.0 mL	1.4 mL
APS 20% *	40 µL	12 µL
TEMED *	8 µL	3 µL

* Added last. Acrylamide mixture: acrylamide:bisacrylamide (48:1.5). Buffer: 3M Tris/HCl, 0.3% SDS, pH 8.5.

The upper and lower chambers were filled, respectively, with cold cathode (0.1 M Tris/HCl, 0.1 M tricine, 0.1% SDS, pH 8.25) and anode (0.2 M Tris/HCl, pH 8.9) buffers. To prepare the stacking gel of the 2D gel, a special comb was used, made by attaching cellophane tape to a regular comb in order to prepare a larger well to

accommodate the trimmed lane of the 1D gel. A regular well was kept to load the marker.

Gels were electroblotted onto Hybond-P PVDF membranes (*Amersham*) and subsequently probed with specific antibodies against His-tag (1:10,000 mouse anti–His–tag, *GenScript*). Detection of immunoreactive proteins was performed using an HRP-conjugated secondary antibody (1:1,000 goat anti–mouse IgG, *GenScript*). Signals were detected using the EZ-ECL Chemiluminescence Detection kit from HRP (*Pierce*™), and immunoblot images were obtained in an automated WB processor Amersham™ Imager 600 (*Cytiva*).

3.7.2. Atomic Force Microscopy (AFM) imaging measurements

AFM is a high–resolution non–optical imaging technique that makes use of a nanometer–sized mechanical probe mounted on a micro–cantilever to measure the forces between said probe and a sample surface (*Fig. 3.22*) (Binnig *et al.*, 1986). In an atomic force microscope, a constant force is maintained between the probe and the sample while the former is raster scanned across the latter. By monitoring the motion of the probe as it scans the surface, a 3D image can be generated (Pang *et al.*, 2015).

AFM data collection and processing for the determination of the oligomeric state of AIF and its protein partners CypA and H2AX were carried out in collaboration with PhD. Carlos Marcuello and PhD. Ana Isabel Gracia Lostao at Institute of Nanoscience of Aragón–University of Zaragoza, following the procedure described below.

Mixture samples were prepared by mixing $AIF_{\Delta 101}$ (0.5 µM) with CypA and/or H2AX in a 1:1 molar ratio for 10 min at 4 °C under mild stirring. These mixtures, as well as free protein samples, were also mixed with 0.05 ng/µl of the pET–28a(+) plasmid –linearized with EcoRI– to visualize protein binding to dsDNA.

Final concentrations were chosen to ensure the observation of individual features and thus, to facilitate complex identification and further analysis. All samples were prepared in phosphate buffered saline (PBS) pH 7.0 (*Thermo Fisher Scientific*). For dsDNA degradation assays, mixtures were prepared in the presence of 5 mM $CaCl_2$ and 5 mM $MgCl_2$ to stimulate nucleolytic activity. Samples were incubated on fresh cleaved mica pieces (*Electron Microscopy Sciences*) for 10 min at RT to achieve molecular immobilization. In the case of samples involving dsDNA, a pre-treatment with 200 mM $MgCl_2$ was applied for 2 min to favor attachment of its strands to the

negative hydroxyl groups at the mica surface (Pallarés *et al.*, 2014). Then, the mica pieces were washed three times with the same buffer to prevent non-desirable interactions among free biomolecules and the AFM tip, which might disturb image acquisition.

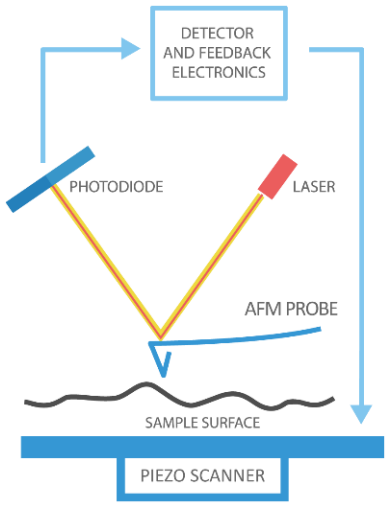

Figure 3.22. Schematic representation of the functioning of AFM. An AFM probe with a sharp tip, mounted on a flexible cantilever, is raster scanned over the sample surface. The lateral and vertical positioning of the probe relative to the surface is controlled with a piezoelectric scanner. As the AFM tip moves over molecules of different height in the sample surface, the deflection of the cantilever is affected. This is tracked by a laser beam that is reflected from the back of the cantilever and directed to a sensitive photodetector. The coordinates tracked by the AFM tip are combined to construct a three–dimensional topographic image of the sample surface. Figure from NanoAndMore GMBH.

At least 10 representative images from 10 different areas of 200 x 200 nm and 400 x 400 nm were analyzed for protein and protein–DNA samples, respectively. The resolution of all AFM images was at least of 512 x 512 pixels and the acquisition rate was defined at 0.5 Hz. Estimation of percentages and their associated errors were calculated as previously described for the different association states (Lostao *et al.*, 2010). Raw AFM images were analyzed using the WSxM free software (Horcas *et al.*, 2007).

3.7.3. Docking and molecular dynamics simulations

Docking and molecular dynamics simulations were performed mostly by PhD. candidate Sergio Boneta and Irene Blasco–Machin during the development of their PhD thesis and End of Degree Project respectively, both under the direction of PhD. Milagros Medina.

3.7.3.1. Macromolecular docking

Macromolecular docking consists on modelling the three-dimensional structure of complexes formed by two or more interacting biomolecules, most commonly proteins. The docking procedure outputs several candidate structures that are evaluated through different methods (i.e., a scoring function) to obtain a ranking. Since docking can be based on purely physical principles, even proteins of unknown function can be docked so long as their structure is available, either experimentally–determined or predicted.

There are two types of docking procedures currently in use: *rigid-body docking*, where bond lengths, bond angles and torsion angles remain fixed; and *flexible docking*, where a significant conformational change is allowed at the cost of immensely increasing the computing time (usually, a small set of possible conformational changes is considered to diminish this effect). Based on prior experimental knowledge, exclusions can be made regarding the binding site for the docking. However, the remaining space has to be sampled exhaustively, evenly and with sufficient coverage to guarantee a successful hit. Afterwards, the candidate complexes must be evaluated to ascertain which is most likely to occur in nature.

3.7.3.2. Molecular dynamics simulations

Molecular dynamics (MD) is a technique used to computationally simulate a system of interacting atoms over a certain period of time, using Newton's equations of motion to describe their behavior (Novo, 2018). The main idea behind it is that knowing the initial coordinates (r) and momenta (p) of every particle in a system, plus the way in which they will interact, it is possible to reach any future conformation.

If we consider a three-dimensional system of N atoms, every combination of 3N coordinates and 3N momenta define a point (a *state* of the system) in a 6N–dimensional phase space. In theory, we can move across this phase space, from one

state to another, using Newton's equations of motion (*Eq. 3.25*) so long as we know the initial coordinates and momenta. In such manner, MD generate a time-dependent sequence of points in the phase space: a so-called *trajectory*.

$$m_i a_{i,\alpha} \equiv m_i \frac{d^2 r_{i,\alpha}}{dt^2} = F_{i,\alpha} \begin{cases} \dfrac{dr_{i,\alpha}}{dt} = v_{i,\alpha} \equiv \dfrac{p_{i,\alpha}}{m} \\ m_i a_{i,\alpha} \equiv m_i \dfrac{dv_{i,\alpha}}{dt} \equiv \dfrac{dp_{i,\alpha}}{dt} = F_{i,\alpha} \equiv -\dfrac{\partial V}{\partial r_{i,\alpha}} \end{cases} \quad \text{(Eq. 3.25)}$$

where the force F_i on a particle i is equal to its mass m_i times the component $\alpha = 1, 2, 3\ldots$ of its acceleration a_i. The second order differential equation is usually rewritten as two first order equations with coordinates r and velocity v or momenta p. V is the potential energy.

A MD simulation can be divided into several consecutive steps (*Fig. 3.23*):

0. *Parametrization.* If the system of interest is a protein with one or more ligands, these have to be previously parametrized (most commonly through quantum mechanics), as available force fields typically only contain parameters for amino acids (stored in topology files).

1. *Preparation.* The interaction model and type of solvent are selected. Then, the box that will contain the system is defined. Solvation in the chosen solvent follows, plus addition of ions to compensate the system's net charge. Finally, an energy minimization is performed to abolish all potential clashes between system atoms and solvent molecules.

2. *Equilibration.* The ensemble specifying the system restraints is selected. A quick MD simulation follows: temperature and pressure are consecutively adjusted, ending with another energy minimization.

3. *Production.* The actual MD simulation is performed for a set time (typically nanoseconds), collecting the state of the system every x step (i.e., every 10 ps).

4. *Post-processing.* Results are analyzed in several different ways (i.e., root–mean–square deviation (RMSD), radius of gyration, secondary structure, energy, distance between residues… as functions of time).

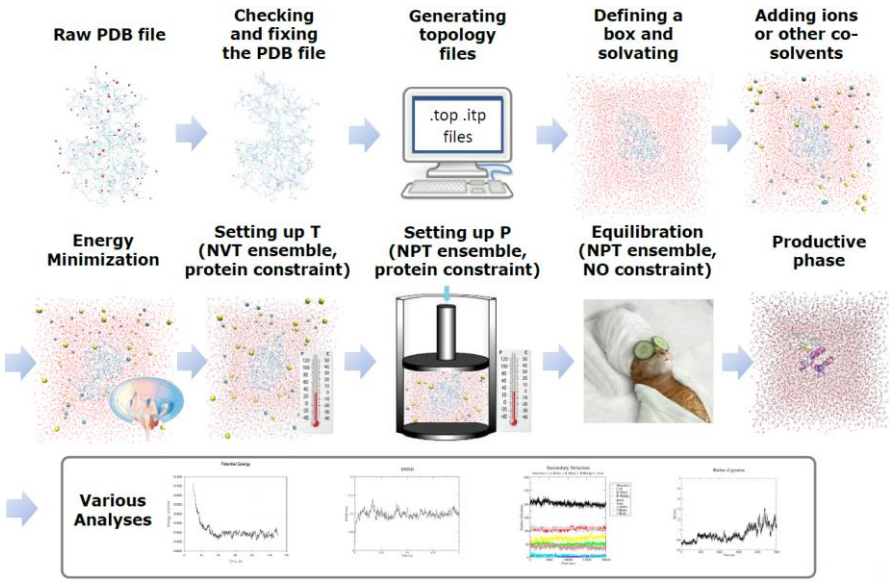

Figure 3.23. Consecutive steps performed in an MD routine. Different properties are fixed in each ensemble, being N number of molecules, V volume, T temperature and P pressure. Figure from Galano–Frutos, 2017.

However, it is vital to understand that MD is neither real nor exact. The integration of Newton's equations of motion generates cumulative errors with each step of the simulation, while interactions amongst particles are modelled with an approximated force field. A balance between computing cost and reliability is key.

Docking and MD of the degradosome

Rigid body docking (pyDockWeb server (Jiménez–García, 2013)) and molecular dynamics (MD) simulations (GROMACS 2018.4. (Abraham *et al.*, 2015)) were used to produce energetically optimized AIF:CypA:H2AX degradosome models.

The initial AIF:CypA model was built using the coordinates from PDB 3K0M for CypA and PDB 4BV6, after modelling the missing C-loop segment, for oxidized AIF (Romero–Tamayo *et al.*, 2021). Restrictions for the regions 55–69 of CypA and/or 370–394 of AIF at the interaction surface were used in the classification of docking energies (Farina *et al.*, 2017). The AIF:CypA lowest energy structure was submitted to MD. Subsequently, H2AX was docked onto the AIF:CypA complex using as receptor different frames obtained in AIF:CypA MD simulations and the PDB 6K1K chain C of H2AX. The 544–560 region of AIF was used to restrict the interacting region during

classification of the docked poses (Baritaud *et al.*, 2010). MD was then performed on the best 3 poses.

For MD simulations, complexes were protonated to pH 7.0 using PROPKA (Olsson *et al.*, 2011). Protein and FAD parameters were generated using respectively pdb2gmx and Gaussian 09 (Frisch *et al.*, 2016). The system was solvated with a TIP3P water model in a triclinic box and neutralized by adding ions. Steepest descent minimization was performed to avoid close contacts. Equilibration was first conducted under a 500 ps NVT ensemble and then under a 500 ps NPT ensemble, with atoms of protein and ligand restrained with a 1000 $kJ{\cdot}mol^{-1}{\cdot}nm^{-1}$ harmonic potential. 50 ns NPT simulations at 310 K with unrestrained positions were then performed. Data were analyzed using GROMACS 2018.4. package tools (Abraham *et al.*, 2015), VMD (Humphrey *et al.*, 1996), PyMol (Delano, 2002) and the graphic software Origin (*Origin Lab*).

The HADDOCK 2.4 web server (van Zundert *et al.*, 2016) was used to explore the preferred docking sites for unspecific dsDNA of 15 to 20 bp sequences on CypA, H2AX and AIF, when free and when forming the degradosome. Residues of either the TopIB or DEK motifs were used to restrict the dsDNA AIF interaction site, while no restrictions were imposed for dsDNA docking on H2AX or CypA. Residues observed in these dockings showing a high propensity to interact with dsDNA were then used to model the wrap of a dsDNA 80 bp strand onto the above built degradosome model by using Graphite–LifeExplorer (Hornus *et al.*, 2013).

4. Beyond a Platform Protein for the Assembly of the Degradosome

The Apoptosis Inducing Factor as an efficient nuclease involved in chromatinolysis

The PhD candidate contributed by performing the following:

- Production and purification of wildtype $AIF_{\Delta 101}$ and its variants, and ligands CypA, H2AX and DNA partially
- Isothermal titration calorimetry of H2AX with CypA, $AIF_{\Delta 101}$:H2AX with CypA, H2AX:DNA with $AIF_{\Delta 101}$:CypA, and the $AIF_{\Delta 101}$ variants with DNA
- EMSA assays
- Nuclease activity assays

ABSTRACT

AIF is a moonlighting FAD–dependent enzyme that partakes in the assembly of the mitochondrial respiratory complexes in healthy cells, but which may just as well trigger DNA cleavage and parthanatos under pathological conditions. Upon apoptotic stimuli, AIF is released from the mitochondria and subsequently translocated into the nucleus. There, it may interact with other proteins such as endonuclease CypA and histone H2AX, leading to the formation of a multi–protein complex known as degradosome. In this chapter, we provide evidence for the molecular assembly of this complex as well as for the cooperative effects that are experienced amongst its protein components, ultimately culminating in the degradation of the genomic DNA into large fragments. We have also uncovered that AIF has nuclease activity that is stimulated in the presence of either Mg^{2+} or Ca^{2+}. Such activity allows AIF to efficiently degrade genomic DNA, either by itself or in cooperation with CypA. Finally, we have identified TopIB and DEK motifs in AIF as responsible for its nuclease activity. These new findings point, for the first time, to AIF as a nuclease able to digest nuclear dsDNA in dying cells, deepening our understanding of its role in promoting apoptosis and opening paths for the development of new therapeutic strategies.

RESUMEN

AIF es una enzima multifunción dependiente de FAD que participa en el ensamblaje de los complejos respiratorios mitocondriales en células sanas, pero que puede también desencadenar la escisión del ADN y el parthanatos en condiciones patológicas. Tras un estímulo apoptótico, AIF es liberada de la mitocondria y posteriormente translocada al núcleo. Ahí puede interactuar con otras proteínas como la endonucleasa CypA y la histona H2AX, resultando en la formación de un complejo multiproteico conocido como degradosoma. En este capítulo, evidenciamos el ensamblaje molecular de este complejo, así como los efectos cooperativos que son experimentados por sus componentes proteicos, culminado finalmente en la degradación del ADN genómico en fragmentos grandes. También hemos descubierto que AIF posee actividad nucleasa que es estimulada en presencia de Mg^{2+} o Ca^{2+}. Tal actividad permite a AIF degradar eficientemente ADN genómico, bien sea por sí misma o en cooperación con CypA. Finalmente, hemos identificado los motivos TopIB y DEK en AIF como responsables de su actividad nucleasa. Estos nuevos descubrimientos señalan, por primera vez, a AIF como una nucleasa capaz de digerir el ADN nuclear en células moribundas, profundizando nuestro conocimiento sobre su papel en la inducción de la apoptosis y abriendo caminos para el desarrollo de nuevas estrategias terapéuticas.

4.1. INTRODUCTION

AIF is a mitochondrial flavoprotein that contributes to both cell life and death (Susin *et al.*, 1999). Under physiological conditions, AIF is anchored to the MIM, facing the IMS, where it interacts with CHCHD4 –a key assembly factor for multisubunit respiratory ETC complexes– and plays an essential role in the maintenance of mitochondrial structure and oxidative phosphorylation (Delavallée *et al.*, 2020; Hangen *et al.*, 2015). Conversely, under pathological conditions, AIF is one of the main effectors of caspase–independent necroptosis. This manner of PCD involves the redistribution of AIF to the nuclear compartment where it induces chromatin condensation, large–scale DNA fragmentation (~20 to 50 kb) and DNA loss (Artus *et al.*, 2010; Cabon *et al.*, 2012).

In response to a variety of cytotoxic stimuli, oxidative stress or DNA alkylating agents, hyperactivation of nuclear PARP–1 initiates a signalling cascade that provokes mitochondrial damage. This results in the release of the soluble truncated pro–apoptotic AIF form –$AIF_{\Delta 101}$ in humans, cleaved by activated calpains proteases– from the mitochondria to the cytosol. Interestingly, the subsequent translocation of AIF to the nucleus is hindered or promoted through its physical interaction with either HSP70 or CypA respectively, by a mechanism still not completely understood (Gurbuxani *et al.*, 2003; Zhu *et al.*, 2007). Once in the nucleus, the lethal activity of AIF is said to rely on its ability to associate or activate nucleases, since AIF apparently lacks genuine endonuclease activity despite being able to bind chromatin (Joza *et al.*, 2009; Susin *et al.*, 1999; Vahsen *et al.*, 2006; Ye *et al.*, 2002). Previous results showed that the synchronized action of AIF, phosphorylated histone H2AX and nuclease CypA is required to provoke chromatin remodelling and DNA loss under alkylating DNA damage upon MNNG–mediated necroptosis (Artus *et al.*, 2010). Indeed, there is strong evidence of a nuclear AIF/H2AX interplay (Artus *et al.*, 2010). This might in some way promote the activation of the latent nuclease activity of CypA, as well as support the association of AIF, H2AX and CypA in a multi–protein complex commonly referred to as the degradosome (Artus *et al.*, 2010). Of note, H2AX participates in DNA damage repair in response to DNA double–strand breaks while simultaneously playing a key role in PCD, likely inducing DNA restructuration to improve accessibility to endonucleases (Baritaud *et al.*, 2012; Fernandez–Capetillo *et al.*, 2003). AIF might also cooperate directly with CypA to promote neuronal death in response to different cellular stress conditions (Cande *et al.*, 2004; Zhu *et al.*, 2007). In

particular, upon cerebral hypoxia–ischemia, the cytosolic AIF/CypA interaction has been proposed to favour the nuclear co–translocation of both proteins (Zhu *et al.*, 2007). Nonetheless, further studies are needed to clarify the molecular mechanisms through which these DNA–degrading complexes execute their lethal action as a function of the particular apoptotic stimuli and even the cellular and tissue nature.

In this scenario, AIF has been proposed as a platform for the assembly of an active DNA–degradosome complex during PCD (Baritaud *et al.*, 2010). This is supported by the fact that AIF may concurrently interact with all of the degradosome components through different surface regions. Thus, AIF would interact with H2AX through a proline–rich motif (aa 544–554 in *Homo sapiens* AIF, part of the flexible regulatory C–loop) in its apoptotic C–terminal domain that is essential for its apoptogenic capacity (Artus *et al.*, 2010). On his part, CypA would specifically associate to the 370–394 amino acid region within the NADH–binding domain of *Homo sapiens* AIF (Farina *et al.*, 2018). Finally, AIF interacts with DNA in a sequence–independent manner based on electrostatic interactions around a positively charged protein crown (Romero–Tamayo *et al.*, 2021; Ye *et al.*, 2002). However, up to date no *in vitro* or *in vivo* evidence exists for the formation of this nuclear chromatinolytic degradosome complex, despite a plausible theoretical molecular model (Baritaud *et al.*, 2010). Furthermore, little is known about the physiological relevance of the mutual interactions among these proteins, their cooperativity or how they operate to promote chromatinolysis.

Using a combination of biophysical and molecular biology methodologies, we prove in this chapter the formation of DNA–degradosome assemblies at the molecular level, being able to enlarge their efficiency on DNA chromatinolysis. In addition, we also demonstrate the capability of AIF to enact DNA nuclease activity by itself, unregimented by either endonuclease CypA or histone H2AX.

4.2. Results and Discussion

4.2.1. Visualizing the degradosome assembly at the molecular level

In sight of accumulated evidences suggesting that AIF associates in the nucleus with CypA and H2AX to form a degradosome multicomplex, we used different methods to prove the ability of apoptotic $AIF_{\Delta 101}$ to *in vitro* simultaneously assemble with CypA and H2AX.

4.2.1.1. Analysis of the degradosome assembly by CN–PAGE and SEC

When incubated with 3–fold excess of either H2AX or CypA (16 and 18 kDa respectively), or with both simultaneously, $AIF_{\Delta 101}$ (58 kDa) migrated as a unique band that shifted towards higher apparent MW (^{app}MWs) in high–resolution clear native electrophoresis (CN–PAGE) and proved for the specific detection of $AIF_{\Delta 101}$ (*Fig. 4.1A*). The progressive reduction of electrophoretic mobility in $AIF_{\Delta 101}$ > $AIF_{\Delta 101}$:H2AX > $AIF_{\Delta 101}$:CypA > $AIF_{\Delta 101}$:H2AX:CypA samples correlated well with the expected ^{app}MWs of these assemblies (83, 85 and 101 kDa respectively). Furthermore, analysis by a second SDS–PAGE of the band containing the degradosome mixture evidenced co–migration of the three proteins (*Fig. 4.1A*).

The stability and stoichiometry of this degradosome assembly was further confirmed by size exclusion chromatography. Binary mixtures containing $AIF_{\Delta 101}$ and either CypA or H2AX eluted mainly as new broad peaks of lower exclusion volume than that of free $AIF_{\Delta 101}$ (*Fig. 4.1B, C*). Table 4.1 summarizes the elution volumes for these peaks, showing that they correspond to assemblies with ^{app}MW of 53 and 50 kDa that respectively match with those of $AIF_{\Delta 101}$:CypA and $AIF_{\Delta 101}$:H2AX hetero–dimers. In the case of ternary mixtures, the deconvolution profile of the principal elution peak (*Fig. 4.1D*) suggests two populations with ^{app}MWs of 57 and 47 kDa in similar proportions. The first matches well with the expected MW for the degradosome assembly, whereas the second corresponds to monomeric free $AIF_{\Delta 101}$.

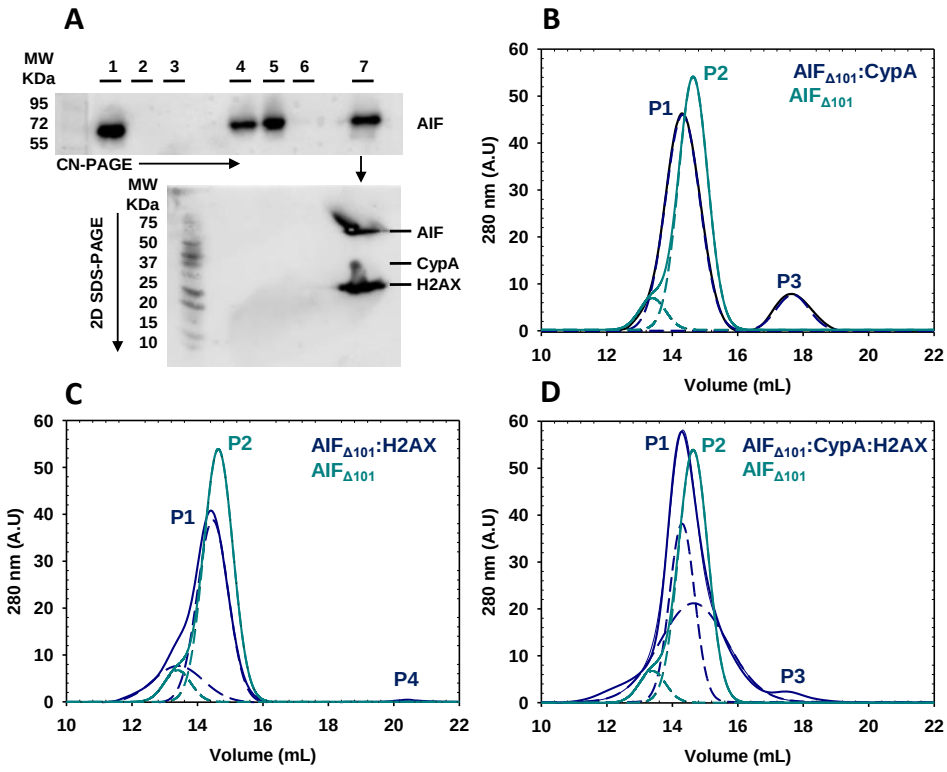

Figure 4.1. The degradosome quaternary organization. (A) WB analyses of degradosome composition. The top panel shows the high–resolution CN–PAGE separation of: lane 1, $AIF_{\Delta101}$; lane 2, CypA; lane 3, H2AX; lane 4, $AIF_{\Delta101}$:CypA (1:3 ratio); lane 5, $AIF_{\Delta101}$:H2AX (1:3 ratio); lane 6, CypA:H2AX (1:3 ratio); lane 7, $AIF_{\Delta101}$:CypA:H2AX (1:3:3 ratio). Mixtures were incubated 15 min at 25 ºC in 50 mM Kpi, pH 7.4, prior to electrophoresis separation. Then, the blot was probed with $AIF_{\Delta101}$ specific antibodies. Lane 7 was excised from the CN–PAGE and loaded into a second SDS–PAGE dimension (lower panel) to separate proteins by MW. The resulting protein spots were Western–analyzed using anti–His–tag. Chromatographic deconvolution profiles of mixtures of $AIF_{\Delta101}$ with (B) CypA, (C) H2AX and (D) both proteins. Samples were incubated at 1:3 or 1:3:3 ratios in binary and ternary mixtures, respectively, for 15 min at 25 ºC in 50 mM Kpi, pH 7.4, before passing through a Superdex™ 200 10/300 GL column using the same buffer supplemented with 10 mM NaCl. The elution profiles for each mixture are shown in blue lines, while control profiles for $AIF_{\Delta101}$ are in light green lines. The respective different populations assigned by Gaussian analysis are depicted in dashed lines.

Table 4.1. Quaternary assemblies of $AIF_{\Delta 101}$ with its apoptotic partners detected by gel filtration chromatography.

Samples	^{app}MW (kDa)				Complex assembly (stoichiometry)
	Peak 1	Peak 2	Peak 3	Peak 4	
$AIF_{\Delta 101}$		47			Monomer
CypA			13		Monomer
H2AX				5	Monomer
$AIF_{\Delta 101}$:CypA	53		13		Hetero–Dimer (1:1)
$AIF_{\Delta 101}$:H2AX	50			5	Hetero–Dimer (1:1)
$AIF_{\Delta 101}$:CypA:H2AX	57	47	14	nd	Hetero–Trimer (1:1:1)

Free proteins and pre–formed mixtures of $AIF_{\Delta 101}$ with different partners (1:3 ratio) in 50 mM Kpi, pH 7.4, were passed through a Superdex™ 200 10/300 GL column in the same buffer supplemented with 10 mM NaCl. ^{app}MWs of the elution peaks were obtained by Gaussian deconvolution of the gel filtration elution profiles (*Fig. 4.1 B–D*). Table shows the calculated ^{app}MW for the principal component of each population. Column calibrated with a set of proteins of known MW. nd: not detected.

4.2.1.2. Analysis of the degradosome assembly by AFM

The multimeric state of the mixtures of $AIF_{\Delta 101}$ with CypA, H2AX or both simultaneously was also analysed at the single molecule level using AFM (*Fig. 4.2*).

When imaging $AIF_{\Delta 101}$, CypA and H2AX on their own (*Fig. 4.2A–C*), their respective average heights of 6.3 ± 0.9 nm, 3.9 ± 0.6 nm and 4.6 ± 0.7 nm agreed well with the dimensions of their corresponding PDB structures, indicating they were visualized mostly as monomers (95–98%). Besides that, no features bigger than occasional homo–dimers were observed (*Table 4.2*). When similarly evaluating mixtures containing $AIF_{\Delta 101}$ and either CypA or H2AX, monomers corresponding well to the dimensions of isolated proteins were identified, but additional imaging features were also observed (*Fig. 4.2D, E*). These features were different when compared to monomeric and homo–dimeric features of isolated proteins, being compatible with the formation of stable hetero–dimeric complexes with similar angles between the two protein components for both complexes (~135 º). Moreover, the greater population of hetero–dimers for CypA than for H2AX (55% vs 30% respectively, *Table 4.2*) suggested the $AIF_{\Delta 101}$:CypA interaction being the most stable.

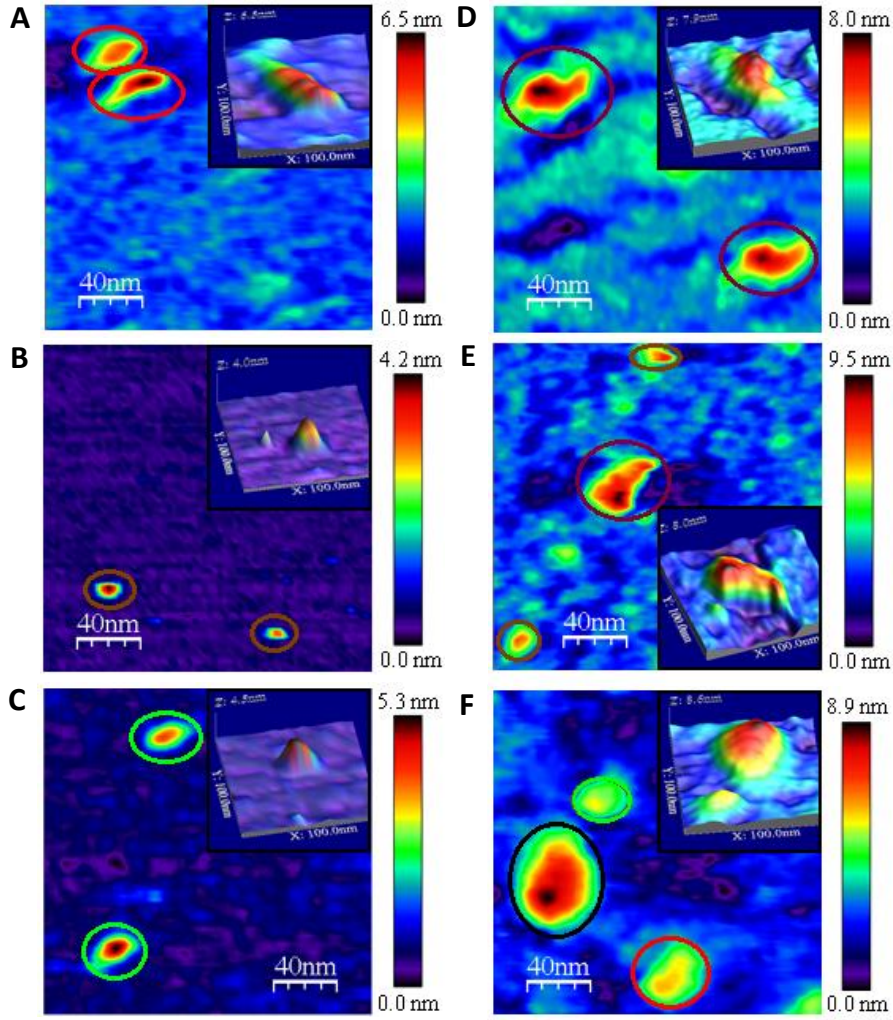

Figure 4.2. AFM topography of protein components of the degradosome and of their binary and ternary assemblies. Imaging of (A) $AIF_{\Delta 101}$, (B) CypA, (C) H2AX, (D) $AIF_{\Delta 101}$:CypA, (E) $AIF_{\Delta 101}$:H2AX and (F) $AIF_{\Delta 101}$:CypA:H2AX. $AIF_{\Delta 101}$ (0.5 µM) was incubated with either H2AX or CypA (1:1 ratio) or both at the same time (1:1:1 ratio) for 10 min at 4 ºC in PBS, pH 7.0. Scan size was 200 nm x 200 nm. Red, brown and green circles indicate $AIF_{\Delta 101}$, CypA and H2AX monomers, hetero–dimers are highlighted in purple and the black circle stands for an $AIF_{\Delta 101}$:CypA:H2AX assembly. The inset panels depict zooms of representative 3D AFM images of the studied monomers, binary or ternary complexes (scan size 100 nm x 100 nm).

Lastly, imaging of mixtures with the three degradosome protein components produced features consistent with the simultaneous detection of monomers (25 %), hetero–dimers (43 %) and hetero–trimers (degradosome, 32 %), with the last two feature types showing elongated arrangements (*Fig. 4.2F and Table 4.2*). Furthermore, overall height of the degradosome assemblies remained similar to those of the monomeric isolated features, suggesting that association of the three proteins takes place at the mica plane.

Table 4.2. Distribution of quaternary species identified by AFM imaging of $AIF_{\Delta 101}$, CypA and H2AX, as well as of their binary and ternary complexes.

Sample mixtures	Monomers (%)	Hetero–Dimers (%)[a]	Hetero–Trimers (%)
$AIF_{\Delta 101}$	98	2	–
CypA	95	5	–
H2AX	95	5	–
$AIF_{\Delta 101}$:CypA	45	55	–
$AIF_{\Delta 101}$:H2AX	70	30	–
$AIF_{\Delta 101}$:CypA:H2AX	25	43	32

Protein samples in PBS, pH 7.0. Mixtures containing 0.5 µM of each indicated protein were pre–incubated before AFM imaging. Percentages are referred to the total number of protein molecules analysed. Percentage error is within 5–10 %. [a]Values correspond to homo–dimers in samples containing a single protein.

4.2.1.3. Structural modelling of the degradosome assembly

A sequential routine of rigid body docking and MD simulations was followed to produce energetically optimized assembles, first for the AIF:CypA binary association (*Fig. 4.3*), and then for the AIF:CypA:H2AX degradosome (*Fig. 4.4*).

Molecular visualization of docking poses and frames of equilibrated MD trajectories, as well as analysis of equilibrated RMSF values for CypA/H2AX Cαs when aligning AIF position, inform of the conformational and flexibility changes within the interacting proteins (*Fig. 4.3*). In both organizations, CypA regions including residues 55–60, 118–121 and 140–150 deviated the least from AIF, whereas larger

displacements were observed at other CypA positions. This suggests that while the above indicated regions maintain the AIF:CypA association, there is a pivotal rotation of CypA onto the AIF interaction surface.

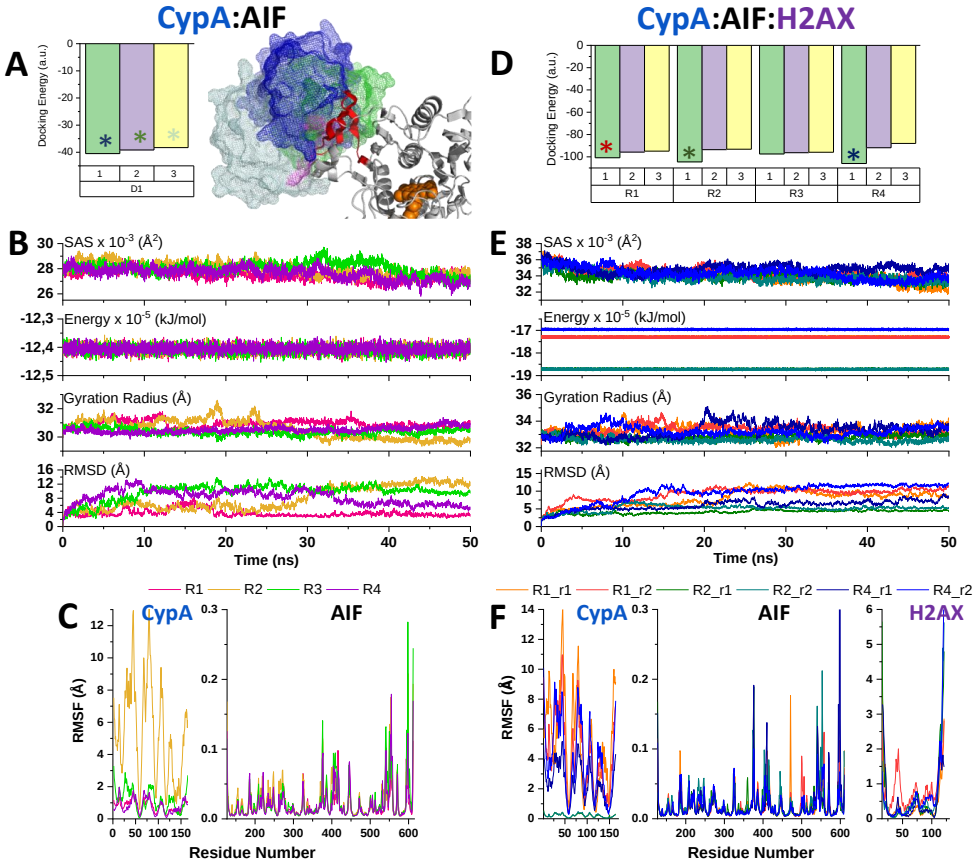

Figure 4.3. Modelling energetically optimized (eo) degradosome assemblies. (A) Docking energies (left) and relative disposition (right) for the three best poses for the docking of CypA onto AIF as receptor. Best three CypA poses are shown in mesh and respectively coloured in metal blue, green and pale green, while AIF is shown as grey cartoon with FAD in orange spheres. CypA and AIF regions used to restrict docking poses are highlighted in magenta and red respectively. (B) SAS, energy, radius of gyration and RMSD (Cα) trajectories showing equilibration along the AIF:CypA MD production. (C) RMSF (Cα) along MD for the proteins making the AIF:CypA complex. (D) Energies for the three best poses for the docking of H2AX to AIF:$CypA_{eo}$ models as receptors. Docking was performed for two selected frames of each of the four MD replicates of the selected AIF:$CypA_{eo}$ docking poses, but for clarity energy data are only shown for one frame in each replicate. Asterisks correspond to the three selected poses for subsequent energy optimization by MD. (E) SAS, energy, radius of gyration and RMSD

(Cα) showing equilibration along the AIF:CypA:H2AX MD production. (F) RMSF (Cα) along MD for the three proteins making the degradosome complex. In (E) and (F) data from the two MD replicates for each of the three selected docking poses are shown. Only frames upon reaching equilibrium (20–50 ns range of the MD production) were used for RMSFs calculation and they were locally aligned considering only the AIF chain.

CypA hot spot residues for binding to AIF particularly include the 58–PGF–60 hydrophobic loop and the R148 side chain, which stay at the interaction surface independently on CypA rotation (*Fig. 4.4B*). Noticeably, the CypA PGF region and W121 are reported as relevant for its peptidylprolyl isomerase activity, cis/trans isomerization of prolines, with key roles in immunity and viral infection. In addition, F60 and W121 also contribute to the stacking of CypA to other proteins or peptides, such as the HIV–1 capsid (Lammers *et al.*, 2010), α–synuclein (Favretto *et al.*, 2020), the CrkII adaptor protein influencing cell motility and invasion (Saleh *et al.*, 2016) or cyclosporin A and derivative immune–suppressive drugs (Dujardin *et al.*, 2018; Jin *et al.*, 2002). As expected, the AIF surface binding CypA is mainly contributed by the antiparallel β–sheet 370–390, being a particular hot spot V374 at its central site. Simulations also point to the 272–276 residues, particularly the E276 side–chain, in CypA binding (*Fig. 4.4B*).

On its side, after MD equilibration of the degradosome assemblies, H2AX keeps mainly bound at the AIF C–loop Pro–rich region that includes a PST motif reported as preferred by this histone for binding to other partners (Salguero *et al.*, 2019) (*Fig. 4.4C, D*). This motif remains as AIF's most flexible region even when H2AX is bound, since the dynamic deformation of H2AX's central α2–helix allows to accommodate its dock.

Altogether, simulations envisage that AIF acts as a docking platform to promote localization of CypA and H2AX, while allowing overall conformational orientation and flexibility. As a consequence, it is envisaged that the degradosome will be able to conformationally evolve upon interaction with other biomolecules, as for example DNA, to facilitate their association as well as subsequent processes involved in chromatin condensation and DNA degradation.

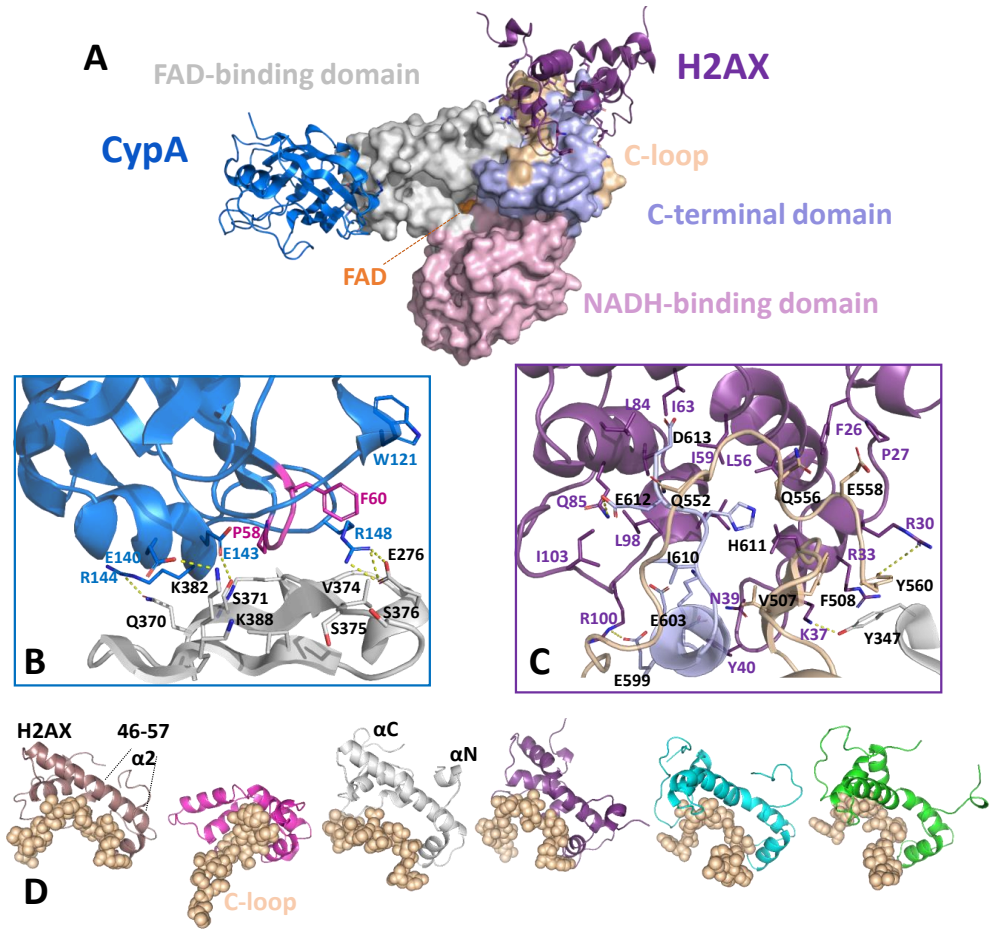

Figure 4.4. Energetically optimized model for the degradosome assembly. (A) Model selected from replicate R2_r2 from Figure 4.3. AIF is shown as surface, with FAD–binding, NADH–binding and C–terminal domains in grey, pink and light violet respectively, the C–loop highlighted in wheat and the FAD as orange spheres. CypA and H2AX are shown as metal blue and dark violet cartoons, respectively, and main residues implicated in the interaction with AIF are in CPK coloured sticks. Enlarged details of (B) AIF:CypA and (C) AIF:H2AX interaction surfaces, showing all proteins as cartoons and highlighting relevant residues as sticks. Some potential polar interactions are shown in yellow dashed lines. (D) Final frames for the six MD replicates of the degradosome complex showing the relative disposition of H2AX (at a different colour for each replicate) and the AIF–Pro rich motif (residues 540–560, orange spheres). To highlight C–loop and H2AX conformational flexibility, H2AX models are shown locally aligned through the N–terminal of their α2–helix (residues 46–57).

4.2.2. DNA–degradosome assembly and cooperativity effects

4.2.2.1. Binary interactions between the components of the degradosome

The interaction within the binary complexes was evaluated among all of its components –namely, $AIF_{\Delta 101}$, CypA, H2AX and dsDNA– by ITC (*Fig. 4.5 and Table 4.3*). Control ITCs were additionally carried out with the ligand in the syringe being titrated into buffer, ensuring that there was no significant dilution effect on the heat change (*Fig. 4.5*, in red).

Binding isotherms were best fitted to a single binding site model with a K_d within the micromolar range for all binary complexes. Thermograms for the titration of $AIF_{\Delta 101}$ with its protein partners, CypA and H2AX (*Fig. 4.5A, B*), demonstrated that the interaction of $AIF_{\Delta 101}$ with CypA is enthalpically guided, whereas binding of AIF to H2AX is driven by a favourable entropic contribution. This suggests that the $AIF_{\Delta 101}$:CypA binary complex rises from specific polar interactions between both proteins, which is in agreement with previous results in the literature (Farina *et al.*, 2017; Romero–Tamayo *et al.*, 2021). On the contrary, the interaction between $AIF_{\Delta 101}$ and H2AX appears to lack such electrostatic specificity. Nevertheless, both binary complexes displayed a significant affinity between their components, with K_d values of 0.7 and 0.8 µM respectively (*Table 4.3*).

Binding of dsDNA to each of the proteins was also separately evaluated (*Fig. 4.5C–E*). All dsDNA binary complexes were entropically driven with an unfavourable enthalpic contribution. The interaction was characterized in all cases by a moderate affinity (*Table 4.3*). Nonetheless, the interactions of $AIF_{\Delta 101}$ and H2AX with dsDNA were stronger in comparison with the CypA:dsDNA one (the latter shows a considerable increase in K_d, *Table 4.3*). In the case of H2AX, this is particularly due to a considerably less unfavourable enthalpic contribution to the binding, despite a just milder favourable entropic contribution (*Fig. 4.5F*). Moreover, these data are consistent with the proposed mechanism of interaction between dsDNA and AIF, which is expected to take place within the clusters of positive charges present throughout the protein's surface (Romero–Tamayo *et al.*, 2021; Ye *et al.*, 2002).

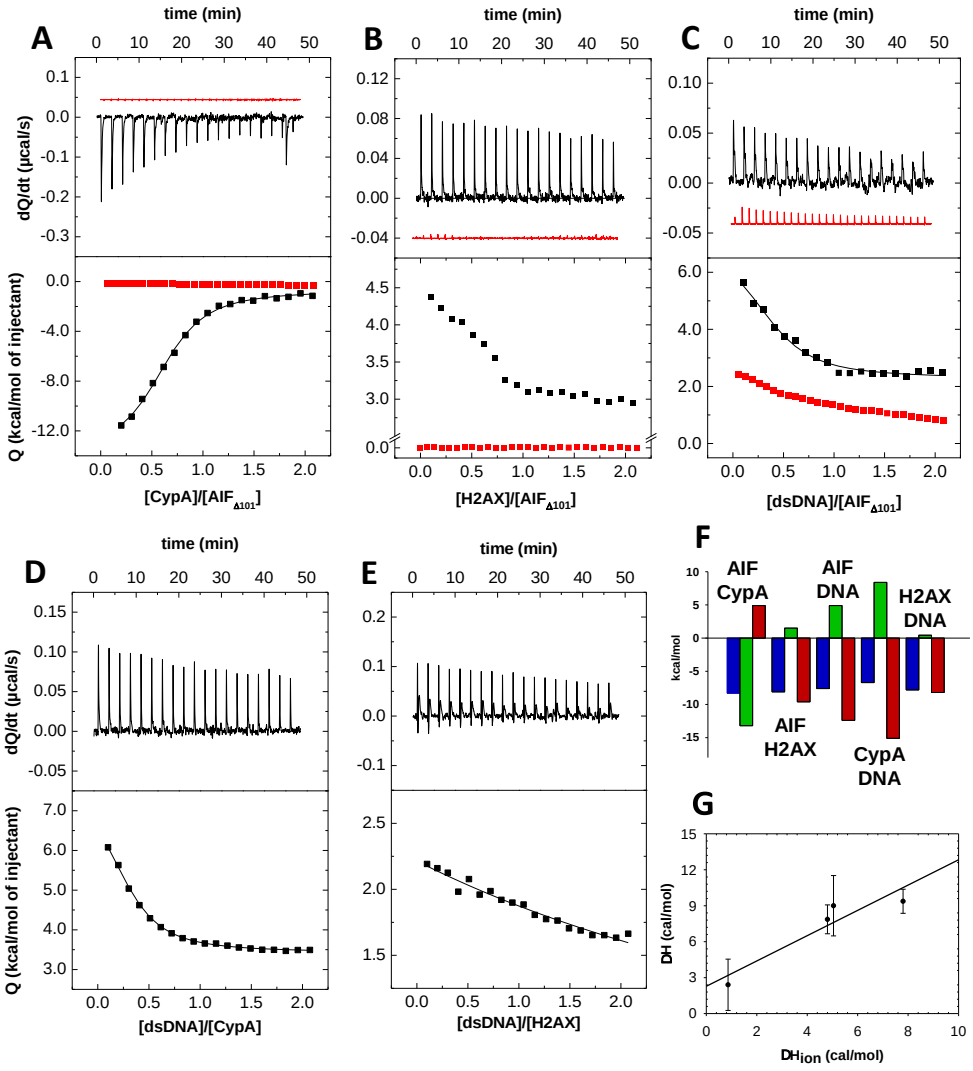

Figure 4.5. Isothermal calorimetric titrations for binary interactions of the degradosome components. ITC profiles for (A) AIF$_{\Delta101}$:CypA, (B) AIF$_{\Delta101}$:H2AX, (C) AIF$_{\Delta101}$:dsDNA, (D) CypA:dsDNA and (E) H2AX:dsDNA complexes. Measurements were performed in 50 mM Kpi, pH 7.4, at 15°C, or at 25 ºC when evaluating interactions involving CypA. In control titrations (panels A to C, superimposed in red), ligands were put in the syringe and titrated against buffer 50 mM Kpi, pH 7.4 at 15 °C, or at 25 °C when evaluating interactions involving CypA. The CypA control data is shown +0.05 µcal to facilitate visualization, as are the H2AX and dsDNA controls -0.04 µcal. The upper panels show the thermograms for the interactions, whereas the lower panels show the corresponding binding isotherms with integrated heats. Data were fitted to a home–derived model for a single binding site (continuous lines in binding isotherms). (F) Thermodynamic dissection of the binary interactions. Gibbs energy (ΔG),

enthalpy (ΔH) and entropy ($-T\Delta S$) contributions to the binding are represented in blue, green and red bars, respectively. (G) Dependence of the measured binding enthalpy (ΔH) for the formation of the $AIF_{\Delta 101}$:dsDNA complex on buffer ionization enthalpy (ΔH_{ion}) at 15 °C. Used buffers are Kpi, TES, MOPS and HEPES at 150 mM ionic strength. The pH was 7.4 and 7.5 respectively in Kpi and TES buffers, and 8.0 for HEPES and MOPS. The solid line represents the fit to a linear regression and provides an estimation of the buffer independent enthalpy ($\Delta H°$) and of the net number of exchanged protons (n_{H+}) upon complex formation. Values show mean ± SD, n=3.

Table 4.3. Thermodynamic parameters for the formation of binary, ternary and degradosome assemblies.

Sample in the calorimetric cell	Titrating ligand	K_d (μM)	N	ΔH (kcal/mol)	ΔG (kcal/mol)	$-T\Delta S$ (kcal/mol)
		Binary complexes				
$AIF_{\Delta 101}$	CypA	0.8	0.6	−13.2	−8.3	4.9
$AIF_{\Delta 101}$	H2AX	0.7	0.6	1.5	−8.1	−9.6
$AIF_{\Delta 101}$	dsDNA	1.6	0.4	4.9	−7.6	−12.4
CypA	dsDNA	8.9	0.6	8.4	−6.7	−15.1
H2AX	dsDNA	1.2	0.8	0.4	−7.8	−8.2
		Ternary complexes				
$AIF_{\Delta 101}$:dsDNA (1:1)	CypA	1.2	0.8	−5.5	−8.1	−2.6
$AIF_{\Delta 101}$:dsDNA (1:2)	CypA	1.9	0.7	−4.8	−7.8	−3.0
$AIF_{\Delta 101}$:dsDNA (1:4)	CypA	2.2	0.5	−3.3	−7.7	−4.4
$AIF_{\Delta 101}$:dsDNA (1:8)	CypA	2.6	0.7	−2.0	−7.6	−5.6
$AIF_{\Delta 101}$:dsDNA (1:1)	H2AX	0.5	0.7	6.3	−8.3	−14.6
$AIF_{\Delta 101}$:dsDNA (1:2)	H2AX	0.4	0.7	1.5	−8.5	−10.0
$AIF_{\Delta 101}$:dsDNA (1:4)	H2AX	0.3	0.7	1.2	−8.6	−10.0
$AIF_{\Delta 101}$:dsDNA (1:8)	H2AX	0.3	0.7	1.0	−8.7	−9.6

$AIF_{\Delta 101}$:CypA (1:1)	dsDNA	9.4	0.8	17.2	−6.6	−23.8
$AIF_{\Delta 101}$:CypA (1:8)	dsDNA	54	1.7	15.6	−5.6	−21.2
$AIF_{\Delta 101}$:H2AX (1:1)	dsDNA	7.4	0.9	28.9	−6.8	−35.6
$AIF_{\Delta 101}$:H2AX (1:8)	dsDNA	1.9	1.6	4.2	−7.5	−11.7
	Degradosome					
$AIF_{\Delta 101}$:CypA	H2AX	0.8	0.7	1.1	−8.4	−9.5
$AIF_{\Delta 101}$:H2AX (1:1)	CypA	2.5	1.2	−26.0	−7.6	18.2
$AIF_{\Delta 101}$:H2AX (1:8)	CypA	0.3	1.7	−23.3	−9.0	14.3
	dsDNA−Degradosome					
$AIF_{\Delta 101}$:CypA: H2AX (1:1:1)	dsDNA	3.3	0.9	9.9	−7.2	−17.0
$AIF_{\Delta 101}$:CypA: H2AX (1:1:2)	dsDNA	1.3	0.9	9.7	−7.8	−17.5
$AIF_{\Delta 101}$:CypA: H2AX (1:1:4)	dsDNA	1.0	0.8	9.7	−7.9	−17.6
$AIF_{\Delta 101}$:CypA: H2AX (1:1:8)	dsDNA	0.9	1.0	11.9	−8.0	−19.9
H2AX:dsDNA (1:1)	$AIF_{\Delta 101}$:CypA	3.6	1.1	−34.1	−7.2	27.0
H2AX:dsDNA (1:8)	$AIF_{\Delta 101}$:CypA	3.3	0.8	−39.5	−7.2	32.3

Values obtained from ITC assays at 15 ºC, or at 25 ºC when evaluating interactions in presence of CypA, in 50 mM Kpi, pH 7.4. N is the calculated binding stoichiometry, usually interpreted as a fraction of binding−competent or active protein. The thermodynamic parameters were calculated using well−known relationships: $K_d = (K_a)^{-1}$, $\Delta G = RT.\ln K_d$ and $-T\Delta S = \Delta G - \Delta H$. Errors considered in the measured parameters (± 30% in K_d and ± 0.4 kcal/mol in ΔG, ΔH and $-T\Delta S$) were taken larger than the standard deviation between replicates and the numerical error after the fitting analysis.

Additional assays were performed with the $AIF_{\Delta 101}$:dsDNA complex in order to estimate the buffer−independent binding enthalpy and the net number of protons exchanged upon complex formation. Buffers with different ionization enthalpies were

employed (*Table 4.4*), resulting in a buffer–independent ionization free enthalpy of 2.2 cal/mol (*Fig. 4.5G and Table 4.5*). Additionally, the interaction was observed to be strongly associated with proton exchange between the complex and the buffer, confirming that the affinity is pH–dependent and that about one proton is released into the bulk solution upon complex formation.

Table 4.4. Enthalpies of ionization of used buffers.

Buffer	Reaction	pK_a	ΔH_{ion} (kcal/mol)
Kpi	$H_2PO_4^- = H^+ + HPO_4^{2-}$	7.19	0.86
HEPES	$HL^{\pm} = H^+ + L^-$ ($HL = C_8H_{18}N_2O_4S$)	7.56	4.80
MOPS	$HL^{\pm} = H^+ + L^-$ ($HL = C_7H_{15}NO_4S$)	7.18	5.04
TES	$HL^{\pm} = H^+ + L^-$ ($HL = C_6H_{15}NO_6S$)	7.76	7.80
Tris/HCl	$HL^+ = H^+ + L$ ($HL = C_4H_{11}NO_3$)	8.07	11.51

Values measured at 298.15 K and 0.1 MPa. Data from (Goldberg, Kishore & Lennen, 2002).

Table 4.5. Thermodynamic parameters determined for the interactions of $AIF_{\Delta 101}$ with dsDNA in different buffers.

Buffer	K_d (μM)	N	ΔH (kcal/mol)	ΔG (kcal/mol)	$-T\Delta S$ (kcal/mol)
Kpi pH 7.4	1.6	0.4	4.9	–7.6	–12.4
HEPES pH 8.0	1.1	0.4	8.5	–7.8	–16.3
MOPS pH 8.0	1.0	1.1	8.8	–7.9	–16.7
TES pH 7.6	0.1	0.7	9.3	–9.1	–18.4

Values obtained from ITC assays at 15 ºC and at 150 mM ionic strength of the above–mentioned buffers. N is the calculated binding stoichiometry, usually interpreted as a fraction of binding–competent or active protein. The thermodynamic parameters were calculated using well–known relationships: $K_d = (K_a)^{-1}$, $\Delta G = RT \cdot \ln K_d$ and $-T\Delta S = \Delta G - \Delta H$. Errors considered in the measured parameters (± 30% in K_a and $\pm$ 0.4 kcal/mol in ΔH and $-T\Delta S$) were taken larger than the standard deviation between replicates and the numerical error after the fitting analysis.

4.2.2.2. Ternary and quaternary interactions between the components of the DNA–degradosome

Subsequently, we moved onto the determination of the binding contributions for the formation of the ternary and quaternary assemblies (*Fig. 4.6 and Table 4.3*).

ITC assays and cooperativity effects

All interactions coursed with moderate affinity. In general terms, the interactions were entropically guided with an unfavourable enthalpic contribution, with the exception of the titrations of $AIF_{\Delta 101}$:dsDNA or $AIF_{\Delta 101}$:H2AX with CypA, which were enthalpically driven. A flowchart diagram of all assessed complexes with their corresponding free energies is presented in Figure 4.7. Of note, the most favourable ternary interaction observed was that of $AIF_{\Delta 101}$:CypA against H2AX, which presented the greatest free energy change (*Table 4.3*). Hence, the most favourable sequential mechanism of formation of the degradosome might be the binding of CypA to $AIF_{\Delta 101}$, followed by that of H2AX to $AIF_{\Delta 101}$:CypA, and finishing with the binding of dsDNA to $AIF_{\Delta 101}$:CypA:H2AX (*Fig. 4.7*).

Additionally, cooperativity effects within ternary and quaternary complexes were assessed (*Fig. 4.6H, and Tables 4.3 and 4.6*). $AIF_{\Delta 101}$ and CypA appeared to avidly compete against each other to interact with dsDNA (negative cooperativity), whereas the interaction of $AIF_{\Delta 101}$ with dsDNA or CypA resulted significantly enhanced in the presence of H2AX (positive cooperativity). The degradosome complex, $AIF_{\Delta 101}$:CypA:H2AX, happened to behave similarly to the latter, portraying a considerably positive cooperativity that resulted in an increased affinity for dsDNA as the concentration of H2AX became greater.

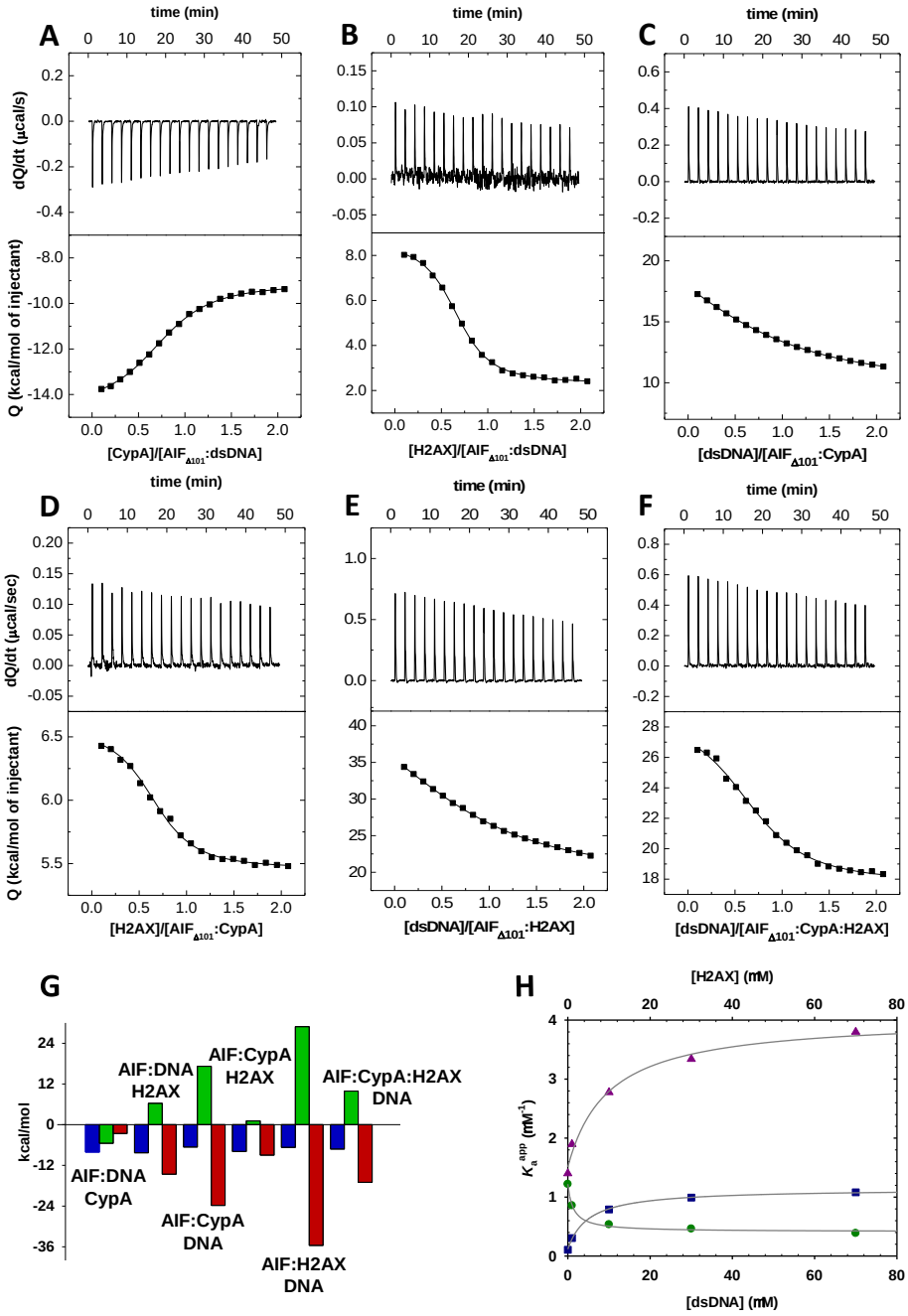

Figure 4.6. Isothermal calorimetric titrations for ternary and quaternary interactions among the degradosome components, and cooperativity effects. Titration with (A) CypA and (B) H2AX of AIF$_{\Delta101}$:dsDNA mixtures. Titration with (C) dsDNA and (D) H2AX of AIF$_{\Delta101}$:CypA mixtures. Titration with (E) dsDNA of AIF$_{\Delta101}$:H2AX mixtures. Titration with (F) dsDNA of the

degradosome. The pre–formed mixtures (1:1: ratio) were incubated 15 min in 50 mM Kpi, pH 7.4, at 25°C. Subsequent ITC measurements were performed in the same buffer at 15°C, or at 25 ºC when evaluating interactions involving CypA. The upper panels show the thermograms for the interactions and the lower panels show the corresponding binding isotherms with integrated heats. Data were obtained by fitting ITC thermograms to a home–derived model for a single binding site (continuous lines in binding isotherms). (G) Thermodynamic dissection of the ternary interactions. Gibbs energy (ΔG), enthalpy (ΔH) and entropy ($-T\Delta S$) contributions to the binding are represented in blue, green and red bars, respectively. (H) Dependence of apparent association constants on the concentration of dsDNA for the binding of CypA ($K_a^{app,CypA}$, green circles) and H2AX ($K_a^{app,H2AX}$, blue squares) to $AIF_{\Delta 101}$:dsDNA ; and dependence of apparent association constants on the H2AX concentration for the binding of dsDNA to $AIF_{\Delta 101}$:CypA:H2AX ($K_a^{app,dsDNA}$, purple triangles). Data were fitted as in section 3.7.2. and the fits represented by lines. All experiments were performed in 50 mM Kpi, pH 7.4, at 15 °C (or at 25 °C when evaluating interactions involving CypA).

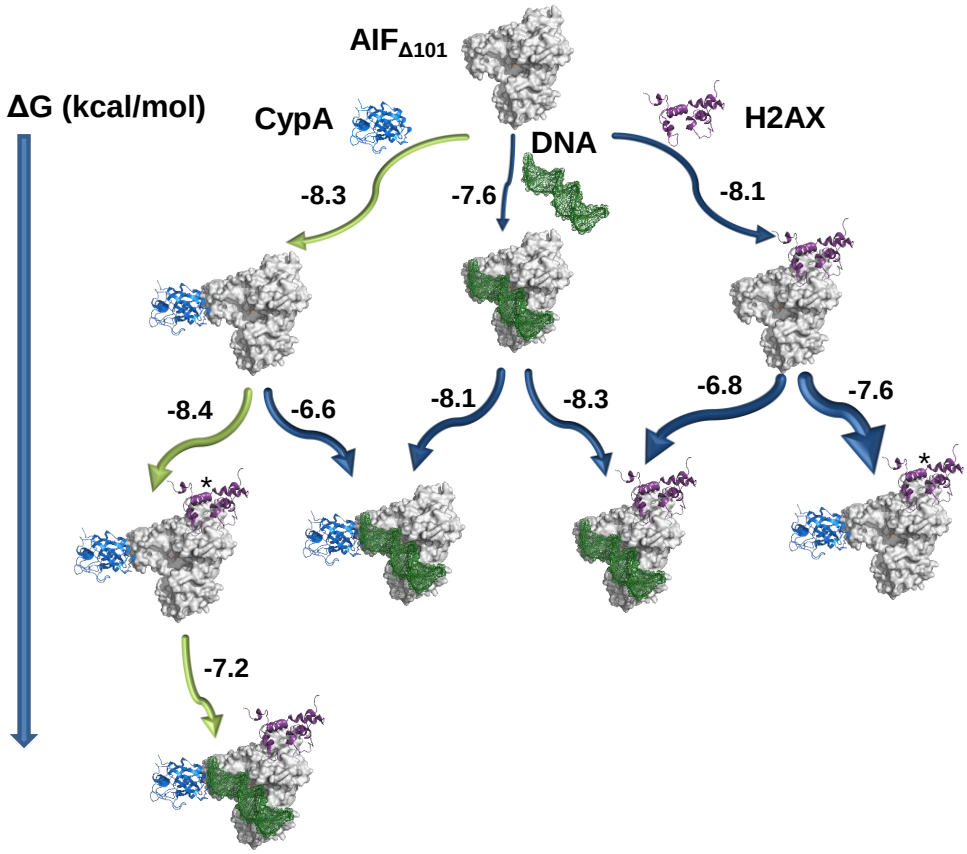

Figure 4.7. Gibbs free energy flowchart for the degradosome assembly routes. The diagram summarizes the Gibbs energy of the interactions of $AIF_{\Delta 101}$ with the different degradosome

components as derived by ITC data in Figures 4.5 and 4.6. CypA (PDB: 3K0M) and H2AX (PDB: 6K1K chain C) are shown as cartoon coloured in blue metallic and dark raspberry, respectively, AIF (PDB: 4BV6) is represented as grey surface and the dsDNA molecule (3'–GGT TAG TTA TGC GCG –5', simulated through SCFBio tool (http://www.scfbio-iitd.res.in/software/drugdesign/bdna.jsp)) is shown as dark green mesh. The length of the arrows is proportional to the ΔG for each interaction (values in kcal·mol^{-1} are indicated in numbers), and their thickness are representative of the fraction of $AIF_{\Delta 101}$ binding the titrating ligand.

Table 4.6. Cooperativity coefficients (α) for the binding of CypA, H2AX and dsDNA to $AIF_{\Delta 101}$.

Mixture in calorimetric cell	Titrating Ligand	α	K_a^{ligand} (μM^{-1})	K_d^{ligand} (μM)	K_a^{dsDNA} (μM^{-1})	K_d^{dsDNA} (μM)
$AIF_{\Delta 101}$:dsDNA	CypA	0.3	1.2	0.8	0.8	0.7
$AIF_{\Delta 101}$:dsDNA	H2AX	2.7	1.5	0.7	0.1	9.8
$AIF_{\Delta 101}$:CypA:H2AX	dsDNA	9.7	0.1	9.1	0.2	5.0

ITC assays were performed at 15 ºC, or at 25 ºC when evaluating interactions with CypA, in 50 mM Kpi, pH 7.4. α represents the heterotrophic cooperativity coefficient of the ligand binding (i.e., influence of one ligand prebound to AIF on the interaction of a second ligand) and K_a^{ligand} is the intrinsic association constant for the titrating ligand upon binding to the $AIF_{\Delta 101}$:dsDNA or the $AIF_{\Delta 101}$:CypA:H2AX complex. α and K_a values estimated from the fit.

Electrophoretic–mobility–shift assays

EMSA were performed to further evaluate potential differing mechanisms for the formation of the DNA–degradosome (*Fig. 4.8*). Binary, ternary and quaternary complexes were obtained through the incubation of their components upon their mixing following different sequential additions.

Remarkably, incubation of CypA with dsDNA led to no observable dsDNA retention, which only appeared after $AIF_{\Delta 101}$ addition. All assessed combinations of CypA and $AIF_{\Delta 101}$ resulted in similar modest mobility dsDNA shift effects, with none achieving that caused by $AIF_{\Delta 101}$ alone. This agrees with the observed negative cooperativity for CypA binding to $AIF_{\Delta 101}$ in the presence of dsDNA. In comparison, H2AX exhibited certain dsDNA retention on its own, which underwent a considerable increase in the presence of $AIF_{\Delta 101}$ and is backed by their positive cooperativity. All combinations of $AIF_{\Delta 101}$, H2AX and dsDNA resulted in comparable mobility shift effects.

In regard to the evaluated quaternary complexes, the sequential addition of H2AX to a preformed $AIF_{\Delta 101}$:CypA complex and, subsequently, of dsDNA to the resulting $AIF_{\Delta 101}$:CypA:H2AX complex led to the greatest dsDNA retention. Once more, this is supported by the significant positive cooperativity effect observed among the three protein partners, and confirms the most favourable degradosome assembly order proposed from the ITC data.

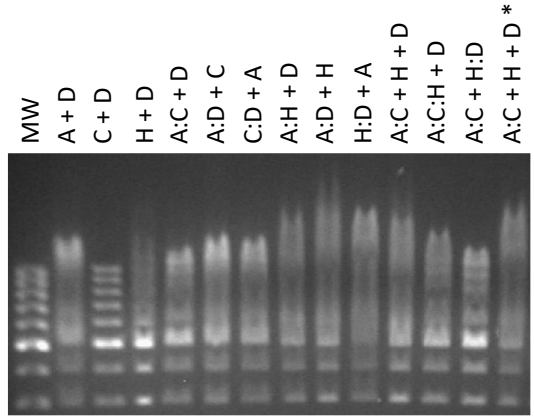

Figure 4.8. EMSA of the degradosome assemblies. 100 bp DNA ladder (Thermo Scientific) (500 ng) was incubated with individual protein components (10 µg of $AIF_{\Delta 101}$, 2 µg of CypA and/or H2AX; as seen in lanes A+D, C+D and H+D respectively) or their combined mixtures in 50 mM Kpi, pH 7.4, at 25 ºC, for 30 minutes, to assess DNA retention. A, C, H and D stand for $AIF_{\Delta 101}$, CypA, H2AX and DNA respectively. MW, stands for DNA molecular weight marker. Starting mixtures of two or three components (A:C, A:D, C:D, A:H, A:D, H:D; A:C:H, A:C) were pre–incubated for 30 minutes before mixing with other components (D, C, A, D, H, A, D, pre–incubated H:D, respectively) and incubated again for 30 minutes. A:C+H+D, stands for $AIF_{\Delta 101}$ and CypA being pre–incubated together for 30 minutes, subsequently mixed with individual samples of H2AX and DNA, and incubated again for an additional 30 minutes. A:C+H+D*, stands for $AIF_{\Delta 101}$ and CypA being pre–incubated together, then mixed with H2AX and incubated again for 30 minutes, and subsequently mixed with DNA and incubated for another additional 30 minutes. Mixtures were separated by electrophoresis in 2 % agarose gel and visualized with ethidium bromide.

Dissecting the assembly of the DNA–degradosome by AFM

The interaction of dsDNA with each isolated protein partner was further analysed using AFM (*Fig. 4.9 and Table 4.7*). Images showed that all proteins remained mainly monomeric, while topography profiles suggestive of dsDNA interacting with the proteins were observed. Heights corresponding to the protein monomeric features

bound to dsDNA, ~9 nm (*Fig. 4.9A*), agreed well with $AIF_{\Delta 101}$ (6.3 ± 0.9 nm; *Fig. 4.2A*) plus free dsDNA (1.5 ± 0.5 nm) (*Fig. 4.9G*). Moreover, $AIF_{\Delta 101}$ induced the stretching and opening of dsDNA strands.

Nonetheless, binding did not appear to be sequence–specific, because distinct sequences along the strands seemed to bind $AIF_{\Delta 101}$ with similar efficacy. The $AIF_{\Delta 101}$:dsDNA interaction also appeared to display cooperativity, as several $AIF_{\Delta 101}$ molecules attach to a DNA strand in a clustered fashion, like "beads on a necklace", while no condensation of isolated dsDNA strands was observed. Figures 4.9B and C also confirmed binding of dsDNA to both CypA and H2AX monomers, according to the height profiles perpendicular to dsDNA molecules (*Table 4.7*).

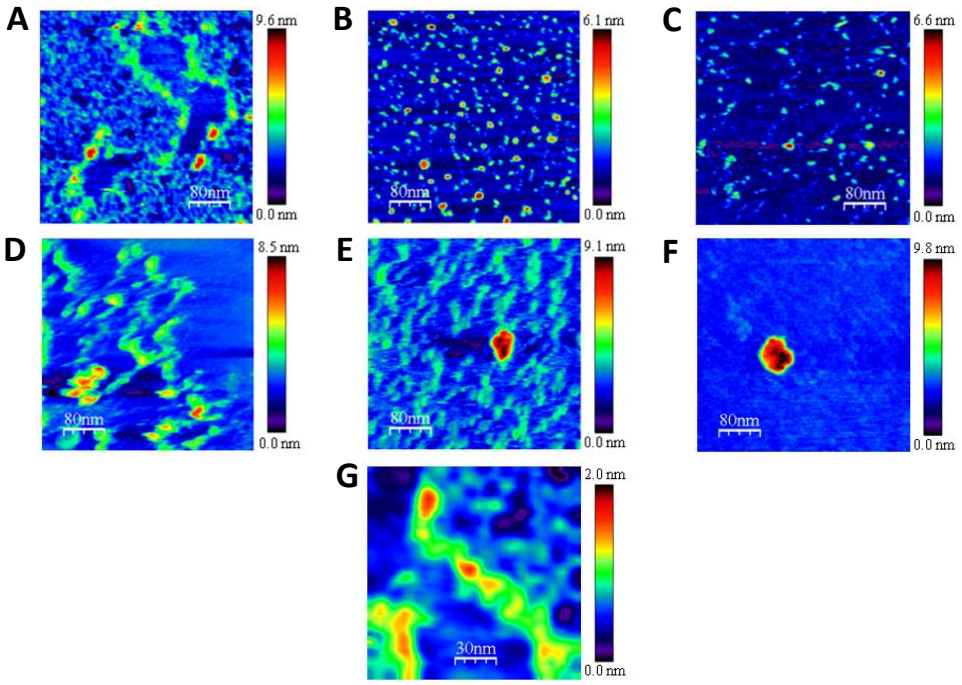

Figure 4.9. AFM topography of assemblies upon formation of the DNA–degradosome complex. Imaging of samples containing (A) $AIF_{\Delta 101}$:dsDNA, (B) CypA:dsDNA, (C) H2AX:dsDNA, (D) $AIF_{\Delta 101}$:CypA:dsDNA, (E) $AIF_{\Delta 101}$:H2AX:dsDNA, (F) and $AIF_{\Delta 101}$:CypA:H2AX:dsDNA assemblies, and (G) Linearized dsDNA. Scan size 400 nm x 400 nm (A–F) and 150 x 150 nm (G). Mixtures of proteins forming the degradosome were prepared as in *Figure 4.2* in the presence of 0.05 ng/µl pET–28a(+) plasmid linearized with EcoRI.

When the $AIF_{\Delta 101}$:CypA and $AIF_{\Delta 101}$:H2AX systems were assayed in the presence of dsDNA (*Fig. 4.9D, E*), percentages of protein–protein association modes remained in

similar ranges as when dsDNA was absent (*Table 4.2*). Moreover, the morphology and angle of these hetero–dimers were maintained, showing only a few ratios with a smaller angle.

Table 4.7. Effect of dsDNA binding on the distribution of quaternary organizations visualized by AFM imaging of $AIF_{\Delta 101}$, CypA and H2AX, as well as of their binary and ternary complexes.

Sample mixtures	Monomers (%)	Hetero–Dimers (%)[a]	Hetero–Trimers (%)	Observed features
$AIF_{\Delta 101}$:dsDNA	98	2	–	DNA binding to protein monomers. Stretching and opening of DNA strands
CypA:dsDNA	95	5	–	DNA binding to protein monomers
H2AX:dsDNA	97	3	–	DNA binding to protein monomers
$AIF_{\Delta 101}$:CypA:dsDNA	45	55	–	DNA binding to protein hetero–dimers. Stretching of DNA
$AIF_{\Delta 101}$:H2AX:dsDNA	60	40	–	DNA binding to protein hetero–dimers. Stretching of DNA
$AIF_{\Delta 101}$:CypA:H2AX: dsDNA	16	32	52	DNA binding to protein complexes

Assays in PBS pH 7.0. Percentages are referred to the total number of protein molecules. Concentrations for components in the incubation mixtures were 0.5 µM and 0.05 ng/µl for proteins and dsDNA, respectively. Percentage error is within 5–10 %. [a]Values correspond to homo–dimers in samples containing a single protein.

Binding of dsDNA to the degradosome (*Fig. 4.9F*) increased the percentage of hetero–trimers by nearly two–fold (from 32 up to 52 %), with a modest decrease of hetero–dimers and monomers (32 % and 16 %, respectively; *Table 4.7*). Hardly any hetero–trimers were found attached to the mica instead of to the dsDNA, as observed by general colour scales and verified by height profiles. This observation can be explained by the net charge exhibited by the proteins forming the degradosome, due to differences in terms of their isoelectric points. At working pH, the $AIF_{\Delta 101}$ electrical charge must be minimal because its isoelectric point is neutral (Candé *et al.*, 2002),

while CypA is slightly negatively charged (pI 6.4–6.5) and H2AX is positively charged (pI 10.7). Such differences reflect different surface electrostatic potentials inducing protein recognition in specific orientations to enable the hetero–trimer formation.

4.2.3. Sources of the nuclease activity within the degradosome

In order to assess the source of the nuclease activity of the degradosome, a plasmid vector was incubated with pure CypA, individually or combined with either pure $AIF_{\Delta 101}$ or pure H2AX, or with both simultaneously, in the presence of 1 mM Ca^{2+} and 1 mM Mg^{2+} (both ions required for the stimulation of the reported CypA nuclease activity (Montague *et al.*, 1997)) (*Fig. 4.10A*).

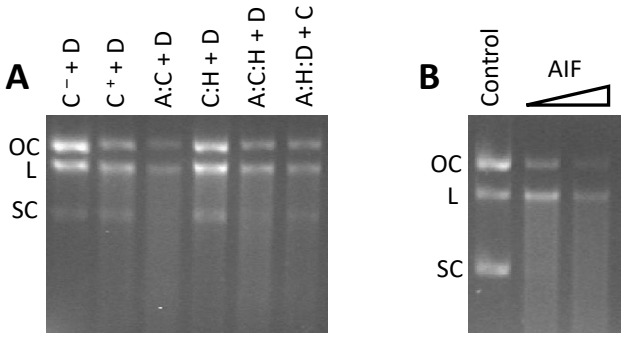

Figure 4.10. Nuclease activity of the degradosome. (A) Nuclease activity observed upon mixing CypA, individually or in combined mixtures with the degradosome components (250 ng of CypA and/or H2AX; and/or 800 ng of AIF, to maintain 1:1 molar ratios), with double–stranded supercoiled pET–28a(+) plasmid (250 ng). The assays were carried out in 20 mM Tris/HCl, pH 8.0, 1 mM $CaCl_2$ and 1mM $MgCl_2$, and final sample combinations were incubated for 1 hour at 37 ºC. A, C, H and D, stand for $AIF_{\Delta 101}$, CypA, H2AX, and plasmidic DNA respectively. C^- and C^+, stand for CypA sample in the absence and presence of ions respectively. Starting mixtures with two or three components (A:C, C:H, A:C:H, A:H:D) were pre–incubated for 15 min at 25 ºC, before mixing with D or C. (B) Nuclease activity of $AIF_{\Delta 101}$ (800 or 1600 ng) observed after mixing with double–stranded supercoiled pET–28a(+) plasmid (250 ng) in 20 mM Tris/HCl, pH 8.0, 1 mM $CaCl_2$ and 1mM $MgCl_2$ upon incubating for 1 hour at 37 ºC. Control, plasmid DNA substrate. OC, L and SC stand for open circular, linear and supercoiled.

Because it is reported that AIF may recruit nucleases such as CypA and the macrophage migration inhibitory factor (MIF) to induce chromatinolysis (Cande *et al.*, 2004; Wang *et al.*, 2016), we expected CypA to be the only actor to cleavage DNA

within the degradosome. Indeed, degradation of dsDNA was observed in all samples containing CypA, while the presence of H2AX offered some sort of dsDNA protection by hindering its degradation over time. Meanwhile, the presence of $AIF_{\Delta 101}$ considerably enhanced the degradation of dsDNA by increasing its smear as previously described (Cande *et al.*, 2004), even though a negative cooperativity effect in the $AIF_{\Delta 101}$:CypA binding to dsDNA has been observed in this chapter.

At this point, it was also worth considering some previous evidences that pointed out to recombinant mouse AIF as able to mediate dsDNA nicking and linearizing activities together, reflected in a discrete gDNA smear (Figures 4, 5 and S10 in references Cande *et al.*, 2004, Susin *et al.*, 2000 and Wang *et al.*, 2016 respectively). To further ascertain this, we incubated the same plasmid vector with pure $AIF_{\Delta 101}$ (*Fig. 4.10B*). Surprisingly, $AIF_{\Delta 101}$ proved able to efficiently degrade the plasmid DNA in a similar fashion to CypA, revealing active nuclease capacity. $AIF_{\Delta 101}$ was able to transform supercoiled dsDNA into its open circular and, subsequently, linear forms prior to degradation to lower MW forms, proving that it possesses both nicking and linearizing activities by itself (*Fig. 4.10B*).

4.2.3.1. Ion, time and concentration dependency of AIF nuclease activity

Subsequently, an assessment of different enhancing divalent ions (Ca^{2+}, Mg^{2+} and Mn^{2+}) was performed, revealing that human $AIF_{\Delta 101}$ nuclease activity can take place in absence of any added ions (although it became optimally stimulated with 0.1 mM Ca^{2+} and 1 mM Mg^{2+}) (*Fig. 4.11A, B*). However, concentrations significantly below or above the optimal values ended up resulting in an inhibitory effect on AIF nuclease activity, similar to that already reported for other nucleases (Belkebir and Azeddoug, 2012; Bendjennat *et al.*, 1997; Pingoud *et al.*, 2009). Additionally, incubation in the presence of inhibiting monovalent ions (K^+ and Na^+) lead to a progressive decrease of the degradation profile, ultimately abolishing most of the nuclease activity (*Fig. 4.11A*).

Moreover, AIF nuclease activity remained evident on human gDNA from HeLa cells in a time– and concentration–dependent manner, initially eliminating the high MW forms (loss of DNA in the well) and gradually increasing the lower MW forms until dsDNA was completely degraded with no detection of the ladder pattern (*Fig. 4.11C, D*).

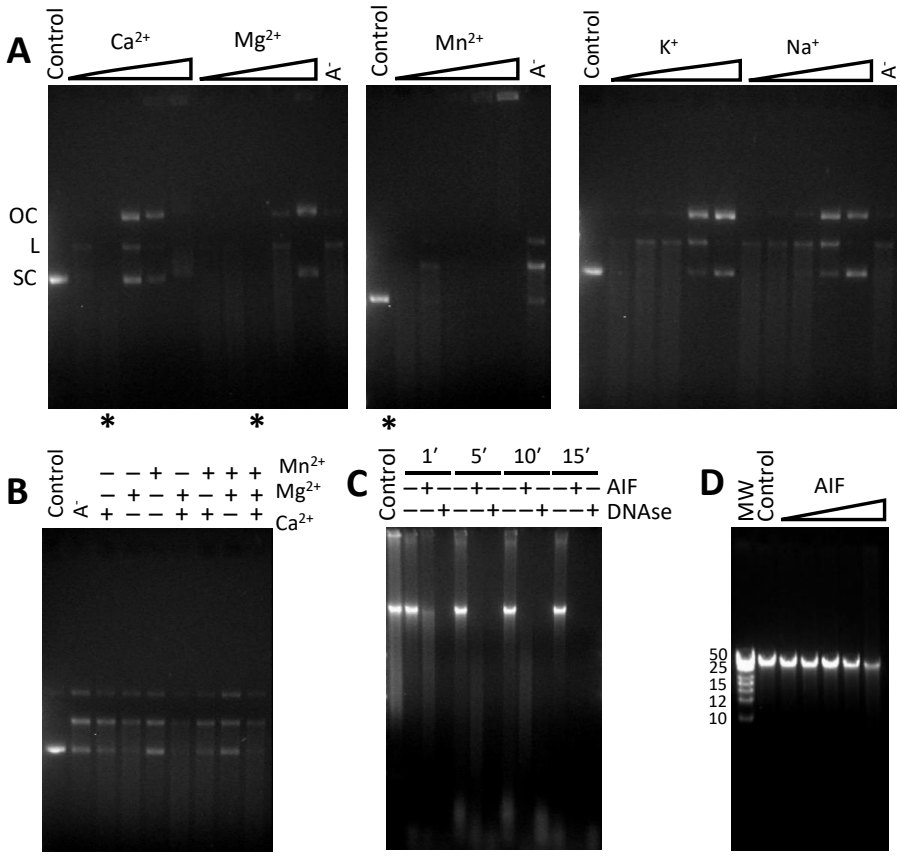

Figure 4.11. Influence of ions, time and concentration on AIF nuclease activity. (A) Effect of different ions expected to promote (Ca^{2+}, Mg^{2+} and Mn^{2+}) or inhibit (K^{+} and Na^{+}) the nuclease activity of $AIF_{\Delta 101}$ against the plasmid DNA substrate. Increasing concentrations of ions (0.01, 0.1, 1, 10 and 100 mM) were evaluated. (B) Cooperative effect of promoting ions. Assays were carried out at the most optimal concentrations observed in (A) (0.01, 0.1 and 1 mM for Mn^{2+}, Ca^{2+} and Mg^{2+} respectively). (C) Effect of the incubation time (1, 5, 10 and 15 min) on $AIF_{\Delta 101}$ nuclease activity against human gDNA. (D) Concentration–dependence of $AIF_{\Delta 101}$ (0.025, 0.250, 2.5, 25 and 250 ng) in its nuclease activity against human gDNA. Unless otherwise stated 250 ng of a double–stranded supercoiled pET–28a(+) plasmid substrate or 500 ng of human gDNA were mixed with 250 ng of purified $AIF_{\Delta 101}$ (or 1 IU of DNase) in 20 mM Tris, pH 8.0 – supplemented with 0.1 mM $CaCl_2$ and 1mM $MgCl_2$ in panels C and D– and incubated for 1 min at 37 ºC. MW, molecular weight marker (GeneRuler High Range DNA Ladder; 10 kbp, 12 kbp, 14 kbp, 15 kbp, 17 kbp, 21 kbp, 25 kbp, 50 kbp). Control, stands for plasmid or genomic DNA substrate alone. A^{-}, stands for plasmid or genomic DNA incubated with $AIF_{\Delta 101}$ in absence of ions (panels A, B). OC, L and SC, stand respectively for open circular, linear and supercoiled.

4.2.3.2. Influence of the different components of the degradosome on AIF nuclease activity

Having defined the optimal conditions for AIF nuclease activity, we studied the effect of the interplay among the degradosome components on DNA degradation.

A set of solution nuclease assays were carried out by incubating the three proteins either separately or in combination with plasmid or genomic DNA samples (*Fig. 4.12*). The latter were also analysed with gDNA ScreenTape assays to determine the size of the remaining gDNA, the concentration of intact dsDNA and the DNA integrity quantified as DIN (*Table 4.8*).

Under the assayed conditions, $AIF_{\Delta 101}$ turned out to be more efficient as a nuclease than CypA on its own, showing a lower amount of remaining intact dsDNA (9% versus 21%) and DIN (7.7 versus 8.1). This is in agreement with the results obtained from the solution nuclease assays, as the activity demonstrated by CypA on its own was estimated to be almost 9 times lower than that of AIF (0.002 vs 0.015 s^{-1}) (*Fig. 4.12A*). However, the CypA:$AIF_{\Delta 101}$ combination hardly showed a slight increase in genomic DNA degradation (DIN 7.0 and 7% of intact dsDNA), possibly due to the negative cooperativity of CypA on DNA binding to $AIF_{\Delta 101}$, but supporting their collaborative effect previously described in chromatinolysis (Cande *et al.*, 2004).

Interestingly, nuclease activities of $AIF_{\Delta 101}$ and CypA induce the generation of ~20 and ~50 kbp DNA fragments respectively, similarly to what is observed during AIF–dependent cell death (Susin *et al.*, 1999; Susin *et al.*, 2000). Moreover, addition of H2AX to $AIF_{\Delta 101}$ has a protective effect on DNA degradation, giving DNA fragments of ~50 kbp. For both plasmid and genomic DNA substrates, the sample that yielded the greatest degradation was that of the $AIF_{\Delta 101}$:CypA:H2AX degradosome (DIN 6.9 for gDNA), which was obtained through simultaneous incubation of the three proteins. The addition of $AIF_{\Delta 101}$ and CypA to a pre–incubated H2AX and gDNA complex led to the lowest DIN (6.6), but it resulted in twice the amount of remaining intact dsDNA (8% versus 4%) when compared to the $AIF_{\Delta 101}$:CypA:H2AX sample.

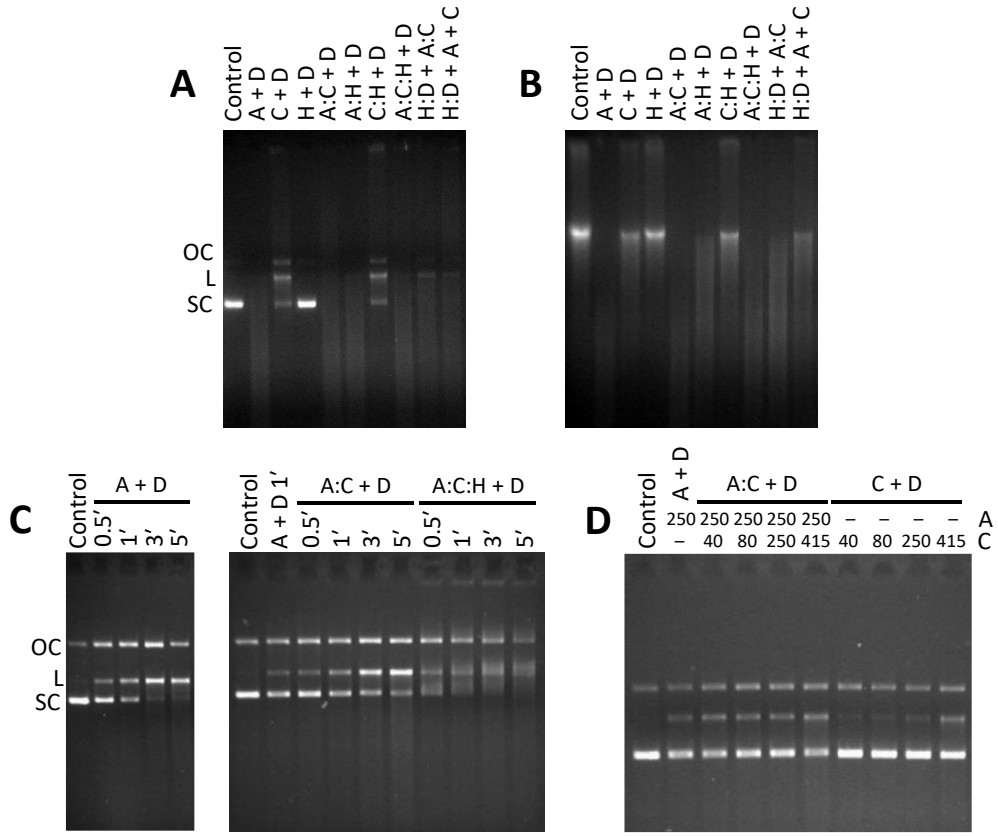

Figure 4.12. Influence of protein partners on AIF nuclease activity. Influence of nuclear physiological partners, CypA and H2AX (in various combinations and equimolecular concentrations), on the $AIF_{\Delta 101}$ nuclease activity against plasmid (A) or genomic (B) DNA substrates. (C) Time course of the influence of CypA and H2AX on the $AIF_{\Delta 101}$ nuclease activity against the plasmid substrate. (D) Concentration-dependence of CypA (ratios 1:0.5, 1:1, 1:3 and 1:5 in micromolar) in $AIF_{\Delta 101}$ nuclease activity. Samples in panels C and D were incubated at 30°C to facilitate visualization of changes. Unless otherwise stated, 250 ng of a double–stranded supercoiled pET–28a(+) plasmid substrate or 500 ng of human gDNA were mixed with 250 ng of purified $AIF_{\Delta 101}$ in 20 mM Tris, pH 8.0 supplemented with 0.1 mM $CaCl_2$ and 1mM $MgCl_2$ and incubated for 1 min at 37 ºC. Protein mixtures were pre–incubated for 15 min at 25 ºC. Control, stands for plasmid or genomic DNA substrate alone. A, C and H, stand for $AIF_{\Delta 101}$, CypA and H2AX, respectively. A^-, stands for plasmid or genomic DNA incubated with $AIF_{\Delta 101}$ in absence of ions (panels A, B). H:D+A:C, stands for H2AX plus DNA and $AIF_{\Delta 101}$ plus CypA being separately pre–incubated and then mixed together. H:D+A+C, stands for H2AX and DNA being first pre–incubated together and subsequently mixed with separate samples of $AIF_{\Delta 101}$ and CypA. OC, L and SC, stand respectively for open circular, linear and supercoiled.

Table 4.8. Nuclease activity of $AIF_{\Delta 101}$ and its variants on gDNA.

Sample	Peak (kbp)	[55– >60 kbp]* (%)	DIN
dsDNA	>60	82	9.5
$AIF_{\Delta 101}$	26	9	7.7
CypA	51	21	8.1
H2AX	>60	52	8.9
$AIF_{\Delta 101}$:CypA	21	7	7.0
$AIF_{\Delta 101}$:H2AX	56	30	8.4
$AIF_{\Delta 101}$:CypA:H2AX	21	4	6.9
$AIF_{\Delta 101}$:CypA + H2AX:dsDNA	25	11	7.2
$AIF_{\Delta 101}$:CypA + H2AX + dsDNA	23	7	7.1
$AIF_{\Delta 101}$ + CypA + H2AX:dsDNA	18	8	6.6

gDNA integrity after nuclease activity assays was analysed using the Genomic DNA ScreenTape assay on the 2200 TapeStation microfluidic platform (Genomic ScreenTape device, Agilent Technologies). Samples were prepared as in the solution nuclease assays (250 ng of protein and 500 ng of gDNA), but were incubated for 5 min at RT. DIN: DNA Integrity Number.

Furthermore, a progressive increase in the time of incubation yielded a proportional increase in DNA degradation (coupled with a greater mobility shift), which was significantly higher for the degradosome (percentage of degraded DNA from 38% to 79% after 5 min) and AIF:CypA complex (7% to 35%) than for AIF on its own (6% to 28%) (*Fig. 4.12C*). Increasing concentrations of CypA in regard to that of AIF were additionally tested (ratios 1:0.5, 1:1, 1:3 and 1:5 in micromolar) at a set time of incubation, leading to a moderate increase in the percentage of degraded DNA (12% at ratio 1:0.5 to 18% at ratio 1:5) for the AIF:CypA complex that was significantly higher than that of AIF alone (10%) and even more so than those of CypA alone at the same concentrations (1% to 6%) (*Fig. 4.12D*).

All these results agree well with the proposed regulation of the chromatinolysis process via DNA–degradosome assembly during programmed necrosis induced by DNA alkylating agents (Artus *et al.*, 2010).

4.2.3.3. Assessment of the degradosome nuclease activity by AFM

The nuclease activity of the degradosome was also visualized by AFM in the presence of divalent cations (*Fig. 4.13 and Table 4.9*).

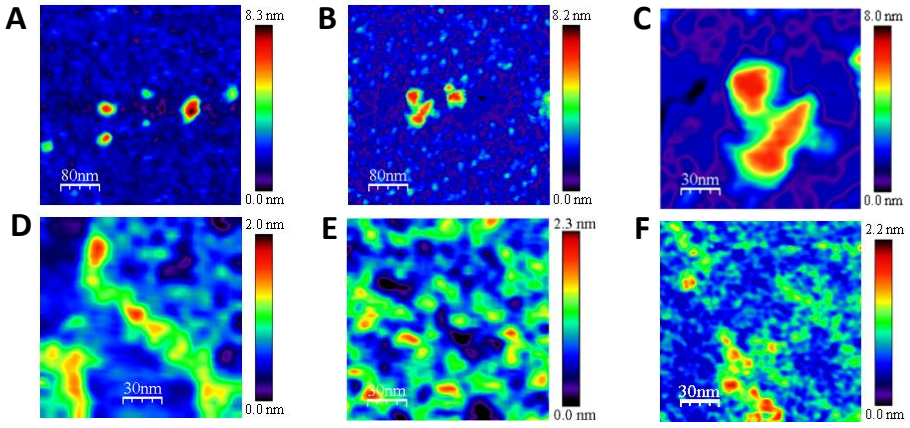

Figure 4.13. AFM topography of assemblies upon formation of the DNA–degradosome complex in the presence of divalent cations. Impact of Ca^{2+} and Mg^{2+} ions on DNA degradation for (A) $AIF_{\Delta 101}$:CypA:dsDNA and (B) $AIF_{\Delta 101}$:CypA:H2AX:dsDNA assemblies. (C) Zoom image of (B) to evaluate the integrity of the hetero–trimers. (D) Linearized dsDNA. (E) DNA fragmented by the nuclease activities of $AIF_{\Delta 101}$ and CypA in presence of Ca^{2+} and Mg^{2+} ions. (F) dsDNA in $AIF_{\Delta 101}$:CypA:H2AX complexes. Scan size 400 nm x 400 nm (A, B) and 150 x 150 nm (C–F). Mixtures of proteins forming the degradosome were prepared as in *Figure 4.2* in the presence of 0.05 ng/µl pET–28a(+) plasmid linearized with *Eco*RI.

Figure 4.13B shows a representative image for $AIF_{\Delta 101}$:CypA:H2AX:dsDNA when incubated with Ca^{2+} and Mg^{2+}. Their presence contributed to overcome the threshold needed by the mica bound complex to degrade dsDNA into very small fragments, as can be observed in different parts of the zoomed images (*Fig. 4.13E, F*). Interestingly, we also observed an equilibrium among open and compact morphologic states of the $AIF_{\Delta 101}$:CypA:H2AX degradosome assemblies. We can conclude that, in the absence of the aforementioned ions, the majority of the hetero–trimers adopt closed forms (*Fig. 4.2F*), which become more compact when bound to dsDNA (*Fig. 4.9F*). However, the presence of ions that favour dsDNA fragmentation induce the observation of more elongated open hetero–trimer conformations in equilibrium with the closed forms (*Fig. 4.13B*). Finally, dsDNA preserved integrity in the absence of nuclease activity (*Fig. 4.13D*), while its fragmentation occurs when activity takes place (*Fig. 4.13E, F*).

Table 4.9. Effect of dsDNA degradation by $AIF_{\Delta 101}$ and CypA, in the presence or absence of H2AX, on the distribution of quaternary organizations visualized by AFM imaging.

Sample mixtures	Monomers (%)	Hetero–Dimers (%)[a]	Hetero–Trimers (%)	Observed features
$AIF_{\Delta 101}$:CypA:dsDNA + Ca^{2+}/Mg^{2+}	53	47	–	DNA binding to protein hetero–dimers. DNA Fragmentation
$AIF_{\Delta 101}$:CypA:H2AX: dsDNA + Ca^{2+}/Mg^{2+}	28	35	37	DNA binding to protein complexes. DNA fragmentation

Assays in PBS pH 7.0. Percentages are referred to the total number of protein molecules. Concentrations for components in the incubation mixtures were 0.5 µM, 5 mM and 0.05 ng/µl for proteins, divalent cations and dsDNA, respectively. Percentage error is within 5–10 %. [a]Values correspond to homo–dimers in samples containing a single protein.

4.2.3.4. Human and mouse AIF share nuclease activity

Purity of the AIF protein samples was confirmed through CN–PAGE, SDS–PAGE followed by Coomassie blue staining (*Fig. 4.14*) and mass spectrometry assays, discarding any adventitious nuclease contamination.

To do so, a purified sample of $AIF_{\Delta 101}$ was separated by high–resolution CN–PAGE in duplicate lanes. One lane was subsequently stained with Coomassie blue (*Fig. 4.14A*) and the corresponding band of $AIF_{\Delta 101}$ was excised from the duplicate lane. The excised band was then incubated with 250 ng of plasmid DNA for 5 min at 37 ºC. Two additional portions of the same lane above and below the $AIF_{\Delta 101}$ band (corresponding to higher and lower molecular weights) were also assayed, as was an additional portion of an empty lane from the same gel. The latter demonstrated a destabilizing effect on dsDNA upon incubation with polyacrylamide, resulting in the apparition of the linear and open circular forms that could be observed in all samples (*Fig. 4.14A*). However, no smearing was apparent in any sample excepting that of the $AIF_{\Delta 101}$ band, confirming that the source of the observed nuclease activity is indeed $AIF_{\Delta 101}$.

Moreover, the AIF nuclease activity was also confirmed with purified mouse AIF (mAIF) using both plasmid and genomic DNA substrates under similar conditions to those for the human protein (*Fig. 4.14B, C*). These assays confirmed that mAIF presents a certain degree of nuclease activity as well, although being significantly less efficient than human AIF. An assessment of different enhancing divalent ions (Ca^{2+}, Mg^{2+} and Mn^{2+}) demonstrated that the nuclease activity of mAIF becomes optimal with 0.1 mM of Mn^{2+} (*Fig. 4.14B*), differing again from human AIF.

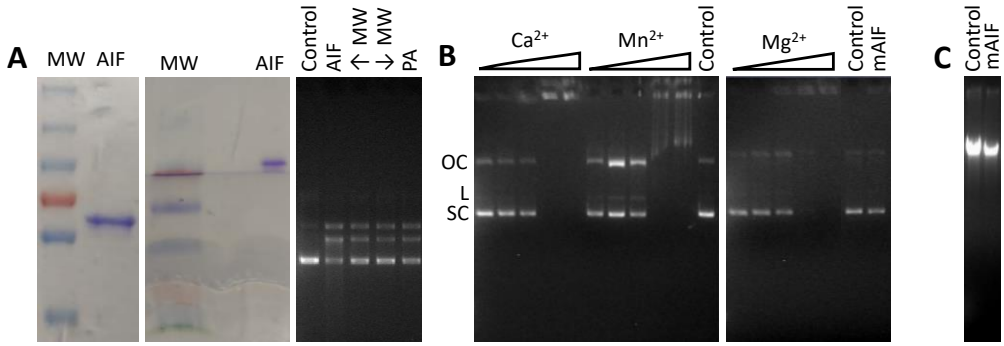

Figure 4.14. Nuclease activity of human and mouse AIFs. (A) SDS–PAGE of $AIF_{\Delta 101}$ after purification to homogeneity (left panel), CN–PAGE pattern of human $AIF_{\Delta 101}$ (AIF, 250 ng) after Coomassie blue staining (middle panel) and nuclease activity of the corresponding excised band of the $AIF_{\Delta 101}$ protein from a CN–PAGE duplicate lane upon mixing with double–stranded supercoiled pET–28a(+) plasmid (250 ng) in 20 mM Tris/HCl, pH 8.0, 0.1 mM $CaCl_2$ and 1mM $MgCl_2$ for 5 minutes at 37ºC (right panel). Portions of gel above or below the AIF band corresponding to higher or lower MWs (lanes ↑ MW and ↓ MW respectively) were similarly incubated with pET–28a(+) and used as negative controls. Additionally, a portion of polyacrylamide gel from a lane without loaded $AIF_{\Delta 101}$ sample was incubated with pET–28a(+) (PA lane). MW, protein molecular weight marker. (B) Effect of different ions expected to promote (Ca^{2+}, Mg^{2+} and Mn^{2+}) or inhibit (K^+ and Na^+) the *in vitro* nuclease activity of mouse $AIF_{\Delta 101}$ (mAIF, 250 ng). Increasing ion concentrations, 0.01, 0.1, 1, 10 or 100 mM, were evaluated while incubating AIF with double–stranded supercoiled pET–28a(+) plasmid (250 ng) in 20 mM Tris/HCl, pH 8.0, for 1 hour at 37ºC. OC, L and SC, stand for open circular, linear and supercoiled. (C) Nuclease activity of $mAIF_{\Delta 101}$ (250 ng) assessed against mouse gDNA (500 ng) after incubating for 4 h at 37 ºC in the presence of 0.1 mM $MnCl_2$. Control stands for either plasmid or genomic DNA substrate. mAIF stands for either plasmid or genomic DNA substrate incubated with mAIF in absence of ions (panel B) or with 0.1 mM $MnCl_2$ (panel C).

4.2.4. Key residues for AIF's nuclease activity

Metal–ion–independent DNases make use of a conserved nucleophile residue to undergo catalysis, by means of an attack on the scissile phosphate of the nucleic acid that is aligned into optimal position by positively–charged side chains nearby (Yang *et al.*, 2011). One of such cases is that of the type IB topoisomerase (TopIB) family, whose active site is made up of two arginine residues, one lysine, one histidine and the nucleophile tyrosine. The DNA backbone is oriented and neutralized by the basic residues, with one conserved arginine hydrogen–bonded to the scissile phosphate and the tyrosine (Yang *et al.*, 2011).

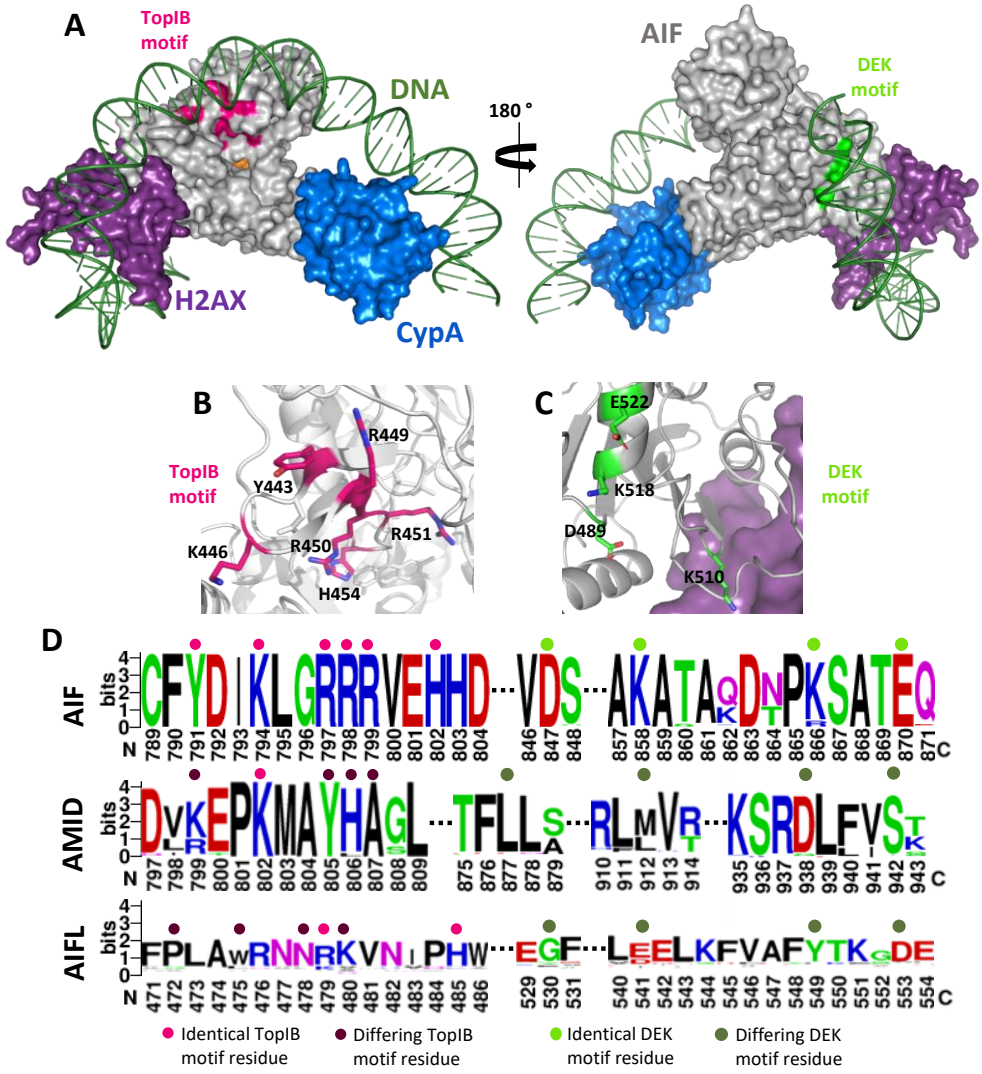

Figure 4.15. Potential nuclease domains in AIF. (A) Model for the binding of dsDNA (green) to the energetically optimized degradosome assembly (colour codes for proteins as in Figure 4.4). The potential nuclease TopIB and DEK motifs appear coloured in magenta and green respectively on the AIF surface. Environment of (B) TopIB and (C) DEK motifs highlighting relevant residues as sticks. (D) Sequence logo (https://weblogo.berkeley.edu/logo.cgi) for the conservation of identified TopIB and DEK motifs in human AIF in sequences of AIF, AIFL and AMID from different organisms. Key residues identical to those in human AIF TopIB and DEK motifs are marked respectively with a pink or green dot on top, while differing residues are marked with darker tones. While the motifs are significantly conserved amongst the AIF family, they do not extend to either the AMID or the AIFL families. AIF motifs, $Yx_2Kx_2RRRx_2H$ and $Dx_9Kx_7Kx_3E$. AMID equivalents, kx_2Kx_2yha and $lx_{33}mx_{23}dx_3s$. AIFL equivalents, $px_2wx_2nRkx_4H$ and $gx_{10}ex_7yx_3d$. Capital letters indicate residues conserved across the different families, lower–case letters stand for those not conserved.

AIF happens to present in its surface a sizeable positively–charged pocket containing a motif that highly resembles that of the TopIB family (residues Y443, K446, R449, R450, R451 and H454) (*Fig. 4.15A, B*). In fact, some of these residues belong to the so–called DNA–crown of AIF, the predicted DNA–binding site (Ye *et al.*, 2002). Following the imaginary line drawn by the residues of the DNA–crown around the protein, another possible nuclease motif, a DEK motif, can be found close to the binding site of H2AX, composed of residues D489, E522 and K510 or K518 (*Fig. 4.15A, C*). DEK motifs are conserved in many nucleases, including the recently identified PARP1–associate nuclease MIF (Kosinski *et al.*, 2005; Yang *et al.*, 2011). Moreover, K510 and K518 residues were already shown to influence the interaction of AIF with dsDNA (Ye *et al.*, 2002).

Noticeably, these putative motifs are fully conserved in AIF sequences (*Fig. 4.15D*), suggesting a common nuclease strategy for DNA degradation within the AIF subfamily. However, they are not conserved in AMID or AIFL, the other two members of the AIF family (Novo *et al.*, 2021). This strongly supports the relevance of these motifs in AIFs and in the different mechanisms during cell death among these three apoptotic effectors.

4.2.4.1. Effect of the $AIF_{\Delta 101}$ TopIB and DEK variants on its nuclease activity

To prove the relevance of the TopIB and DEK motifs in AIF, we generated single–site mutants of all the aforementioned TopIB positions and double–site mutants for the potential DEK motif (namely: D489A/K518A, K518A/E522A and K510A/K518A). All

variants were purified to homogeneity and exhibited similar absorbance and CD spectra to the wild–type (WT), indicating that mutations did not significantly compromise the interaction with the cofactor or folding (*Fig. 4.16*).

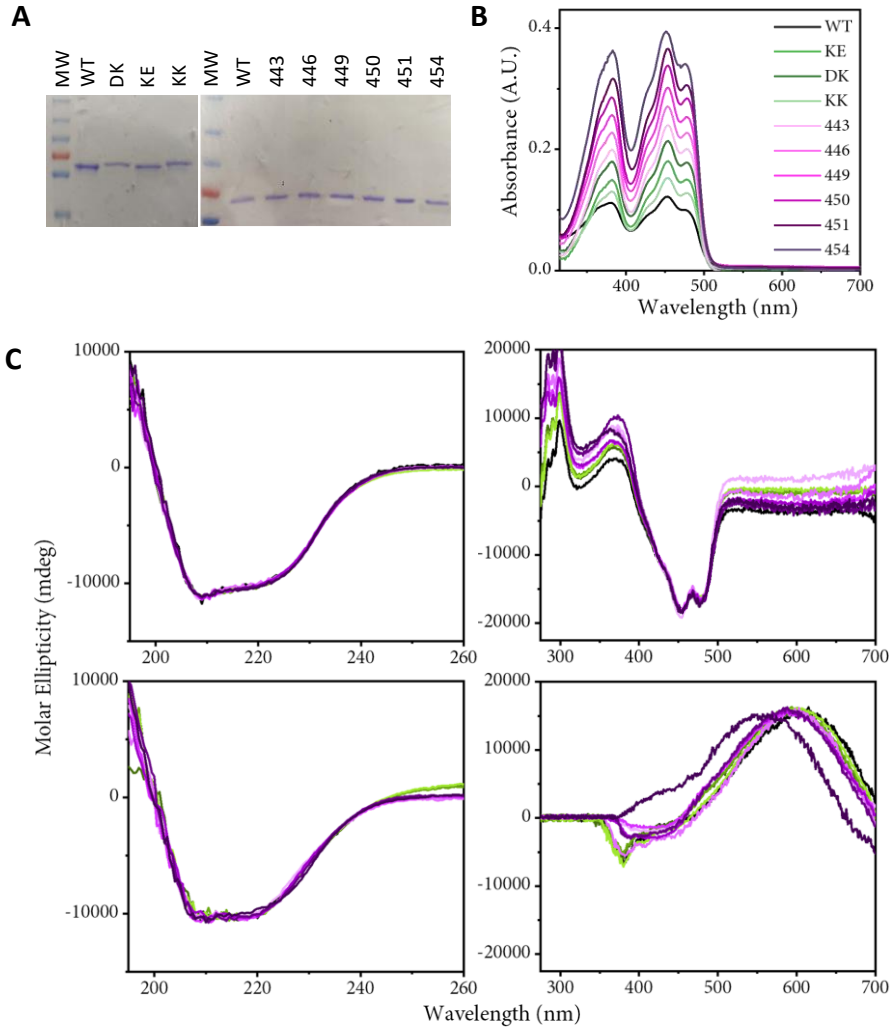

Figure 4.16. SDS–PAGE, visible absorption and CD spectra of the TopIB and DEK variants of $AIF_{\Delta 101}$. (A) SDS–PAGE of WT $AIF_{\Delta 101}$ and variants after purification to homogeneity. (B) Visible absorption spectra of purified WT $AIF_{\Delta 101}$ and variants recorded in 50 mM Kpi, pH 7.4, at 25 °C. Different protein concentrations were employed to facilitate visualization. (C) CD spectra of WT $AIF_{\Delta 101}$ and variants in the far–UV (2 µM samples) and in the near–UV/Vis (20 µM samples) are shown in right and left panels respectively. The assays were performed in the absence (upper) and presence (lower) of 100–fold excess NADH. WT $AIF_{\Delta 101}$ is shown in black, variants D489A/K518A, K518A/E522A and K510A/K518A in increasingly darker shades of

green, and variants Y443A, K446A, R449A, R450A, R451A and H454S in increasingly darker shades of purple. Code for mutated residue in $AIF_{\Delta 101}$ variants in panel A: 443, Y443A; 446, K446A; 449, R449A; 450, R450A; 451, R451A; 454, H454S; DK, D489A/K518A; KE, K518A/E522A; KK, K510A/K518A.

The nuclease activity of said $AIF_{\Delta 101}$ variants was evaluated using both plasmid and human genomic DNA substrates (*Fig. 4.17*). Remarkably, all variants yielded a significant impairment of the nuclease activity of $AIF_{\Delta 101}$, regardless of the substrate, and required at least one hour for the linearizing activity to become apparent (versus less than one minute for the WT protein). In addition, most variants produced a DNA retention effect that was not apparent for the WT under the assayed conditions (*Fig. 4.17*). EMSA assay (*Fig. 4.18*) demonstrated that all variants yielded a considerably higher retention of the DNA substrate compared to the WT (with the sole exception of Y443A, for which it was only slightly greater). Moreover, variants D489A/K518A and K510A/K518A considerably increased affinity for dsDNA (K_d 0.5 vs 2.9 µM for WT) (*Table 4.10*).

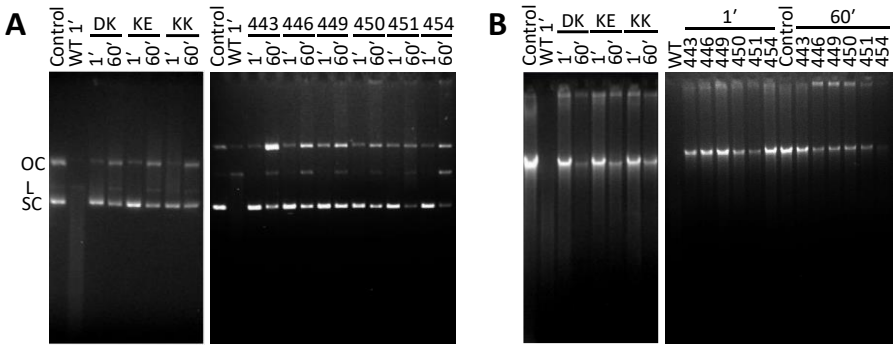

Figure 4.17. Nuclease activity of the $AIF_{\Delta 101}$ TopIB and DEK variants. 250 ng of a double–stranded supercoiled pET–28a(+) plasmid (A) or 500 ng of human gDNA (B) substrates were respectively mixed with 250 ng of the $AIF_{\Delta 101}$ variants in 20 mM Tris, pH 8.0, 0.1 mM $CaCl_2$ and 1mM $MgCl_2$. Samples were incubated for 1 and 60 minutes at 37 ºC. Control, stands for plasmid or genomic DNA substrate alone. OC, L and SC, stand for open circular, linear and supercoiled, respectively. Code for mutated residues in $AIF_{\Delta 101}$ variants: 443, Y443A; 446, K446A; 449, R449A; 450, R450A; 451, R451A; 454, H454S; DK, D489A/K518A; KE, K518A/E522A; KK, K510A/K518A.

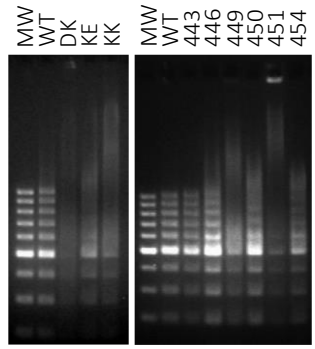

Figure 4.18. Effect of TopIB and DEK mutations on DNA retention. 500 ng of 100 bp DNA ladder, MW, (Thermo Scientific) were incubated with 6 µg of WT $AIF_{\Delta 101}$ or its variants for 30 min in 50 mM Kpi, pH 7.4, at 25 ºC, to assess DNA retention. Code for mutated residues in $AIF_{\Delta 101}$ variants: 443, Y443A; 446, K446A; 449, R449A; 450, R450A; 451, R451A; 454, H454S; DK, D489A/K518A; KE, K518A/E522A; KK, K510A/K518A. Mixtures were separated by electrophoresis in 2 % agarose gel and visualized with ethidium bromide.

Table 4.10. Thermodynamic parameters for the interaction of $AIF_{\Delta 101}$ variants with dsDNA.

$AIF_{\Delta 101}$ variant	Titrating ligand	K_d (µM)	ΔH (kcal/mol)	ΔG (kcal/mol)	$-T\Delta S$ (kcal/mol)
WT	dsDNA	2.9	5.9	–7.3	–13.2
Y443A	dsDNA	3.0	8.4	–7.2	–15.6
K446A	dsDNA	3.0	5.7	–7.3	–13.0
R449A	dsDNA	2.3	5.2	–7.4	–12.6
R450A	dsDNA	2.9	7.4	–7.3	–14.7
R451A	dsDNA	2.0	4.7	–7.5	–12.2
H454A	dsDNA	2.4	6.3	–7.4	–13.6
K510A/K518A	dsDNA	0.5	3.8	–8.3	–12.1
D489A/K518A	dsDNA	0.5	2.5	–8.3	–10.8
K518A/E522A	dsDNA	5.7	10.6	–6.9	–17.5

Values obtained from ITC assays at 15 ºC in 50 mM Kpi, pH 7.4. N is the calculated stoichiometry for binding. The thermodynamic parameters were calculated using well–known relationships: $K_d = (K_a)^{-1}$, $\Delta G = RT.\ln K_d$ and $-T\Delta S = \Delta G - \Delta H$. Errors considered in the measured parameters (± 30% in K_d and $\pm$ 0.4 kcal/mol in ΔH and $-T\Delta S$) were taken larger than the standard deviation between replicates and the numerical error after the fitting analysis.

Regarding the impact of mutations on gDNA integrity (*Table 4.11*), K510A/K518A produced the lowest DIN (6.9), hinting that K510 might not belong to the potential DEK motif of AIF. In comparison, D489A/K518A and K518A/E522A produced much higher DIN values (8.4 and 8.3 respectively) and did not experience a shift in the size of the gDNA peak (>60 kbp for both, versus 42 kbp for K510A/K518A). Consequently, the potential DEK motif of AIF may be made up of residues D489, K518 and E522. On the other hand, all variants of the potential TopIB motif gave rise to significantly high DIN values (>8.7) and no shift in the size of the DNA peak (>60 kbp for all except R451A, whose peak was at 58 kbp). The Y443A, K446A and R449A variants yielded the highest DIN values (>9.6), in agreement with the expected critical roles for these residues during the nucleophilic attack on dsDNA.

Table 4.11. Nuclease activity of $AIF_{\Delta 101}$ and its variants on gDNA.

Sample	Peak (kbp)	[55– >60 kbp]* (%)	DIN
dsDNA	>60	82	9.5
WT	26	9	7.7
Y443A	>60	60	9.6
K446A	>60	60	9.6
R449A	>60	64	9.7
R450A	>60	64	9.5
R451A	58	39	8.7
H454S	>60	41	8.7
D489A/K518A	>60	45	8.4
K518A/E522A	>60	42	8.3
K510A/K518A	42	17	6.9

gDNA integrity after nuclease activity assays analysed using the Genomic DNA ScreenTape assay on the 2200 TapeStation microfluidic platform (Genomic ScreenTape device, Agilent Technologies). Samples were prepared as in the solution nuclease assays (250 ng of protein and 500 ng of gDNA), but were incubated for 5 min at RT. DIN: DNA Integrity Number.

Altogether, these results confirm the existence of TopIB and DEK motifs on AIF, granting the protein the potential ability to *in vivo* degrade dsDNA. Such hypothesis is further supported by the fact that variants at these motifs were inefficient apoptosis sensitizers or unable to induce cell death in cell–free systems as well as in intact transfected cells (Ye *et al.*, 2002).

4.2.4.2. Insights into the molecular mechanism of AIF nuclease activity

Since mutations at the DEK and TopIB motifs do not hinder dsDNA binding, their evidently negative effect on the ability of AIF to degrade genomic DNA (*Table 4.11*) must be caused by a direct alteration of the nuclease catalytic process. To better illustrate this possibility at the molecular level, the relative orientations of the residues at the DEK and TopIB motifs regarding dsDNA were evaluated (*Fig. 4.19*).

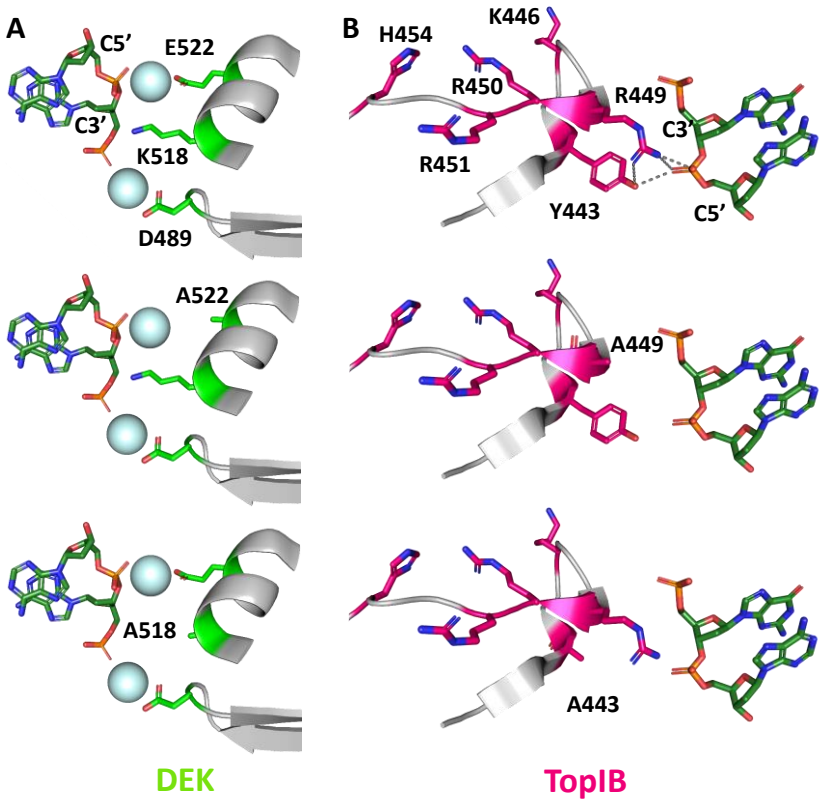

Figure 4.19. Molecular simulation of the impact of mutations at the DEK and TopIB motifs of AIF on its interplay with DNA. (A) Model for a potential organization of the AIF DEK motif and the target DNA during DEK nuclease activity. The top panel shows the WT model, while middle and bottom panels represent the potential impact of the E522A and K518A mutations. Removal of any of the three side–chains of the DEK motif will negatively impact the structural DEK–DNA–divalent cation organization. (B) Model for a potential organization of the AIF TopIB motif and the target DNA during TopIB nuclease activity. The top panel shows the WT model, while medium and bottom panels represent potential impact of the R449A and Y443A mutations. Removal of these side–chains will prevent achievement of the catalytically–competent geometry expected for TopIB nuclease activity. Residues of the DEK and TopIB

motifs are highlighted in sticks with carbons respectively coloured in green and magenta. Target nucleotides from the docked DNA chain to each motif are in sticks CPK–coloured with carbons in dark green. The DEK motif shows in pale blue spheres a potential position for the two divalent cations (placed as observed in other DEK motifs to compensate the acidic residues), while in the TopIB the top panel highlights as dashed lines the proposed interplay among R449, Y443 and the target DNA phosphate occurring during nuclease activity. dsDNA:AIF models are shown as produced by the HADDOCK 2.4 web server using dsDNA molecules of 15 to 20 bp as ligands and the conformation of AIF in the energetically optimized degradosome model as the receptor (*Figs. 4.3, 4.4*).

In AIF, the cation–dependent DEK motif appears to localise between a β-hairpin and the α-helix that is directly connected to it (*Fig. 4.19A*). This is not surprising, as said motif has been shown to adapt to diverse surrounding tertiary structures in different nuclease activities by being diverse and permissive in its primary sequence (Yang, 2011). The negatively–charged residues within the motif contribute to stabilize the divalent cations that bind the target dsDNA, while the third residue, a lysine in AIF, usually establishes a H–bond to the dsDNA through a nucleophilic water that is attributed to aid in the recognition of the target (Lee *et al*., 2005). As shown in figure 4.19A, Ala replacements of any of these three residues undoubtedly lead to an alteration of either the nuclease catalytic step and/or the achievement of the competent geometry for said reaction to take place.

Regarding the TopIB motif, the expected arginine, lysine, histidine and nucleophilic tyrosine residues are present in AIF, with the basic residues oriented to neutralize the DNA backbone as reported before (Davies *et al*., 2006; Yakovleva *et al*., 2008). The model shows that highly conserved R449 can H–bond both the scissile DNA phosphate and the postulated nucleophile Y443, while the other charged residues might contribute as general acids to protonate the 5' leaving group of the DNA. Again, as shown in figure 4.19B, Ala replacements at any of these positions would lead to the interruption of the sequential events proposed for the TopIB motif nuclease activity.

Furthermore, mutant models were directly produced on the WT AIF_{eo} molecular model to evaluate the impact of the mutations on the protein ESP. As shown in figure 4.20, replacements to Ala produced very minor changes in the overall ESP, with subtle changes being only observed for some of the variants at the position of the introduced mutation. Considering that the binding of dsDNA to AIF is non-specific and contributed by several residues and regions on the protein surface, this agrees with

none of the mutations preventing dsDNA binding and with some even favouring it (*Table 4.10*).

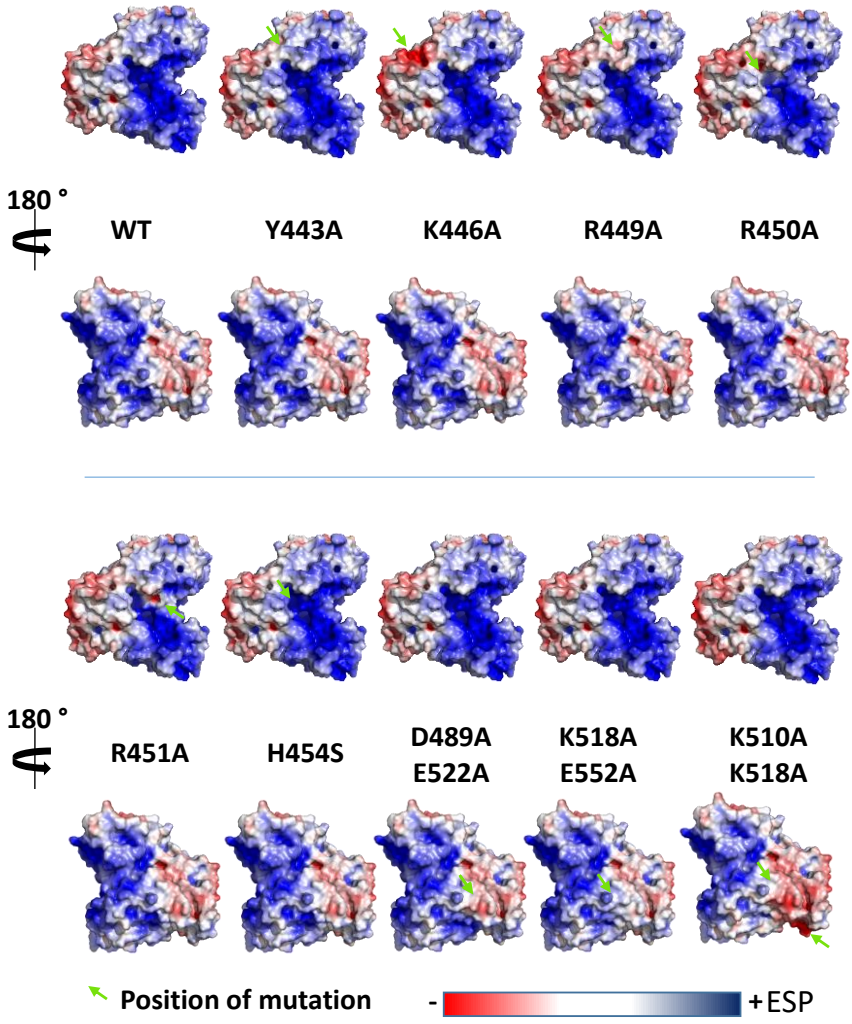

Figure 4.20. Impact of mutations at the TopIB and DEK motifs on the AIF electrostatic surface potential. ESP for each variant was calculated at pH 7.0 using the APBS-PDB2PQR software suite (https://www.poissonboltzmann.org/) and then plotted using PyMOL. Position of mutation(s) for each variant is indicated by a green arrow.

4.2.5. Concluding remarks and unresolved issues

Since AIF was discovered as a mitochondrial flavoprotein able to induce chromatin condensation in purified nuclei (Susin *et al.*, 1999), a tremendous number of studies have identified it as one of the main effectors of caspase–independent cell death. However, the exact molecular mechanism through which AIF provokes chromatin remodelling, large–scale DNA fragmentation and DNA loss remains unknown. Moreover, AIF's contribution to PCD and its interactions with pro–death partner executers appear to be highly dependent on organism, cell type and kind of apoptotic stimulus (Cande *et al.*, 2002; Joza *et al.*, 2001; Joza *et al.*, 2009; Modjtahedi *et al.*, 2006; Susin *et al.*, 2000).

In this chapter, we have delved into the mechanism of AIF's pro–apoptotic action. The interaction of AIF with H2AX and CypA as a tool to regulate chromatinolysis was previously described in programmed necrosis activated by alkylating DNA agents (Artus *et al.*, 2010). Here, we evidence for the first time the assembly of this degradosome complex at the molecular level. Moreover, we identify cooperative effects between AIF and H2AX, as well as among the three protein components of the degradosome, to promote dsDNA binding and degradation. These *in vitro* results agree with the required synchronized presence of these three proteins in the nucleus to provoke DNA degradation (Artus *et al.*, 2010). Alternatively, the nuclear AIF:CypA co–translocation and cooperation was proposed in damaged neurons after hypoxia–ischemia to promote DNA degradation (Cande *et al.*, 2004; Zhu *et al.*, 2007). This model is also compatible with a high plasticity of AIF for interplaying with the different degradosome components, being the interaction with CypA the most favourable and the only one appearing specific.

Interestingly, in the above caspase–independent PCD models, as well as in others described in the literature, the DNA–degrading capacity of AIF is associated with the recruitment of nucleases, such as CypA, MIF or Endonuclease G (Cande *et al.*, 2004; Wang *et al.*, 2002; Wang *et al.*, 2016). However, the depletion of these nucleases resulted in lower levels of chromatinolysis and cell death induced by MNNG, while the depletion of AIF was an absolute requirement to block caspase–independent cell death (Delavallée *et al.*, 2020). Our work breaks away from this paradigm, providing compelling evidence that $AIF_{\Delta 101}$ is endowed with both endo– and exonuclease activities. Thus, here it is shown that AIF can act as an efficient nuclease to cleave gDNA into large fragments by itself or in cooperation with CypA. Moreover, mutation

of key residues in its TopIB and DEK nuclease motifs markedly reduced its *in vitro* nuclease activity and even prevented cell death (Ye *et al.*, 2002). Therefore, beyond being a platform protein or recruitment factor, AIF also behaves as an apoptotic nuclease. These findings open trails for further researches focused on the *in vivo* involvement of AIF's nuclease activity in dying cells during apoptosis, and on how it might modulate or coordinate to degrade chromosomal DNA in mammalian systems. This knowledge will be key to develop novel therapy strategies to treat or prevent diseases associated with the aberrant behaviour of AIF.

5. A Portray of Two Recently–Discovered Pathological Mutations of AIF

Tipping the balance between life and death

The PhD candidate contributed by performing the following:

- Production and purification of wildtype $AIF_{\Delta 77}$, $AIF_{\Delta 101}$ and its variants
- Conservation and structural analysis
- Spectroscopic characterization
- Size exclusion chromatography and crosslinking experiments
- Pre–steady and steady state kinetics measurements
- Reoxidation assays
- Midpoint reduction potential assays
- Thermal stability assays
- Isothermal titration calorimetry measurements

ABSTRACT

AIF is a moonlighting flavoenzyme that renders an essential role in the bioenergetics and redox metabolism of mitochondria in healthy cells, but which may also trigger caspase–independent cell death upon pro–apoptotic stimuli. AIF dimerizes after reduction of its FAD cofactor by the NADH coenzyme, prompting the formation of a remarkably stable $FADH^{-}$:NAD^{+} CTC. The monomer–dimer equilibrium that is hence established can be envisaged as a sensor of the mitochondrial redox state in terms of the NADH/NAD^{+} levels, being further arbitrated by the allosteric binding of a second non–catalytic NADH molecule. Defects in AIF give rise to major dysfunctions in oxidative phosphorylation, resulting in human pathogenic disorders coursing with severe neurodegeneration amongst other considerable symptoms. In this chapter, we have performed the biophysical characterization of two variants recently identified and related to disease: Met340Thr and Thr141Ile, localized in the protein NADH–dependent and FAD–dependent domains respectively. In order to elucidate their participation on the reported pathological phenotypes, we have evaluated the impact of these replacements on NADH oxidase activity, CTC stability, overall protein stability and interaction with key biological partners.

RESUMEN

AIF es una flavoenzima multifunción que presenta un papel esencial en la bioenergética y el metabolismo redox de las mitocondrias en células sanas, pero que puede también desencadenar muerte celular independente de caspasas ante estímulos pro–apoptóticos. AIF dimeriza tras la reducción de su cofactor FAD por la coenzima NADH, provocando la formación de un CTC $FADH^{-}$:NAD^{+} extraordinariamente estable. El equilibrio monómero–dímero que se establece de esta forma puede ser concebido como un sensor del estado redox mitocondrial en término de los niveles de NADH/NAD^{+}, siendo además arbitrado por la unión alostérica de una segunda molécula no catalítica de NADH. Defectos en AIF dan lugar a disfunciones mayores en la fosforilación oxidativa, resultando en desórdenes patogénicos humanos que cursan con neurodegeneración severa entre otros síntomas considerables. En este capítulo, hemos llevado a cabo la caracterización biofísica de dos variantes identificadas recientemente y relacionadas con la enfermedad: Met340Thr y Thr141Ile, localizadas en los dominios proteicos dependiente de NADH y dependiente de FAD respectivamente. Para poder elucidar su participación en los fenotipos patológicos reportados, hemos evaluado el impacto de estas sustituciones en la actividad NADH oxidasa, la estabilidad del CTC, la estabilidad general de la proteína y la interacción con parejas biológicas clave.

5.1. INTRODUCTION

AIF is a moonlighting FAD–dependent enzyme that exerts an essential role in the bioenergetics and redox metabolism of mitochondria in healthy cells, but which may just as well trigger caspase–independent cell death under pathological conditions (chapter 4, Novo *et al.*, 2023; Susin *et al.*, 1999). Upon pro–apoptotic stimuli, AIF can be released from the mitochondria and subsequently translocated to the nucleus, where it promotes large–scale DNA fragmentation and chromatin condensation (Artus *et al.*, 2010; Baritaud *et al.*, 2010; Cabon *et al*., 2012) through the formation of the AIF:CypA:H2AX degradosome complex, as well as by itself (chapter 4, Novo *et al.*, 2023).

Otherwise, the mature mitochondrial form of AIF resides in the IMS, anchored to the MIM by means of its N–terminal MLS. As a flavoenzyme, AIF presents a FAD cofactor that may be reduced by the NADH coenzyme, prompting the formation of a remarkably stable $FADH^{-}$:NAD^{+} CTC and the dimerization of the protein (Ferreira *et al*., 2014). The monomer–dimer equilibrium that is hence established has been envisaged as a sensor of the mitochondrial redox state in terms of the NADH/NAD^{+} levels, being further arbitrated by the allosteric binding of a second non–catalytic NADH molecule (Ferreira *et al*., 2014). Furthermore, AIF aids the mitochondrial import of CHCHD4 and its adequate localization in the IMS, indirectly limiting in turn the import and assembly of some of the subunits that conform the respiratory complexes of the ETC (Delavallée *et al*., 2020; Hangen *et al.*, 2015; Modjtahedi *et al*., 2015; Salscheider *et al.*, 2022). Because of these pro–life functions, defects in AIF give rise to major dysfunctions in OXPHOS (secondary to the deficiency of CHCHD4) that result in severe human pathogenic disorders (Meyer *et al.*, 2015; Modjtahedi *et al.*, 2016). The unspecific nature and significant variability of symptoms makes diagnosis of AIF–related disorders noticeably challenging.

As has been stated before, AIF plays a crucial part in the bioenergetics and redox metabolism of mitochondria in general; but it also happens to be vastly expressed in hairy cells and spiral ganglion within the inner ear, which envisages a more specific role in maintaining the normal function of the auditory nerve (Zong *et al.*, 2015). Therefore, most afflicted patients of AIF deficiency demonstrate either mitochondrial encephalomyopathies of variable severity and onset (typically severe and neonatal) or sensorineural hearing loss and auditory neuropathy, with other unique presentations

including motor neuron disease, skeletal dysplasia and colour blindness (Bogdanova-Mihaylova *et al.*, 2019; Heimer *et al.*, 2018).

A symptom that occasionally appears in intermediate severity phenotypes, although it is not inherent to all AIF-related disorders, is cerebellar ataxia. This symptom can be associated with other diverse and unspecific manifestations that are suggestive of OXPHOS dysfunction (such as hearing loss, neuropathy or external ophthalmoplegia) but it is regretfully not determining (Heimer *et al.*, 2018). However, its appearance is not arbitrary and can be easily explained by the existence of the harlequin mouse (Klein *et al.*, 2002). This well-known model of cerebellar and retinal neuron degeneration presents an intronic mutation in its AIF homologue that causes an 80% loss of protein expression, resulting in a heightened susceptibility to exogenous and endogenous peroxide-mediated apoptosis. Overexpression of AIF can inhibit this oxidative stress-mediated neurodegeneration, reinforcing its crucial role as a free radical scavenger.

Recently, two distinct pathogenic mutations of AIF coursing with progressive ataxia, brain atrophy and auditory neuropathy have been identified: Thr141Ile (nucleotide alteration c.422C>T), a variant found within the FAD-binding domain, and Met340Thr (c.1019T>C), a rare variant that resides in the NADH-binding domain (Heimer *et al.*, 2018). The latter could not be found at even minimal allele frequencies in large genome databases (Bogdanova-Mihaylova *et al.*, 2019), reinstating its pathogenic capability. In both cases, treatment of patients with riboflavin gave rise to a discrete improvement of symptoms (Heimer *et al.*, 2018), highlighting the therapeutical relevance of understanding the molecular basis for this disorder.

In this chapter, we present the biophysical, biochemical and structural characterization of disease-related mutations T141I and M340T of AIF. In order to elucidate their participation on the reported pathological phenotypes, we have thoroughly evaluated the impact of these mutations on NADH oxidase activity, CTC stabilization, overall protein stability and interaction with key biological partners.

5.2. Results and Discussion

5.2.1. Sequence conservation and structural analysis

An initial evaluation of the sequence conservation of the T141 and M340 residues in AIF was performed with the ConSurf server (Ashkenazy *et al*., 2016), demonstrating that both are not only significantly conserved in themselves but also happen to reside within remarkably–conserved clusters (*Fig. 5.1*). T141 localises in the protein core and is predicted by the server to be structurally crucial, whereas M340 is exposed to the surface and may play a functional role of significant calibre.

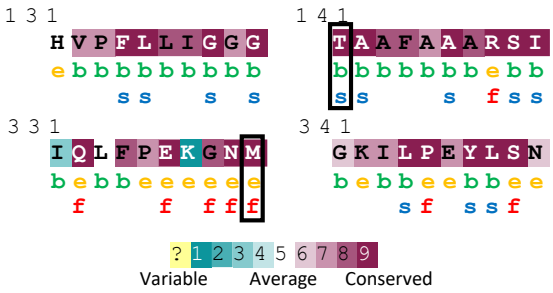

Figure 5.1. Sequence conservation of residues T141 and M340. (A) Sequence conservation scores of *H. sapiens* AIF were calculated by the ConSurf server (https://consurf.tau.ac.il) and represented in the environment of the pertaining residues, labelled with respect to their predicted location ("b", buried; or "e", exposed) and relevance ("s", key structural residue; or "f", key functional residue). Residues are highlighted according to their conservation score from deep teal, less conserved, to deep maroon, most conserved.

These estimations, however, are provided by the ConSurf server based solely on their conservation score, and may hence not be sufficiently substantiated. Consequently, molecular visualization of AIF's crystal structures was performed to further evaluate the significance of residues T141 and M340 (*Figs. 5.2–5.4*). Indeed, a potentially critical pathogenic effect can be envisaged for either variant, as both residues are found in very close proximity to the enzyme's active site and may thus easily alter its conformation and/or properties once replaced.

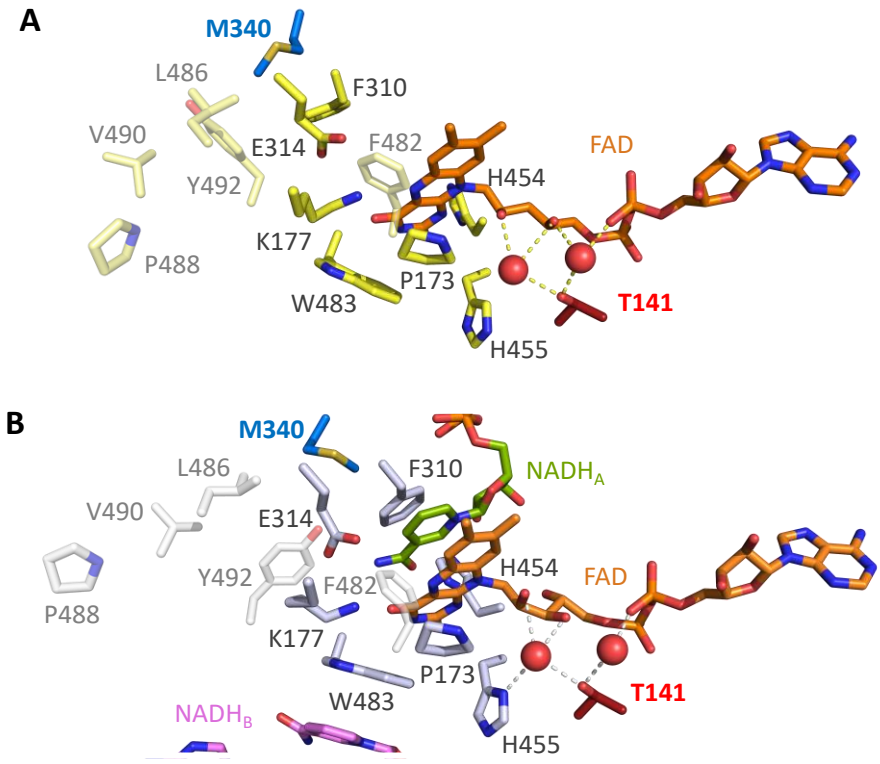

Figure 5.2. Overall structural environment of residues T141 and M340. Active site of (A) AIF_{ox} or (B) AIF_{rd}:2NADH (PDB 4BV6 and 4BUR respectively). All residues are shown as sticks CPK-coloured in yellow for panel A or in white for panel B, excepting the pathogenic residues T141 and M340 which are coloured in red and blue respectively in both panels. The cofactor and coenzymes are labelled and represented as sticks CPK coloured in orange for the FAD, in green for $NADH_A$ and in violet for $NADH_B$. Residues T141 and M340 are labelled in red and blue respectively, key residues of the catalytic site in black, and other relevant residues in a lighter shade with 40% of transparency.

On the one hand, residue T141 is found within the FAD-binding domain of the protein and specifically belongs to an α-helix that is directly adjacent to the α-helix that contains catalytic histidine H454 (*Fig. 5.3*). This histidine residue plays a decisive role in the dimerization process of the protein, with changes in its environment potentially hindering monomer-monomer interactions during dimer stabilization (Ferreira *et al.*, 2014; Villanueva *et al.*, 2015). Indeed, a rough simulation of the T141I replacement in PyMOL leads to a considerable impact in the conformation of several of AIF's key active site residues, including the aforementioned histidine H454 and proline P173 to a greater extent, and lysine K177 and tryptophan W483 in a moderate

manner. Previous work in our group confirmed that residues P173 and K177 are crucial for the regulation of AIF's reductase activity, severely affecting its affinity for the NADH coenzyme as well as the retention and adequate conformation of the FAD cofactor (Villanueva *et al.*, 2015). W483 is also expected to play a critical role in the environment of the active site, and will be characterized in depth in the following chapter. Furthermore, the T141 residue appears to be involved in a network of H-bonds that aids the stabilization of the ribityl pyrophosphate moiety of the FAD cofactor, potentially interacting with two water molecules close to the active site (*Fig. 5.3*).

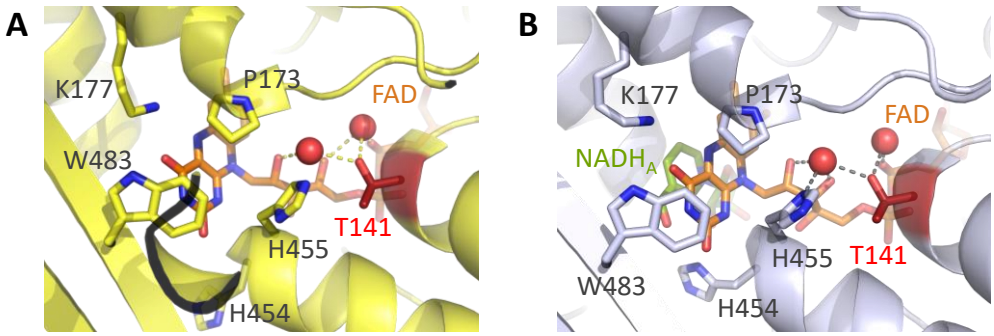

Figure 5.3. Interaction network of residue T141. In-depth visualization of the key interactions of residue T141 with nearby residues and/or other molecules in the oxidized (left panel) or reduced (right panel) structure of AIF (PDB 4BV6 and 4BUR respectively). Images were generated as in figure 5.2, excepting the representation of the protein backbone as cartoon.

On the other hand, residue M340 localises in the NADH-binding domain of the protein, specifically within a disordered loop in the outer surface that may potentially modulate the conformation of the catalytic NADH pocket (*Fig. 5.4*). Indeed, other relevant pathogenic variants (namely G338E and L344F) have also been found in this same loop, coursing with relatively similar phenotypes (COXPD6 and DFNX5, respectively) (Diodato *et al.*, 2016; Sevrioukova, 2016; Zong *et al.*, 2015). The M340T replacement, as has been observed for variant G338E, may significantly alter the electrostatic potential of the NADH-binding channel, hindering the interaction between the protein and the coenzyme (Sevrioukova, 2016). Additionally, the unfolding of the regulatory C-loop (aa 509-560) upon reduction of the protein may also be indirectly affected by these replacements (Diodato *et al.*, 2016; Sevrioukova, 2016). The loop in which G338, M340 and L344 reside is in direct contact with the central β-sheet (aa 481-496), which is in turn in close proximity to the

aforementioned C–loop (*Fig. 5.4A, B*). In fact, the conformation of residues F482, L486, P488, V490 and Y492 in the environment of M340 experiences changes when comparing the oxidized and reduced states of the protein, in the form of a slight retraction of the central β–sheet from the active site when the CTC is formed (*Fig. 5.4C, D*).

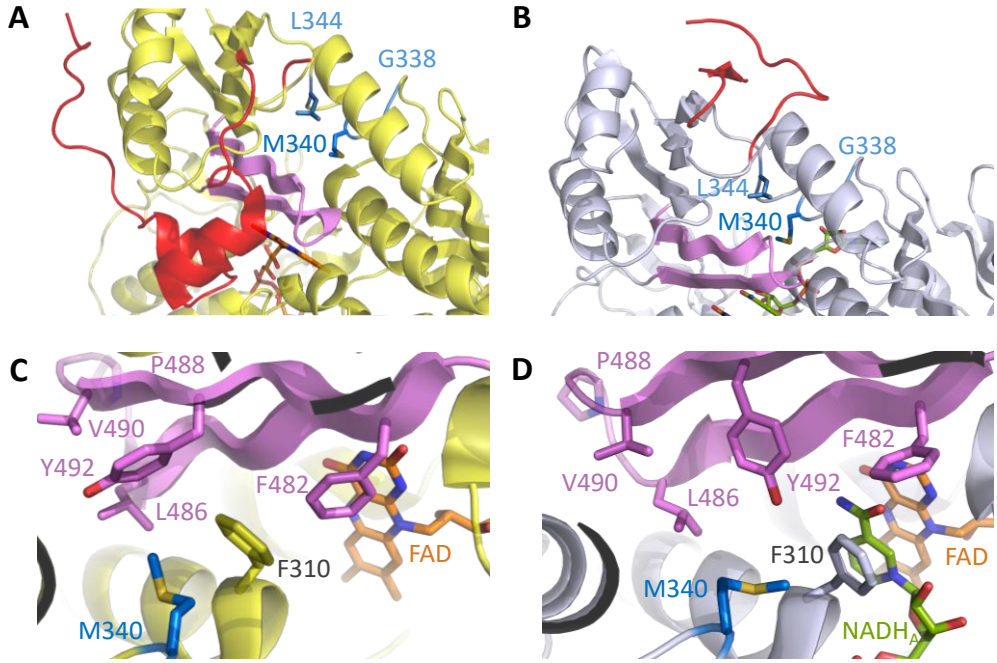

Figure 5.4. Interaction network of residue M340. Gross (A, B) and in–depth (C, D) visualization of the key interactions of residue M340 with nearby residues in the oxidized (left panels) or reduced (right panels) structure of AIF (PDB 4BV6 and 4BUR respectively). Images were generated as in figure 5.2, excepting the representation of the protein backbone as cartoon, and the CPK–colouring of the C–loop and the central β–sheet in red and violet respectively.

Furthermore, residue M340 is able to interact directly with F310, a key active site residue that plays a critical role in the binding and stabilization of the $NADH_A$ molecule through the stacking of its nicotinamide moiety (*Fig. 5.4C, D*) (Villanueva *et al.*, 2015). Consequently, the M340T variant might alter this interaction, potentially modulating the HT process as well as the stabilization of the CTC.

5.2.2. Spectroscopic properties

5.2.2.1. UV/Visible absorption spectra

UV/Visible absorption spectra of the T141I and M340T AIF_{ox} variants were recorded once purified to homogeneity to ascertain that the flavin was correctly incorporated and in the oxidized state. Minor differences could already be noted in WT AIF between its soluble mitochondrial (Δ77) and apoptotic (Δ101) forms (*Fig. 5.5*). A_{280}/A_{452} ratios were respectively 6.9 and 8.5, demonstrating that the apoptotic form might have a marginally diminished holoenzyme population. The distinctive flavin bands I and II at 452 and 380 nm could be clearly distinguished in both forms, as well as the shoulder at 480 nm, with A_{380}/A_{452} ratios of 0.8 and 0.9 respectively and A_{452}/A_{480} ratios of 1.2 (similarly to that previously reported for $AIF_{\Delta 101}$ (Villanueva *et al*., 2015)).

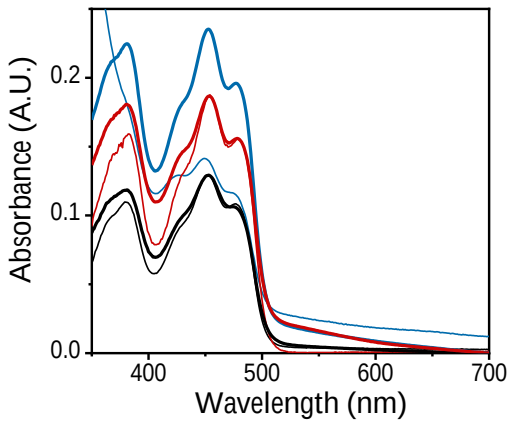

Figure 5.5. UV/Vis absorption spectra of WT AIF and the T141I and M340T variants in their mitochondrial and apoptotic forms. Bold lines represent the spectra of the apoptotic forms, thin lines represent that of the mitochondrial forms. WT data is shown in black, T141I in red and M340T in blue. Measurements were performed at different protein concentrations (WT ~10 µM, T141I ~15 µM and M340T ~20 µM) to facilitate visualization of the figure, in 50 mM Kpi buffer, pH 7.4, at 25 °C. $M340T_{\Delta 77}$ potentially results in a grave alteration of the active site which becomes apparent through its considerably altered flavin spectrum, yielding a significantly lower signal around the 450 nm range.

The T141I replacement yielded analogous spectra to that of the WT protein, both in its mitochondrial and apoptotic forms (*Fig. 5.5*). A_{280}/A_{452} ratios were practically native (7.8 and 8.9 for each form), as were the A_{452}/A_{480} ratios of ~1.2. The only remarkable difference was a slight decrease in the A_{380}/A_{452} ratio of $T141I_{\Delta 77}$ (0.8 vs 1.0 for the

mitochondrial form) which, coupled to an increase in intensity in the 500–700 nm range, could hint towards a certain degree of modulation in the flavin environment.

Conversely, the mitochondrial and apoptotic forms of the M340T substitution differed considerably among themselves. Similar to the T141I variant, M340T$_{\Delta 101}$ presented an almost native spectrum with A_{280}/A_{452}, A_{380}/A_{452} and A_{452}/A_{480} ratios of 8.0, 1.0 and 1.2 respectively. In contraposition, the spectrum of M340T$_{\Delta 77}$ demonstrated a grave alteration of the cofactor conformation and/or state, with an outstanding A_{280}/A_{452} ratio of 25.5 (similar to that previously reported for other unstable AIF variants, Villanueva *et al*., 2015) and a A_{380}/A_{452} ratio of 1.3 (the A_{452}/A_{480} ratio remained surprisingly unchanged). Furthermore, both the flavin bands I and II presented remarkably diminished intensities and the sample colour after purification was observed to be moderately green. Overnight incubation with oxidating compounds (specifically, potassium ferrocyanide) did not result in the recovery of the intensity at the flavin bands, demonstrating that the protein could not achieve or maintain a native oxidised conformation.

5.2.2.2. Far–UV and near–UV/Vis CD spectra

Almost identical far–UV CD spectra were observed for both variants, independently of their form, in the oxidized state when compared to the WT, portraying minima at ~208 and ~222 nm typical of a high α–helix content (*Fig. 5.6A*). Upon incubation with NADH, a decrease in the relative intensity of the 208 nm minimum could be observed (*Fig. 5.6B*), seconding that secondary structure content had not been significantly affected by either mutation.

Near–UV/Vis CD spectra of the T141I replacement, as well as of M340T$_{\Delta 101}$, were analogous to that of the WT. Characteristic maxima (~300 nm and ~365 nm) and minima (~453 and 477 nm) were consistent in the oxidized state, as were the changes expected after FAD reduction and CTC stabilization (lack of signal at 300 nm and in the 350–500 nm range, and broad bands at ~600 nm). The only exception was the appearance of a minimum at ~400 nm in WT$_{\Delta 101}$, which was almost non–existent in both apoptotic variants and slightly shifted in their mitochondrial form. Noticeably, such a minimum has also been reported to disappear in pathogenic variants R201, G308E and E493V in their apoptotic forms (Villanueva *et al*., 2019).

Conversely, near–UV/Vis CD spectra (*Fig. 5.6C, D*) displayed large spectral perturbations in the M340T$_{\Delta 77}$ variant in both states, hinting to a significant degree of

structural alteration in the isoalloxazine ring environment and a potentially hindered CTC. The M340T replacement, that exchanges a medium-sized hydrophobic residue with a smaller, polar one, potentially results in a significant loss of flexibility and hydrophobicity in said position that may easily abolish the ability of residue 340 to stack with neighbour F310 (*Fig. 5.4D*). In losing this interaction, F310 would gain freedom of movement and hence may experience a greater difficulty in reaching the optimal conformation to adequately stack the nicotinamide ring of the NADH coenzyme, ultimately causing a destabilization of the CTC. The interaction with other relevant active site residues may further alter the conformation of the FAD cofactor, leading to a higher solvent exposure and/or looser stacking and, subsequently, to the observed perturbations in both absorbance and CD spectra in the absence of NADH.

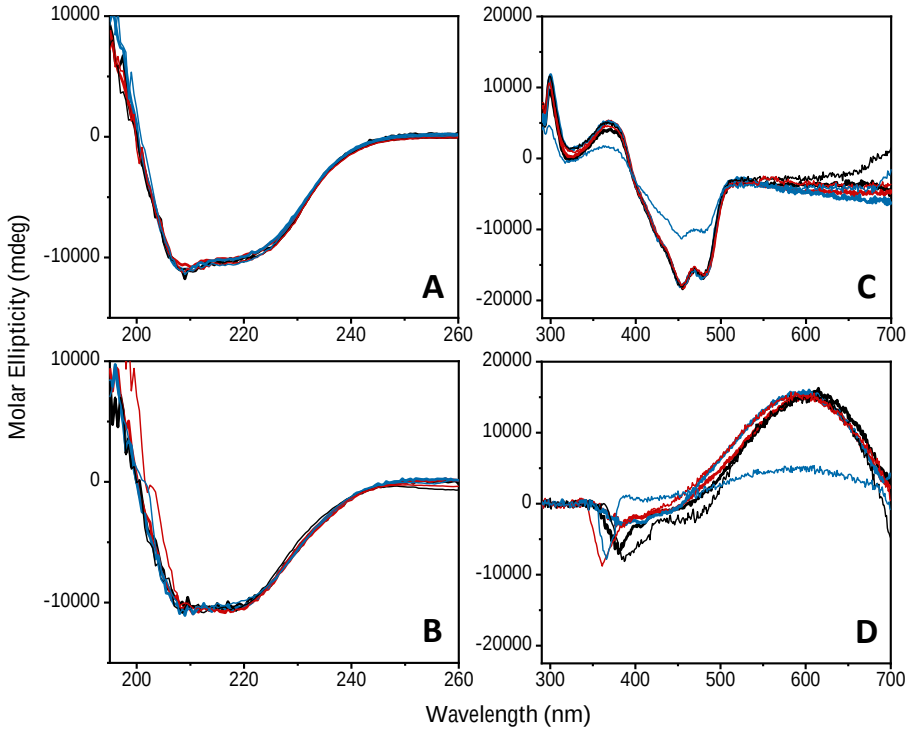

Figure 5.6. CD spectra of WT AIF and the T141I and M340T variants in their mitochondrial and apoptotic forms. Far-UV (A, B) and near-UV/Vis (C, D) CD spectra of the oxidized (upper panels) and reduced (lower panels) states of the proteins were recorded at 25 °C in 50 mM Kpi buffer, pH 7.4, at a final ionic strength of 150 mM. To generate the reduced form, 100-fold excess of NADH was added to the sample prior to the measurement. Spectra are represented as in figure 5.5. Spectra were recorded at protein concentrations of 2 µM and 20 µM for the far-UV and near-UV/Vis CD respectively.

5.2.2.3. Mid–point reduction potential

In order to further evaluate the impact of the T141I and M340T replacements on the environment of the FAD cofactor, an assessment of the flavin's redox potential was carried out with the xanthine oxidase method. WT $AIF_{\Delta 77}$ and $AIF_{\Delta 101}$ yielded E_m values of –377 ± 9 mV and –345 ± 2 mV respectively, both in range of that previously reported for mouse AIF (–353 mV) (Sevrioukova, 2016). Surprisingly, both of the M340T variant forms appeared to maintain an almost native FAD environment, with E_m values of ~-369 mV (ΔE_m = +8 mV) and ~-341 mV (ΔE_m = +4 mV) despite the significantly–shifted CD spectra that had been observed in the mitochondrial form. As residue 340 does not belong to the FAD–binding domain and only indirectly influences the active site from the NADH side, it is possible that the M340T replacement does not affect the cofactor's ability to accept or donate electrons under the assayed conditions, even though it clearly impacts its environment otherwise.

In contrast, the T141I $AIF_{\Delta 77}$ and $AIF_{\Delta 101}$ variant forms each displayed E_m values of ~–286 mV (ΔE_m = +91 mV) and ~-281 mV (ΔE_m = +64 mV), unveiling a significant impact on the environment of the isoalloxazine ring that had not been apparent in prior assays. The T141I replacement, which does take place in the FAD–binding domain, potentially obliterates one or both of the water bridges that are directly established in the WT protein between the side chain of the threonine residue, H455 and the ribityl pyrophosphate moiety of the cofactor (*Fig. 5.3*). The loss of these interactions could result in a considerably altered anchoring of the FAD molecule, somehow leading to a significant increase in its natively–subsided ability to accept electrons from the NADH coenzyme (E_m = –350 mV, Sevrioukova, 2016).

5.2.3. Quaternary assemblies

5.2.3.1. SEC assays

Gel filtration chromatography was performed to analyze the effect of pathogenic variants T141I and M340T on the ability of AIF to undergo NADH–linked dimerization (*Fig. 5.7*) (Villanueva *et al*., 2015).

Once more, some manner of divergence could already be observed in the behaviour of WT $AIF_{\Delta 77}$ and $AIF_{\Delta 101}$. In the oxidized state, $AIF_{\Delta 77}$ eluted as a monomer of an ^{app}MW of ~75 kDa (theoretical monomer MW of 61 kDa), as opposed to $AIF_{\Delta 101}$, which eluted with an ^{app}MW of ~57 kDa (theoretical monomer MW of 57 kDa). This

may indicate that the monomeric conformation of $AIF_{\Delta 77}$ is quite less compact than that of its apoptotic form, resulting in a noticeable displacement of the elution peak. Upon incubation with NADH, $AIF_{\Delta 77}$:NAD^+ CTC eluted as a single peak of a slightly higher ^{app}MW (~101 kDa, theoretical dimer MW of 122 kDa) whereas $AIF_{\Delta 101}$:NAD^+ CTC presented a broad double peak with an ^{app}MW around ~96–144 kDa (theoretical dimer MW of 114 kDa). This suggests that, in the case of $AIF_{\Delta 77}$, the dimerization process may induce a significant change of conformation in the protein towards a much more compact structure, resulting in the observed minor displacement of its monomeric peak compared to that of $AIF_{\Delta 101}$.

Peak deconvolution demonstrated different conformational populations in both samples, where at least one overlapped with each oxidized sample indicating the presence of some remaining monomers. $AIF_{\Delta 101rd}$ presented one more population than its mitochondrial form, proposing a greater degree of variability in its dimer conformational pool.

The T141I replacement did not significantly impact the dimerization ability of AIF in either of its forms, although $T141I_{\Delta 101}$:NAD^+ CTC did elute as a single peak of an ^{app}MW of ~100 kDa instead of the broad double peak that had been previously observed for the WT. Of note, $AIF_{\Delta 77}$ presented an additional peak at high MWs in both samples, which could most probably be attributed to the presence of aggregates, demonstrating the greater instability of the variant protein.

Finally, the M340T replacement yielded differing profiles in each of its forms. $M340T_{\Delta 101}$ behaved similarly to the T141I variant, losing the double peak in the $M340T_{\Delta 101}$:NAD^+ CTC sample but exhibiting a similar displacement of the monomeric peak to that of the WT (~57 to ~100 kDa of ^{app}MW).

On the other hand, $M340T_{\Delta 77}$ eluted as a broad double peak both in the absence and presence of NADH, and presented a slightly greater peak shift to that of the WT (~67 to ~112 kDa of ^{app}MW). As the M340T pathogenic substitution takes place within the NADH-binding domain, it does not come as a surprise that it might impact the NADH-mediated dimerization process, maybe even promoting the dimerization of the protein in absence of the coenzyme. The broadness of the observed peaks hints to a greater variability of conformational populations in both samples, and most possibly reflects the presence of both monomers and dimers independently of the addition of NADH. Two additional peaks could also be observed at higher MW, most probably corresponding to aggregates or abnormal oligomerization states.

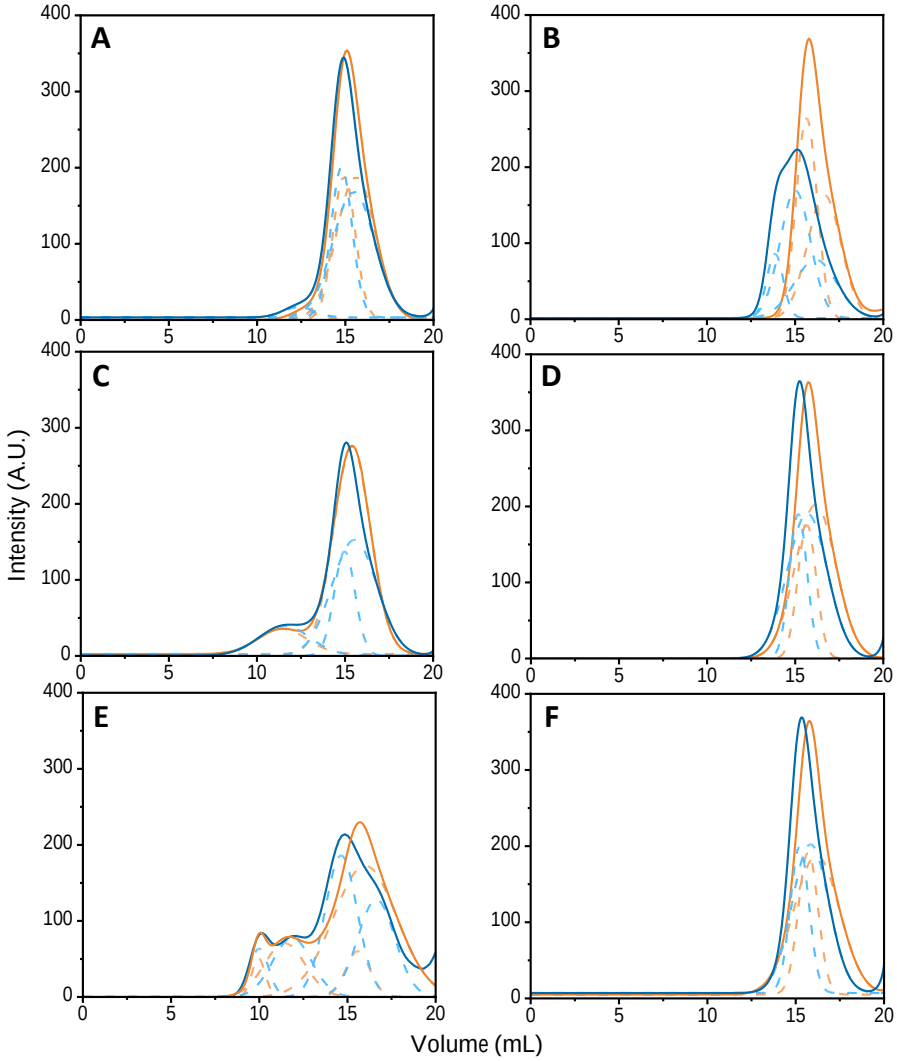

Figure 5.7. Effect of the pathogenic variants on the ability of AIF to stabilize dimers. Elution profiles of (A) $WT_{\Delta 77}$, (B) $WT_{\Delta 101}$, (C) $T141I_{\Delta 77}$, (D) $T141I_{\Delta 101}$, (E) $M340T_{\Delta 77}$ and (F) $M340T_{\Delta 101}$ on a Superdex™ 200 10/300 GL column in 50 mM Kpi buffer, pH 7.4, 150 mM NaCl at 6 °C. Assays were performed in absence (orange lines) or presence (blue lines) of a 100–fold excess of NADH (premixed). Populations assigned by Gaussian analysis are depicted as dashed lines.

5.2.3.2. Chemical crosslinking assays

As previous results indicated that dimer stability might have been compromised to some extent in both variants, further studies were performed in the presence of the BS^3 crosslinker, as it has the ability to covalently conjugate AIF dimers (*Fig. 5.8*).

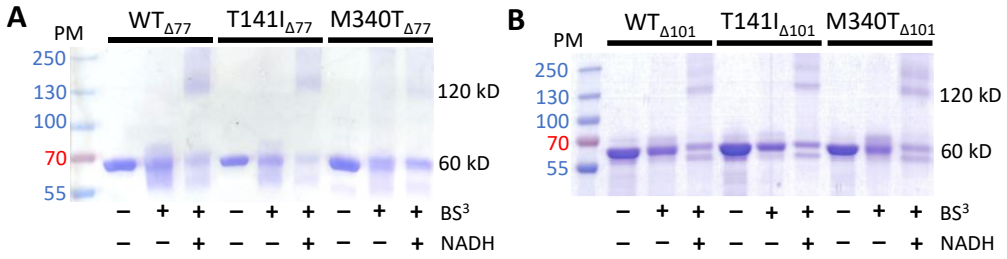

Figure 5.8. Chemical crosslinking of the pathogenic variants of AIF. Protein samples (~3 µM) were incubated with 100–fold excess of the BS^3 crosslinker in the absence or presence of 100–fold excess of NADH. After 30 minutes of incubation, reactions were stopped by the addition of bromophenol sample buffer and resolved by 12% SDS–PAGE.

After incubation of T141I$_{\Delta77ox}$ and T141I$_{\Delta101ox}$ with a 100–fold excess of BS^3, a single band at ~60 kDa could be isolated through SDS–PAGE corresponding to the monomeric form in both protein samples (*Fig. 5.8*). Incubation with BS^3 in the presence of NADH resulted in the apparition of another band at ~120 kDa of MW, confirming the proteins' ability to undergo dimerization upon NADH binding as in the WT (Ferreira *et al*., 2014). Consequently, it was concluded that the previously observed chromatographic changes in the T141I variant were most probably related to a diminished CTC lifetime, rather than to an altered dimer conformation.

In contrast, incubation of M340T$_{\Delta77ox}$ with the chemical crosslinker resulted in a diffuse smear at higher molecular weights indicative of the formation of oligomeric species even in the absence of NADH, which could not be observed in the M340T$_{\Delta101ox}$ sample (*Fig. 5.8A*) and which reinforced that which had been observed in the SEC assays. The M340T replacement may hence lead to a significant conformational alteration, possibly through its indirect interaction with the regulatory C–loop, that favors the displacement of the monomer–dimer equilibrium towards the dimeric form even in the oxidized state. These conformational changes could potentially be related to the perturbations that were previously observed in the CD spectra, demonstrating a relationship between the stability or conformation of the CTC state and the somewhat–altered quaternary structure.

5.2.4. NADH–dependent reductase activity

5.2.4.1. Steady–state assays

The ability of the T141I and M340T variants of AIF to efficiently oxidize NADH was first evaluated under steady–state conditions, using DCPIP as the electron acceptor (*Fig. 5.9, Tables 5.1 and 5.2*) (Ferreira *et al*., 2014).

Once more, important differences were already detected between the mitochondrial and apoptotic forms of WT AIF, with the former demonstrating a significantly greater efficiency (60–fold) arising from both a higher turnover rate and substrate affinity.

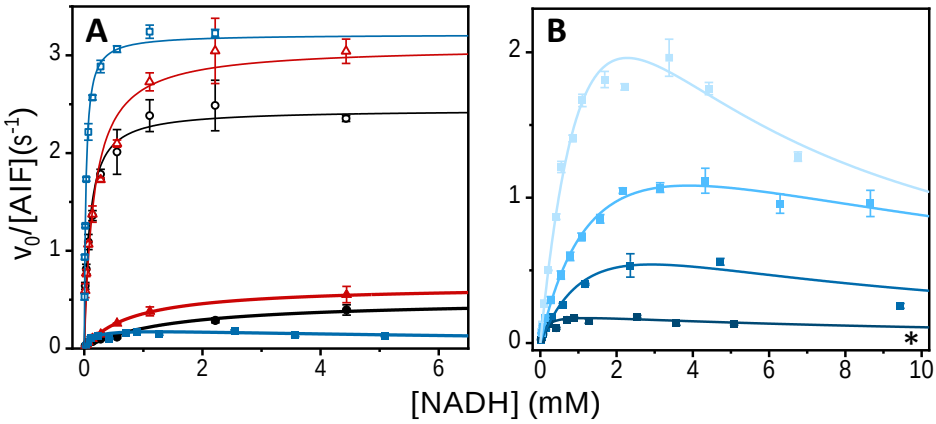

Figure 5.9. Steady–state kinetics of NADH oxidation by WT AIF and its variants T141I and M340T. (A) The diaphorase activity of WT (black) AIF and variants T141I (red) and M340T (blue) in their mitochondrial (open symbols) and apoptotic (closed symbols) forms was measured using NADH as the electron donor and 95 μM DCPIP as the electron acceptor. Reactions were followed at 620 nm and performed under aerobic conditions in 50 mM Kpi, pH 7.4, at 25°C. Initial reaction rates at different NADH concentrations (~0.03–10 mM) are shown fitted to the Michaelis–Menten equation (thin lines for mitochondrial forms, bold lines for apoptotic ones). Substrate inhibition could be observed and had to be incorporated into the fitting procedure for the M340T$_{\Delta 101}$ variant, for which a representative profile is shown (* in panel B). (B) Increasing loss of activity of M340T$_{\Delta 101}$ samples as they aged (approximately 0, 2, 7 and 14 days old, from light to dark blue). Measurements were taken as in panel A. Samples were stored at –80 °C in 50 mM Kpi, pH 7.4, excepting the hours–old samples, which were measured immediately after purification. As the sample ages, the diaphorase activity of M340T$_{\Delta 101}$ suffers a considerable decrease, associated to a potential shift in the protein populations towards species with lower activity but also a lower substrate inhibition effect.

Table 5.1. Steady–state kinetic parameters in WT AIF and its variants T141I and M340T.

AIF variant	k_{cat} (s^{-1})	K_M^{NADH} (mM)	K_I^{NADH} (mM)	k_{cat}/K_M^{NADH} ($s^{-1}mM^{-1}$)
$WT_{\Delta 77}$	2.4	0.1	–	24
$T141I_{\Delta 77}$	3.1	0.2	–	16
$M340T_{\Delta 77}$	3.2	0.03	–	107
$WT_{\Delta 101}$	0.5	1.4	–	0.4
$T141I_{\Delta 101}$	0.6	0.8	–	0.8
$*M340T_{\Delta 101}$	0.2	0.1	8.7	2.0

Performed at 25 °C in 50 mM Kpi, pH 7.4. Errors considered in the measured parameters (below ± 5% or 20% for k_{cat} and $K_{M/I}^{NADH}$ respectively) were taken larger than the numerical error after the fitting analysis. $*M340T_{\Delta 101}$ data corresponds to the stable oldest sample.

Despite its noticeable difference in E_m, the T141I variant exhibited a similar profile and analogous kinetic parameters to that of the WT in both its mitochondrial and apoptotic forms (*Fig. 5.9A, Table 5.1*). A slight decrease in efficiency could be observed in $T141I_{\Delta 77}$, possibly associated to its lower affinity for the coenzyme, while $T141I_{\Delta 101}$ displayed a small increase in efficiency arising from a slightly higher affinity. These small differences manifest that, while the environment of the FAD must have been somehow significantly affected by the replacement, said perturbations do not impact the exceptionally–low efficiency of AIF as an NADH oxidase.

In contrast, $M340T_{\Delta 77}$ showed a moderate increase in efficiency (~5–fold more than the WT) that was similar to that previously reported for the F310G variant in its apoptotic form (Villanueva *et al.*, 2015). The most remarkable finding, however, came from $M340T_{\Delta 101}$, showing a novel substrate–inhibition profile that had never before been observed in AIF regardless of form or nature. Surprisingly, said profile could only be observed in the apoptotic form of the M340T variant, and was directly dependent on the age of the sample (*Fig. 5.9B, Table 5.2*). Samples measured immediately after purification yielded the highest turnover rate, which progressed in a steep decline as the time passed in storage at –80 °C. Samples over a week old reached a plateau where the turnover rate was the lowest, but the efficiency became similar to that in the freshest samples (~5–fold more than the WT). This evolution was hypothesized to arise from a shift in the protein populations towards species of closer

resemblance to the WT (and consequently, lower toxicity), coursing with a low NADH oxidase activity but also a smaller substrate inhibition effect.

Table 5.2. Steady–state kinetic parameters in M340T$_{\Delta 101}$ according to sample age.

Sample age (days)	k_{cat} (s^{-1})	K_M^{NADH} (mM)	K_I^{NADH} (mM)	k_{cat}/K_M^{NADH} ($s^{-1}mM^{-1}$)
0	4.6	1.7	3.2	2.7
2	2.1	1.8	8.4	1.2
7	1.1	1.7	5.7	0.6
14	0.2	0.1	8.7	2.0

Performed at 25 °C in 50 mM Kpi, pH 7.4. Errors considered in the measured parameters (below ± 5% or 20% for k_{cat} and $K_{M/I}^{NADH}$ respectively) were taken larger than the numerical error after the fitting analysis. Samples were stored at –80 °C in 50 mM Kpi, pH 7.4, excepting the hours–old samples, which were measured immediately after purification.

5.2.4.2. Transient–state assays

Subsequently, the potential effect of the T141I and M340T variants on the HT process efficiency was assessed through SF transient kinetics. Kinetic traces were recorded at increasing NADH concentrations, portraying a basically irreversible two–electron reduction process for the FAD cofactor paired with the formation of the long–wavelength broad band around 500–800 nm that reflects the stabilization of the AIF$_{rd}$:NAD$^+$ CTC species (*Fig. 5.10*).

WT AIF$_{\Delta 77}$ and AIF$_{\Delta 101}$ presented almost analogous spectra and kinetic parameters, with a slight increase in efficiency (~3–fold) and a mild decrease in CTC signal intensity (~50% of initial CTC stabilization) in the mitochondrial form (*Fig. 5.10A, B; Fig. 5.11, Table 5.3*). These differences could also be observed between the forms of both pathogenic variants. Global analyses of the spectral range time evolutions (*Fig. 5.11*) were best fitted to a one–step model (A → B) as previously described (Ferreira *et al.*, 2014). Obtained k_{obs} values exhibited hyperbolic dependency on the concentration of NADH in all samples, allowing the determination of k_{HT} and K_d^{NADH} upon fitting to equation 3.17 (*Fig. 5.11, Table 5.3*).

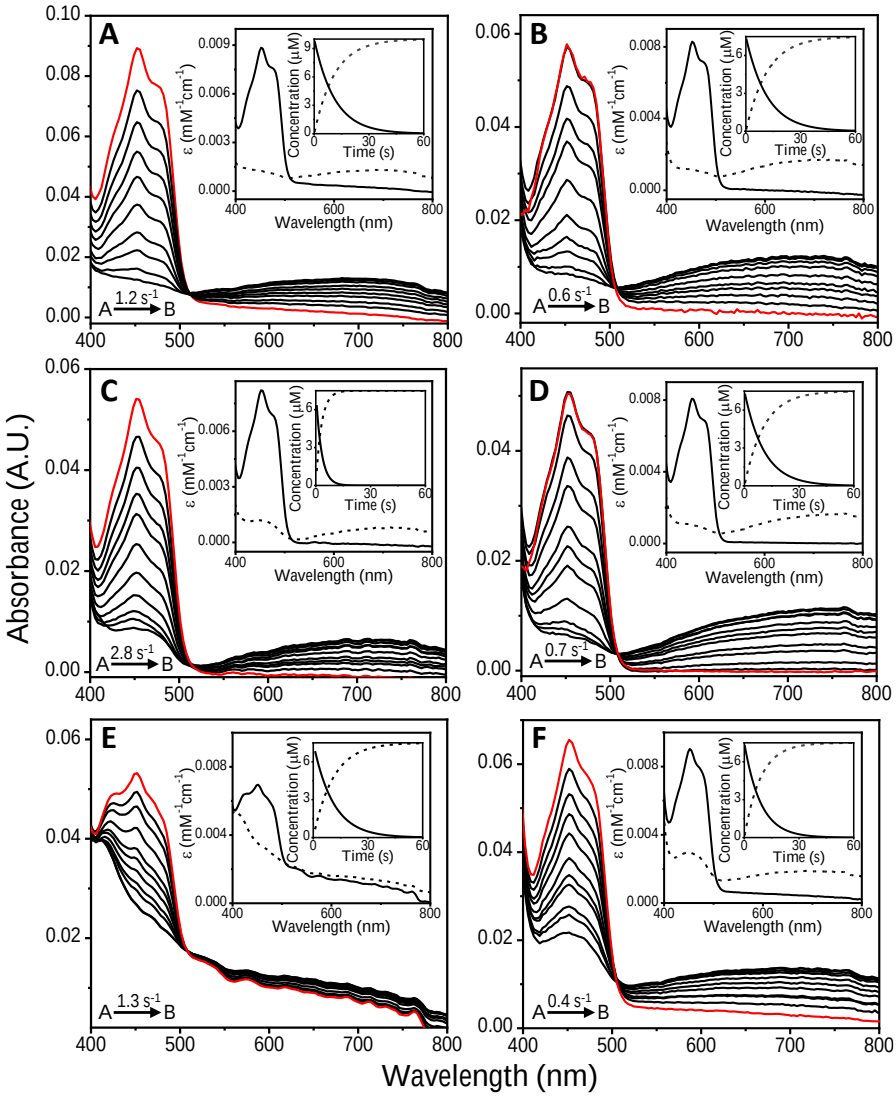

Figure 5.10. Transient kinetics of NADH oxidation in WT AIF and its variants T141I and M340T. Spectral evolution of flavin reduction on a 0–60 s timescale of (A) $WT_{\Delta 77}$, (B) $WT_{\Delta 101}$, (C) $T141I_{\Delta 77}$, (D) $T141I_{\Delta 101}$, (E) $M340T_{\Delta 77}$ and (F) $M340T_{\Delta 101}$ at a concentration of 7.5 μM after mixing with 2.5 mM NADH in air–saturated 50 mM Kpi, pH 7.4, at 25°C. Lines in red correspond to the spectra of the oxidized enzymes. The corresponding insets portray the absorbance spectra of the predicted initial and final species obtained by fitting the spectral evolution to a single step model (A→B), and the evolution of the concentration for each species.

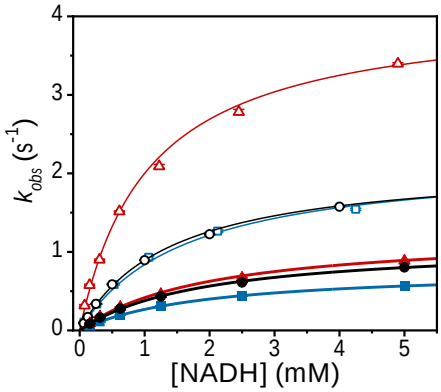

Figure 5.11. Analysis of transient kinetics in WT AIF and its variants T141I and M340T. Dependence of the observed rate constants for flavin reduction on the concentration of NADH for the WT (black circles) and variants T141I (red triangles) and M340T (blue squares) in their mitochondrial (open symbols) or apoptotic (closed symbols) forms. Lines (thin for the mitochondrial forms, bold for the apoptotic forms) represent fitting of the experimental data to equation 3.17.

Table 5.3. Transient–state kinetic parameters in WT AIF and its variants T141I and M340T.

AIF variant	k_{HT} (s^{-1})	K_d^{NADH} (mM)	k_{HT}/K_d^{NADH} ($s^{-1}mM^{-1}$)
$WT_{\Delta 77}$	2.1	1.4	1.6
$T141I_{\Delta 77}$	4.1	1.1	3.9
$M340T_{\Delta 77}$	2.2	1.6	1.4
$WT_{\Delta 101}$	1.2	2.0	0.6
$T141I_{\Delta 101}$	1.4	2.4	0.6
$M340T_{\Delta 101}$	0.8	1.9	0.4

Performed at 25 °C in 50 mM Kpi, pH 7.4. Errors considered in the measured parameters (below ± 5% or 20% for k_{HT} and K_d^{NADH} respectively) were taken larger than the numerical error after the fitting analysis.

For its part, the T141I variant barely differed from the WT in its apoptotic form, and demonstrated only a small increase in efficiency in its mitochondrial form (*Fig. 5.10B, C; Fig. 5.11, Table 5.3*) that could be explained by its significantly greater tendency to accept electrons. The efficiency of $T141I_{\Delta 77}$ as a hydride acceptor doubled when compared to that of the WT, arising from a similar boost in its HT rate constant but an almost identical affinity for the NADH substrate.

Meanwhile, the M340T replacement yielded analogous kinetic parameters but remarkable differences in flavin reduction and CTC initial stabilization (*Fig. 5.10D, E; Fig. 5.11, Table 5.3*). Noticeably, M340T$_{\Delta 77}$ could achieve complete reduction of its flavin cofactor after one cycle, but was unable to stabilize more than 10% of the CTC compared to the WT. On the other hand, M340T$_{\Delta 101}$ could not be fully reduced at lower concentrations of NADH, reaching equilibrium before the reaction was completely finished. This could be explained by an alteration of the AIF$_{rd}$:NAD$^+$ complex's redox potential towards a value closer to that of AIF$_{ox}$.

5.2.4.3. Reactivity of the CTC towards O_2

Subsequently, the effect of the pathogenic variants on the reactivity of the CTC towards O_2 was assessed in their mitochondrial and apoptotic forms (*Fig. 5.12*).

WT AIF$_{\Delta 77}$ and AIF$_{\Delta 101}$ displayed significant differences on themselves regarding the reoxidation process (*Fig. 5.12A, B*), with the most noticeable change being the stabilization of an anionic semiquinone state (FAD$_{sq}^{\bullet -}$) with two characteristic local maxima around 400 and 475 nm in the mitochondrial form (*Fig. 5.13A*, in blue) that has never before been observed in the apoptotic form.

Moreover, CTC lifetime appears to be out of sync with that of the flavin in the mitochondrial form (CTC decay half–life of 20 min vs 76 min for FAD$_{ox}$ formation, *Fig. 5.12A, F*), an effect that might further support the aforementioned stabilization of the semiquinone state. This is in contrast with the apoptotic form, where CTC half–life does coincide with that of the FAD$_{ox}$ (CTC half–life of 58 min, *Fig. 5.12B, F*).

In comparison, the T141I variant presented interesting alterations that varied from one form to the other (*Fig. 5.12C, D*). T141I$_{\Delta 77}$ demonstrated an almost native behaviour in regard to its CTC decay (24 min) and FAD$_{ox}$ formation (66 min) out–of–sync half–lives, but the stabilization of the FAD$_{sq}^{\bullet -}$ state was not as apparent as in the WT (*Fig. 5.12C*). Meanwhile, T141I$_{\Delta 101}$ CTC appeared to be remarkably less stable against reoxidation by O_2, presenting a significantly decreased CTC half–life of 16 min (~4–fold less than the WT). Therefore, the T141I replacement appears to favor O_2 access to the FAD cofactor in the AIF$_{rd}$:NAD$^+$ CTC state, weakening the stability of the CTC and, ultimately, of the dimeric form, seconding the behaviour that was observed in the SEC assays. Furthermore, the T141I variant may present a significantly less compact CTC active site than that of the WT protein due to the loss

of critical H–bonds (*Fig. 5.3*), possibly leading as well to an alteration of the conformation and/or stability of the potentially–formed semiquinone state.

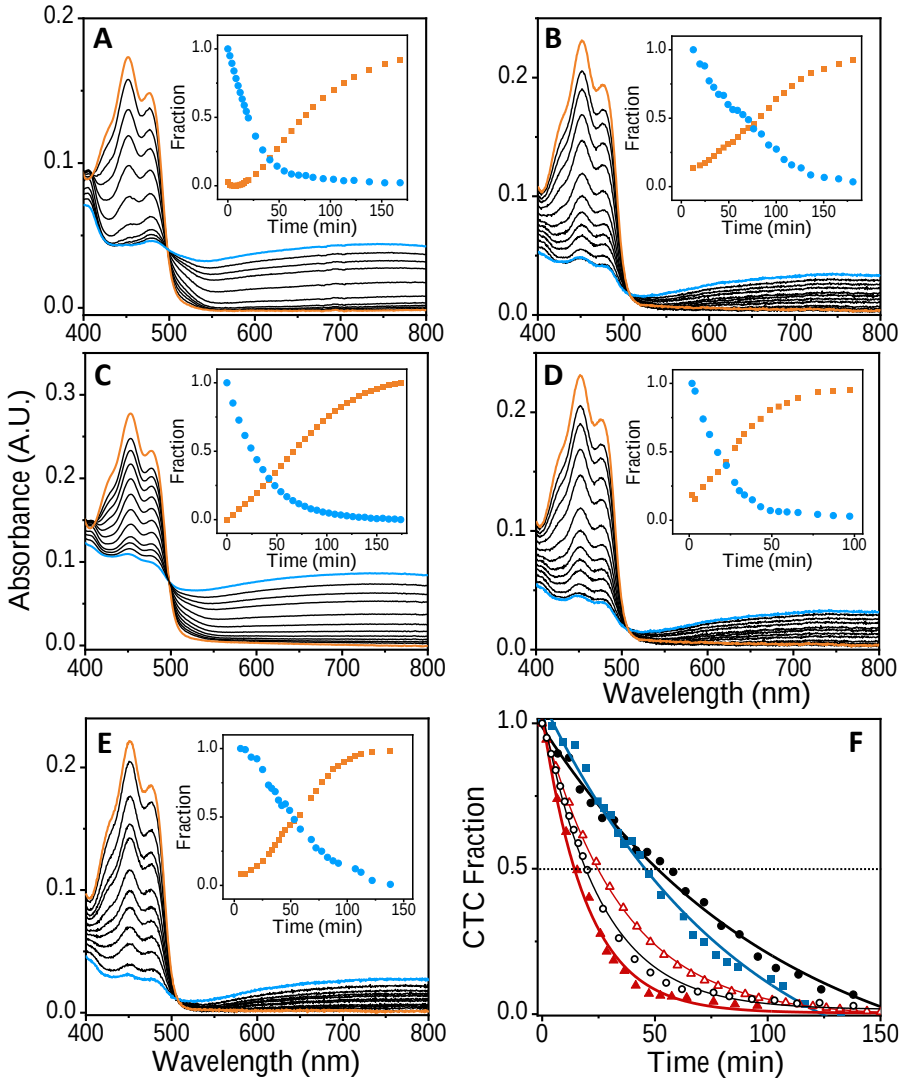

Figure 5.12. Effect of the T141I and M340T pathogenic variants on CTC half–life. Spectral evolution of (A) $WT_{\Delta 77}$, (B) $WT_{\Delta 101}$, (C) $T141I_{\Delta 77}$, (D) $T141I_{\Delta 101}$ and (E) $M340T_{\Delta 101}$ across time for the decay of their CTC species and reoxidation of their FAD. Samples were obtained by mixing oxidized protein (orange lines) with 1.5–fold NADH, leading to the formation of AIF_{rd}:NAD^+ CTC (blue lines). Insets show the evolution of CTC (blue circles) and FAD band-I (orange circles), corresponding to the normalized absorbance at 700 nm and 450 nm respectively. Assays were performed in 50 mM Kpi, pH 7.4, at 25 °C. (F) Reactivity of the CTC towards O_2 in WT (black circles), T141I (red triangles) and M340T (blue squares) in their

mitochondrial (open symbols) or apoptotic (closed symbols) forms. AIF_{rd}:NAD^+ CTC decay was monitored at 700 nm in air–saturated 50 mM Kpi , pH 7.4, at 25 °C. Traces were normalized from 1 to 0 as a fraction of the remaining CTC along time. Lines (thin for $AIF_{\Delta 77}$, bold for $AIF_{\Delta 101}$ samples) represent the fit to a single–exponential decay process. Data on $M340T_{\Delta 77}$ could not be recorded as it did not stabilize the CTC under the assayed conditions.

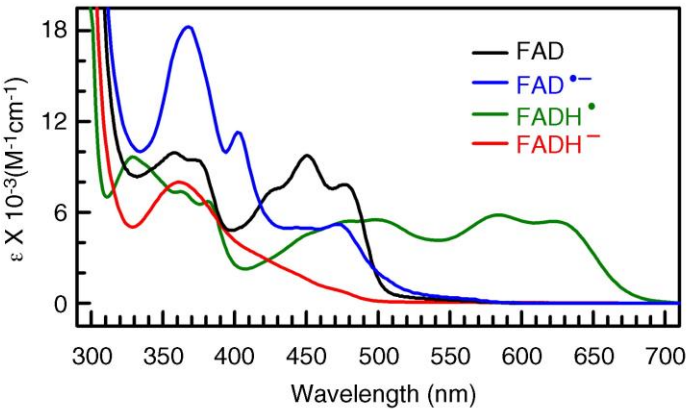

Figure 5.13. UV/Visible absorption spectra of a flavoprotein sample in different redox forms. Figure taken from Liu, 2010 (Fig. 1b).

Similarly, differing behaviours were observed in the two forms of the M340T variant. While $M340T_{\Delta 101}$ CTC displayed a practically native reactivity towards O_2 with only a slightly influenced CTC half–life of 48 min (*Fig. 5.12E, F*), reduction of $M340T_{\Delta 77}$ could not be achieved under the assayed conditions.

Influence of CHCHD4 on AIF reactivity towards O_2

As neither mitochondrial variant behaved exactly like $WT_{\Delta 77}$, an additional assay was performed in the presence of mitochondrial protein partner CHCHD4 (*Fig. 5.14*) to evaluate whether its association would facilitate the stabilization of the AIF_{rd}:NAD^+ CTC state. Indeed, previous results in our group have demonstrated that the interaction of $AIF_{\Delta 77rd}$ with CHCHD4 indefinitely prolongs CTC lifetime (and, subsequently, the dimeric form) (*Fig. 5.14A*), envisaging its vital role in AIF's function as a sensor of the mitochondrial redox state through the displacement of its monomer–dimer equilibrium.

Surprisingly, the interaction of $T141I_{\Delta 77rd}$ with CHCHD4 enabled the distinct stabilization of the $FAD_{sq}^{\bullet-}$ state that had been previously observed in $WT_{\Delta 77rd}$, becoming apparent through its characteristic peaks at approximately 400 and 475 nm

(*Fig. 5.14B*). Consequently, the conformational changes induced by the binding of CHCHD4 upon AIF appear to be enough to compensate for the altered active site of the T141I variant.

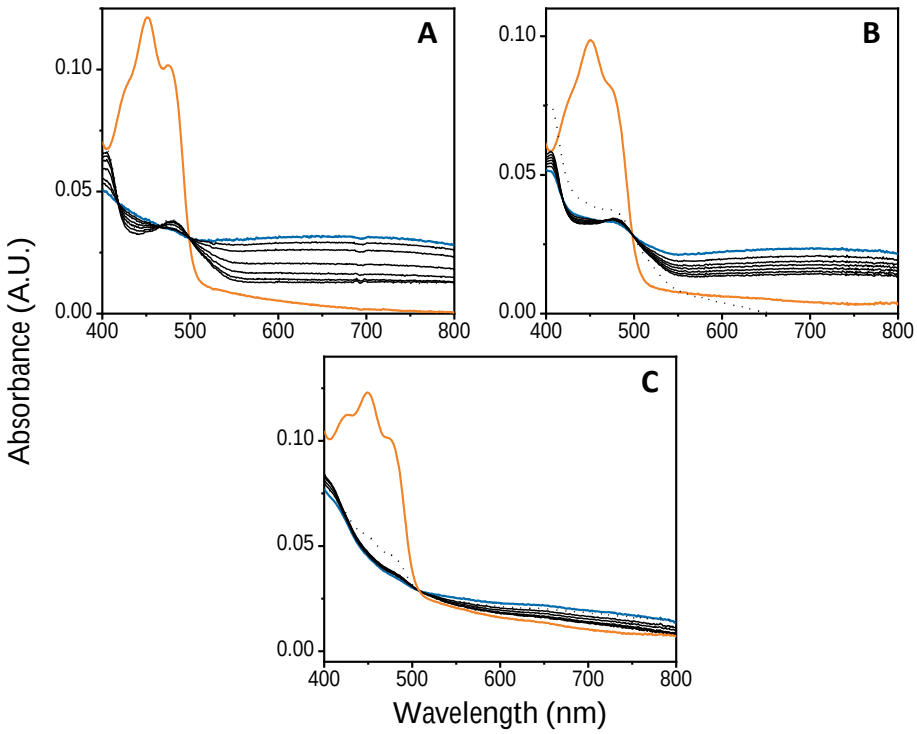

Figure 5.14. Influence of CHCHD4 on the reactivity of AIF and its variants towards O_2. Spectral evolution of (A) $WT_{\Delta 77rd}$:CHCHD4, (B) $T141I_{\Delta 77rd}$:CHCHD4 and (C) $M340T_{\Delta 77rd}$:CHCHD4 upon reduction with 1.5–fold NADH. CHCHD4 was added in a 1:3 ratio with respect to AIF and incubated for 15 min at 25 °C prior to mixing with NADH. Spectra were recorded for up to 24 hours (dotted lines represent the last recorded spectrum). Orange lines represent the spectra of the oxidized flavin prior to the addition of NADH, while blue lines represent that of the reduced flavin immediately after (t = 0). Assays were performed in air–saturated 50 mM Kpi, pH 7.4, at 25 °C.

In contrast, the presence of CHCHD4 did result in the indefinite reduction of $M340T_{\Delta 77}$, but no semiquinone peak could be observed and the intensity of the broad band around 700 nm representing the CTC was found to be remarkably weak (*Fig. 5.14C*). This occurrence can be seconded by its near–UV/Vis CD spectrum, where the intensity of the CTC signal was barely 35% of that of the WT even with 100–fold excess of NADH. Furthermore, an F310 variant (F310G) was also reported to present a

significant reduction in the intensity of its CTC band, attributed to a significant loss of compactness in the enzyme's active site (Villanueva *et al.*, 2015). These results envisage that the M340T replacement either gravely affects the stability of the CTC or leads to a differing charge distribution between the reacting rings, most possibly due to the hindered stacking of the nicotinamide ring of the NADH that was already at play in previous assays.

5.2.5. Thermal stability

Protein thermal unfolding was performed to evaluate the impact of the T141I and M340T replacements on protein–FAD interaction integrity and overall stability, both in the oxidized and reduced states. Curves were recorded through fluorescence emission following FAD release, far–UV and near–UV/Vis CD (*Fig. 5.15, Table 5.4*).

The mitochondrial and apoptotic forms of WT AIF behaved in an analogous manner in both states, with the former presenting a slightly greater thermal stability than the latter (T_m values ~ 5 degrees higher, *Table 5.4*). As has been previously reported for the apoptotic form (Villanueva *et al*., 2019), WT AIF follows a three–states unfolding mechanism (N↔I↔U) that becomes apparent in the near–UV/Vis CD data, while the far–UV CD and FAD fluorescence emission transitions take place exclusively at $T_{m,1}$ or $T_{m,2}$ respectively. This proves that alteration of the secondary structure (reported by the far–UV CD data) is favoured over FAD release (reflected in the near–UV/Vis CD and fluorescence emission data), probably in an attempt to warrant the protein's functionality. This results in an intermediate conformation that has lost part of its structure but which still retains an adequate folding of the isoalloxazine environment. Noticeably, the formation of the CTC in AIF_{rd}:NAD^+ gives rise to a deleterious effect on protein stability ($T_m^{CTC} - T_m$ values of ~ –11 in both forms), promoting protein unfolding and FAD release. This counter–intuitive ligand–binding destabilizing effect is attributed to the unfolding of the regulatory C–loop in the apoptotic domain of AIF_{rd}, which results in looser tertiary structure contacts at the active site that in turn facilitate cofactor dissociation (Villanueva *et al*., 2019).

Regarding the pathological variants of interest, the T141I replacement resulted in a severe structural destabilization that was easily apparent in both forms (ΔT_m values of ~ –11 in the oxidized state and ~ –8 in the reduced state, in comparison to the WT) (*Table 5.4*). This increased susceptibility to thermal denaturation could be attributed to the expected alteration of the active site's H–bond network in the T141I variant

(specifically, the loss of the water bridges established between T141, H455 and the ribityl pyrophosphate moiety of the FAD), which could potentially lead to a less compact –and subsequently weaker– tertiary structure. Formation of the CTC upon reduction with NADH still induced a destabilizing effect, which was almost identical to that observed in the WT ($T_m^{CTC} - T_m$ values of ~ –8).

A significant change in the contribution of each process could also be observed in the T141I variant, with both transitions of the unfolding mechanism becoming apparent in the far–UV CD data. This suggests that the unfolding process in the oxidized protein starts with conformational changes within the active site that only slightly affect the overall structure and do not cause flavin release (observed through far–UV and near–UV/Vis CD), and finishes with the generalized loss of structure and the concomitant cofactor dissociation (observed through both CD and fluorescence emission data) (*Fig. 5.15C, D*). Meanwhile, in the reduced state, $T141I_{\Delta 101}$ suffers significant changes within the active site that result in total release of the cofactor during the first transition (the fluorescence emission data reflect exclusively $T_{m,1}$), while a certain degree of structure is retained up to the second transition. In contrast, $T141I_{\Delta 77rd}$ regains an almost native profile, where the structure of the protein is partly lost before the cofactor is completely released.

For its part, the M340T replacement presented a manner of structural destabilization that could only be observed in the mitochondrial form, and which was particularly grave in its oxidized state (ΔT_m values of ~ –13) but barely relevant in its reduced state (ΔT_m values of ~ –3) (*Table 5.4*). Indeed, the ligand–binding destabilizing effect was almost completely absent in this form, as has been previously reported for other deleterious variants of AIF (Villanueva *et al.*, 2019). This altered behaviour could be partly attributed to the binding of the NAD^+, which would most likely cause an increase in the compactness of the structure and, as such, a boost in stability. However, most of the effect is envisaged to arise from the indirect impact of the M340T replacement on the conformation of the C–loop (through its interaction with the central β–sheet), which potentially results in the motif's prompt unfolding. This would yield the significantly lower T_m values that were observed in the oxidized state, while simultaneously explaining the almost native values in the reduced state.

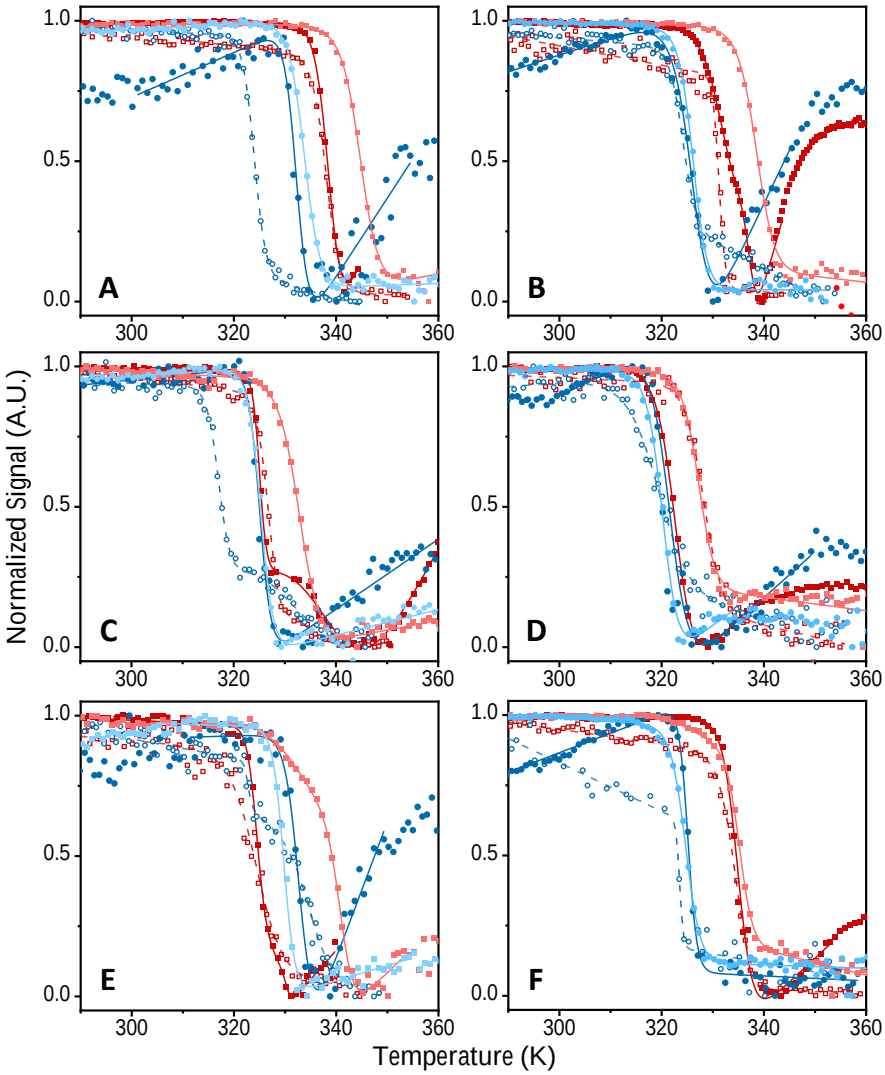

Figure 5.15. Thermal stability of WT AIF and its variants T141I and M340T. Thermal unfolding and flavin release curves of (A) $WT_{\Delta 77}$, (B) $WT_{\Delta 101}$, (C) $T141I_{\Delta 77}$, (D) $T141I_{\Delta 101}$, (E) $M340T_{\Delta 77}$ and (F) $M340T_{\Delta 101}$. Thermal denaturation was monitored through far–UV CD (oxidized protein: 210 nm, open red squares; NADH–reduced protein: 220 nm, open blue circles), near–UV/Vis CD (oxidized protein: 300 nm, closed red squares; NADH–reduced protein: 420 nm, closed blue circles) and FAD fluorescence upon release (excitation at 450 nm and emission at 530 nm, oxidized protein: closed light–red squares; NADH–reduced protein: closed light–blue circles). Data are shown roughly normalized from 0 to 1, with lines representing the individual fittings to a one– or two–transitions unfolding models (eqs. 3.8 and 3.9). Curves were recorded in 50 mM Kpi, at a final ionic strength of 150 mM, along a 10 to 90°C temperature ramp. Reduced AIF samples were obtained by premixing the protein with 100–fold excess of NADH.

Table 5.4. Thermal stability of WT AIF and its variants T141I and M340T in the oxidized and CTC states.

AIF variant	AIF_{ox}								CTC AIF_{rd}:NAD^+								$T_m^{CTC} - T_m$ (K)		
	T_m (K)			ΔH (kcal/mol)			ΔT_m (K)		T_m^{CTC} (K)			ΔH^{CTC} (kcal/mol)			ΔT_m^{CTC} (K)				
	1	*2*	*3*	*1*	*2*	*3*	*1*	*2*	*1*	*2*	*3*	*1*	*2*	*3*	*1*	*2*	*1*	*2*	*3*
$WT_{\Delta 77}$	338	345	–	190	136	–	–	–	326	334	–	215	162	–	–	–	–12	–11	–
$T141I_{\Delta 77}$	327	333	–	171	108	–	–11	–12	317	325	–	213	142	–	–9	–9	–10	–8	–
$M340T_{\Delta 77}$	325	331	338	97	124	155	–13	–14	324	330	335	133	120	201	–2	–4	–1	–1	–3
$WT_{\Delta 101}$	333	339	–	124	129	–	–	–	323	327	–	179	125	–	–	–	–10	–12	–
$T141I_{\Delta 101}$	322	328	–	139	120	–	–11	–11	314	321	–	139	130	–	–9	–6	–8	–7	–
$M340T_{\Delta 101}$	333	336	–	175	176	–	–1	–3	322	326	–	95	246	–	–1	–1	–11	–10	–

Values obtained by individual fitting of the far–UV CD, near–UV/Vis CD and fluorescence thermal denaturation curves to a one– or two–transitions unfolding model. Data recorded in 50 mM Kpi, pH 7.4, at a final ionic strength of 150 mM, from 10 to 90 °C (283 to 363 K). Protein concentrations were 2 μM for the fluorescence and far–UV CD assays, or 20 μM for the near–UV/Vis CD assays. NADH concentration was in 100–fold excess. Errors considered in the measured parameters (± 2 °C and 0.4 kcal/mol for T_m and ΔH respectively) were taken larger than the numerical error after the fitting analysis (n = 2).

In regard to the contribution of each process in $M340T_{\Delta 77}$, a novel four–states unfolding mechanism ($N \leftrightarrow I_1 \leftrightarrow I_2 \leftrightarrow U$) could be observed. The first and second transitions became apparent in the far–UV CD data in both states, while a third transition was detected in the fluorescence emission data of $M340T_{\Delta 77ox}$. This demonstrated that FAD release began partly in parallel to the secondary structure loss, but was still the last process to take place.

Adversely, no significant decrease in stability could be observed in $M340T_{\Delta 101}$, in either its oxidized or reduced states (ΔT_m values of ~ –2). The only significant change that could be noted was the detection of both transitions of the unfolding process in the fluorescence emission data of $M340T_{\Delta 101rd}$, demonstrating that the isoalloxazine environment begins to lose its structure during the first transition.

5.2.6. Interaction with Physiological Partners

The impact of the $T141I_{\Delta 101}$ and $M340T_{\Delta 101}$ variants on the interaction network of AIF was evaluated using three representative ligands: CHCHD4, a mitochondrial partner vital in OXPHOS and energy homeostasis; and H2AX and DNA, nuclear partners critical for chromatinolysis and programmed cell death. The binding parameters that describe the formation of the binary complexes between AIF and each ligand were determined through ITC. Binding isotherms best fitted to a single binding site model with a K_d within the micromolar range for all ligands (*Figs. 5.16, 5.17; Table 5.5*).

As previous results have demonstrated the lack of interaction between AIF_{ox} and CHCHD4 (Hangen *et al*., 2015; Romero-Tamayo *et al*., 2021), all protein samples were made to interact with CHCHD4 in their CTC state, obtained by preincubation with NADH. Both variants displayed an interaction with a significant favourable enthalpic contribution (indicative of specific binding) and a lesser unfavourable entropic contribution (suggesting a structurally more organized system) (*Fig. 5.16; Table 5.5*). $M340T_{\Delta 101}$ CTC resembled the thermodynamic profile of $WT_{\Delta 101}$ CTC, but significantly increased the magnitude of both the favourable enthalpic and unfavourable entropic contributions. In contraposition, the thermodynamic profile of $T141I_{\Delta 101}$ CTC demonstrated a greatly reduced unfavourable entropic contribution and a slightly reduced favourable enthalpic contribution.

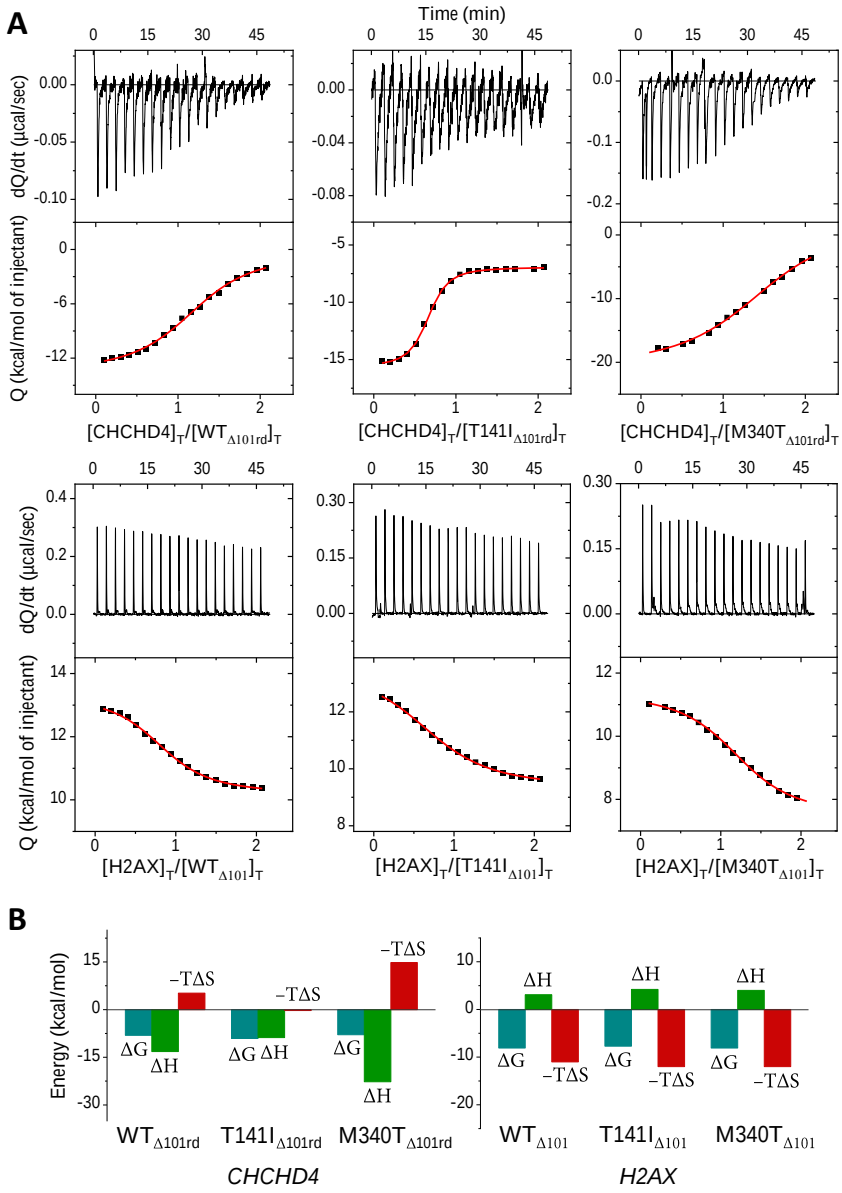

Figure 5.16. Binding assays of physiological partners CHCHD4 and H2AX to AIF$_{\Delta 101}$. (A) Calorimetric titrations of AIF WT$_{\Delta 101rd}$:NAD$^+$ CTC, T141I$_{\Delta 101rd}$:NAD$^+$ CTC and M340T$_{\Delta 101rd}$:NAD$^+$ CTC with CHCHD4, and of AIF WT$_{\Delta 101ox}$, T141I$_{\Delta 101ox}$ and M340T$_{\Delta 101ox}$ with H2AX. The upper plots show the thermograms (thermal power as a function of time) while the lower plots show the binding isotherm (normalized heats as a function of the ligand/protein molar ratio). Measurements were performed in 50 mM Kpi, pH 7.4, at 25°C. CTC samples were obtained by premixing AIF$_{\Delta 101ox}$ with 100–fold excess of NADH. Binding parameters were estimated through nonlinear least–squares regression applying a single–

ligand binding model (continuous lines in binding isotherms). (B) Energetic profiles of the titrations of AIF $WT_{\Delta 101}$, $T141I_{\Delta 101}$ and $M340T_{\Delta 101}$ with CHCHD4 (left) or H2AX (right).

In terms of the affinity for CHCHD4, the T141I variant showed a significant increase (K_d ~6–fold lower), while $M340T_{\Delta 101}$ presented only a slight decrease. The competent interaction between AIF_{rd}:NAD^+ CTC and CHCHD4 is proposed to depend on the proper architecture of the CTC, which favors the assembly of certain disordered regions within both proteins to achieve the optimal conformation for interaction (Romero-Tamayo *et al*., 2021). Thus, the observed alteration of the CTC environment in the T141I variant may somehow strengthen the interaction between the enzyme and CHCHD4.

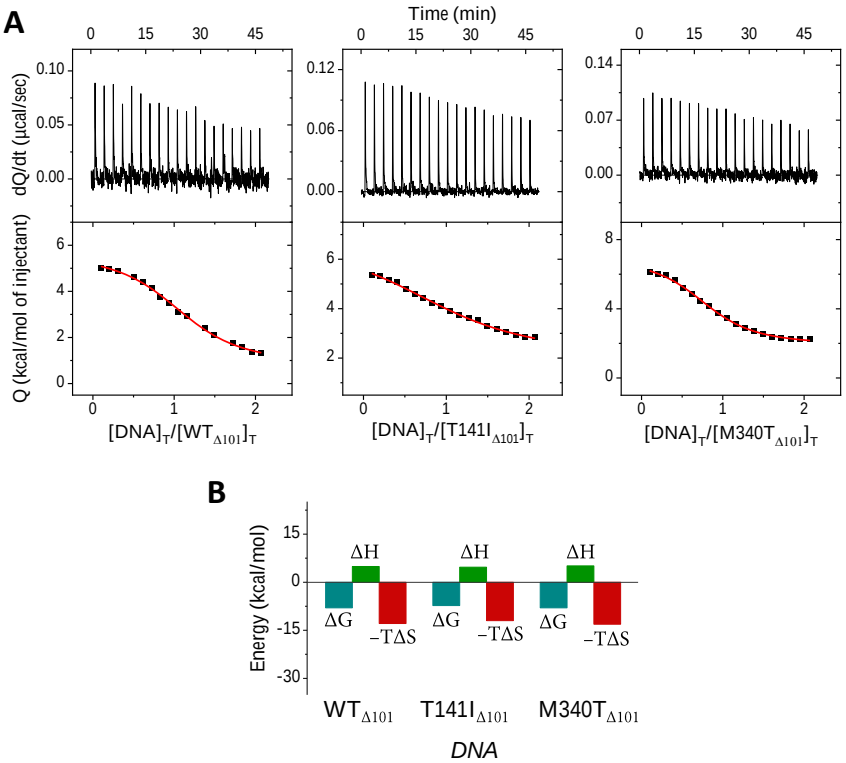

Figure 5.17. Binding assays of physiological partner DNA to $AIF_{\Delta 101}$. (A) Calorimetric titrations of AIF $WT_{\Delta 101ox}$, $T141I_{\Delta 101ox}$ and $M340T_{\Delta 101ox}$ with DNA. The upper plots show the thermograms (thermal power as a function of time) while the lower plots show the binding isotherm (normalized heats as a function of the ligand/protein molar ratio). Measurements were performed in 50 mM Kpi, pH 7.4, at 15°C. Binding parameters were estimated through nonlinear least–squares regression applying a single–ligand binding model (continuous lines

in binding isotherms). (B) Energetic profiles of the titrations of AIF $WT_{\Delta 101}$, $T141I_{\Delta 101}$ and $M340T_{\Delta 101}$ with DNA.

Table 5.5. Thermodynamic parameters for the binary interaction of AIF $WT_{\Delta 101}$ and variants $T141I_{\Delta 101}$ and $M340T_{\Delta 101}$ with physiological partners CHCHD4, H2AX and DNA.

$AIF_{\Delta 101}$ variant	Titrate	N	K_a (μM^{-1})	K_d (μM)	ΔH (kcal/mol)	$-T\Delta S$ (kcal/mol)	ΔG (kcal/mol)
WT_{rd}	CHCHD4	1.3	0.9	1.2	–13.2	5.2	–8.1
$T141I_{rd}$		0.6	4.4	0.2	–8.8	–0.3	–9.1
$M340T_{rd}$		1.6	0.6	1.6	–22.7	14.8	–7.9
WT	H2AX	0.9	0.8	1.2	3.1	–11.2	–8.1
T141I		0.9	0.4	2.2	4.2	–11.9	–7.7
M340T		1.3	0.9	1.1	4.0	–12.1	–8.1
WT	DNA	1.2	0.7	1.4	4.9	–12.9	–8.0
T141I		1.2	0.2	4.3	4.7	–12.0	–7.3
M340T		0.9	0.8	1.3	5.1	–13.1	–8.0

Values obtained at 25°C (excepting DNA assays, at 15°C) in 50mM Kpi, pH 7.4. N is the calculated binding stoichiometry. Thermodynamic parameters were calculated by $K_d = (K_a)^{-1}$, $\Delta G = RT \cdot \ln K_d$ and $-T\Delta S = \Delta G - \Delta H$. Reduced samples were obtained through previous incubation with 100–fold NADH. Errors considered in the measured parameters (± 30% in K_d and K_a and ± 0.4 kcal/mol in ΔG, ΔH and $-T\Delta S$) were taken larger than the numerical error after the fitting analysis.

In contrast, the interaction of nuclear partner H2AX with $AIF_{\Delta 101}$ is entropically guided, having demonstrated an apparent lack of electrostatic specificity (*Fig. 5.16; Table 5.5*). Both variants gave rise to analogous thermodynamic profiles to that of the WT, with a greater entropic contribution and an overall favourable free energy. Affinity values were also in line with those obtained for the WT, demonstrating that the binding of H2AX had not been significantly affected by either replacement.

Similarly, the parameters obtained for the titration of $AIF_{\Delta 101}$ with dsDNA indicated the formation of an entropy–driven binary complex with an unfavorable enthalpic contribution to the binding (*Fig. 5.17; Table 5.5*). AIF presents clusters of positive

charges throughout its surface which may be fundamental in DNA binding; however, this interaction is expected to be unspecific, as AIF is able to recognize RNA and several ribonucleoproteins as well (Vahsen *et al.*, 2006). Indeed, the entropy–driven interaction observed between $AIF_{\Delta 101}$ and the dsDNA corroborates such lack of specificity. In regard to the affinity for the DNA, the M340T variant maintained that of the WT, while the T141I variant slightly impaired it (K_d ~3–fold higher). The thermodynamic patterns as well as the entropic and enthalpic binding contributions of both replacements appeared to be analogous to that of the WT.

5.2.7. Concluding remarks and unresolved issues

The moonlighting character of AIF culminates in a duplexity of flanks from which diverse pathogenic mechanisms may arise, impacting either its ability to protect mitochondrial homeostasis and, consequently, to keep the cell alive, or its capacity to mediate programmed cell death. Phenotypes of ample variability converge in severe neurodegeneration diseases when the pro–life function of AIF is affected (Ardissone *et al.*, 2015; Bano and Prehn, 2018; Berger *et al.*, 2011; Bogdanova–Mihaylova *et al.*, 2019; Diodato *et al.*, 2016; Ghezzi *et al.*, 2010; Heimer *et al.*, 2018; Kettwig *et al.*, 2015; Miyake *et al.*, 2017; Morton *et al.*, 2017; Pandolfo *et al.*, 2020; Rinaldi *et al.*, 2012; Sancho *et al.*, 2017; Zong *et al.*, 2015), while serious cancers and tumour metastases emerge when the pro–death function is targeted (Jeong *et al.*, 2006; Lewis *et al.*, 2012; Scott *et al.*, 2016; Urbano *et al.*, 2005).

In this chapter, we have delved into the biophysical, biochemical and structural deficiencies developed by two pathogenic missense mutations of AIF of recent discovery. The T141I and M340T replacements are of significantly rare prevalence and both derive in a neurodegenerative disease known as Cowchock syndrome (a.k.a. CMTX4). These variants, while of similar phenotypes, course respectively with: (i) a grave infantile mitochondrial encephalomyopathy and (ii) an early–onset axonal sensorimotor neuropathy coupled with hearing loss and, in some of the few reported cases, colour–blindness (Bogdanova–Mihaylova *et al.*, 2019; Heimer *et al.*, 2018).

The substitution of T141 with an Ile residue results in a significant loss of polarity and space, in a position of close proximity to the enzyme's active site. This replacement in the FAD–binding domain may have two direct and significant consequences: firstly, nearby residues with key roles in catalysis and the dimerization process (such as P173, K177, H454 and W483) suffer an alteration of their environment; and secondly, the

H–bond network that aids the stabilization of the FAD cofactor (specifically of its ribityl pyrophosphate moiety) is cut short. The T141I replacement does not impact the expression or folding of AIF in any way but it increases its redox potential by more than 60 mV, significantly boosting its ability to accept electrons from the NADH coenzyme. This development, combined with easier O_2 access to the FAD as the most likely result of the loss of the H–bonds, leads to a considerably reduced CTC stability. The alteration of the environment of H454 (a key residue in the dimerization process) may just as well be at play, modifying the monomer–monomer interactions to yield the observed lessened dimer stability but untouched ability to dimerize. A slight increase was also observed in the enzyme's HT efficiency that was not reflected in its diaphorase activity, demonstrating that while the higher redox potential must result in a more favourable HT between the cofactor and the coenzyme, the reaction is still limited by either the binding of the substrate or the release of the product (indeed, almost analogous K_d values were obtained). Furthermore, the thermal stability was significantly impaired, but the destabilizing effect of the binding of the NADH was still present and yielded almost identical values to that of the native protein.

In contrast, the M340T aberration takes place in the NADH–binding domain of AIF, within a loop that plays a key role modulating the conformation of the catalytic NADH pocket. Remarkably, the behaviour presented by the mitochondrial form of the protein differed greatly from that of its apoptotic form, reinstating the observed variations already present between both forms in the WT. The only significant change that could be noted in $M340T_{\Delta 101}$ was the apparition of a novel substrate–inhibition profile in the steady–state, whose parameters converged to almost that of the WT as the sample aged. This demonstrated the presence of a toxic population that was slowly displaced by a more native–alike one as the time passed.

$M340T_{\Delta 77}$, however, reported a remarkable accumulation of changes, coursing with a significant structural alteration in the active site (as seen in its UV/Vis absorption and CD spectra) but no apparent impact on its redox potential when free. The substitution of a medium–sized hydrophobic residue such as M340 with a small polar Thr results in a considerable gain of space and polarity, which potentially impedes the variant residue's ability to interact with neighbour F310. The increased freedom of movement of F310 would lead in turn to a greater difficulty in reaching the optimal conformation to properly stack the nicotinamide ring of the NADH coenzyme, resulting in the observed inability to stabilize the CTC even in the presence of protein partner CHCHD4 (although its capacity to indeterminately stabilize the reduced protein

reflects its potential use as a therapeutical treatment). Additionally, the acquisition of a more spacious binding pocket may lead to the reported higher affinity of the variant towards its NADH substrate, which coupled with the high CTC instability results in a remarkable increase in the enzyme's efficiency as an NADH oxidase. Finally, the conformational changes caused by the replacement seemed to indirectly impact the C–loop through its mutual interaction with the central β–sheet, leading to the premature unfolding of the regulatory motif. This change would lead as a consequence to two important effects: a displacement of the monomer–dimer equilibrium towards the dimeric form even in the absence of NADH; and a higher thermal instability with no apparent ligand binding destabilizing effect.

In essence, these findings on the structural, biochemical and biophysical alterations suffered by the T141I and M340T replacements aspire to better the understanding of the structure/function relationships in human AIF, particularly pertaining to the associated neurodegenerative diseases that arise from defects on its critical pro–life function. Diagnosis and treatment of AIF–related disorders are still notoriously hard nowadays, reinstating the key therapeutical importance of shedding some light into the molecular basis of these diseases. Further research is deemed necessary to devise a specific regimen to target the reported deficiencies of the variants of interest.

6. W483 IN THE APOPTOSIS INDUCING FACTOR

Critical aftermath on NADH oxidation

The PhD candidate contributed by performing the following:

- Production and purification of WT $AIF_{\Delta 77}$ and $AIF_{\Delta 101}$ as well as its W483 variants
- Spectroscopic characterization (excepting the CD spectra of the $AIF_{\Delta 101}$ variants)
- Midpoint reduction potential assays
- Pre–steady state kinetics measurements (excepting those of the $AIF_{\Delta 101}$ variants)
- Kinetic isotopic effect assays
- Thermal stability assays

Abstract

As a key mitochondrial flavoprotein, AIF aids the scrupulous functioning of mitochondria in healthy cells, supporting the maintenance and stability of the respiratory supercomplexes. However, upon pro–apoptotic stimuli it may be translocated to the nucleus, where it triggers caspase–independent cell death through chromatin condensation and DNA fragmentation. The FAD cofactor of AIF can be reduced by the NADH coenzyme, leading to dimerization and the formation of a significantly stable $FADH^{-}$:NAD^{+} CTC. The resulting monomer–dimer equilibrium is further regulated by the allosteric binding of non–catalytic $NADH_B$. Tryptophan 483 enacts a fundamental part in this process, as it is involved in an extensive H–bond network that stabilizes the conformation of the catalytic $NADH_A$ while concurrently T–stacking between the flavin isoalloxazine ring and the nicotinamide of $NADH_B$. This permits the formation of a catalytically–competent complex for HT between the FAD and $NADH_A$, determining the low efficiency of AIF as an NADH oxidase. Three W483 variants expected to alter the environment of the flavin isoalloxazine ring (W483G, W483L and W483Y) had been previously generated in our group, producing remarkable effects in both HT and dissociation rates. Said replacements are further characterized in this chapter, proving their critical implications on the efficiency and dynamics of HT, redox potential and thermodynamic stability.

RESUMEN

Como flavoproteína mitocondrial clave, AIF ayuda en el meticuloso funcionamiento de las mitocondrias en células sanas, apoyando el mantenimiento y la estabilidad de los supercomplejos respiratorios. Sin embargo, ante estímulos pro–apoptóticos puede ser translocada al núcleo, donde desencadena muerte celular independiente de caspasas mediante la condensación de la cromatina y la fragmentación del ADN. El cofactor FAD de AIF puede ser reducido por la coenzima NADH, resultando en la dimerización de la proteína y la formación de un CTC $FADH^{-}$:NAD^{+} significativamente estable. El equilibrio monómero–dímero resultante está además regulado por la unión alostérica del $NADH_B$ no catalítico. El triptófano 483 desempeña un papel fundamental en este proceso, ya que está involucrado en una extensa red de puentes de hidrógeno que estabiliza la conformación del $NADH_A$ catalítico mientras simultáneamente se apila entre el anillo isoaloxazina de la flavina y la nicotinamida del $NADH_B$. Esto permite la formación de un complejo catalíticamente competente para la transferencia de hidruro entre el FAD y el $NADH_A$, determinando la baja eficiencia de AIF como una NADH oxidasa. Tres variantes del W483 que podían potencialmente alterar el entorno del anillo isoaloxazina de la flavina (W483G, W483L y W483Y) fueron previamente generadas en nuestro grupo, produciendo efectos notables tanto en la transferencia de hidruro como en las tasas de disociación. Dichas sustituciones quedan caracterizadas en mayor extensión en este capítulo, demostrando sus implicaciones críticas en la eficiencia y dinámica de la transferencia de hidruro, el potencial redox y la estabilidad termodinámica.

6.1. INTRODUCTION

As a paramount human mitochondrial flavoenzyme, AIF aids the scrupulous functioning of mitochondria in healthy cells, supporting the maintenance and stability of the respiratory supercomplexes as well as the control of the mitochondrial ROS (Delavallé *et al.*, 2020; Hangen *et al.*, 2015; Modjtahedi *et al.*, 2015). Under normal conditions, AIF resides within the IMS, anchored to the IM in an equilibrium between its oxidized and reduced forms. However, upon pro–apoptotic stimuli it may be cleaved and subsequently translocated to the nucleus, where it triggers caspase–independent cell death by promoting chromatin condensation and DNA fragmentation (Artus *et al.*, 2010; Baritaud *et al.*, 2010; Cabon *et al.*, 2012) through its interaction with protein partners CypA and H2AX, as well as on its own (chapter 4, Artus *et al.*, 2010; Baritaud *et al.*, 2012; Cande *et al.*, 2004; Novo *et al.*, 2022; Susin *et al.*, 1999). Due to its crucial –albeit contradictory– functions, defects in AIF give rise to major dysfunctions in oxidative phosphorylation, resulting in human pathogenic disorders that typically course with severe neurodegeneration (Meyer *et al.*, 2015; Modjtahedi *et al.*, 2016).

The cell survival function of AIF stems from its oxidoreductase domain (Miramar *et al.*, 2001). AIF is ubiquitously expressed across eukaryotes (Novo *et al.*, 2021), but it happens to present two unique insertions in mammalian cells that are in fact of substantial importance: a flexible regulatory motif known as the C–loop (aa 509–560 in human AIF) and a key β–hairpin structural motif (aa 190–202 in human AIF) (Ferreira *et al.*, 2014; Sevrioukova, 2009) (*Fig. 6.1*). The regulatory C–loop motif happens to belong to the C–terminal domain of AIF and it contributes to occlude access to the enzyme's active site in a redox–dependent manner (Sevrioukova, 2009; Villanueva *et al.*, 2019). Thus, when the protein FAD is in the oxidized state, the C–loop folds towards the flavin's isoalloxazine ring, but any direct contact with the redox cofactor is efficiently blocked by the side chain of residue tryptophan 483. In combination with this W483, the C–loop 517–533 moiety (folded into two short α–helices in the oxidized protein) is able to dwindle solvent accessibility to the flavin cofactor, while also directly interacting with the other basic regulatory motif of AIF, the 190–202 β–hairpin, through residue R201 (*Fig. 6.2A*).

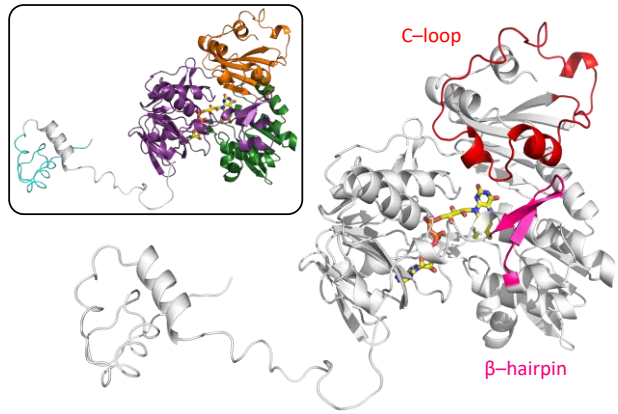

Figure 6.1. Unique insertions of mammalian AIFs. Crystal structure of human AIF (PDB 4BV6) with the 1–127 N–terminal region modelled in RaptorX. The structure is shown as cartoon, with the FAD cofactor represented as sticks CPK coloured in yellow. The C–loop (509–560) and β–hairpin (190–202) insertions appear highlighted in red and pink respectively. The inset shows the same structure with the bipartite FAD–binding, NADH–binding and apoptotic C–terminal protein domains respectively in violet, green and orange, and the MLS in light blue.

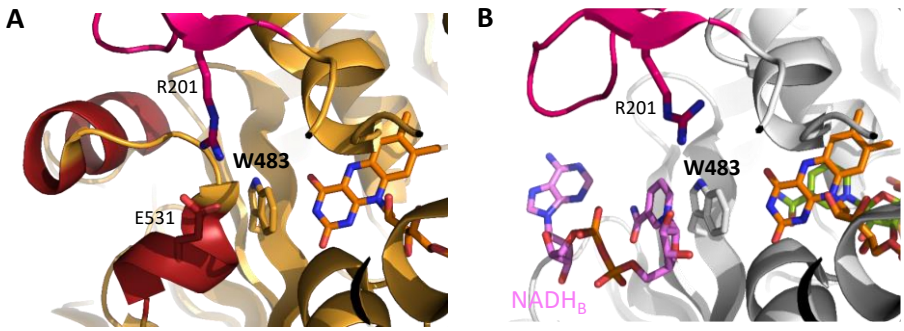

Figure 6.2. W483 blocks access of the C–loop and NADH$_B$ to the active site. Cartoon representation of (A) AIF$_{ox}$ and (B) AIF$_{rd}$:2NADH (PDB 4BV6 and 4BUR respectively) CPK coloured in light orange and white respectively. The 190–202 β–hairpin and the 517–533 C–loop moiety (folded in AIF$_{ox}$ into two short α–helices, comprising residues 517–524 and 529–533 respectively, and disordered in AIF$_{rd}$:2NADH) are CPK coloured in red and pink. Key residues are labelled and represented as sticks. The cofactor and coenzymes are represented as sticks CPK coloured in orange for the FAD, in green for NADH$_A$ and in violet for NADH$_B$.

The FAD cofactor of AIF is reduced by NADH, leading to the dimerization of AIF and to the formation of a significantly stable FADH$^-$:NAD$^+$ CTC. The resulting monomer–dimer equilibrium is thought to act as a sensor of the mitochondrial redox state, specifically regarding the NADH/NAD$^+$ levels (Brosey *et al.*, 2016; Ferreira *et*

al., 2014). However, upon reduction of the protein the two short α–helices of the C–loop become disordered, clearing the path for the binding of a second non–catalytic NADH molecule, $NADH_B$ (*Fig. 6.2B*). This molecule is of particular relevance, as it is envisaged to allosterically regulate certain functions of AIF (Brosey *et al*., 2016; Ferreira *et al*., 2014; Ferreira *et al*., 2018; Sorrentino *et al*., 2015).

W483 becomes of critical importance in this context, as it enacts a fundamental part in the binding of both NADH molecules (*Fig. 6.3*). On the one side, it takes part in an extensive H–bond network (involving residues G308, F310, L311, E314, E336, G399, E453 and H454, as well as itself) that stabilizes the conformation of catalytic $NADH_A$, allowing its nicotinamide ring to properly stack between the *re*–face of the FAD and the ring of residue F310. This permits the formation of a catalytically–competent CTC for HT between the FAD and $NADH_A$ which is additionally remarkably stable against molecular oxygen reoxidation, determining the low efficiency of AIF as an NADH oxidase and reinforcing its ability to act as a redox sensor (Ferreira *et al*., 2014).

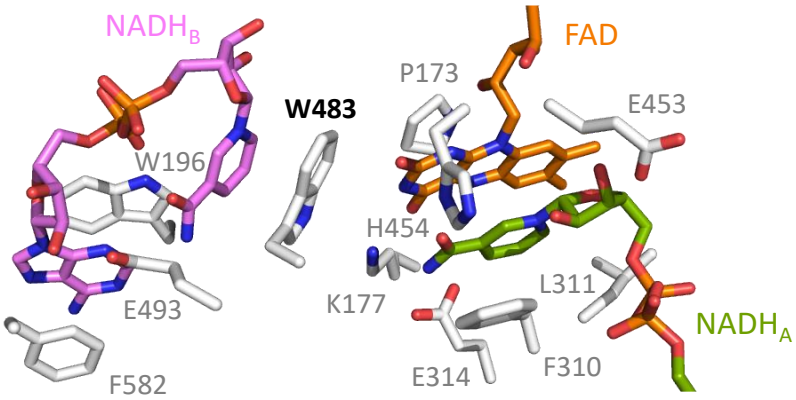

Figure 6.3. Architecture of W483 in the binding sites of $NADH_A$ and $NADH_B$. Environment of the binding sites for the redox active motifs of FAD, $NADH_A$ and $NADH_B$ in AIF_{rd}:2NADH (PDB 4BUR). Key residues involved in the network of H–bonds and hydrophobic stacking interactions are labelled and represented as sticks, CPK coloured in white. The cofactor and coenzymes are labelled and represented as in figure 6.2.

On the other side, W483 concurrently stacks between the flavin isoalloxazine ring (T–stack) and the nicotinamide of $NADH_B$ (π–stack), which happens to bind at the *si*–face of the FAD cofactor, effectively blocking external access to the active site and potentially limiting its action to that of an allosteric factor. Residues W196, E493 and F582 also contribute to $NADH_B$ binding (*Fig. 6.3*), with the former belonging to the

key β–hairpin. W196 and E493, in particular, have been previously proven to modulate the properties of AIF as a low efficient NADH oxidase through the stabilization of its CTC state (Ferreira *et al.*, 2014; Romero–Tamayo *et al.*, 2021; Villanueva *et al.*, 2019).

In order to shed light into the critical role of W483, three replacements expected to alter the environment of the flavin isoalloxazine ring (Gly, Leu and Tyr) were generated in our group (Villanueva, 2015). The W483G substitution was expected to severely impact the stabilization of the FAD cofactor, potentially resulting in a major alteration of the environment. Similarly, the W483L variant would diminish the aromaticity of the active site, and significantly reduce the stacking capability of position 483. Furthermore, both replacements should lead to a boost of flexibility in the FAD environment as a consequence of their more compact side–chains, potentially facilitating solvent access. In comparison, W483Y would act as a conservative replacement, substituting the indole ring of the Trp with the phenol ring of the Tyr. This change is still expected to result in a slight increase of polarity and a minor reduction of the W483 stabilization effect, as it decreases the charge delocalization caused by its stacking with $NADH_B$.

The characterization of the three W483 variants in their apoptotic form was initiated by Raquel Villanueva in her PhD thesis (chapter 7 in Villanueva, 2015), hoping to establish the implications of this tryptophan residue on the redox activity of AIF. The stability of the CTC was not notably altered by any of the replacements, but the ability to dimerize of the glycine and leucine variants appeared to be somehow affected, indicating that W483 may be involved in dimer formation to some extent. Furthermore, a significantly higher efficiency of the reductase activity could be clearly observed in all variants (although the effect was remarkably greater in the more aggressive substitutions), coupled with an improved affinity for NADH. Steady–state assays demonstrated that the HT process from NADH to the FAD cofactor was also considerably more efficient, hinting to the critical role of W483 in the modulation of the redox potential and the overall catalytic mechanism of the enzyme.

These three W483 functional variants are further characterized in this chapter, both in their soluble mitochondrial ($AIF_{\Delta 77}$) and apoptotic ($AIF_{\Delta 101}$) forms, in order to deepen our understanding on their crucial implications on the efficiency and dynamics of the HT mechanism, as well as on the protein mid–point reduction potential and thermodynamic stability.

6.2. Results and Discussion

6.2.1. Spectroscopic properties

6.2.1.1. UV/Visible absorption spectra

UV/Vis absorption spectra of the W483 AIF_{ox} variants were recorded once purified to homogeneity in order to establish whether the flavin was correctly incorporated and in the oxidized state (*Fig. 6.4*). Minor differences could be noted between the soluble apoptotic and mitochondrial forms in all samples, as had been previously reported in chapter 5 for the WT protein.

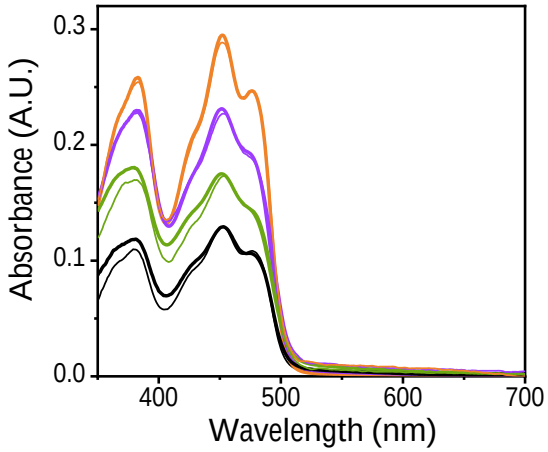

Figure 6.4. UV/Vis absorption spectra of WT AIF and the W483 variants in their soluble mitochondrial and apoptotic forms. Bold lines represent the spectra of the apoptotic forms, thin lines represent that of the mitochondrial forms. WT data are shown in black, W483G in green, W483L in purple and W483Y in orange. Measurements were performed in 50 mM Kpi buffer, pH 7.4, at 25 °C and at different protein concentrations (WT ~10 µM, W483G ~15 µM, W483L ~20 µM and W483Y ~25 µM) to facilitate visualization of the figure.

The distinctive flavin bands I and II at 452 and 380 nm respectively could be clearly distinguished in all variants, as well as the characteristic shoulder at 480 nm. This shoulder was particularly marked in the W483Y variants, but appeared slightly shielded in the other replacements. A_{380}/A_{452} and A_{452}/A_{480} ratios were slightly higher in the W483G and W483L variants than in the WT or variant W483Y in both forms (A_{380}/A_{452} = 1.0 vs 0.9 and A_{452}/A_{480} = 1.3 vs 1.2), reinstating the potential modulation of the FAD cofactor environment by the side chain of residue 483. A_{280}/A_{452} ratios

followed a similar pattern, with greater values for the mitochondrial and apoptotic forms of W483G (12.1 and 8.8 respectively) and W483L (12.1 and 10.6) in comparison to that of the WT (6.9 and 8.5) or variant W483Y (8.0 and 7.8). This observation indicates that the glycine and leucine variants, as potentially more aggressive replacements, might modify the conformation of the redox centre in a way that compromises the binding environment and/or binding stability of the FAD cofactor, ultimately resulting in a significantly lower population of holoenzyme particularly apparent in the soluble mitochondrial forms.

6.2.1.2. Far–UV and near–UV/Vis CD spectra

Far–UV and near–UV/Vis CD spectra of the W483 variants in their mitochondrial form were recorded, both in presence and in absence of the reducing NADH coenzyme, to analyse the effect of each replacement on the protein's secondary structure and environment of the FAD cofactor. The same had been previously performed in our group by PhD. Raquel Villanueva for the apoptotic form, whose results are also shown and analysed here.

Far–UV CD spectra indicated some manner of divergence in the variants as compared to the WT, with $W483Y_{\Delta 77}$ actually exhibiting the greatest degree of alteration both in its oxidized (*Fig. 6.5A*) and reduced states (*Fig. 6.5B*). Characteristic minima at ~208 and ~222 nm could mostly still be observed in all oxidized samples, indicating a high α–helix content, although the decrease in the relative intensity of the 208 nm minimum upon NADH–induced reduction observed in the WT was only slightly apparent in the more aggressive glycine and leucine replacements. In fact, both the $W483G_{ox}$ and $W483L_{ox}$ variants presented spectra that more closely resembled that of WT_{rd} (being significantly narrower, particularly in their apoptotic form, and presenting a decrease in the relative intensity of the ~222 nm minimum), demonstrating that their structure remained mostly unchanged after reduction. This is in agreement with previous dimerization assays performed by PhD. Raquel Villanueva, where it can be clearly observed that both variants are able to form dimers even in absence of NADH (Villanueva, 2015). Meanwhile, both minima were slightly shifted in the mitochondrial form of $W483Y_{ox}$ and the local maximum between the peaks was significantly more pronounced, hinting to a potential increase in the percentage of random coils. Remarkably, this local maximum between the peaks was not lost upon reduction, although its intensity diminished somewhat.

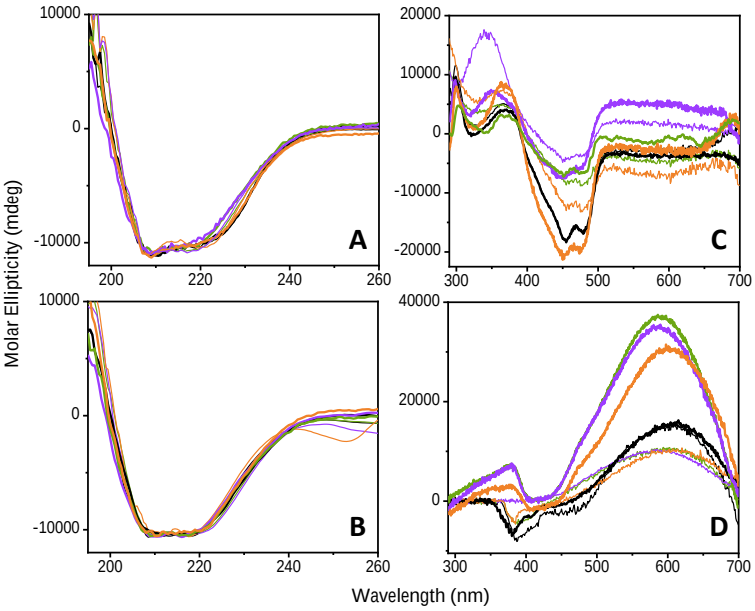

Figure 6.5. CD spectra of WT AIF and the W483 variants in their mitochondrial and apoptotic forms. Far–UV (A, B) and near–UV/Vis (C, D) CD spectra of the oxidized (upper panels) and reduced (lower panels) states were recorded at 25 °C (10 °C for the apoptotic form) in 50 mM Kpi buffer, pH 7.4, at a final ionic strength of 150 mM. To generate the reduced form, 100–fold excess of NADH was added to the sample prior to the measurement. Spectra are represented as in figure 6.4. Spectra were recorded at protein concentrations of 2 µM and 20 µM for the far–UV and near–UV/Vis CD respectively.

Near–UV/Vis CD spectra further alerted to the severe fallout of every W483 replacement regarding the conformation of the active site. The characteristic maxima (~300 nm and ~365 nm) and minima (~453 and 477 nm) exhibited by WT_{ox}, which reflect the burial of the FAD cofactor within the protein environment, were considerably altered in shape, intensity and position in the $W483_{ox}$ variants (*Fig. 6.5C*), with $W483L_{\Delta 77ox}$ actually presenting an inversion/displacement of intensity in the ~300–400 nm range. The degree of alteration appeared to be the greatest in the glycine and leucine replacements independently of their form, reinstating their severe impact. The changes expected after FAD reduction and CTC stabilization (lack of signal at 300 nm and in the 350–500 nm range, and broad bands at ~600 nm) were surprisingly mostly apparent in all variants (possibly hinting towards a somewhat stabilizing effect of the NADH binding), although a significant increase of the intensity of the broad band corresponding to the CTC could be observed in their apoptotic forms (*Fig. 6.5D*). Furthermore, the spectra of $W483G_{rd}$ and $W483L_{rd}$ exhibited a clear shift of the

maximum at ~600 nm towards values closer to 550 nm, both in their apoptotic and mitochondrial forms, which was not the case for conservative substitution W483Y.

The modulation indicated by the near–UV/Vis CD spectra of the glycine and leucine replacements demonstrates that these variants are remarkably disruptive with regard to the environment of the FAD cofactor and the NADH binding mode. This suggests that these mutations severely compromise the role of position 483 in the interaction network of the active site through the loss of both the ability to stack and to form H–bonds. In comparison, the tyrosine replacement results in an only moderate alteration of the H–bond network and it maintains to a lesser degree the capacity to stack other aromatic rings, potentially still fulfilling the role of position 483 in the stabilization of the enzyme's active site.

6.2.1.3. Mid–point reduction potential

The mid–point reduction potential of the FAD cofactor is directly and markedly modulated by its environment within the protein. As the previous results obtained with the W483 $AIF_{\Delta 101}$ variants by PhD. Raquel Villanueva together with the spectroscopic characterization seemed to indicate that this property might have been seriously affected, the xanthine oxidase method was employed to study the impact of the W483 replacements on the conformation of the active site (*Table 6.1*). Compared to WT AIF, which exhibited values of –377 mV and –345 mV for its mitochondrial and apoptotic forms respectively, the tyrosine substitution yielded the smallest variation, with values of –391 mV (ΔE_m = –14 mV) and –297 mV (ΔE_m = +48 mV) respectively. This observation agrees well with the W483Y variant being the most conservative replacement and reinforces the importance of residue W483, as even the least variation in its side–chain leads to a noticeable reshaping of the electronic environment of the isoalloxazine ring.

Table 6.1. Mid–point reduction potential of WT AIF and the W483 variants.

AIF	WT		W483G		W483L		W483Y	
variant	Δ77	Δ101	Δ77	Δ101	Δ77	Δ101	Δ77	Δ101
E_m (mV)	–377	–345	–197	–175	–248	–213	–391	–297

Performed at 25 °C in 50 mM Kpi, pH 7.4. Errors considered in the measured parameters (below ± 5%) were taken larger than the numerical error after the fitting analysis.

Meanwhile, the W483G and W483L replacements both resulted in an ample displacement of the flavin's mid–point reduction potential towards less negative values, presenting values of –197 mV (ΔE_m = +180 mV) and –175 mV (ΔE_m = +170 mV) for the mitochondrial and apoptotic forms of W483G respectively, and of –248 mV (ΔE_m = +129 mV) and –213 mV (ΔE_m = +132 mV) for that of W483L. In both cases the observed effect was of significant magnitude, reinstating the impact of said aberrations on the flavin environment. The loss of aromaticity that arises from these replacements potentially increases the solvent accessibility to the isoalloxazine ring and alters its interacting network, severely affecting its redox properties. This could also explain why the effect of the glycine replacement is slightly greater than that of the leucine, as the latter might still be able to interact with its neighbours by means of its hydrophobic side–chain and somehow better shield the flavin from the solvent.

6.2.2. NADH oxidase activity

6.2.2.1. Transient–state assays

Previous studies in our group have already proved the critical impact of the W483 substitutions under study here on the NADH oxidase activity of AIF in its apoptotic form, yielding a robust increase in efficiency (up to ~480–fold for W483G) and in the affinity towards the NADH substrate (Villanueva, 2015). In order to deepen our understanding on this matter, the effect of the W483 variants on HT efficiency of the AIF semi–reductive half reaction was also analysed in their mitochondrial form through SF transient kinetics. In all cases, kinetic traces were recorded at increasing NADH concentrations, portraying a basically irreversible two–electron reduction process for the FAD cofactor paired with the formation of a long–wavelength broad band around 500–800 nm reflecting the stabilization of the AIF_{rd}:NAD^+ CTC species (*Fig. 6.6*). Global analyses of the spectral range time evolutions (*Fig. 6.7*) were best fitted to a one–step model (A → B) as previously described for the WT (Ferreira *et al.*, 2014). Obtained k_{obs} values exhibited hyperbolic dependency on the concentration of NADH, allowing the determination of k_{HT} and K_d^{NADH} upon fitting to equation 3.17 (*Fig. 6.7, Table 6.2*).

The behaviour exhibited by the W483 $AIF_{\Delta 77}$ variants was analogous to the precedent of their apoptotic forms (*Table 6.2*) (Villanueva, 2015). A substantial increase in efficiency was demonstrated by all variants for the HT process, fundamentally caused

by a significant boost in their k_{HT} values, with the glycine and leucine replacements yielding by far the greatest gain (>260–fold and ~80–fold in efficiency respectively, versus ~3–fold for W483Y$_{\Delta 77}$). This observation reinstates that neither the W483G nor the W483L variants are limited in their NADH oxidase activity by the HT step, similarly to their apoptotic forms (*Table 6.2*) (Villanueva, 2015). Furthermore, their observed increased efficiency coupled with their significantly greater mid–point reduction potentials envisage for the W483 residue a critical role in determining the otherwise remarkably low efficiency of WT AIF as an NADH oxidase, through its practically unassisted momentous modulation of the environment of the redox centre.

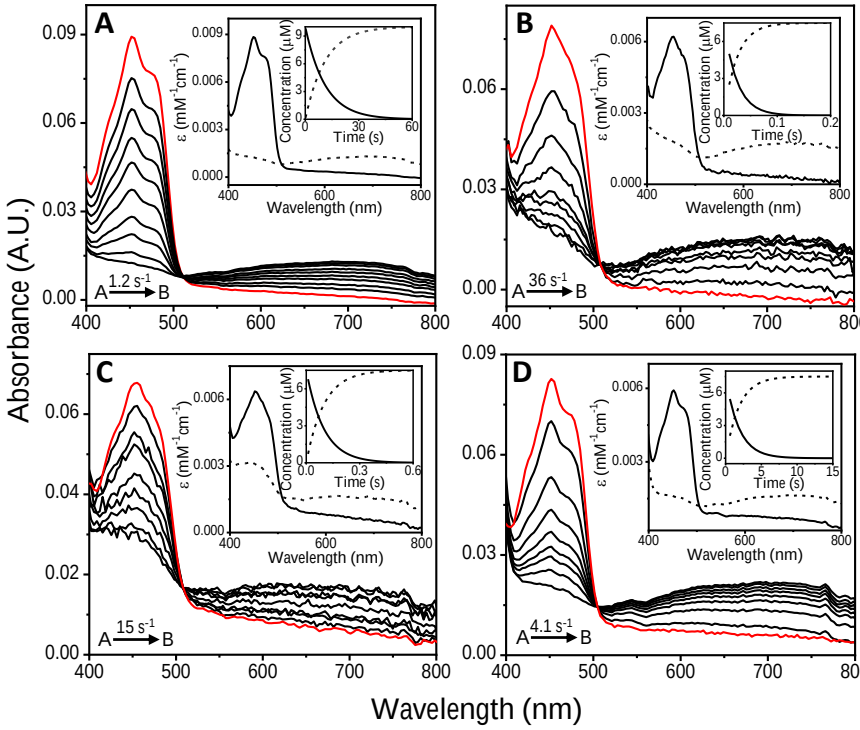

Figure 6.6. Transient kinetics of NADH oxidation in WT AIF and the W483 variants in their mitochondrial form. Spectral evolution of flavin reduction of 7.5 μM (A) WT$_{\Delta 77}$, (B) W483G$_{\Delta 77}$, (C) W483L$_{\Delta 77}$ and (D) W483Y$_{\Delta 77}$ after mixing with NADH (75 or 150 μM for W483G$_{\Delta 77}$ and W483L$_{\Delta 77}$ respectively, and 2.5 mM for WT$_{\Delta 77}$ and W483Y$_{\Delta 77}$ AIF) in air–saturated 50 mM Kpi, pH 7.4, at 25°C. Spectra were recorded in the 0.6–60 s range for WT$_{\Delta 77}$ and W483Y$_{\Delta 77}$ or in the 0.01–1 s range for W483G$_{\Delta 77}$ and W483L$_{\Delta 77}$ after mixing. Lines in red correspond to the spectra of the oxidized enzymes before mixing. The corresponding insets portray the absorbance spectra of the predicted initial and final species obtained by fitting the spectral evolution to a single step model (A→B), and the evolution of the concentration for each species.

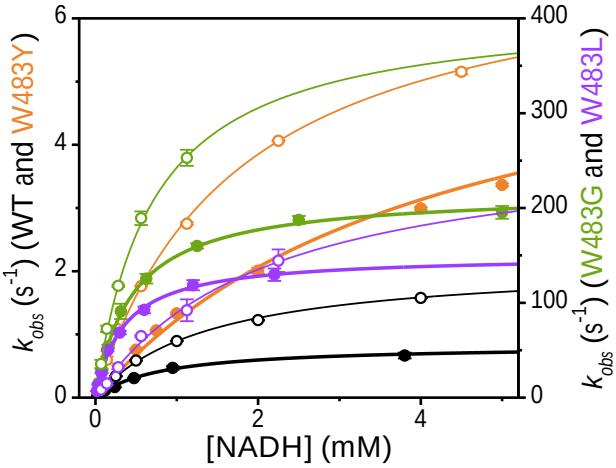

Figure 6.7. Analysis of transient kinetics for NADH oxidation by WT AIF and the W483 variants in their mitochondrial and apoptotic forms. Dependence of the observed rate constants for flavin reduction on the concentration of NADH for WT AIF (black) and variants W483G (green), W483L (purple) and W483Y (orange) in their mitochondrial (open symbols) and apoptotic (closed symbols) forms. Lines (thin for the mitochondrial forms, bold for the apoptotic forms) represent fitting of the experimental data to equation 3.17. Data from the apoptotic forms taken from the PhD thesis of Raquel Villanueva.

Table 6.2. Kinetic parameters for the FAD semi–reductive half reaction of the NADH oxidase activity in WT AIF and the W483 variants.

AIF variant	k_{HT} (s^{-1})	K_d^{NADH} (mM)	k_{HT}/K_d^{NADH} ($s^{-1}mM^{-1}$)
$WT_{\Delta 77}$	2.1	1.4	1.6
$W483G_{\Delta 77}$	>300	0.7	>420
$W483L_{\Delta 77}$	276	2.1	130
$W483Y_{\Delta 77}$	7.2	1.7	4.2
$WT_{\Delta 101}$*	1.0	1.1	0.9
$W483G_{\Delta 101}$*	216	0.4	540
$W483L_{\Delta 101}$*	150	0.3	500
$W483Y_{\Delta 101}$*	8.2	5.7	1.4

Performed at 25 °C in 50 mM Kpi, pH 7.4. Errors considered in the measured parameters (below ± 5% or 20% for k_{HT} and K_d^{NADH} respectively) were taken larger than the numerical error after the fitting analysis. * Data from Villanueva, 2015, performed at 25 °C (8 °C for $W483G_{\Delta 101}$) in 50 mM Kpi, pH 8.

In contrast, the impact of the W483 $AIF_{\Delta 77}$ variants on the dissociation constant of the NADH (K_d^{NADH}) was not as pronounced when compared to that of the HT constant (~0.5–fold, ~1.5–fold and ~1.2–fold for $W483G_{\Delta 77}$, $W483L_{\Delta 77}$ and $W483Y_{\Delta 77}$), indicating that the binding of the coenzyme to the variants was only marginally affected despite the potential key role of W483 in its stabilization. Indeed, the action of W483 is performed indirectly on the catalytic $NADH_A$ through its interaction with the isoalloxazine ring of the FAD, while other residues stabilize the coenzyme's nicotinamide ring for its proper stacking with the cofactor (Villanueva *et al.*, 2015). The replacement of W483 modifies the mid–point reduction potential of the cofactor in a considerable manner, ultimately making the reaction significantly faster.

6.2.2.2. Kinetic Isotope Effect assays

Fast kinetics measurements were additionally employed to determine the 1° and 2° KIEs for HT from NADH to the W483 variants in their mitochondrial and apoptotic forms, as well as the temperature dependence of the rate constants and KIEs through the use of the Arrhenius equation (Knapp and Klinman, 2002). The resulting parameters provide crucial information on the structural organization and dynamics of the active site during the HT process (Sánchez, 2013), while the degree of temperature dependence is a key descriptor of the reaction coordinate coursing with tunnelling (Anoz–Carbonell *et al.*, 2020b). The environmentally–coupled tunnelling model was employed to determine HT and deuterium transfer (DT) observed rate constants at different temperatures. An exhaustive description of the method and its background is provided in chapter 3, section 3.5.2.2.

Primary KIE

The 1° KIE can be observed when the bond to the isotopic substituent is formed or broken during HT catalysis, and it provides valuable information regarding the structure of the transition state. Available crystallographic structures of AIF suggest that the hydride molecule that is exchanged from the C4 of the nicotinamide of the NADH coenzyme to the N5 of the isoalloxazine ring of the FAD cofactor is actually found in position 4S of the former (*Fig. 6.8*) (Ferreira *et al.*, 2014). As a consequence, the 1° H/D KIE of WT AIF and its W483 variants was studied through the use of the 4S–NADD isotopologue (*Fig. 6.9, Table 6.3*).

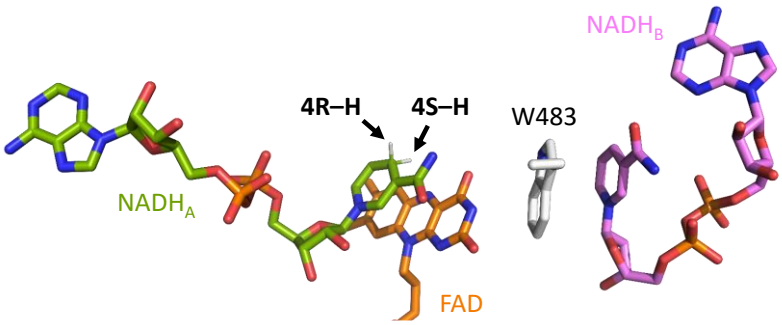

Figure 6.8. Expected localization of the two C4n hydrogen atoms of the NADH coenzyme that may potentially participate in the HT process to the FAD cofactor. Interaction model for the potential arrangement of the AIF_{rd}:2NADH reactant species constructed based on the relative disposition of the NADH and FAD molecules in the AIF_{rd}:2NADH (PDB 4BUR) structure. Residue W483 is CPK coloured in white and represented as sticks. The cofactor and coenzymes are represented as sticks CPK coloured in orange for the FAD, in green for $NADH_A$ and in violet for $NADH_B$. Hydrogen 4S of $NADH_A$ is found at the optimal position for HT to the N5 of the FAD cofactor, whereas hydrogen 4R is most probably not directly involved in the reaction.

Observed rate constants for WT $AIF_{\Delta 77}$ and $AIF_{\Delta 101}$ remained within similar ranges at all assayed temperatures. Both forms exhibited parallel lines in their Arrhenius plots for HT and DT (*Fig. 6.9A, B*), identical E_a values and close to unity A_H/A_D ratios (*Table 6.3*). These features are typically associated with passive dynamics contributions to the reaction coordinate, and agree well with active sites suited for the particular reaction they must carry out (with the donor and acceptor molecules stabilized at the optimal distance). As such, they do not require the additional boost of energy provided by an increase in the temperature for the HT/DT transfer to take place. Moreover, the lack of a temperature dependence on the KIE reflects the existence of a tunnel–ready conformation.

Noticeably, the use of the 4S–NADD isotopologue resulted in a primary KIE value of approximately 1 for WT $AIF_{\Delta 77}$, and a value only slightly greater than one for WT $AIF_{\Delta 101}$ (*Fig. 6.9C, D*). Such small KIE values might indicate the presence of a transition state that is either asymmetrical (with the C–H bond broken less, in an earlier transition state, or more, in a later one) or nonlinear in the WT (Anoz–Carbonell *et al.*, 2020b; Westheimer, 1961; Zuidema *et al.*, 2008). This observation would be in agreement with AIF greatly stabilizing one of its two potential CTC states (namely,

NAD^+:$FADH^-$) during the HT/DT process, where the hydride moiety is found closer to the FAD acceptor than to the NADH donor.

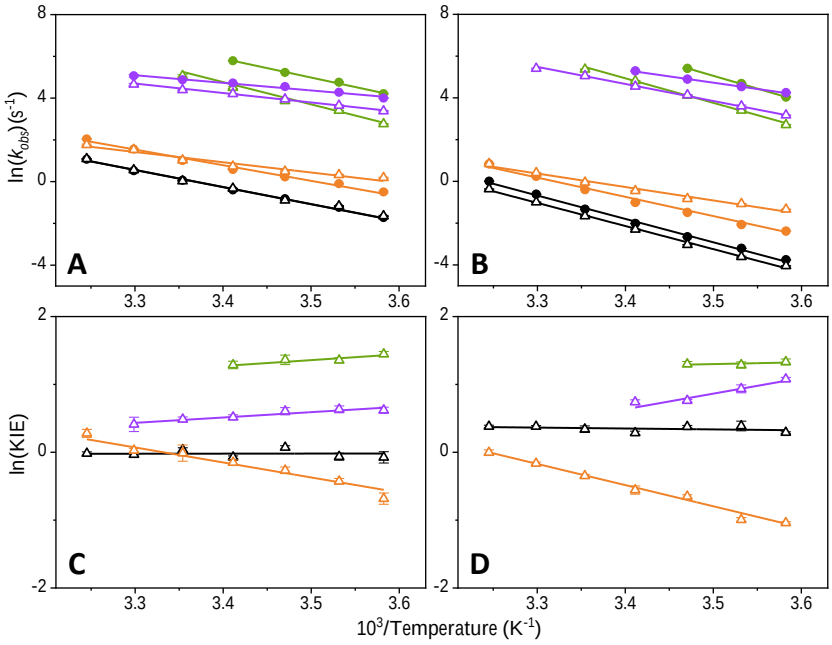

Figure 6.9. Temperature dependence of the kinetic parameters for the HT/DT processes from NADH/4S–NADD to WT AIF and the W483 variants. Arrhenius plots of the observed kinetic constants for the mitochondrial (A) and apoptotic (B) forms of WT AIF and the W483 variants. Data from the NADH HT and 4S–NADD DT processes are respectively shown as solid circles and blank triangles. Solid lines represent the fitting to the linearized Arrhenius equation (eq. 3.21). Temperature dependence of the estimated 1° KIEs for the mitochondrial (C) and apoptotic (D) forms. Data from WT, W483G, W483L and W483Y AIF are respectively shown in black, green, purple and orange.

In contraposition, all W483 variants yielded a more significant temperature dependence in their 1° H/D KIE, exhibiting intersecting lines in their Arrhenius plots for HT and DT, slightly differing E_a values and A_H/A_D ratios considerably away from the unity (*Fig. 6.9, Table 6.3*). These indicate that the active sites of the variants potentially suffer a significant modulation of their environment for the HT process to take place, which ultimately leads to the donor and acceptor molecules being forced to remain in alternative conformations that do not typically coincide with their optimized native ones. As such, active (a.k.a. gating) protein dynamics are usually required to sample the donor–acceptor distance in search for the most optimal

condition for tunnelling. Under these circumstances, the extra energy supplied by the temperature becomes critical, as it may provide sufficient to overcome the energetic barrier otherwise stablished by the unoptimized disposition of the reactants.

A particularly intriguing profile was exhibited by the W483Y replacement regardless of its form (although the effect was moderately greater in W483Y$_{\Delta 101}$) (*Fig. 6.9, Table 6.3*). Surprisingly, $^{DT}k_{obs}$ turned out to be significantly greater than $^{HT}k_{obs}$ in this variant (the DT reaction took place faster than the HT) at lower temperatures, resulting in a KIE value smaller than 1 (0.5 and 0.4 for the mitochondrial and apoptotic forms at 5 °C respectively). However, the KIE appeared to increase with the temperature, overcoming the unity at temperatures over 25 °C or 35 °C for the mitochondrial and apoptotic forms respectively. This phenomenon is known as inverse KIE and it is of extremely rare occurrence, with scarce representation in the literature nowadays (Harijan *et al*., 2017; Maharjan *et al.*, 2015; Sander *et al.*, 2008; Sucharitakul et al., 2020; Tse et al., 2016).

Although its causes are still up to debate, one potential explanation for this observation is the presence of a severe steric limitation within the active site to achieve the catalytically–competent conformation, suffered either by the reactants themselves or by the transition state during the rate–limiting step (Sander et al., 2008; Tse et al., 2016). The minimal difference in length that exists between the C–H and C–D bonds may prove critical if the pertaining bond is found at a sterically–demanding position, in which instance the shorter C–D bond could actually turn out to be beneficiary, leading to a less occluded active site (Tse et al., 2016). In the case of the W483Y replacement, the resulting alteration of the active site might be such that the catalytic NADH molecule is forced into a more sterically–compromised conformation, yielding the observed inverse KIE. Indeed, the presence of a stiff hydrogen bond (representing a high–frequency donor–acceptor motion), a small inner–sphere (where the acceptor and donor molecules are found in close proximity) and small solvent reorganization energies would further explain the inverse temperature dependence of the KIE (which increases with the temperature) that was additionally observed in this variant (Ludlow et al., 2009).

Table 6.3. Kinetic parameters for the HT/DT processes from NADH/4S–NADD to WT AIF and the W483 variants.

AIF variant	HT (AIF_{ox} + NADH)			DT (AIF_{ox} + 4S–NADD)			KIE [a]	$E_{aDT} - E_{aHT}$ (kcal/mol)	A_H/A_D	KIE Temperature dependence	Dynamics profile
	$^{HT}k_{obs}$ [a] (s^{-1})	E_{aHT} (kcal/mol)	A_H (s^{-1})	$^{DT}k_{obs}$ [a] (s^{-1})	E_{aDT} (kcal/mol)	A_D (s^{-1})					
$WT_{\Delta77}$	0.2	16	$9.6\cdot10^{11}$	0.2	16	$9.4\cdot10^{11}$	0.9	0.0	1.0	No	Environmental
$W483G_{\Delta77}$ [c]	67	18	$1.1\cdot10^{16}$	16	21	$2.4\cdot10^{17}$	4.3	2.0	0.1	Yes	Gating
$W483L_{\Delta77}$ [c]	55	7	$2.6\cdot10^{7}$	29	9	$2.3\cdot10^{8}$	1.9	2.0	0.1	Yes	Gating
$W483Y_{\Delta77}$	0.6	15	$1.5\cdot10^{11}$	1.2	10	$4.6\cdot10^{7}$	0.5 / 1.3[b]	–4.8	$3.3\cdot10^{3}$	Inverted	Gating
$WT_{\Delta101}$	0.02	22	$6.1\cdot10^{15}$	0.02	22	$2.7\cdot10^{15}$	1.3	0.0	2.3	No	Environmental
$W483G_{\Delta101}$ [c]	57	24	$5.3\cdot10^{20}$	15	23	$1.2\cdot10^{19}$	3.8	–1.0	44	Hardly detected	Gating
$W483L_{\Delta101}$ [c]	70	12	$1.6\cdot10^{11}$	24	16	$1.3\cdot10^{14}$	2.9	4.3	0.001	Yes	Gating
$W483Y_{\Delta101}$	0.09	18	$2.0\cdot10^{13}$	0.3	13	$2.0\cdot10^{9}$	0.4 / 1.0[b]	–5.0	$9.6\cdot10^{3}$	Inverted	Gating

Data measured in 50 mM Kpi, pH 7.4, from 5 to 35 °C. Protein concentrations were 7.5 µM. NADH or 4S–NADD final concentration was 1 mM. Errors considered in the measured parameters (below ± 30%) were taken larger than the numerical error after the fitting analysis ($n \geq 3$). E_a and A values were obtained by fitting the data to the linearized Arrhenius equation (eq. 3.21). [a] Data measured at 5 °C. [b] Data measured at 35 °C. [c] k_{obs} values at the highest evaluated temperatures are close to the detection limit of the instrument, therefore, only few points were available to determine E_{aHT} and A_H, and KIE temperature dependences.

Secondary KIE

The 2° KIE can be measured when the bond to the isotopic substituent is close enough to the bond that is formed or broken during catalysis to be able to "feel" its effect. As a consequence, it is usually of a lower magnitude than the 1° KIE, but it may provide useful insights. The 2° KIE of WT AIF and its W483 variants was studied through the use of the 4R–NADD isotopologue (*Fig. 6.10, Table 6.4*).

WT $AIF_{\Delta 77}$ and $AIF_{\Delta 101}$ presented analogous profiles but differing kinetic parameters. Once more, both samples displayed parallel lines in their Arrhenius plots for HT and DT (*Fig. 6.10A, B*) and no temperature dependence of the KIE (*Fig. 6.10C, D*), demonstrating that their active sites possess the natively enhanced structural environment that employs passive (a.k.a. environmental) protein dynamics. However, the magnitude of the 2° KIE observed in $AIF_{\Delta 77}$ was markedly greater than that of the supposedly 1° KIE (0.9 vs 1.8 for the 1° and 2° KIEs respectively) (*Tables 6.3, 6.4*). This was not the case for $AIF_{\Delta 101}$, which actually behaved as was to be expected (presenting a smaller 2° KIE, 1.3 vs 1.0). We have not found any representation in the literature of 2° KIEs being larger than 1° KIEs. Nonetheless, this discrepant behaviour might suggest that the optimized conformation of the catalytic NADH molecule does not coincide in the mitochondrial and apoptotic forms of AIF, a possibility that could also explain their slightly disparate mid–point reduction potentials, thermal stability and transient–state kinetic parameters (*Table 6.2*).

The W483 variants displayed differing behaviours amongst each other (*Fig. 6.10A, B; Table 6.4*), although they all caused the distinct temperature dependence (*Fig. 6.10C, D*) typical of deleterious variants and indicative of an altered active site that needs to relay on active dynamics for the HT process to take place. W483L exhibited similar differences between its mitochondrial and apoptotic forms to those that had been observed in the WT, presenting a greater 2° KIE than the 1° KIE in $W483L_{\Delta 77}$ (1.9 vs 2.6 for the 1° and 2° KIEs at 5 °C respectively) but not in $W483L_{\Delta 101}$ (2.2 vs 1.0). The W483G and W483Y substitutions, however, demonstrated identical behaviours regardless of their forms, with the glycine replacement resulting in a smaller 2° KIE (4.3 vs 1.9 for the 1° and 2° KIEs at 5 °C respectively in $W483G_{\Delta 77}$, compared to 3.8 vs 1.1 in $W483G_{\Delta 101}$) and the tyrosine substitution leading to a greater 2° KIE with no apparent inversion (0.5 vs 1.7 for the 1° and 2° KIEs respectively at 5 °C in $W483Y_{\Delta 77}$, compared to 0.4 vs 1.3 in $W483Y_{\Delta 101}$).

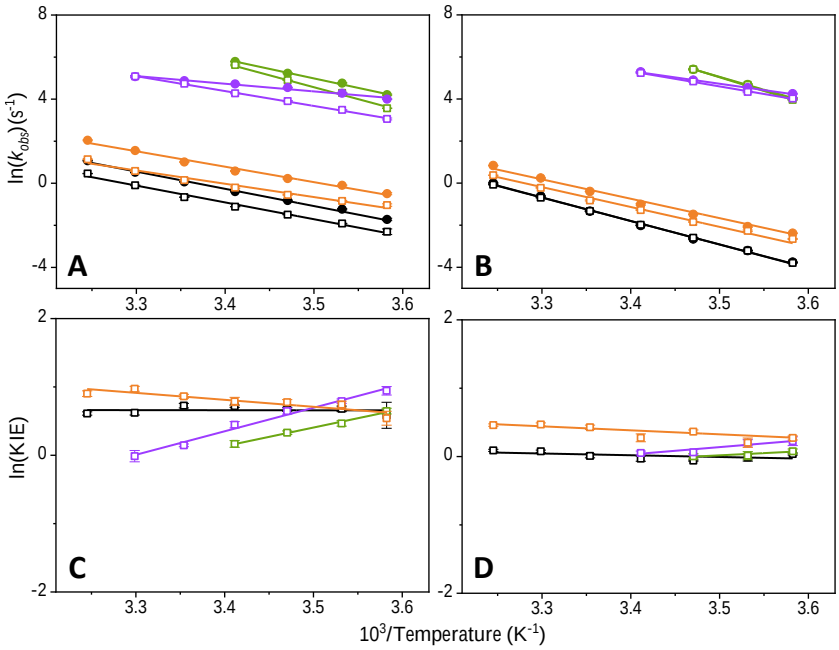

Figure 6.10. Temperature dependence of the kinetic parameters for the HT/DT processes from NADH/4R–NADD to WT AIF and the W483 variants. Arrhenius plots of the observed kinetic constants for the mitochondrial (A) and apoptotic (B) forms of WT AIF and the W483 variants. Data from the NADH HT and 4R–NADD DT processes are respectively shown as solid circles and blank squares. Solid lines represent the fitting to the linearized Arrhenius equation (eq. 3.21). Temperature dependence of the estimated 2° KIEs for the mitochondrial (C) and apoptotic (D) forms. Data from WT, W483G, W483L and W483Y AIF are respectively shown in black, green, purple and orange.

Table 6.4. Kinetic parameters for the HT/DT processes from NADH/4R–NADD to WT AIF and the W483 variants.

AIF variant	HT (AIF_{ox} + NADH)			DT (AIF_{ox} + 4R–NADD)			KIE [a]	$E_{aDT} - E_{aHT}$ (kcal/mol)	A_H/A_D	KIE Temperature dependence	Dynamics profile
	$^{HT}k_{obs}$ [a] (s^{-1})	E_{aHT} (kcal/mol)	A_H (s^{-1})	$^{DT}k_{obs}$ [a] (s^{-1})	E_{aDT} (kcal/mol)	A_D (s^{-1})					
$WT_{\Delta 77}$	0.2	16	$9.6 \cdot 10^{11}$	0.1	16	$2.6 \cdot 10^{11}$	1.8	0.0	3.7	No	Environmental
$W483G_{\Delta 77}$ [c]	67	18	$1.1 \cdot 10^{16}$	35	24	$8.8 \cdot 10^{19}$	1.9	6.0	0.1	Yes	Gating
$W483L_{\Delta 77}$ [c]	55	7	$2.6 \cdot 10^{7}$	21	14	$2.2 \cdot 10^{12}$	2.6	7.0	0.1	Yes	Gating
$W483Y_{\Delta 77}$	0.6	15	$1.5 \cdot 10^{11}$	0.4	13	$2.1 \cdot 10^{9}$	1.7 / 2.5[b]	–2.0	72	Inverted	Gating
$WT_{\Delta 101}$	0.02	22	$6.1 \cdot 10^{15}$	0.02	22	$4.3 \cdot 10^{15}$	1.0	–0.2	1.4	No	Environmental
$W483G_{\Delta 101}$ [c]	57	24	$5.3 \cdot 10^{20}$	53	25	$2.0 \cdot 10^{21}$	1.1	0.8	0.3	Hardly detected	Gating
$W483L_{\Delta 101}$ [c]	70	12	$1.6 \cdot 10^{11}$	54	14	$8.5 \cdot 10^{12}$	1.3	2.3	0.02	Yes	Gating
$W483Y_{\Delta 101}$	0.09	18	$2.0 \cdot 10^{13}$	0.07	19	$2.9 \cdot 10^{13}$	1.3 / 1.6[b]	0.5	0.7	Inverted	Gating

Data measured in 50 mM Kpi, pH 7.4, from 5 to 35 °C. Protein concentrations were 7.5 µM. NADH or 4R–NADD final concentration was 1 mM. Errors considered in the measured parameters (below ± 30%) were taken larger than the numerical error after the fitting analysis ($n \geq 3$). E_a and A values were obtained by fitting the data to the linearized Arrhenius equation (eq. 3.21). [a] Data measured at 5 °C. [b] Data measured at 35 °C. [c] k_{obs} values at the highest evaluated temperatures are close to the detection limit of the instrument, therefore, only few points were available to determine E_{aHT} and A_H, and KIE temperature dependences.

6.2.3. Thermal stability

Protein thermal unfolding was carried out to evaluate the impact of the W483 variants on protein–FAD interaction integrity and overall stability, both in the oxidized and reduced states. Curves were recorded through fluorescence emission following FAD release (*Fig. 6.11, Table 6.5*). An in–depth analysis of the results obtained for WT $AIF_{\Delta 77}$ and $AIF_{\Delta 101}$ is available in the previous chapter.

All W483 variants presented some manner of increased susceptibility to thermal denaturation, although their behaviour varied slightly depending on their form and state. Once more, the W483G and W483L aggressive substitutions yielded the greatest degree of alteration, both presenting a ΔT_m of ~–30 degrees compared to the WT in their oxidized state (*Table 6.5*). This premature release of the FAD cofactor reflects once again the significant alteration suffered by the redox centre which had already become apparent in previous assays.

Formation of the CTC upon reduction of the proteins with NADH led to differing behaviours in their mitochondrial and apoptotic forms. $W483G_{\Delta 77rd}$ and $W483L_{\Delta 77rd}$ demonstrated a similar destabilization to what had been observed in their oxidized state, with a ΔT_m^{CTC} of ~–25 degrees (T_m^{CTC} of 311 and 308 K respectively, compared to 334 K for the WT). On the contrary, a significant ligand–stabilizing effect became apparent in $W483G_{\Delta 101rd}$ and $W483L_{\Delta 101rd}$, resulting in an increase of the T_m^{CTC} all the way up to the native value (T_m^{CTC}s of 326 and 324 K respectively, compared to 326 K for the WT). This complete loss of the remarkable NADH destabilizing effect typically suffered by AIF has been previously reported in other deleterious variants, such as the deletion of residue R201 at the β–hairpin (Villanueva *et al.*, 2019), and may be justified by the boost in compactness given by the NADH molecule to the altered active site. In the case of the W483 variants, the binding of the non–catalytic $NADH_B$ molecule might be of similar importance, possibly compensating the destabilization of the immediate environment of position 483 as well as the active site's increased accessibility to the solvent.

The aforementioned destabilizing effect of the NADH on AIF is associated to the unfolding of the C–loop upon formation of the CTC (chapter 5, Villanueva *et al*., 2019); however, in the W483 variants this motif might have already lost all or part of its structure in the oxidized form as a consequence of the loss of its interaction with the tryptophan residue, resulting in both the observed destabilization of the oxidized

state and the lack of the apparent NADH–destabilizing effect in the reduced state. This would be in agreement with the previously observed CD spectra, as the effect of the W483 variants on the conformation of the active site appeared to be far more remarkable in their oxidized state than in the reduced state (*Fig. 6.5C, D*), as well as with the previous dimerization assays performed with the apoptotic forms by PhD. Raquel Villanueva (chapter 7 in Villanueva, 2015), in which both the glycine and leucine variants appeared to stabilize the dimeric state even in absence of NADH.

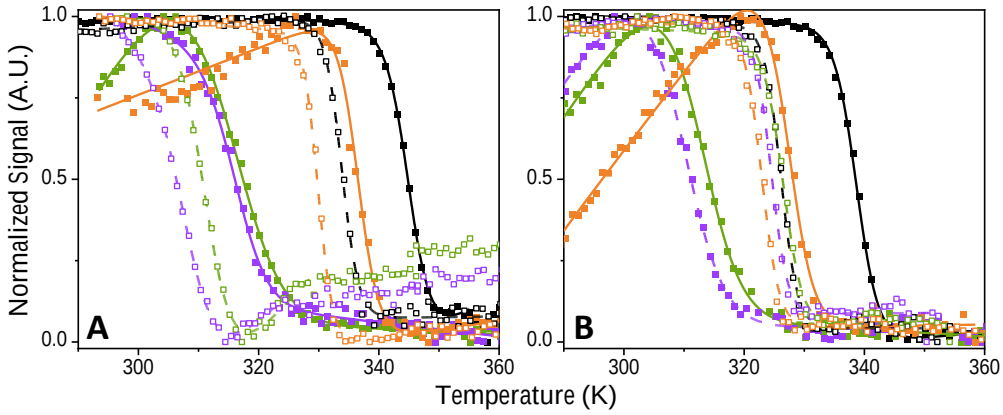

Figure 6.11. Thermal stability of WT AIF and the W483 variants. Flavin release curves of (A) the mitochondrial and (B) apoptotic forms of AIF WT (black), W483G (green), W483L (purple) and W483Y (orange). Thermal denaturation was monitored through FAD fluorescence upon release (excitation at 450 nm and emission at 530 nm, oxidized protein: closed symbols; NADH–reduced protein: open symbols). Data are shown roughly normalized from 0 to 1, with lines (solid for the oxidized protein, dashed for the NADH–reduced protein) representing the individual fittings to a one–transition unfolding model (eq. 3.8). Curves were recorded in 50 mM Kpi, pH 7.4, at a final ionic strength of 150 mM, along a 10 to 90°C temperature ramp. Reduced samples were obtained by premixing with 100–fold excess of NADH.

In comparison, the W483Y conservative replacement yielded a significantly smaller tendency to release the FAD cofactor (ΔT_m of ~–11 degrees and ΔT_m^{CTC} of ~–4 degrees compared to the WT) and maintained the ligand–destabilizing effect induced by NADH upon protein reduction regardless of its form (*Fig. 6.11, Table 6.5*). This is in agreement with previous assays, in which this variant also led to the smallest apparent changes.

Table 6.5. Thermal stability of WT AIF and the W483 variants in the oxidized and CTC states.

	AIF_{ox}			CTC AIF_{rd}:NAD^+			
AIF variant	T_m (K)	ΔH (kcal/mol)	ΔT_m (K)	T_m^{CTC} (K)	ΔH^{CTC} (kcal/mol)	ΔT_m^{CTC} (K)	$T_m^{CTC} - T_m$ (K)
$WT_{\Delta 77}$	345	129	–	334	151	–	–11
$W483G_{\Delta 77}$	313	38	–32	311	77	–23	–2
$W483L_{\Delta 77}$	316	69	–29	308	67	–26	–8
$W483Y_{\Delta 77}$	336	126	–9	330	175	–4	–6
$WT_{\Delta 101}$	339	124	–	326	152	–	–13
$W483G_{\Delta 101}$	312	55	–27	326	128	0	+14
$W483L_{\Delta 101}$	309	53	–30	324	152	–2	+15
$W483Y_{\Delta 101}$	327	98	–12	323	140	–3	–4

Values obtained by individual fitting of the fluorescence thermal denaturation curves to a one–transition unfolding model. Data recorded in 50 mM Kpi, pH 7.4, at a final ionic strength of 150 mM, from 10 to 90 °C (283 to 363 K). Protein concentrations were 2 µM. NADH concentration was in 100–fold excess. Errors considered in the measured parameters (± 2 °C and 0.4 kcal/mol for T_m and ΔH respectively) were taken larger than the numerical error after the fitting analysis (n = 2).

6.2.4. Concluding remarks

Even though two of its three domains are fundamentally dedicated to this task, AIF is astonishingly weak as an NADH oxidase (Ferreira *et al.*, 2014; Miramar *et al.*, 2001). This is primarily due to the exceptional stability of its $FADH^-$:NAD^+ CTC, which relies on an extensive network of both T–stacking and H–bond interactions within the enzyme's active site. The marked inefficiency of AIF potentially grants it the ability to act as a key redox sensor of the mitochondrial NAD(H/$^+$) levels, substantially aiding the bioenergetics and overall homeostasis of the organelle (Ferreira *et al.*, 2014).

In this chapter, we have shed some light on the role of residue W483, a potentially lead player in the interaction network that configures AIF's active site and, subsequently, its inefficiency in catalysis. In order to do so, we have delved further into the biochemical and biophysical characterization of three W483 substitutions previously–generated in our group (Villanueva, 2015): aggressive replacements W483G and W483L, which considerably boost the enzyme's efficiency through a potentially severe modulation of the cofactor's and coenzymes' environment, and conservative variant W483Y, whose impact is not quite as great but remains nevertheless mechanistically significant.

Some manner of divergence was already observed in the absorbance spectra of the W483G and W483L aberrations, suggesting the presence of a moderately affected active site coupled with a compromised binding and/or stability of the FAD cofactor. Near–UV/Vis CD spectra of the oxidized proteins further backed this observation, demonstrating a grave alteration of the FAD environment which was slightly greater in the leucine variant than in the glycine one. The apparent impact on the reduced state was considerably lower in both samples, implying a stabilizing effect upon the binding of the NADH coenzyme. Such phenomenon has already been observed in other deleterious variants (Villanueva, 2019) and is typically associated with a destabilization of the regulatory C–loop motif. This motif is present as two short α–helices in the oxidized structure of AIF and is potentially able to seal off access to the active site in collaboration with W483 (Ferreira *et al.*, 2014). The reduction of the protein prompts its unfolding, opening up the binding site for the non–catalytic $NADH_B$ molecule. If the interactions that stabilize the conformation of the C–loop are affected, however, this motif might prematurely unfold in the oxidized state, yielding a structure more closely resembling that of the reduced state even in the absence of

NADH. Indeed, far–UV CD spectra of the W483G$_{ox}$ and W483L$_{ox}$ variants presented slight variations in agreement with the presence of a "reduced state" alike structure, as well as the previous dimerization assays performed with the apoptotic forms by PhD. Raquel Villanueva (chapter 7 in Villanueva, 2015).

Similar conclusions could be reached from the thermal denaturation studies. Both replacements yielded a substantial susceptibility to thermal denaturation (ΔT_ms of ~–30 degrees), reinstating the presence of a gravely altered active site with a tendency to prematurely release the FAD cofactor. Furthermore, a significant ligand stabilizing effect upon the binding of the NADH coenzyme became apparent in both samples in their apoptotic forms (ΔT_m^{CTC}s of ~–1 degree), reinforcing what had been previously observed in the near–UV/Vis CD data of the reduced samples. The untimely unfolding of the C–loop potentially caused the destabilization of the oxidized structures, while binding of the catalytic and non–catalytic NADH molecules may have increased the stability of the reduced structures by boosting the compactness of the active site and of the environment of residue 483.

The impact of the aggressive replacements on the kinetic properties of AIF was also readily evident. Both the glycine and leucine variants displayed a considerable gain in efficiency to oxidize NADH in the transient–state kinetic assays (~370–fold and ~80–fold respectively), demonstrating as well a significant increase in their mid–point reduction potential (ΔE_m ~+175 and ~+130 mV respectively). The subsequent loss of aromaticity produced by both substitutions in the 483 position potentially leads to an inability to properly stack the isoalloxazine ring of the FAD cofactor from the *si*–face, where W483 would typically act, severely affecting the redox properties of the cofactor and markedly destabilizing the FADH$^-$:NAD$^+$ CTC. As a result, the HT process seems to be substantially favoured in the W483G and W483L variants. This finding becomes even more remarkable when the analyses of the KIEs are taken into account, as they indicate the presence of an altered active site in which the donor and acceptor molecules (in this case, NADH$_A$ and FAD) are not found at the optimal distance for the HT to take place and instead require of active protein dynamics to sample the donor–acceptor distance. Whereas the HT might not be as direct as in WT AIF, which indeed presents an optimized active site, the acute destabilization of the CTC seems to be more than enough to still significantly enhance catalysis in the W483 aggressive variants. This finding demonstrates the critical importance of AIF's remarkably stable FADH$^-$:NAD$^+$ CTC, which makes it a very poor NADH oxidase, potentially determining its ability to act as a sensor of the mitochondrial redox state.

In contrast, the W483Y variant yielded the smallest impact on the structural and biochemical properties of AIF, in agreement with it being the most conservative replacement of the three under study. A moderate degree of modulation was still apparent, however, reinforcing the criticality of W483's function on the enzyme's redox centre. W483Y presented the least discrepant near–UV/Vis CD spectra both in its oxidized and reduced state, although some manner of alteration in the FAD environment could still be observed, and a fairly shifted far–UV CD spectra, actually presenting a heightened local maximum around 215 nm which was not as marked in the WT data or in either of the other two variants. The susceptibility of W483Y to thermal denaturation was additionally the least impaired (ΔT_m of ~–11 degrees), and the NADH–binding destabilizing effect typical of the WT protein was maintained in both forms (ΔT_m^{CTC} of ~–4 degrees).

Kinetic properties were similarly affected, resulting in a minor increase in the catalytic efficiency (~3–fold) and a slight modification of the redox potential (ΔE_m of –14 mV and +48 mV for the mitochondrial and apoptotic forms respectively). The most exceptional –and unique– effect that was observed in the W483Y substitution was the appearance of an inverse KIE coupled with an inverse KIE dependence on the temperature, where the rate of the kinetic reaction appeared to be twice as fast for DT than for HT at temperatures below 25 °C or 35 °C for the mitochondrial and apoptotic forms respectively. Although both the primary and secondary KIEs demonstrated the presence of an altered active site requiring active dynamics, only the former turned out to be inverted. This observation suggests that the catalytic NADH molecule is found in a sterically–compromised conformation in the W483Y variant, which might significantly differ from that of either the WT or the other studied replacements. This could ultimately result in the observed higher DT rate, as the C–D bond is shorter than the C–H and subsequently generates a less occluded active site, where the necessary sampling of the donor–acceptor distance is not as limited. Once more, this observation remarks the crucial role of W483 in configuring the active site, as even the most conservative substitution here analysed can potentially lead to a considerable alteration of the enzyme's redox centre.

7. The Apoptosis Inducing Factor–Like

Trials and hardships in the overexpression of an iron–sulphur flavoprotein

The PhD candidate contributed by performing the following:

- Functional and structural analyses
- Molecular biology assays (excepting those at the IBS–ISBG)
- Production and purification assays (excepting those at the IBS–ISBG)

ABSTRACT

The human AIF family consists on a group of three flavoenzymes which share an oxidoreductase domain and the ability to induce PCD, albeit through differing mechanisms. AIF is the founding member and the best characterized to date. In contrast, AIFL is a member of the AIF protein family for which surprisingly scarce information is available regarding both its structure and function. AIFL possesses a Rieske–type ferredoxin domain with an Fe–S cluster that is unique within the family, envisaging a potentially vital function for this protein as a free radical scavenger *in vivo*. Unfortunately, no experimentally–determined structure is available for AIFL up to date. However, computational models of full-length AIFL suggests that electron transfer could theoretically take place between its redox centers, being a NADH coenzyme the potential donor molecule. In this chapter, various protein expression assays were performed in *E. coli* in hopes of purifying soluble, active AIFL to homogeneity, but no significant soluble expression could be observed even after screening several different strains and conditions. The difficulties encountered here might be explained by AIFL's inability to fold properly while within the cell, which could be secondary to a faulty incorporation of the Fe–S cluster in the Rieske domain.

RESUMEN

La familia AIF humana consiste en un grupo de tres flavoenzimas que comparten un dominio oxidorreductasa y la habilidad para inducir muerte celular programada, aunque a través de mecanismos diferentes. AIF es la miembro fundadora y la mejor caracterizada hasta el momento. En contrate, AIFL es una miembro de la familia proteica AIF para la cual hay disponible una cantidad sorprendentemente escasa de información con respeto tanto a su estructura como a su función. AIFL posee un dominio ferredoxina de tipo Rieske con un clúster Fe–S que es único en la familia, concibiendo para esta proteína una función potencialmente vital como eliminadora de radicales libres *in vivo*. Desafortunadamente, ninguna estructura determinada experimentalmente está disponible para AIFL actualmente. Sin embargo, los modelos computacionales de AIFL en su forma completa sugieren que la transferencia de electrones podría teóricamente tener lugar entre sus centros redox, siendo la coenzima NADH la potencial molécula donante. En este capítulo, varios experimentos de expresión proteica han sido llevados a cabo en *E. coli* con la esperanza de purificar la AIFL soluble y activa en homogeneidad, pero no se ha podido observar una expresión soluble significativa ni siquiera tras el cribado de varias cepas y condiciones diferentes. Las dificultades afrontadas aquí pueden ser explicadas por la inhabilidad de AIFL para plegarse adecuadamente mientras está dentro de la célula, lo cual podría ser secundario a una incorporación incorrecta del clúster Fe–S en el dominio Rieske.

7.1. INTRODUCTION

AIFL is a mitochondrial Fe–S flavoprotein that belongs to the human AIF family, and which has remained the most severely uncharacterized of the three members since its discovery almost twenty years ago (Xie *et al.*, 2005). In spite of apparently lacking a canonical MLS, AIFL localizes primarily in the mitochondria anchored to the MIM and does not translocate to the nucleus upon apoptosis induction, unlike its sister AIF, promoting instead a caspase–dependent pathway that courses with the release of cytochrome c from the mitochondria and the scission of caspase 3 (Xie *et al.*, 2005). Although phylogenetic studies suggest that AIFL is most closely related to AIF amongst the flavoprotein pool, the only attributes both proteins seem to have in common is the presence of a flavin–dependent oxidoreductase domain (with a 27% sequence identity) and the ability to induce cell–death, albeit through differing mechanisms (chapter 1; Novo *et al.*, 2021).

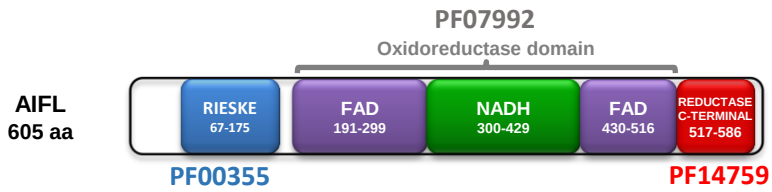

Figure 7.1. Schematic representation of the domains of human AIFL. The Rieske–type, bipartite FAD–binding, NADH–binding, and reductase C–terminal protein domains are respectively shown in blue, violet, green and red, and the corresponding Pfam domain codes are specified. Residues comprising each domain are indicated.

Three domains compose AIFL, of which only one –the aforementioned oxidoreductase domain– is shared with the rest of its family (chapter 1; Novo *et al.*, 2021) (*Fig. 7.1*). As was the case in AIF, the oxidoreductase domain of AIFL is composed of a bipartite FAD–binding domain encasing a single NADH–binding domain (*Fig. 7.2*), both of which present a significantly similar conformation to that of AIF (although the unique β–hairpin insertion of AIF is expectedly missing in AIFL). Indeed, the active site of AIFL bears a remarkably close resemblance to that of AIF (*Fig. 7.2C*), with virtually all key residues seemingly partaking in identical roles (conserved residues R235, P236, S239, K240, F342, L343, E346, H485, W486 and W514 in AIFL corresponding to R172, P173, S176, K177, F310, L311, E314, H454, H455 and W483 in AIF).

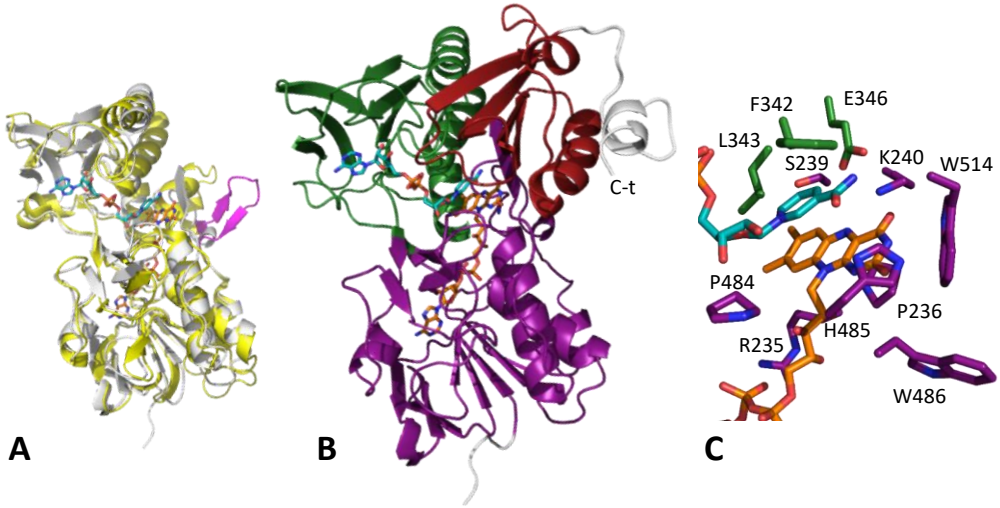

Figure 7.2. The oxidoreductase domain of human AIFL. (A) Alignment of the modelled oxidoreductase domain of AIFL (in white) to that of AIF (in yellow, PDB 4BUR). The AIFL structure was obtained using a ferredoxin reductase as a template (PDB 3LXD) in the RaptorX server. The unique β–hairpin of AIF is shown in pink. (B) Cartoon representation of the oxidoreductase and reductase–C terminal domains of modelled AIFL. (B) FAD– and NADH–binding sites of AIFL. Key residues are represented as sticks and labelled black. Cofactor and coenzyme molecules are represented as sticks and CPK–coloured in orange and teal respectively. The colour scheme in panels B and C corresponds to that of figure 7.1.

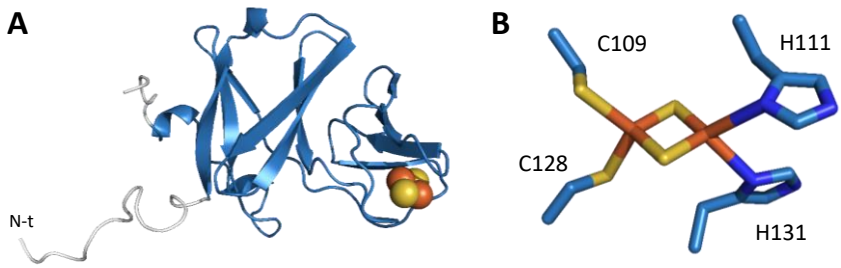

Figure 7.3. The Rieske–type domain of human AIFL. (A) Cartoon representation of the Rieske domain of modelled AIFL. The structure was obtained using a ferredoxin as template (PDB 5BOK) in the RaptorX server. The colour scheme corresponds to that of figure 7.1. (B) Coordination site of the [2Fe–2S] cluster of AIFL. Key residues are represented as sticks and labelled black. Iron atoms are CPK–coloured in orange and sulphur atoms in yellow, both represented as spheres in A or as sticks in B (to facilitate visualization of the covalent bonds).

The other two unique domains of AIFL, however, envisage an unparalleled function within the family for this forsaken protein. The first domain of AIFL is an N–terminal

Rieske domain, oftentimes found in proteins composing the mitochondrion ETC, which is able to bind a [2Fe–2S] cluster through conserved key residues C109, H111, C128 and H131 (Novo, 2018) (*Fig. 7.3*). This Rieske domain is followed by the FAD– and NADH–binding oxidoreductase domain, after which a reductase C–terminal domain can be found. The reductase C domain is mainly encountered at the C terminus of several reductase enzymes, and it is involved in the interaction of the FAD–containing NADH–ferredoxin reductase (BphA4) with Rieske–type [2Fe–2S] ferredoxin (BphA3) (Senda *et al*., 2007).

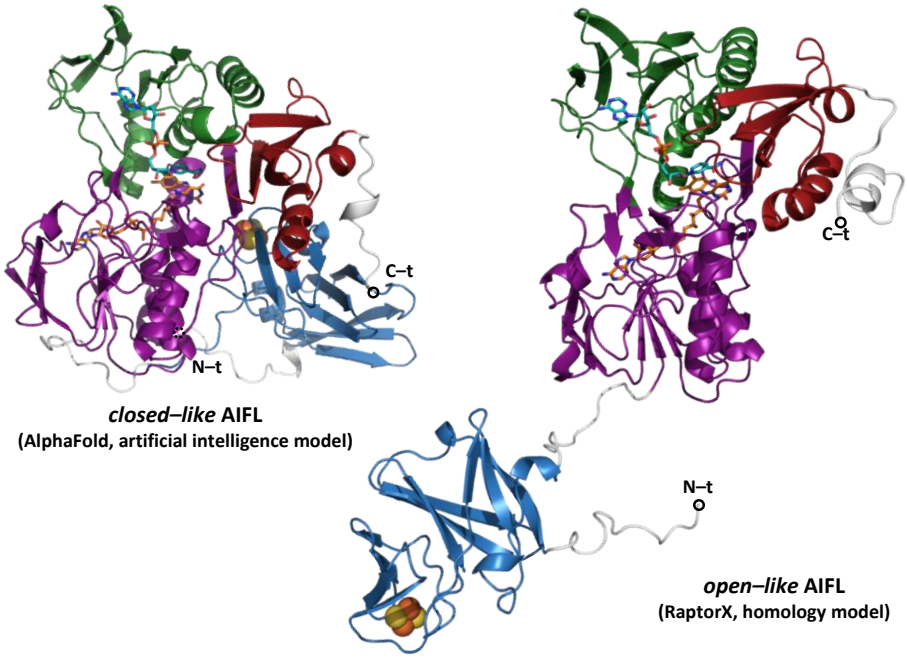

Figure 7.4. Alternate models of human AIFL. Cartoon representation of human AIFL as modelled by (left) the artificial intelligence system of the AlphaFold program or (right) homology modelling in the RaptorX server. The colour scheme corresponds to that of figure 7.1. Cofactor and coenzyme molecules are represented as sticks and CPK–coloured in orange and teal respectively. Iron atoms are CPK–coloured in orange and sulphur atoms in yellow, both represented as spheres.

The particular combination of domains in AIFL envisages an interesting flux of electrons for this protein, from a potentially donor NAD(P)H coenzyme to the FAD cofactor of the oxidoreductase domain, and in exchange from this cofactor to the [2Fe–2S] cluster of the Rieske domain. The reductase C–terminal domain of AIFL could potentially be in charge of stabilizing and/or promoting the interaction between

the Rieske and the oxidoreductase domains during the charge transfer, as each of them share a considerable similarity to putative ferredoxin and NAD(P)H:ferredoxin reductase domains (Novo, 2018). Indeed, although earlier homology modelling programs like RaptorX simulate the structure of AIFL with the Rieske domain separated from the other two domains (Novo *et al.*, 2021), the novel AlphaFold artificial intelligence system developed by DeepMind predicts AIFL as a globular, compact protein in which the three domains are in intimate contact (Jumper *et al.*, 2021) (*Fig. 7.4*). These two alternate modelled structures may potentially correspond to two plausible conformations of AIFL *in vivo*, "open"– and "closed"–like states, suggesting that the Rieske domain may be able to pivot between the oxidoreductase domain of AIFL, from which it could "take" the charge, and an unknown client protein, to which it would transfer said charge (*Fig. 7.5*).

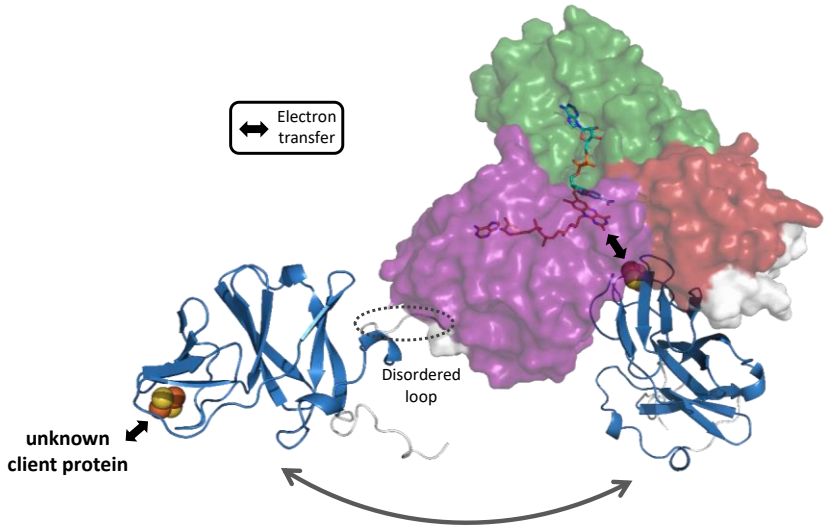

Figure 7.5. Potential electron transfer mechanism in AIFL. The Rieske–type domain of AIFL may be able to pivot between the oxidoreductase domain of the protein and an unknown client protein, transferring the electrons from the FAD cofactor to the latter, thanks to the potential freedom of movement provided by the disordered loop that connects the smaller domain with the rest of the protein. The structure of modelled human AIFL is represented as surface with a 40% transparency excepting the Rieske domain, which appears as cartoon for easier visualization. The colour scheme corresponds to that of figure 7.1. Cofactor and coenzyme molecules are represented as sticks and CPK–coloured in orange and teal respectively. Iron atoms are CPK–coloured in orange and sulphur atoms in yellow, both represented as spheres.

AIFL is ubiquitously expressed in humans and significantly conserved across all eukaryotes (Novo *et al*., 2021), envisaging a potentially critical housekeeping function for this protein. Indeed, the scarce literature that is available on AIFL seems to indicate that it may act as a free radical scavenger within the mitochondria of healthy cells, supporting their bioenergetics and overall survival (Lozic *et al.*, 2021; Murata *et al.*, 2011). This hypothesis is further backed by the electron transfer possibilities of AIFL, which may potentially be able to employ either its Rieske–type or its oxidoreductase domain, or even both in collaboration, to modulate the levels of reducing and oxidating agents (such as ROS or the NADH coenzyme). AIFL has also been found to be aberrantly expressed in some cancers (particularly cholangiocarcinoma and breast cancer), possibly aiding the metabolism and ROS resistance of tumour cells (Chuan–on *et al.*, 2022; Zheng *et al.*, 2019).

All in all, these observations highlight the critical importance of shedding some light into the molecular mechanisms of action of this severely uncharacterized protein, for which only a scant number of cellular and clinical studies are available as of today. AIFL has never been overexpressed or purified to homogeneity neither for any species nor in any type of expression system yet, even though this could provide invaluable insight on its vital functions within the cell. Consequently, we have aimed to examine an overexpression and purification protocol for human AIFL in the *E. coli* prokaryotic model, as it is significantly cheap, fast and easy to use. A deeper understanding on the moonlighting functions of AIFL could have potentially vital benefits particularly in chemotherapy treatments, as it may serve as a key target molecule or even a prognostic biomarker (Araujo *et al.*, 2021; Chua–on *et al.*, 2022; Zheng *et al.*, 2019).

7.2. Results and Discussion

7.2.1. Previous attempts

7.2.1.1. Experimentally–synthetized AIFL construct

In a previous degree research project (Novo, 2017), we experimentally synthetized a bacterial expression vector (named pNNH1) containing the *aifm3* human gene (NCBI NM_144704.2) optimized for *E. coli* expression and with a C–terminal His–tag in a pET–28a(+) backbone. *E. coli* BL21(DE3) cells were unsuccessfully transformed through heat–shock, after which electroporation was employed. A scarce number of colonies were obtained and subsequently cultured (grown to OD_{600nm} = 0.6–0.8, then induced with 1 mM IPTG at 37 °C for 3 hours). Only minimal protein expression could be observed after performing an anti–His–tag WB, which further presented a significantly high content of apparent aggregation and degradation (*Fig. 7.6A*).

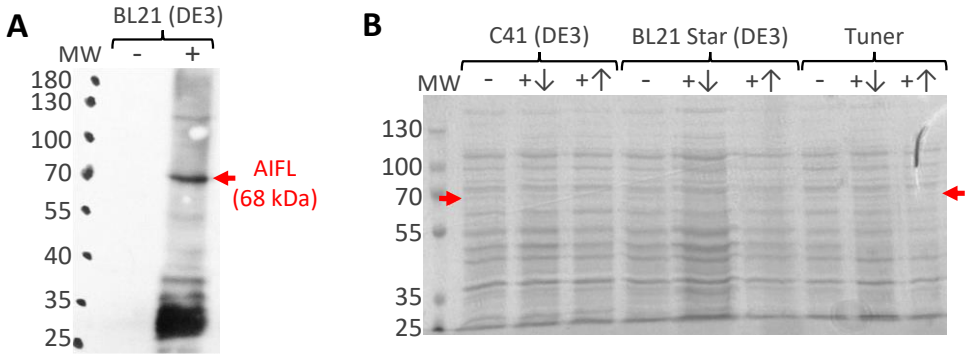

Figure 7.6. First attempts at overexpressing human AIFL in E. coli. (A) Anti–His–tag WB analysis of human AIFL after transformation in the *E. coli* strain BL21 (DE3) with the pNNH1 vector (pET–28a(+)–AIFL), and subsequent incubation and induction at 37 °C for 3 hours with 1 mM IPTG. The band corresponding to AIFL (68 kDa) is indicated by a red arrow, and showed limited expression. Remaining bands and overall smear demonstrate a high content of aggregated and degraded protein. (B) SDS–PAGE analysis of the expression assays of human AIFL in three different strains of *E. coli* (C41 (DE3), BL21 Star (DE3) and Tuner) at a low (18 °C, indicated by a downwards arrow) or high (37° C, indicated by an upwards arrow) temperature. Induction was performed with 1 mM IPTG O/N. Minus signs indicate that no IPTG was added to the sample (negative control), while positive signs indicate that 1 mM IPTG was added at the time of induction (OD_{600nm} = 0.6–0.8). Samples correspond to raw extracts in both panels.

In the following master research project (Novo, 2018), we introduced the pNNH1 vector (pET–28a(+)–AIFL) into three other strains of *E. coli* (C41 (DE3), specialized in the expression of toxic and membrane proteins; BL21 Star (DE3), which promotes mRNA stability; and Tuner, which maximizes entry of IPTG into the cell). We also added supplements to the medium to promote the synthesis of the FAD cofactor and the Fe–S cluster (8 µg/mL riboflavin and 1mM $FeSO_4$ of final concentration). Protein expression was tested at low and high temperatures (18 and 37 °C, O/N), as the former tends to promote proper folding and the latter to improve the overexpression (*Fig. 7.6B*). However, AIFL expression remained minimal and, upon separation of the soluble and insoluble fractions, predominantly appeared in the latter.

As AIFL is naturally found anchored to the MIM, we pondered the possibility that it was being properly expressed but ended up being insoluble because of its potential anchorage to the cell's membrane. Hence, a screening of several detergents (Tween 20, Tween 80, Triton X–100, sodium cholate and N–dodecyl–β–maltoside) was performed in hopes of solubilizing the protein (*Fig. 7.7*). The *E. coli* C41 (DE3) strain was tested, inducing with 1 mM of IPTG at 37 °C O/N, and the detergent of choice was added at 1% after cell membrane recollection by centrifugation. The *E. coli* BL21 (DE3) strain was used as comparison, as it had shown scarce expression in prior assays. Nevertheless, the effect was still virtually non–existent, suggesting that the AIFL construct may be unable to either be expressed at all or to adequately fold once translated, leading to its degradation and/or to insoluble protein inclusion bodies.

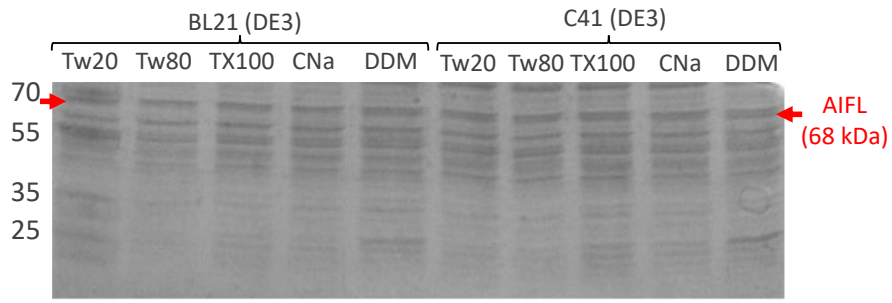

Figure 7.7. Screening of various detergents to solubilize human AIFL in E. coli. Samples of *E. coli* BL21 (DE3) and C41 (DE3) transformed with pNNH1 (pET–28a(+)–AIFL) were incubated, induced and subsequently centrifuged to separate the cell membrane fraction. Samples were then treated with Tween 20 (Tw20), Tween 80 (Tw80), Triton X–100 (TX100), sodium cholate (CNa) or n–dodecyl–β–maltoside (DDM) to solubilize the proteins present in the cell membrane fraction. The band corresponding to AIFL (68 kDa) is indicated by a red arrow.

7.2.1.2. Commercially–synthetized AIFL constructs

A prior analysis of the potential post–translational modifications (PTM) suffered by human AIFL indicated a significantly high probability of the protein presenting myristoylation of its N–terminus. This PTM courses with the irreversible attachment of a myristoyl group to an N–terminal glycine residue after cleavage of the leading methionine, serving as a lipid anchor to the different cell membranes (Novo, 2018), and might potentially stabilize the typically flexible and disordered N–terminus. In order to bypass the absence of this PTM in *E. coli*, we decided to order the commercial synthesis of an AIFL construct lacking the first 64 residues of its sequence ($AIFL_{\Delta 64}$) in a pET–28a(+) vector. As the Rieske domain presents the covalently bound [2Fe–2S] cluster, whose incorporation and posterior folding might also be problematic, we additionally ordered two other constructs presenting either the Rieske domain ($AIFL_{65–168}$) or the oxidoreductase and C–terminal domains ($AIFL_{\Delta 195}$). All constructs were given a C–terminal His–tag excepting $AIFL_{65–168}$, for which an N–terminal His–tag was added in hopes of stabilizing its N–terminus.

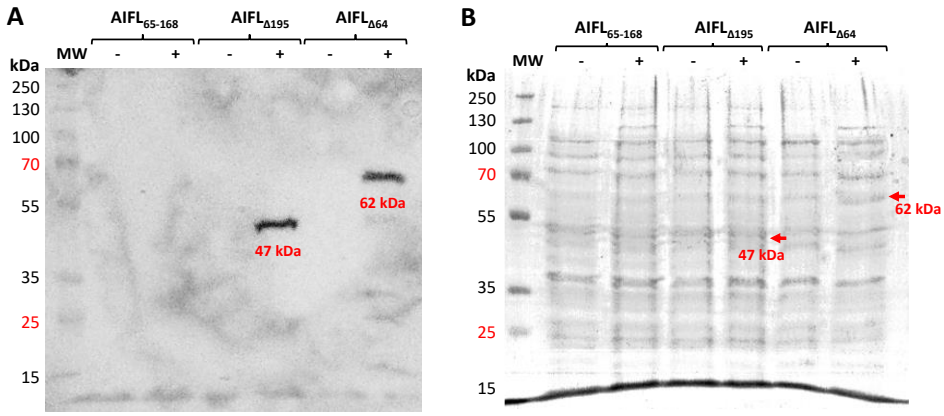

Figure 7.8. Expression assays with the commercial constructs of human AIFL. (A) Anti–His–tag WB analysis and (B) equivalent SDS–PAGE gel of the expression assays of the AIFL commercial constructs. Minus signs indicate that no IPTG was added to the sample (negative control), while positive signs indicate that 1 mM IPTG was added at the time of induction (OD_{600nm} = 0.6–0.8). Induction was performed O/N at 18 °C for $AIFL_{65–168}$ and $AIFL_{\Delta 195}$, and at 37 °C for $AIFL_{\Delta 64}$ (the most optimal conditions according to the previous assay). Samples correspond to raw extracts. The smaller Rieske domain cannot be observed because of its size (15 kDa), which proved to be too small for the resolution of the gel employed (12% polyacrylamide). Later assays with this construct were performed in 17 % SDS–PAGE gels.

As had been previously done for the experimentally–synthetized vector, the three commercial AIFL constructs were transformed into the *E. coli* C41 (DE3) strain and protein expression was assessed at low and high temperatures (18 and 37 °C) O/N and after 42 hours. Unfortunately, expression remained minimal for all three constructs, but a WB analysis at least demonstrated that both the full–length ($AIFL_{\Delta 64}$) and the oxidoreductase domain ($AIFL_{\Delta 195}$) constructs did not present either significant aggregation or degradation (*Fig. 7.8*). Additional conditions were surveyed (addition of 3% ethanol after induction (Chhetri *et al.*, 2015) and a screening of IPTG concentrations (0.01, 0.2 and 0.5 mM)) but none proved fruitful.

7.2.2. Current trials

7.2.2.1. Overexpression and purification assays with $AIFL_{\Delta 64}$ and $AIFL_{\Delta 195}$

At the beginning of this PhD thesis, and in order to ascertain that the cell culture was in top condition, *E. coli* C41 (DE3) cells were transformed once more with the $AIFL_{\Delta 64}$ and $AIFL_{\Delta 195}$ constructs (as some degree of expression had been previously achieved with both of them). The Rieske domain construct, $AIFL_{65–168}$, was deemed too unstable to be overexpressed in the present conditions and was subsequently put aside.

The chosen AIFL constructs were overexpressed under the same conditions typically employed for sister protein AIF (induction at an OD_{600nm} = 0.8–1.0 with 1 mM IPTG, see section 3.3.1), and a screening of temperatures was carried out (induction at 18, 25 or 37 °C O/N). Upon chromatographic separation, an acceptable overexpression could be noted for the first time in the $AIFL_{\Delta 64}$ sample, although it remained predominantly insoluble (particularly at higher temperatures) (*Fig. 7.9*). As a consequence, subsequent assays were performed inducing at 18 °C, when the ratio of soluble/insoluble protein was deemed to be the highest. In hopes of improving the level of overexpression as well as the solubility of the protein, additional screenings were performed on the concentration of IPTG (0.2, 0.5 and 1 mM), the growth medium (TB instead of LB) and the OD_{600nm} at the time of induction (0.5, 0.8 and 1.0) (*Fig. 7.10*). Ultimately, the most optimal conditions were deemed to be growth in LB medium and induction at an OD_{600nm} = 0.8 with 0.5 mM IPTG, at 18 °C O/N. As no significant expression could be noted for the $AIFL_{\Delta 195}$ construct regardless of the conditions on trial, following assays were exclusively performed with $AIFL_{\Delta 64}$.

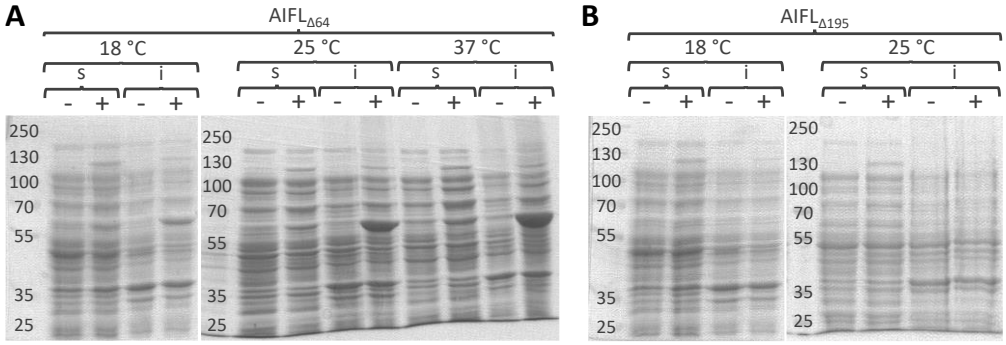

Figure 7.9. Expression assays of AIFL$_{\Delta 64}$ and AIFL$_{\Delta 195}$ at different temperatures. E. coli C41 (DE3) cells containing the (A) AIFL$_{\Delta 64}$ (62 kDa) or (B) AIFL$_{\Delta 195}$ (47 kDa) constructs were grown at 37 °C and 180 rpm until they reached an OD_{600nm} = 0.8–1.0 and subsequently induced with 1 mM IPTG O/N at 100 rpm. Three different temperatures (18, 25 or 37 °C) were screened at the time of induction. Minus signs indicate that no IPTG was added to the sample (negative control), while positive signs indicate that 1 mM IPTG was added at the time of induction. s, soluble fraction; i, insoluble fraction.

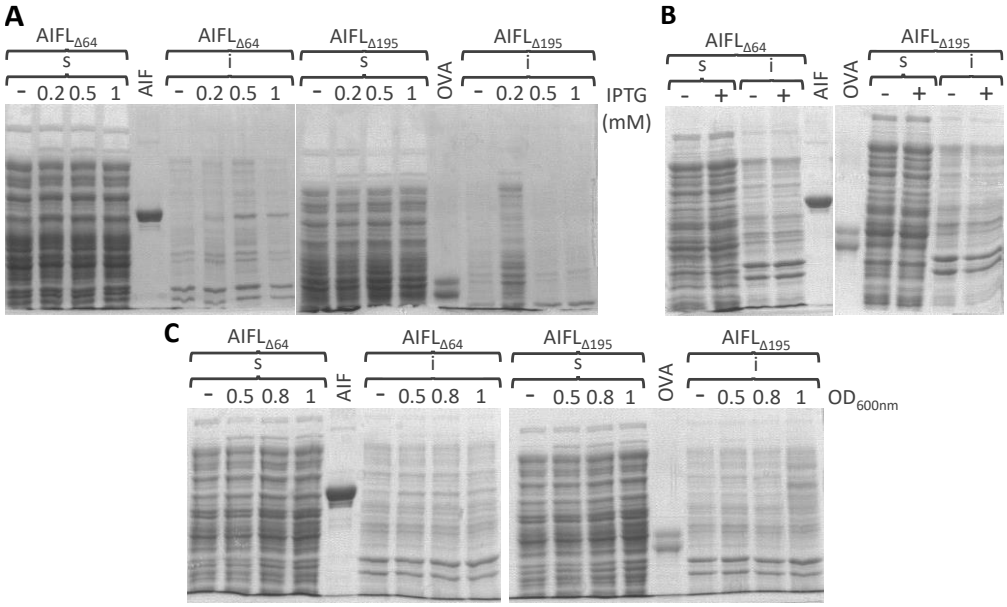

Figure 7.10. Expression assays of AIFL$_{\Delta 64}$ and AIFL$_{\Delta 195}$ screening IPTG concentration, growth medium and OD_{600nm} at the time of induction. (A) The concentration of IPTG (0.2, 0.5 and 1 mM), (B) the growth medium (TB) and (C) the OD_{600nm} at the time of induction (0.5, 0.8 and 1.0) were independently screened. Unless otherwise stated, the procedure and conditions for cell culture were the same as in the previous figure. A sample of either AIF (60 kDa) or

ovalbumin (OVA, 43 kDa) was additionally loaded to the gels to respectively facilitate identification of the $AIFL_{\Delta 64}$ (62 kDa) or $AIFL_{\Delta 195}$ (47 kDa) bands, as each pair is of comparable molecular weight. Minus signs indicate that no IPTG was added to the sample (negative control). In panel A, numbers indicate the concentration of IPTG added at the time of induction (0.2, 0.5 or 1 mM). In panel B, positive signs indicate that 1 mM IPTG was added at the time of induction. In panel C, numbers indicate the OD_{600nm} at the time of induction (0.5, 0.8 or 1). s, soluble fraction; i, insoluble fraction.

A small–scale purification assay was carried out after expression of $AIF_{\Delta 64}$ under the best established conditions. Different concentrations of imidazole (1, 4, 8, 12 and 20 mM) and KCl (0.1, 0.25 and 0.4 M) in the binding buffer (50 mM Kpi, pH 7.4) were screened (*Fig. 7.11*). These two components potentially play a fundamental part during the purification procedure, as they may hinder the unspecific binding of impurities to the activated resin. For the remaining part, the same procedure as that of sister protein AIF was followed (see section 3.3.3). Once the most optimal conditions for purification had been determined (4 mM imidazole and 0.1 M KCl), a large–scale production (10 L) was carried out, followed by purification.

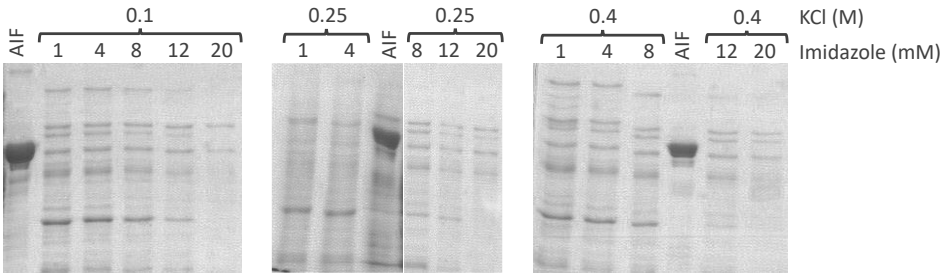

Figure 7.11. Small–scale purification assay of $AIFL_{\Delta 64}$. Different concentrations of imidazole (1, 4, 8, 12 and 20 mM) and KCl (0.1, 0.25 and 0.4 M) were screened in 50 mM Kpi, pH 7.4. A sample of AIF (60 kDa) was additionally loaded to the gels to facilitate identification of the $AIFL_{\Delta 64}$ (62 kDa) band.

However, the majority of the purified sample turned out to be either impurities or degraded protein (*Fig. 7.12A*). Indeed, a local maximum around 410 nm (characteristic of iron–containing proteins) could be observed in the absorption spectra of some purification fractions (*Fig. 7.12B*), but these samples appeared to be predominantly impure upon separation by SDS–PAGE. Consequently, the signal was taken to belong to a cytochrome impurity rather than to the actual protein of interest, which was deemed too unstable to purify to homogeneity in the assayed conditions.

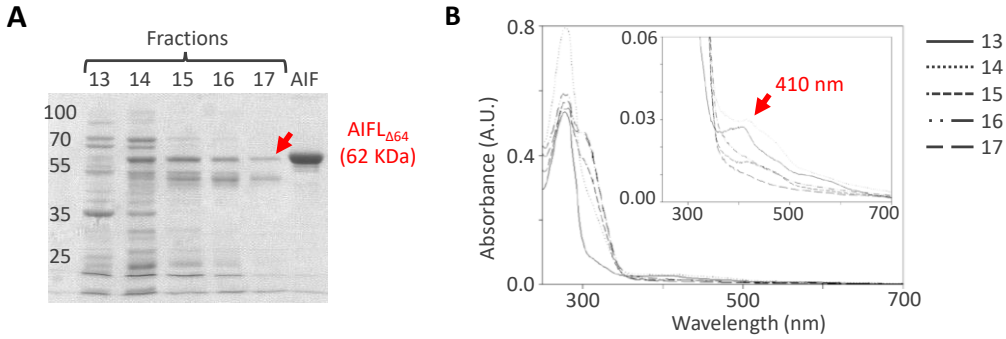

Figure 7.12. Large–scale production and purification assay of AIFL$_{\Delta64}$. The AIFL$_{\Delta64}$ construct was overexpressed and subsequently purified at the most optimal conditions previously assayed. A Ni^{2+}–activated IMAC gel was employed for the purification, from which the protein was eluted using an imidazole gradient (details on the purification procedure are provided in section 3.3.3). Fractions potentially containing the target protein (13–17) were separately analysed by performing (A) an SDS–PAGE and (B) absorption spectra measurements. All samples appeared to contain mostly impurities and/or degraded protein. A sample of AIF (60 kDa) was additionally loaded to the gel to facilitate identification of the AIFL$_{\Delta64}$ (62 kDa) band.

7.2.2.2. The Fe–S cluster operon expressing plasmid

The inability to properly incorporate the Fe–S cluster to the Rieske domain could potentially explain the apparent instability demonstrated by AIFL in the previous assays, as the cluster is bound covalently to the protein and might subsequently determine its adequate folding. On this behalf, we decided to delve into prior accounts on the literature regarding the soluble overexpression of Fe–S proteins, and subsequently encountered the existence of the *isc* operon expressing plasmid (pISC) (Catalano–Dupuy *et al.*, 2011; Nakamura *et al.*, 1999).

The pISC vector was designed and synthetized by Nakamura *et al.* in 1999, and it contains the denominated *isc* gene cluster of *E. coli* (ORF1–ORF2–iscS–iscU–iscA–hscB–hscA–fdx–ORF3), which is potentially involved in the formation and/or repair of Fe–S proteins in the bacterium. This gene cluster significantly potentiated the assembly of Fe–S clusters upon co–expression with several ferredoxins in *E. coli*, and it did not present any notable specificity for either the protein sequence or the type of Fe–S cluster (Nakamura *et al.,* 1999). Catalano–Dupuy *et al.* (2011) employed this same vector to successfully overexpress two different ferredoxins in *E. coli* C41 cells under similar conditions to those previously assessed by our group (LB medium,

induction with 0.25 mM IPTG at 18 °C O/N), and additionally supplemented the medium with ammonium ferric citrate. Upon request, Eduardo Ceccarelli kindly provided us with *E. coli* C41 cells containing the pISC vector (which had in turn been provided to him by Nakamura's group), which we made chemically competent and subsequently transformed with the $AIFL_{\Delta 64}$ construct. As the pISC vector provides resistance to tetracycline and the pET–28a(+)–$AIFL_{\Delta 64}$ construct to kanamycin, following assays were performed in presence of both antibiotics to maintain selectivity. Additionally, 1 mM cysteine and 2 mM ammonium ferric citrate were added to the medium, together with the 1mM $FeSO_4$ and 8 µg/mL riboflavin, to facilitate the synthesis and incorporation of the Fe–S cluster and the FAD cofactor.

Indeed, co–expression of the *isc* gene cluster with $AIFL_{\Delta 64}$ yielded some manner of improvement in the soluble expression of the protein when compared to what had been previously observed in absence of the *isc* chaperones (*Fig. 7.13*). However, the overall protein production appeared to be moderately decreased and the bast majority of the target protein still wound up in the insoluble fraction. Performed screenings of differing conditions (induction at 18 or 25 °C; IPTG concentration of 0.2, 0.5 or 1 mM) did not result in any noticeable increase of soluble protein.

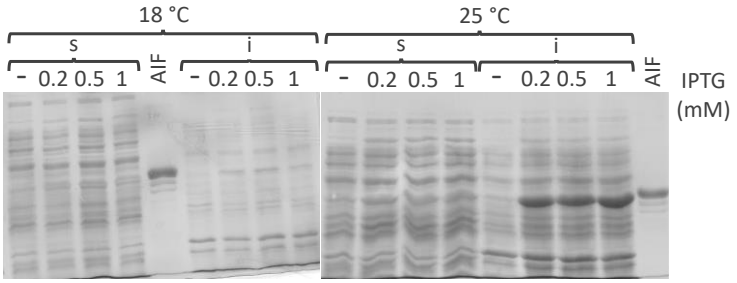

Figure 7.13. Expression assays of $AIFL_{\Delta 64}$ in co–expression with the Fe–S cluster operon expressing plasmid. E. coli C41 (DE3) cells containing the $AIFL_{\Delta 64}$ construct and pISC vector were grown at 37 °C and 180 rpm until they reached an OD_{600nm} = 0.8 and subsequently induced with IPTG O/N at 100 rpm. Different temperatures (18 or 25 °C) and IPTG concentrations (0.2, 0.5 and 1 mM) were screened at the time of induction. A sample of AIF (60 kDa) was additionally loaded to the gels to facilitate identification of the $AIFL_{\Delta 64}$ (62 kDa) band. Minus signs indicate that no IPTG was added to the sample (negative control), while numbers indicate the concentration of IPTG added at the time of induction. s, soluble fraction; i, insoluble fraction.

7.2.2.3. Expression of Soluble Proteins by Random Incremental Truncation

In face of these daunting results, we decided to explore the possibility of employing an external service specialized in the expression of challenging proteins. Instruct–ERIC (Structural Biology European Research Infrastructure Consortium, https://instruct-eric.org/) is a pan–European research infrastructure that offers leading technologies and methods of such type to European researchers, enabling them to make use of the services themselves or to carry out projects in collaboration with high–end groups. One such Instruct–ERIC centre is the IBS–ISBG (Structural Biology Institute – Integrated Structural Biology Grenoble) in France, which provides a top–notch technology known as ESPRIT (Expression of Soluble Proteins by Random Incremental Truncation) (Mas and Hart, 2017; Yumerefendi *et al.*, 2010).

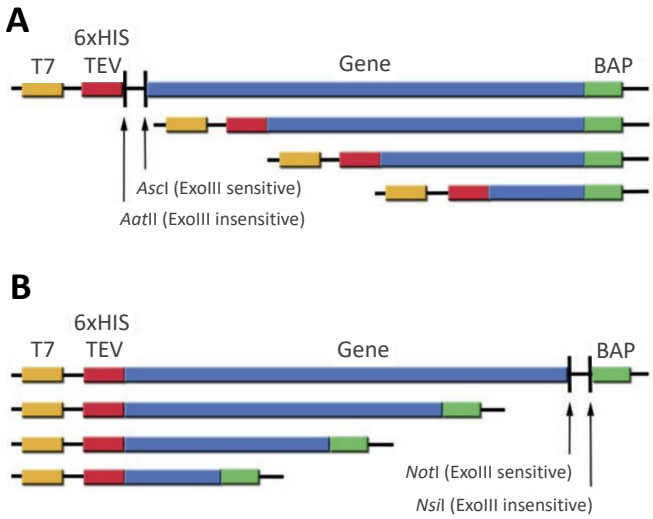

Figure 7.14. Schematic representation of the ESPRIT truncation library strategies. (A) N–terminally or (B) C–terminally truncated constructs are encoded by a 5' or 3' DNA truncation library respectively. To generate the library, the plasmid is firstly double digested, leaving an exonuclease III resistant end (*Aat*II or *Nsi*I) and a hydrolysable end (*Asc*I or *Not*I) to enable the posterior unidirectional truncations. After the truncation steps, the vector is re–circularized, leading to the respective fusion of the His–tag (for the N–terminal constructs) or the biotin acceptor peptide (BAP, for the C–terminal constructs) to the final truncated construct. Figure from Mas and Hart, 2017.

ESPRIT is a directed evolution–type process that combines random deletion mutagenesis with high throughput solubility screening to design high yielding, soluble expression constructs (Mas and Hart, 2017; Yumerefendi *et al.*, 2010). An exonuclease

(ExoIII) is employed to truncate the target gene sequence, generating random truncation libraries with all possible construct termini (*Fig. 7.14*). Thousands of clones (up to 28,000) can then be isolated with colony picking robots and subsequently gridded out to form high density colony arrays, which are tested for soluble protein expression through the use of *in vivo* biotinylation. Clones expressing both the N–terminal His–tag (to facilitate purification) and the C–terminal biotinylated biotin acceptor peptide (BAP, to ensure solubility) are identified by fluorescence imaging (*Fig. 7.15*). Finally, ninety–six positive clones are induced in liquid culture and subsequently affinity purified with a plate base purification to confirm solubility.

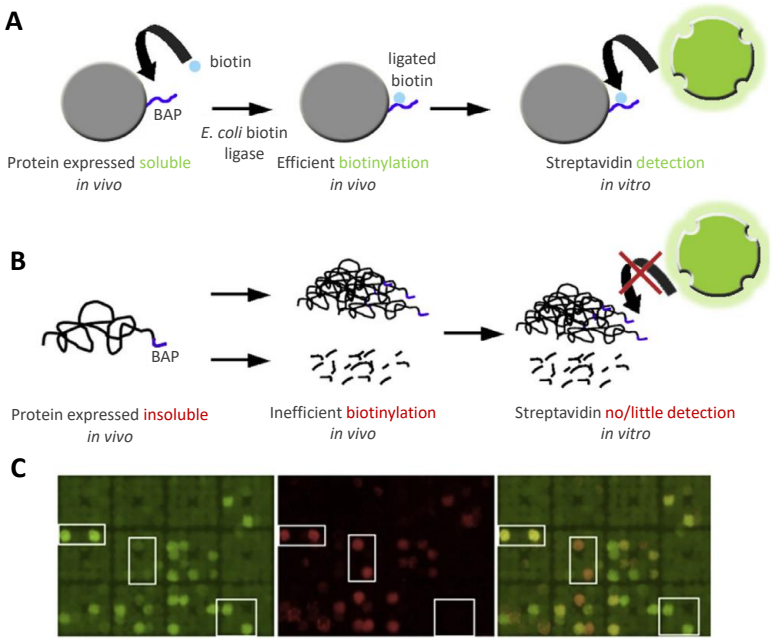

Figure 7.15. Colony array testing for soluble protein expression. Target constructs are expressed as fusion proteins with an N–terminal His–tag and a C–terminal BAP. If proteins are expressed as soluble (A), *E. coli* is able to efficiently biotinylate them, which is not the case for insoluble or degraded proteins (B). As a consequence, the solubility and integrity of each protein construct can be determined through (C) simultaneous hybridization of fluorescent streptavidin (green) to the BAP and of a fluorescent secondary antibody (red) to the His–tag. The merged image on the right shows a potentially interesting construct (top left, yellow signal; presents both the N–terminal His–tag and the C–terminal BAP), a poorly soluble or degraded construct (centre, red signal; lacks the BAP) and a soluble but degraded construct (bottom right, green signal; lacks the His–tag). Figure from Yumerefendi *et al.*, 2010.

In collaboration with director PhD. Darren Hart and platform engineer Philippe Mas, and financed by Instruct–ERIC, the ESPRIT technology was applied to human AIFL in hopes of finding a soluble, high expression construct. Truncation steps were performed on six starting sequences, of which half were to be truncated from the 3' end and the other half from the 5' end (*Fig. 7.16*). In order to avoid ensuing complications, the flexible N–terminus (aa 0–64) was directly eliminated from all constructs. N–terminal anchoring points were subsequently set at the beginning of the Rieske domain (Q65), in between the Rieske and oxidoreductase domains (S168) and at the beginning of the oxidoreductase domain (S192) (*Fig. 7.16A*). In this way, the Rieske domain, which may prove problematic during the folding procedure because of its covalently–bound cluster, was taken out of two truncation libraries, in principle increasing the chances of finding a soluble expression construct. On the other hand, C–terminal anchoring points were set at the end of the protein (S605), at the end of the reductase C–terminal domain (L587) and at the beginning of the reductase C–terminal domain (G526) (*Fig. 7.16A*). Thus, an additional truncation library was generated where the reductase C–terminal domain was also missing, in case it was somehow disrupting the protein's adequate folding. All related experimental assays were performed at the IBS–ISBG by Phillipe Mas.

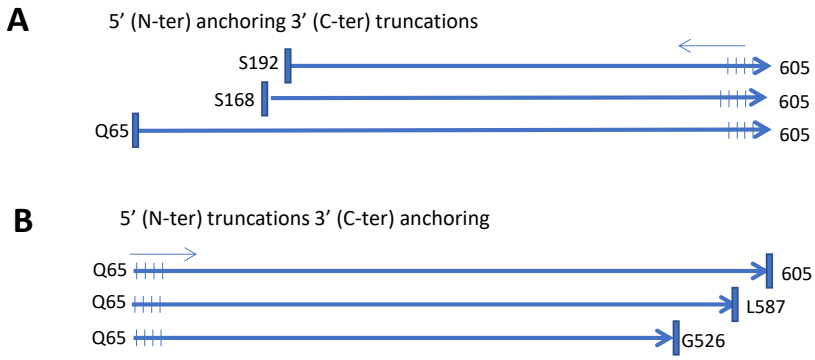

Figure 7.16. Starting sequences of human AIFL for the ESPRIT truncation library strategy. Six DNA constructs were generated to be truncated from either (A) the 3' end or (B) the 5' end. N–terminal anchoring points (indicated by thick lines in A) were set at the beginning of the Rieske domain (Q65, to eliminate the flexible N–terminus), in between the Rieske and the oxidoreductase domains (S168) and at the beginning of the oxidoreductase domain (S192). C–terminal anchoring points (indicated by thick lines in B) were set at the very end of the protein (S605), at the end of the reductase C–terminal domain (L587) and at the beginning of the

reductase C–terminal domain (G526). Truncations steps (indicated by thin, repetitive lines) began from the end of the protein (S605) or from the beginning of the Rieske domain (Q65).

In total, 18,432 clones were successfully isolated and screened. However, no strong expression of any intact clone (presenting both the N–terminal His–tag and the C–terminal BAP) could be observed (*Fig. 7.17*). Instead, fragments with either one end or the other yielded an overall weak degree of expression, suggesting that all the isolated clones had either no significant expression or were somehow degraded. In the end, it was concluded that there may be a region in the centre of the protein that is significantly unstable, which leads to the complete or partial degradation of the whole protein (regardless of its starting and ending points) during the expression procedure.

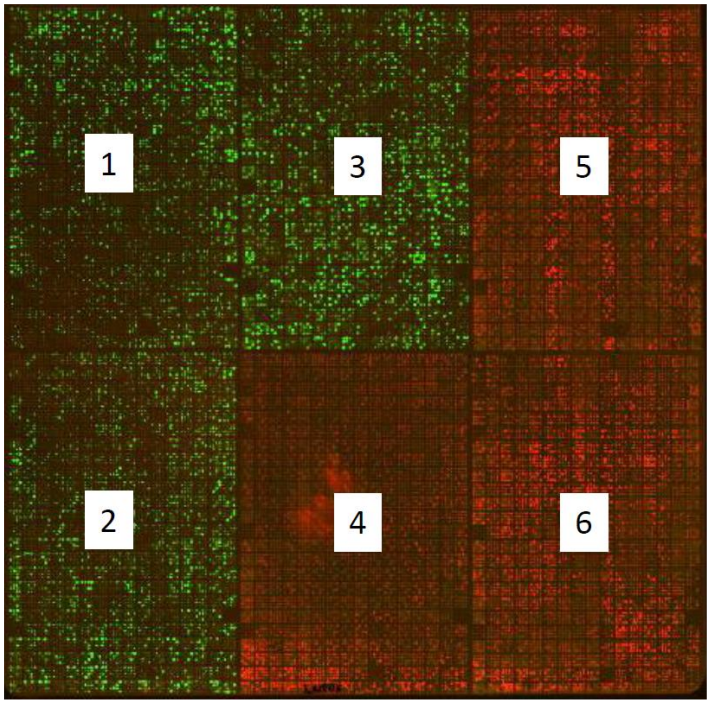

Figure 7.17. Resulting colony array of the AIFL clones. Probing was performed with fluorescent detection reagents against the N–terminal His–tag (red signal) and the C–terminal BAP (green signal). The merge of both channels should lead to the apparition of yellow, indicative of strong double tag signals. However, no intact AIFL clone can be observed. Fields 1, 2 and 3 correspond to the 5' end truncations; fields 4, 5 and 6 to the 3' end truncations.

7.2.3. Concluding remarks

Fe–S flavoproteins constitute a vast and expanding class of complex, multi–domain and typically multi–subunit enzymes in which the archaic Fe–S clusters can be found working side by side with the versatile flavin cofactors (Vanoni, 2021). Thanks to this particular disposition, proteins of this kind usually participate in oxidoreduction reactions acting as switches between donors of electron pairs and acceptors of single electrons, or the other way around (Vanoni, 2021).

One such Fe–S flavoprotein is AIFL, a mitochondrial enzyme that possesses a Rieske domain with a covalently–bound [2Fe–2S] cluster followed by an FAD–dependent oxidoreductase domain. AIFL is the only protein in its family featuring an Fe–S cluster, and as a consequence it offers a distinct flux of electrons (from a donor NADH coenzyme to the FAD cofactor, then to the Fe–S cluster and finally to another acceptor protein) that cannot be achieved by either of its sisters, AIF and AMID (Novo *et al.*, 2021). The synergy between both domains of AIFL may be modulated by its third domain, the C–terminal reductase domain, as it has been previously reported to mediate the interaction between a ferredoxin reductase (presenting an oxidoreductase domain) and its partner ferredoxin (with a Rieske–type domain) (Senda *et al.*, 2007). Indeed, computational modelling of AIFL suggests that it may exhibit a "closed"–like conformation, where the Rieske domain is found in intimate contact with the oxidoreductase and C–terminal reductase domains, or an "open"–like conformation, where the Rieske domain "runs free" thanks to the flexible loop that connects it with the rest of the protein (*Fig. 7.4*) (Novo *et al.*, 2021).

Indeed, a substantial housekeeping function can be envisaged for AIFL as a free radical scavenger, which is further supported by it being both ubiquitously expressed in humans and significantly conserved throughout the eukaryotic kingdoms (Novo *et al.*, 2021). AIFL is gravely uncharacterized as of today, but still the available clinical studies already punctuate its potentially critical role in maintaining the bioenergetics of healthy cells (Lozic *et al.*, 2021; Murata *et al.*, 2011) and assisting the metabolism and ROS resistance of tumour cells (Chuan–on *et al.*, 2022; Zheng *et al.*, 2019). AIFL additionally yields the ability to induce apoptosis, although it may do so in a caspase–dependent manner with no apparent translocation to the nucleus, unlike AIF (Xie *et al.*, 2005).

In this chapter, several protein production procedures have been assessed in search for the optimal conditions in which to overexpress and purify human AIFL to homogeneity. Firstly, a construct of the full gene was experimentally synthesized through molecular biology (pNNH1, with a pET–28a(+) backbone) and subsequently transformed into *E. coli* BL21 (DE3) cells. However, the resulting protein turned out to be mostly degraded upon expression, which was attributed to the potential presence of an N–terminal PTM site for N–myristoylation. A commercial synthesis ensued, in this case generating three different constructs (full–length without the N–terminus, $AIFL_{\Delta 64}$; the Rieske domain, $AIFL_{65-168}$; and the oxidoreductase and C–terminal domains, $AIFL_{\Delta 195}$) in all of which the potentially problematic N–terminus (aa 0–64) had been eliminated. However, only a mild overexpression was achieved with the $AIFL_{\Delta 64}$ construct, while the other two constructs presented minimal to no expression. This observation suggests that the interaction between the Rieske and oxidoreductase domains of AIFL may be necessary to ensure the proper folding of the protein, possibly acquiring a conformation similar to that of the modelled "closed"–like state.

Over the course of this, various settings of different nature were tested in regard to the strain (BL21 (DE3), C41 (DE3), BL21 Star (DE3) and Tuner), temperature after induction (18, 25 and 37 °C), OD_{600nm} at the time of induction (0.5, 0.8 and 1.0), IPTG concentration (0.2, 0.5 and 1 mM) and medium (LB and TB), but none proved successful in improving the overexpression of $AIFL_{\Delta 64}$. Furthermore, several supplements were added to the medium in hopes of promoting the synthesis of the Fe–S cluster and the FAD cofactor (1mM $FeSO_4$, 1 mM cysteine, 2 mM ammonium ferric citrate and 8 µg/mL riboflavin), to no apparent improvement. Only minor soluble expression could be observed, with the majority of the protein appearing in the insoluble fraction. A purification assay was performed, resulting in degraded protein mixed up with a considerable number of impurities.

As a consequence, it was concluded that one of the most probable causes for the instability of the AIFL construct was a faulty incorporation of the Fe–S cluster to the Rieske domain, as this cofactor needs to be covalently bound to the protein and as such might determine its adequate folding within the cell. A vector containing several proteins potentially involved in the formation and/or repair of Fe–S proteins in *E. coli* (pISC) (Nakamura *et al.,* 1999) was kindly provided by the group of Eduardo Ceccarelli and subsequently co–expressed with the $AIFL_{\Delta 64}$ construct. However, the improvement on the solubility of the target during the expression procedure was at best mild. Finally, with the aid of the European infrastructure Instruct–ERIC, a

collaboration was established with the IBS–ISBG centre in Grenoble, through which the high–end ESPRIT technology was employed to generate six different truncation libraries of AIFL. However, regretfully none of the over 18,000 clones that were tested yielded a soluble, well–expressed construct. At the present time, a sample of *E. coli* C41(DE3) cells containing the pISC plasmid has been sent to the IBS–ISBG, and expression is currently being tested with the same truncation libraries but in co–expression with the Fe–S cluster chaperones.

8. Discussion

Current insights on the human AIF family already envisage a significant role in tipping the delicate balance between cell life and cell death. Since its discovery in 1997 (Susin *et al.*, 1997), AIF has already amassed more than 18,000 entries in PubMed, with approximately 700 new entries appearing every passing year. In comparison, the AMID and AIFL enzymes possess only ~110 and ~25 total entries respectively, even though they share the same oxidoreductase domain and the ability to induce PCD (Novo *et al.*, 2021). Furthermore, despite its grave lack of characterization, AIFL presents a unique potential flux of electrons that cannot be achieved by either AIF or AMID, suggesting a particularly remarkable and exclusive function for this protein.

The main objective of this PhD thesis was to expand our knowledge on the pro–life and pro–death functions of human AIF, as well as to shed light into how these properties may be affected in pathology. Furthermore, we aimed to evaluate several overexpression procedures for the uncharacterized AIFL enzyme.

8.1. The Role of AIF in Cell–Death

AIF is a paramount moonlighting flavoenzyme that typically resides within the mitochondria of healthy cells, in an NADH–dependent equilibrium between its oxidized monomeric form and its reduced dimeric form (Ferreira *et al.*, 2014). Under these physiological conditions, AIF may interact with protein partner CHCHD4, indirectly sustaining the bioenergetics and oxidative phosphorylation of mitochondria (Delavallée *et al.*, 2020; Hangen *et al.*, 2015). However, upon pro–apoptotic stimuli, AIF becomes a leading effector of caspase–independent necroptosis, travelling to the nucleus to induce chromatin condensation and large–scale DNA fragmentation through the formation of the DNA–degradosome (Artus *et al.*, 2010; Cabon *et al.*, 2012). In chapter 4 of this PhD thesis, we aspired to characterise the *in vitro* molecular interactions between AIF, protein partners CypA and H2AX, and the DNA, in hopes of deepening our understanding on the mechanism of formation of the degradosome. Furthermore, we aimed to describe the nuclease activity of the degradosome, which does not reside solely in the CypA nuclease but also unexpectedly in AIF itself.

The mature mitochondrial form of AIF is naturally found inside the mitochondria, anchored to the MIM through the transmembrane helix of its N–terminal MLS and facing the IMS, where it carries out vital, mostly uncharacterized functions through

its interaction with other biomolecules such as NADH or CHCHD4 (Modjtahedi *et al.*, 2006; Otera *et al.*, 2005; Robinson and Lemire, 1996). However, under pathological conditions, AIF can be proteolytically cleaved and its soluble pro–apoptotic form released into the cytosol. At this point, the subsequent translocation of AIF to the nucleus can be either frustrated or potentiated by its respective interaction with protein partners HSP70 or CypA, providing a regulatory step for the cell prior to its death (Gurbuxani *et al.*, 2003; Zhu *et al.*, 2007). Once in the nucleus, the synchronized action of AIF, phosphorylated histone H2AX and nuclease CypA is proposed to be imperative to induce chromatin remodelling and DNA loss, through their association in the multi–protein complex that is known as degradosome (Artus *et al.*, 2010). Previous studies have suggested that H2AX is able to provoke DNA restructuration in order to enhance its accessibility to endonucleases, while the latter (such as CypA) would perform the degradation of the DNA (Joza *et al.*, 2009; Susin *et al.*, 1999; Vahsen *et al.*, 2006; Ye *et al.*, 2002). In this context, AIF was envisaged to act exclusively as a platform for the assembly of the DNA–degradosome, as it possesses the theoretical capability to concurrently interact with all of the components through different regions (Artus *et al.*, 2010; Baritaud *et al.*, 2010; Farina *et al.*, 2018; Romero–Tamayo *et al.*, 2021; Ye *et al.*, 2002).

In this PhD thesis, as presented in chapter 4, we have contributed to the description of the assembly of the DNA–degradosome at the molecular level. Through the use of various experimental techniques (namely, 2D electrophoresis, SEC, AFM and ITC) we have characterized the interaction between and amongst every component of the multi–protein complex, culminating in the proposal of a plausible mechanism for the events that are required for the formation of the DNA–degradosome during caspase–independent necroptosis.

Our study of the binary and tertiary interactions between the components of the degradosome demonstrates that AIF holds a significant plasticity to interplay with protein partners CypA and H2AX, as well as with the dsDNA, both separately and simultaneously. These findings agree with the required synchronized presence of AIF, CypA and H2AX in the nucleus to induce DNA degradation (Artus *et al.*, 2010), while simultaneously refuting previous results in which no interaction was reported between AIF and CypA in absence of H2AX (Baritaud *et al.*, 2010). In fact, the interaction of the AIF:CypA binary complex appeared to be the most favourable and the only one presenting some manner of specificity. Additionally, we have identified

cooperative effects between AIF and H2AX, as well as among the three protein components of the degradosome, to promote dsDNA binding and degradation. Although further research is imperative, the data here provided envisages a significantly plausible mechanism for the formation of the degradosome and its subsequent binding to DNA. In this sequential mechanism, the pro–apoptotic soluble form of AIF would bind CypA in the cytosol, promoting their nuclear co–translocation, as has been previously proposed in the literature (Cande *et al.*, 2004; Farina *et al.*, 2017; Zhu *et al.*, 2007). Once in the nucleus, the AIF:CypA complex would recruit H2AX, giving rise to the degradosome. The presence of H2AX would in turn stimulate the subsequent binding of dsDNA to the degradosome, which could then be restructured by the histone to improve its accessibility for the endonucleases (Joza *et al.*, 2009; Susin *et al.*, 1999; Vahsen *et al.*, 2006; Ye *et al.*, 2002).

The DNA–degrading capacity of AIF has traditionally been exclusively attributed to its recruitment of nucleases like CypA (Cande *et al.*, 2004; Wang *et al.*, 2002; Wang *et al.*, 2016), even though AIF depletion seems to be an absolute requirement to abolish caspase–independent PCD (Delavallée *et al.*, 2020). In chapter 4 of this PhD thesis, we have presented compelling proof that AIF can carry out nuclease activity by itself. Furthermore, we have demonstrated that AIF is able to cleave genomic DNA into large fragments both on its own and in cooperation with CypA, in which case the nuclease activity of both proteins appears to be significantly favoured by the presence of the other. The nuclease activity of AIF resides in two different motifs, a TopIB and a DEK motif, both of which are located in the surface at the DNA–binding crown (Romero–Tamayo *et al.*, 2021; Ye *et al.*, 2002). Mutation of key residues in these nuclease motifs greatly impact the *in vitro* nuclease activity of AIF, going as far as preventing cell death in some previous unrelated cellular studies (Ye *et al.*, 2002). Consequently, we have here established that the role of AIF in the degradosome goes far beyond that of a simple platform for the assembly of the multi–protein complex, being able to act as an apoptotic nuclease on its own. This knowledge opens trails for further studies on the implications of AIF in cell death, as well as to develop new therapeutical strategies for AIF–associated diseases.

8.2. Pathology in AIF

AIF dimerizes upon reduction of its FAD cofactor by catalytic $NADH_A$, eliciting the formation of an exceptionally stable $FADH^-$:NAD^+ CTC (Ferreira *et al.*, 2014). The resulting monomer–dimer equilibrium is proposed to act as a sensor of the mitochondrial redox state through the levels of NADH/NAD^+, being potentially modulated by the binding of non–catalytic $NADH_B$ (Brosey *et al.*, 2016; Ferreira *et al.*, 2014). In addition, AIF is an essential player in the import of CHCHD4 to the mitochondria and in its subsequent localization within the IMS, ultimately dictating the import and assembly of several of the respiratory complexes (Delavallée *et al.*, 2020; Hangen *et al.*, 2015; Modjtahedi *et al.*, 2015; Salscheider *et al.*, 2022). By virtue of these irreplaceable pro–life roles, faults in AIF lead to significant limitations in OXPHOS as an indirect consequence of the deficiency of CHCHD4, resulting in grave human pathogenic disorders that typically course with severe neurodegeneration (Meyer *et al.*, 2015; Modjtahedi *et al.*, 2016). Diagnosis of AIF–associated disorders can be substantially arduous, in view of the usually unspecific and significantly variable symptoms.

In chapter 5 of this PhD thesis, we aimed to characterize the structural and functional deficiencies experienced by two recently–discovered pathogenic mutations of AIF: T141I, located in the FAD–binding domain, and M340T, which resides in the NADH–binding domain (Heimer *et al.*, 2018). Both variants give rise to a neurodegenerative disease known as Cowchock syndrome, although their phenotypes are not exactly identical (Bogdanova–Mihaylova *et al.*, 2019; Heimer *et al.*, 2018).

The T141I replacement provokes a loss of both polarity and space at position 141, which in turn results in an alteration of the environment of nearby key catalytic residues such as P173, K177, H454 and W483 (Villanueva *et al.*, 2015). Furthermore, it affects the H–bond network that surrounds the FAD cofactor in AIF, moderately impacting both its properties and its stability. Indeed, we have demonstrated that variant T141I considerably shifts the mid–point reduction potential of the FAD, significantly decreasing as a result the stability of the CTC. Moreover, the T141I substitution gives rise to a considerably lessened dimer stability, most possibly because of the indirect alteration of the environment of H454. The observed diminished CTC stability could potentially abolish the ability of the T141I variant to undertake the function of a sensor of the mitochondrial redox state, completely bypassing one of its

critical pro–life roles. Additionally, its difficulty in maintaining a dimeric conformation could result in a shift of the monomer–dimer equilibrium *in vivo*, leading to a greater population of monomers and consequently exposing the protein to the proteolytic cleavage that initiates its PCD mechanism. This latter behaviour could also somewhat hinder the interplay of the T141I variant with CHCHD4, as its interaction depends on AIF being in the reduced dimeric state (Hangen *et al.*, 2015; Romero-Tamayo *et al.*, 2021). We have additionally demonstrated that the thermal stability of AIF is considerably debilitated by the T141I replacement, which may lead to its unfolding and subsequent degradation *in vivo*. Overall, the T141I aberration results in a relatively unstable protein that experiences a moderate difficulty in performing the essential roles typically carried out by AIF.

On the other hand, the replacement of M340 with a threonine residue takes place within the binding pocket of $NADH_A$, and it leads to a significant gain of polarity and space at the site. Our study of variant M340T has demonstrated that it is unable to stabilize the CTC in its mitochondrial form, even in the presence of protein partner CHCHD4. This aberrant behaviour might be the result of the increased freedom of movement provided by the M340T replacement to F310, deteriorating in consequence the essential role of the F310 residue in the stabilization of $NADH_A$ (Villanueva *et al.*, 2015). Indeed, soluble $M340T_{\Delta 77}$ exhibited a remarkable structural alteration in its active site and a significant increase in its efficiency as an NADH oxidase, most probably due to its inability to stabilize the CTC. Furthermore, we have here demonstrated that the M340T aberration somehow indirectly promotes the premature unfolding of the C–loop, resulting in a displacement of the monomer–dimer equilibrium towards the dimeric state in absence of NADH and to a higher thermal instability that cannot be overcome by the binding of the coenzyme. On the whole, these findings envisage for the M340T variant a severe difficulty in fulfilling its pro–life functions in the mitochondria, particularly pertaining its inability to effectively stabilize the CTC state and its NADH–desensitized dimerization.

8.3. The NADH Oxidase Activity of AIF

The reduced AIF_{rd}:2NADH crystal structure of AIF (PDB 4BUR) presents two NADH molecules bound to the protein monomer that are denoted as $NADH_A$ (which partakes in the charge transfer) and $NADH_B$ (which may act as an allosteric factor)

(Brosey *et al.*, 2016; Ferreira *et al.*, 2014; Ferreira *et al.*, 2018; Sorrentino *et al.*, 2015). Residue W483 can be found at the active site of AIF, and it happens to play a critical role in the binding of both coenzyme molecules. W483 belongs to an extensive H–bond network that stabilizes the extended conformation of $NADH_A$, facilitating the proper stacking of its nicotinamide ring between the *re*–face of the flavin isoalloxazine ring and the side chain of F310 (Ferreira *et al.*, 2014; Villanueva *et al.*, 2015). In this manner, the most optimal conformation for HT can be achieved, yielding a catalytically–competent CTC that is remarkably stable against molecular oxygen reoxidation. This property of AIF dictates its significantly low efficiency as an NADH oxidase, supporting its potentially key role as a sensor of the mitochondrial redox state (Ferreira *et al.*, 2014). In addition to W483, whose crucial part we have demonstrated in chapter 6 of this PhD thesis, residues W196 and E493 also aid in the regulation of AIF's low efficient NADH oxidase activity through the stabilization of its CTC state (Ferreira *et al.*, 2014; Romero–Tamayo *et al.*, 2021; Villanueva *et al.*, 2019). With respect to the binding of $NADH_B$, W483 concurrently stacks between the *si*–face of the isoalloxazine ring of the FAD cofactor and the coenzyme's nicotinamide, effectively blocking external access to the active site and potentially limiting the action of $NADH_B$. While on the oxidized state, the two short α–helices of the C–loop (which become disordered in the reduced state, opening up the $NADH_B$ binding pocket) are in close proximity to W483, further restricting solvent accessibility to the FAD.

The study we have presented in chapter 6 of this PhD thesis aimed to follow up on the characterization of the critical role of W483 in AIF, through the investigation of three replacements (Gly, Leu and Tyr) expected to alter the flavin environment to a greater or lesser degree. This study was initiated in 2015 by PhD. Raquel Villanueva in her own PhD thesis, and it already demonstrated the substantial implications of this tryptophan residue on the NADH oxidase activity of AIF. Here, we have proven that W483 significantly modulates the stability of the enzyme's active site through its contribution to the interaction network, with its replacement resulting in a grave constriction of the flavin's environment and the subsequent premature release of the cofactor upon thermal denaturation. Furthermore, W483 influences the conformation and stability of the nearby C–loop, leading to its early unfolding while still in the oxidized state in the aggressive W483G and W483L variants. Both of these effects give rise to two correlated consequences: in the first place, they lead to an abnormal population of dimers in the absence of NADH; and, in the second place, they result in a considerable decrease of the protein's thermal stability and the

disappearance of the NADH–destabilizing effect that is typically experienced by WT AIF. This is in agreement with previous results obtained by PhD. Raquel Villanueva, where both aggressive replacements resulted in a significant alteration of AIF's ability to dimerize and a significant decrease of their thermal stability (Villanueva, 2015).

Back in the day, the replacement of W483 with either an aggressive or a conservative mutation additionally yielded a considerable increase in the efficiency of the HT process from NADH to FAD, already envisaging the residue's decisive implications on the catalytic mechanism and mid–point reduction potential of the enzyme (Villanueva, 2015). Indeed, we have demonstrated here that W483 regulates the efficiency of AIF as an NADH oxidase through the moderation of its mid–point reduction potential, as well as through the remarkable stabilization of its $FADH^-$:NAD^+ CTC state. The replacement of W483 with conservative residue Tyr already resulted in a precarious alteration of the active site, leaving $NADH_A$ in a sterically–compromised conformation and further backing the residue's importance on determining the binding and stability of the catalytic coenzyme. Every variant here studied led to a structurally jeopardized active site, in which the donor NADH molecule and the acceptor FAD were not found at the optimal distance for HT and had to rely instead in active distance sampling. However, even with these complications all replacements gave rise to a considerable improvement of the HT process, proving that W483's modulatory action does not depend on setting the optimal conformation for HT but on stabilizing a long–lasting CTC.

8.4. The Apoptosis Inducing Factor–Like

AIFL is also a mitochondrial flavoenzyme; however, it possesses an additional Rieske–type domain with an [2Fe–2S] cluster that is unique in the human AIF family. AIFL shares its flavin–dependent oxidoreductase domain with both AIF and AMID, and it is able to induce PCD as well, but it does so through a caspase–dependent mechanism that is unlike that of AIF and which does not involve its translocation to the nucleus (Xie *et al.*, 2005). In chapter 7 of this PhD thesis, we have presented what we believe to be the most interesting property of AIFL: its potential flux of electrons. With its particular combination of domains, AIFL may be able to transfer electrons from a donor NADH coenzyme to the FAD cofactor of its oxidoreductase domain, then to its Fe–S cluster in the Rieske domain, and finally to an unknown acceptor protein.

This specific electron flow could theoretically be performed in one or the other direction (Vanoni, 2021), and it would be exclusive to AIFL amongst the AIF family. The required interaction between the Rieske and oxidoreductase domains of AIFL would possibly rely on its third domain, a reductase C–terminal domain, which has already been reported to modulate the binding of ferredoxin reductases with their client ferredoxins (Senda *et al.*, 2007). Indeed, the computational models performed for AIFL envisage the plausible existence of a "closed"–like conformation, where the Rieske domain is found in direct contact with the oxidoreductase and C–terminal reductase domains, and an "open"–like conformation, where the Rieske domain is separated from the rest by a flexible loop (Novo *et al.*, 2021). This uncommon characteristic of AIFL could provide the enzyme with a fundamental moonlighting function, enabling it to act as a free radical scavenger to support the bioenergetics of healthy cells (Lozic *et al.*, 2021; Murata *et al.*, 2011) or to aid in the survival of cancer cells (Chuan–on *et al.*, 2022; Zheng *et al.*, 2019).

In chapter 7 of this PhD thesis, we have followed a wide variety of overexpression procedures in search for the most optimal conditions in which to produce soluble, pure AIFL. Although a substantial effort is still required in further research to yield a soluble, high–expression construct, our findings in this matter have shed some light into the complications that may arise during AIFL's production. In specific, two independent circumstances have been esteemed to be critical for the soluble expression of active AIFL: on the one hand, an adequate interaction may be necessary between the Rieske and oxidoreductase domains to aid in the proper folding of the protein *in vitro*, envisaging the "closed"–like conformation as the most stable; and, on the other hand, a faulty incorporation of the Fe–S cluster to the Rieske domain may compromise the overall folding of the protein, significantly increasing its instability and subsequent degradation. As has been previously stated, further studies are required to establish the conditions necessary for the overexpression of a soluble AIFL construct, but here we have contributed to the knowledge with the presented advances and have set posterior trials in motion.

9. Conclusions

9.1. The Role of AIF in Cell–Death

9.1.1. $AIF_{\Delta 101}$ is able to interact with every component of the DNA–degradosome complex separately, and all protein binary complexes can interact with dsDNA.

9.1.2. $AIF_{\Delta 101}$ can simultaneously interact with CypA, H2AX and dsDNA, proving the *in vitro* AIF–mediated formation of the degradosome and its interaction with dsDNA.

9.1.3. $AIF_{\Delta 101}$ and CypA compete against each other to interact with dsDNA, whereas the interaction of $AIF_{\Delta 101}$ with dsDNA or CypA is enhanced in the presence of H2AX. The degradosome complex, $AIF_{\Delta 101}$:CypA:H2AX, has a similar behaviour to the latter.

9.1.4. AIF acts as a docking platform to promote localization of CypA and H2AX, but still allows overall conformational orientation and flexibility. Consequently, the degradosome can conformationally evolve upon interaction with dsDNA, facilitating its association and the subsequent chromatin condensation and DNA degradation.

9.1.5. The most favourable sequential mechanism of formation of the degradosome might be the binding of CypA to $AIF_{\Delta 101}$, followed by that of H2AX to $AIF_{\Delta 101}$:CypA, and finishing with the binding of dsDNA to $AIF_{\Delta 101}$:CypA:H2AX.

9.1.6. $AIF_{\Delta 101}$ can efficiently degrade plasmid and genomic DNA. It also presents both nicking and linearizing activities, transforming supercoiled dsDNA into its open circular and linear forms prior to degradation to lower MW forms.

9.1.7. AIF presents in its surface a large positively–charged pocket with a TopIB motif (residues Y443, K446, R449, R450, R451 and H454). A DEK motif (D489, E522 and K518) can also be found close to the binding site of H2AX. All variants generated from these motifs yielded a significant impairment of the nuclease activity of $AIF_{\Delta 101}$.

9.2. Pathology in AIF

9.2.1. Variant T141I significantly improves AIF's ability to accept electrons from NADH and might alter the flavin environment because of its negative impact on the H–bond network. As a consequence, CTC stability is considerably reduced.

9.2.2. Variant T141I directly influences the environment of H454, altering the monomer–monomer interactions and subsequently hindering dimer stability without significantly affecting AIF's ability to dimerize.

9.2.3. Variant M340T$_{\Delta 101}$ presents a novel substrate–inhibition profile in the steady–state that diminishes significantly as the sample ages. This demonstrates the presence of a toxic population that is slowly displaced by one more similar to the WT.

9.2.4. The M340T replacement increases the freedom of movement of F310, resulting in a greater difficulty to reach the optimal conformation to stack the nicotinamide ring of the NADH and consequently destabilizing the CTC.

9.2.5. Variant M340T may present a more spacious binding pocket, increasing its affinity towards NADH. Coupled with a high CTC instability, this results in a considerable increase in its efficiency as an NADH oxidase.

9.2.6. The M340T replacement leads to conformational changes in the protein that indirectly impact the C–loop through its mutual interaction with the central β–sheet, leading to premature unfolding and a displacement of the monomer–dimer equilibrium towards the dimeric form even in the absence of NADH.

9.3. The NADH Oxidase Function of AIF

9.3.1. W483 modulates the conformation and stability of the C–loop in AIF, promoting its premature unfolding in the oxidized state in aggressive W483 variants.

9.3.2. W483 significantly influences the stability of AIF's active site through its key role in the interaction network. This results in a grave alteration of the FAD environment upon mutation of the residue and in the subsequent premature release of the cofactor during thermal denaturation.

9.3.3. W483 regulates the efficiency of AIF as an NADH oxidase through the moderation of its mid–point reduction potential and the significant stabilization of the $FADH^-$:NAD^+ CTC, potentially determining its ability to act as a sensor of the mitochondrial redox state.

9.3.4. The replacement of W483 in AIF results in a significantly altered active site in which the donor and acceptor molecules are not found at the optimal distance for HT.

9.3.5. W483 plays a fundamental role in determining the conformation of $NADH_A$ within the active site, leading to a sterically–compromised conformation for the coenzyme in the conservative W483Y replacement.

9.4. The Apoptosis Inducing Factor–Like

9.4.1. AIFL models present a "closed"–like conformation, where the Rieske domain is in direct contact with the oxidoreductase and C–terminal reductase domains, and an "open"–like conformation, where the Rieske domain is separated. This backs the proposed flux of electrons from an NADH donor to the FAD of the oxidoreductase domain, then to the Fe–S cluster of the Rieske domain and finally to an acceptor unknown client protein.

9.4.2. The interaction between the Rieske and oxidoreductase domains of AIFL may be necessary to ensure the proper folding of the protein *in vitro*.

9.4.3. A faulty incorporation of the Fe–S cluster to the Rieske domain may be one of the main causes for the AIFL constructs' instability, as the cofactor needs to be covalently bound and might consequently determine the protein's adequate folding.

9'. Conclusiones

9'.1. El Papel de AIF en la Muerte Celular

9'.1.1. $AIF_{\Delta 101}$ es capaz de interactuar con cada componente del complejo ADN–degradosoma de forma separada, y todos los complejos proteicos binarios pueden interactuar con el ADN.

9'.1.2. AIF puede interactuar de forma simultánea con CypA, H2AX y el ADN, demostrando la formación *in vitro* del degradosoma mediada por AIF y su interacción con el ADN.

9'.1.3. $AIF_{\Delta 101}$ y CypA compiten la una contra la otra por la interacción con el ADN, mientras que la interacción de $AIF_{\Delta 101}$ con el ADN o con CypA se ve promovida por la presencia de H2AX. El complejo del degradosoma, $AIF_{\Delta 101}$:CypA:H2AX, presenta un comportamiento similar al caso anterior.

9'.1.4. AIF actúa como una plataforma de atraque para promover la localización de CypA y H2AX, pero aún así permite cierta orientación y flexibilidad conformacional. Como consecuencia, el degradosoma puede evolucionar conformacionalmente ante la interacción con el ADN, facilitando su asociación y la posterior condensación de la cromatina y degradación del ADN.

9'.1.5. El mecanismo secuencial de formación del degradosoma más favorable podría ser la unión de CypA a $AIF_{\Delta 101}$, seguido de la de H2AX al complejo $AIF_{\Delta 101}$:CypA, y terminando con la unión del ADN al complejo $AIF_{\Delta 101}$:CypA:H2AX.

9'.1.6. $AIF_{\Delta 101}$ puede degradar eficientemente el ADN plasmídico y genómico. También presenta tanto actividades de linealizar como de mellar, transformando ADN superenrollado en sus formas circulares y lineales antes de degradarlo a formas de menor peso molecular.

9'.1.7. AIF presenta en su superficie un gran bolsillo de carga positiva con un motivo TopIB (residuos Y443, K446, R449, R450, R451 y H454). Un motivo DEK (D489, E522 y K518) también puede encontrarse cerca del sitio de unión de H2AX. Todas las variantes generadas a partir de estos motivos dieron lugar a una deficiencia significativa de la actividad nucleasa de $AIF_{\Delta 101}$.

9'.2. La Patología en AIF

9'.2.1. La variante T141I mejora significativamente la habilidad de AIF para aceptar electrones del NADH y puede alterar el entorno de la flavina debido a su impacto negativo en la red de puentes de hidrógeno. Como consecuencia, la estabilidad del CTC se ve considerablemente reducida.

9'.2.2. La variante T141I influencia de forma directa el entorno de H454, alterando las interacciones monómero–monómero y posteriormente disminuyendo la estabilidad del dímero sin afectar significativamente la habilidad de AIF para dimerizar.

9'.2.3. La variante M340T$_{\Delta 101}$ presenta un perfil novel de inhibición por sustrato en el estado estacionario que disminuye significativamente conforme envejece la muestra. Esto demuestra la presencia de una población tóxica que es lentamente desplazada por otra más similar a la nativa.

9'.2.4. La sustitución M340T aumenta la libertad de movimiento de F310, resultando en una mayor dificultad para alcanzar la conformación óptima para apilar el anillo de nicotinamida del NADH y consecuentemente desestabilizando el CTC.

9'.2.5.La variante M340T podría presentar un bolsillo de unión más espacioso, aumentando su afinidad por el NADH. Junto con una mayor inestabilidad del CTC, esto resulta en un aumento considerable de su eficiencia como NADH oxidasa.

9'.2.6. La sustitución M340T da lugar a cambios conformacionales en la proteína que impactan indirectamente en el bucle C mediante su interacción mutua con la hebra β central, resultando en un desplegamiento prematuro y en el desplazamiento del equilibrio monómero–dímero hacia la forma dimérica incluso en ausencia de NADH.

9'.3. La Función NADH Oxidasa de AIF

9'.3.1. W483 modula la conformación y estabilidad del bucle C en AIF, promoviendo su desplegamiento prematuro en el estado oxidado en las variantes agresivas de W483.

9'.3.2. W483 influencia significativamente el centro activo de AIF mediante su papel clave en la red de interacción. Esto resulta en una grave alteración del entorno del FAD tras la mutación del residuo y en la consecuente liberación prematura del cofactor durante la desnaturalización térmica.

9'.3.3. W483 regula la eficiencia de AIF como NADH oxidasa mediante la moderación de su potencial de reducción de punto medio y la estabilización significativa del CTC $FADH^{-}$:NAD^{+}, determinando potencialmente su habilidad para actuar como sensor del estado redox mitocondrial.

9'.3.4. La sustitución de W483 en AIF resulta en un centro activo significativamente alterado en el cual las moléculas donante y aceptora no se encuentran en la distancia óptima para la transferencia de hidruro.

9'.3.5. W483 juega un papel fundamental en la determinación de la conformación de $NADH_A$ dentro del centro activo, resultando en una conformación estéricamente comprometida para la coenzima en la sustitución conservativa W483Y.

9'.4. El Factor Inductor de Apoptosis 3

9'.4.1. Los modelos de AIFL presentan una conformación de estilo cerrado, donde el dominio Rieske está en contacto directo con los dominios oxidorreductasa y reductasa C–terminal, y una conformación de estilo abierto, donde el dominio Rieske está separado. Esto apoya el flujo de electrones propuesto desde la donante NADH al FAD del dominio oxidorreductasa, entonces al clúster Fe–S del dominio Rieske y finalmente a una proteína cliente aceptora desconocida.

9'.4.2. La interacción entre los dominios Rieske y oxidorreductasa de AIFL podría ser necesaria para asegurar el plegamiento adecuado de la proteína *in vitro*.

9'.4.3. La incorporación defectuosa del clúster Fe–S al dominio Rieske podría ser una de las causas principales de la inestabilidad de los constructos de AIFL, dado que el cofactor necesita estar unido covalentemente y podría consecuentemente determinar el plegamiento adecuado de la proteína.

Bibliography

Abraham, M. J., Murtola, T., Schulz, R., Páll, S., Smith, J. C., *et al.* (2015) GROMACS: High performance molecular simulations through multi–level parallelism from laptops to supercomputers. *SoftwareX* **1–2**, 19–25

Alano, C. C., Garnier, P., Ying, W., Higashi, Y., Kauppinen, T. M., *et al.* (2010) NAD+ depletion is necessary and sufficient for poly(ADP–ribose) polymerase–1–mediated neuronal death. *J Neurosci* **30**, 2967–2978

Aliverti, A., Curti, B., and Vanoni, M. A. (1999) Identifying and quantitating FAD and FMN in simple and in iron–sulfur–containing flavoproteins. *Methods in molecular biology* (Clifton, N.J.), **131**, 9–23

Anoz–Carbonell, E., Timson, D. J., Pey, A. L. and Medina, M. (2020) The catalytic cycle of the antioxidant and cancer–associated human NQO1 enzyme: hydride transfer, conformational dynamics and functional cooperativity. *Antioxidants* **9**, 772

Araujo, A. N., Camacho, C. P., Mendes, T. B., Lindsey, S. C., Moraes, L., *et al.* (2021) Comprehensive assessment of copy number alterations uncovers recurrent *aifm3* and *dlk1* copy gain in medullary thyroid carcinoma. *Cancers* **13**(2), 218

Ardissone, A., Piscosquito, G., Legati, A., Langella, T., Lamantea, E., *et al.* (2015) A slowly progressive mitochondrial encephalomyopathy widens the spectrum of AIFM1 disorders. *Neurology* **84**, 2193–2195

Artus, C., Boujrad, H., Bouharrour, A., Brunelle, M. N., Hoos, S., *et al.* (2010) AIF promotes chromatinolysis and caspase–independent programmed necrosis by interacting with histone H2AX. *EMBO J* **29**, 1585–1599

Ashkenazy, H., Abadi, S., Martz, E., Chay, O., Mayrose, *et al.* (2016) ConSurf 2016: an improved methodology to estimate and visualize evolutionary conservation in macromolecules. *Nucleic Acids Res* **44**, 344–350

Bano, D., and Prehn, J. H. M. (2018) Apoptosis–Inducing Factor (AIF) in Physiology and Disease: The Tale of a Repented Natural Born Killer. *EBioMedicine* **30**, 29–37

Baritaud, M. *et al.* (2012) AIF–mediated caspase–independent necroptosis requires ATM and DNA–PK–induced histone H2AX Ser139 phosphorylation. *Cell Death Dis* **3**, e390

Baritaud, M., Boujrad, H., Lorenzo, H.–K., Krantic, S. and Susin, S. (2010) Histone H2AX The missing link in AIF–mediated caspase–independent programmed necrosis. *Cell cycle (Georgetown, Tex.)* **9**, 3166–3173

Bazhabayi, M., Qiu, X., Li, X., Yang, A., Wen, W., *et al.* (2021) CircGFRA1 facilitates the malignant progression of HER–2–positive breast cancer via acting as a sponge of miR–

1228 and enhancing AIFM2 expression. *Journal of Cellular and Molecular Medicine* **25**(21), 10248–10256

Belkebir, A. and Azeddoug, H. (2012) Purification and characterization of SepII a new restriction endonuclease form Staphylococcus epidermidis. *Microbiol Res* **167**, 90–94

Bendjennat, M., Blanchard, A., Loutfi, M., Montagnier, L. and Bahraoui, E. (1997) Purification and characterization of Mycoplasma penetrans Ca^{2+}/Mg^{2+}–dependent endonuclease. *J Bacteriol* **179**, 2210–2220

Berger, I., Ben–Neriah, Z., Dor–Wolman, T., Shaag, A., Saada, A., *et al.* (2011) Early prenatal ventriculomegaly due to an AIFM1 mutation identified by linkage analysis and whole exome sequencing. *Mol Genet Metab* **104**, 517–520

Biasini, M., Bienert, S., Waterhouse, A., Arnold, K., Studer, G., *et al.* (2014) SWISS–MODEL: modelling protein tertiary and quaternary structure using evolutionary information. *Nucleic acids research* **42**(Web Server issue), 252–258

Bilyy, R., Kit, Y., Hellman, U., and Stoika, R. (2008) AMID: new insights on its intracellular localization and expression at apoptosis. *Apoptosis* **13**, 729–732

Binnig, G., Quate, F. and Gerber, Ch. (1986) Atomic Force Microscope. *Phys Rev Lett* **56**, 930

Bogdanova–Mihaylova, P., Alexander, M. D., Murphy, R. P., Chen, H., Healy, D. G., *et al.* (2019) Clinical spectrum of AIFM1–associated disease in an Irish family, from mild neuropathy to severe cerebellar ataxia with colour blindness. *Journal of the Peripheral Nervous System* **24**(4), 348–353

Brosey, C. A., Ho, C., Long, W. Z., Singh, S., Burnett, K., *et al.* (2016) Defining NADH–Driven Allostery Regulating Apoptosis–Inducing Factor. *Structure* **24**, 2067–2079

Cabon, L. *et al.* (2012) BID regulates AIF–mediated caspase–independent necroptosis by promoting BAX activation. *Cell Death Differ* **19**, 245–256

Cande, C., Cecconi, F., Dessen, P., Kroemer, G. (2002) Apoptosis–inducing factor (AIF): key to the conserved caspase–independent pathways of cell death? *J Cell Sci* **115**, 4727–4734

Cande, C., Vahsen, N., Kouranti, I., Schmitt, E., Daugas, E., *et al.* (2004) AIF and cyclophilin A cooperate in apoptosis–associated chromatinolysis. *Oncogene* **23**, 1514–1521

Catalano–Dupuy, D. L., Musumeci, M. A., López–Rivero, A., and Ceccarelli, E. A. (2011) A highly stable plastidic–type ferredoxin–NADP(H) reductase in the pathogenic bacterium Leptospira interrogans. *PLOS one* **6**(10), e26736

Chen, Y., and Wang, X. (2020) miRDB: an online database for prediction of functional microRNA targets. *Nucleic Acids Res* **48**, 127–131

Cheng, H., Chang, S., Xu, R., Chen, L., Song, X., *et al.* (2020) Hypoxia–challenged MSC–derived exosomes deliver miR–210 to attenuate post–infarction cardiac apoptosis. *Stem Cell Res Ther* **11**, 224

Chhetri, G., Kalita, P., and Tripathi, T. (2015) An efficient protocol to enhance recombinant protein expression using ethanol in *Escherichia coli*. *MethodsX* **2**, 385–391

Cho, J., Teshigawara, R., Kameda, M., Yamaguchi, S., and Tada, T. (2019) Nucleus–localized adiponectin is survival gatekeeper through miR–214–mediated AIFM2 regulation. *Genes Cells* **24**, 126–138

Choudhury, S., Bae, S., Ke, Q., Lee, J. Y., Kim, J., *et al.* (2011) Mitochondria to nucleus translocation of AIF in mice lacking Hsp70 during ischemia/reperfusion. *Basic Res Cardiol* **106**, 397–407

Christgen, S. L., Becker, S. M., & Becker, D. F. (2019) Methods for determining the reduction potentials of flavin enzymes. *Methods in enzymology* **620**, 1–25

Chua–on, D., Proungvitaya, T., Techasen, A., Limpaiboon, T., Roytrakul, S., *et al.* (2022) Bioinformatic prediction of novel signalling pathways of apoptosis–inducing factor, mitochondrion–associated 3 (AIFM3) and their roles in metastasis of cholangiocarcinoma cells. *Cancer Genomics & Proteomics* **19**(1), 35–49

Dai, E., Zhang, W., Cong, D., Kang, R., Wang, J., *et al.* (2020) AIFM2 blocks ferroptosis independent of ubiquinol metabolism. *Biochem Biophys Res Commun* **523**, 966–971

Davies, D. R., Mushtaq, A., Interthal, H., Champoux, J. J. and Hol, W. G. J. (2006) The structure of the transition state of the heterodimeric topoisomerase I of Leishmania donovani as a vanadate complex with nicked DNA. *J Mol Biol* **357**, 1202–1210

Delano, W. L. (2002) PyMOL: an open–source molecular graphics tool. *CCP4 Newsletter On Protein Crystallography* **40**, 82–92

Delavallée, L., Mathiah, N., Cabon, L., Mazeraud, A., Brunelle–Navas, M. N., *et al.* (2020) Mitochondrial AIF loss causes metabolic reprogramming, caspase–independent cell death blockade, embryonic lethality, and perinatal hydrocephalus. *Mol Metab* **40**, 101027

di Salvo, M. L., Mastrangelo, M., Nogués, I., Tolve, M., Paiardini, A., *et al.* (2017) Biochemical data from the characterization of a new pathogenic mutation of human pyridoxine–5'–phosphate oxidase (PNPO). *Data Brief* **15**, 868–875

Diodato, D., Tasca, G., Verrigni, D., D'Amico, A., Rizza, T., *et al.* (2016) A novel AIFM1 mutation expands the phenotype to an infantile motor neuron disease. *Eur J Hum Genet* **24**, 463–466

Doll, S., Freitas, F. P., Shah, R., Aldrovandi, M., da Silva, M. C., *et al.* (2019) FSP1 is a glutathione–independent ferroptosis suppressor. *Nature* **575**, 693–698

Duan, Y., Wu, C., Chowdhury, S., Lee, M. C., Xiong, G., *et al.* (2003) A point–charge force field for molecular mechanics simulations of proteins based on condensed–phase quantum mechanical calculations. *Journal of computational chemistry*, 24(16), 1999–2012

Dupuis, J., Langenberg, C., Prokopenko, I., Saxena, R., Soranzo, N., *et al.* (2010) New genetic loci implicated in fasting glucose homeostasis and their impact on type 2 diabetes risk. *Nat Genet* **42**, 105–116

Elguindy, M. M., and Nakamaru–Ogiso, E. (2015) Apoptosis–inducing Factor (AIF) and Its Family Member Protein, AMID, Are Rotenone–sensitive NADH:Ubiquinone Oxidoreductases (NDH–2). *J Biol Chem* **290**, 20815–20826

Elvitigala, D. A., Jayasooriya, R. G., Whang, I., and Lee, J. (2015) First report on the gastropod proapoptotic AIF3 counterpart from disk abalone (Haliotis discus discus) deciphering its transcriptional modulation by induced pathogenic stress. *Fish Shellfish Immunol* **47**, 697–705

Erdogan, A. J., Ali, M., Habich, M., Salscheider, S. L., Schu, L., *et al.* (2018) The mitochondrial oxidoreductase CHCHD4 is present in a semi–oxidized state in vivo. *Redox Biol* **17**, 200–206

Evans, M. G. and Polanyi, M. (1935) Some applications of the transition state method to the calculation of reaction velocities, especially in solution. *Trans Faraday Soc* **31**, 875

Eyring, H. (1935) The Activated Complex in chemical reactions. *J Chem Phys* **3**, 107

Fan, F. Y., Deng, R., Yi, H., Sun, H. P., Zeng, Y., *et al.* (2017) The inhibitory effect of MEG3/miR–214/AIFM2 axis on the growth of T–cell lymphoblastic lymphoma. *Int J Oncol* **51**, 316–326

Farina, B. *et al.* (2018) Binding mode of AIF(370–394) peptide to CypA: insights from NMR, label–free and molecular docking studies. *Biochem J* **475**, 2377–2393

Farina, B., Di Sorbo, G., Chambery, A., Caporale, A., Leoni, G., *et al.* (2017) Structural and biochemical insights of CypA and AIF interaction. *Sci Rep* **7**, 1138

Fernandez–Capetillo, O., Celeste, A., Nussenzweig, A. (2003) Focusing on foci: H2AX and the recruitment of DNA–damage response factors. *Cell Cycle* **2**, 426–427

Ferreira, P., and Medina, M. (2021) Anaerobic Stopped–Flow Spectrophotometry with Photodiode Array Detection in the Presteady State: An Application to Elucidate

Oxidoreduction Mechanisms in Flavoproteins. In: Barile, M. (eds) *Flavins and Flavoproteins. Methods in Molecular Biology*, **2280**. Springer, New York, NY

Ferreira, P., Villanueva, R., Cabon, L., Susín, S. A., and Medina, M. (2013) The oxido–reductase activity of the apoptosis inducing factor: a promising pharmacological tool? *Curr Pharm Des* **19**, 2628–2636

Ferreira, P., Villanueva, R., Martínez–Julvez, M., and Medina, M. (2018) Apoptosis–Inducing Factor 1, Mitochondrion–associated, 1. In *Encyclopedia of Signaling Molecules* (Choi, S., ed), 361–366

Ferreira, P., Villanueva, R., Martínez–Júlvez, M., Herguedas, B., Marcuello, C., *et al.* (2014) Structural insights into the coenzyme mediated monomer–dimer transition of the pro–apoptotic apoptosis inducing factor. *Biochemistry* **53**, 4204–4215

Frisch, M. J. *et al.* (2016) Gaussian 09. *Gaussian, Inc.*, Wallingford CT

Galano–Frutos, J. J. (2017) "GROMACS, VMD" lecture from the Biomolecular Simulation course. Master in Quantitative Biotecnology, University of Zaragoza (Zaragoza, Spain)

Ghezzi, D., Sevrioukova, I., Invernizzi, F., Lamperti, C., Mora, M., *et al.* (2010) Severe X–linked mitochondrial encephalomyopathy associated with a mutation in apoptosis–inducing factor. *Am J Hum Genet* **86**, 639–649

Gong, M., Hay, S., Marshall, K. R., Munro, A. W., and Scrutton, N. S. (2007) DNA binding suppresses human AIF–M2 activity and provides a connection between redox chemistry, reactive oxygen species, and apoptosis. *J Biol Chem* **282**, 30331–30340

Greenfield N. J. (2006) Using circular dichroism spectra to estimate protein secondary structure. *Nature protocols*, **1**(6), 2876–2890

Grimson, A., Farh, K. K., Johnston, W. K., Garrett–Engele, P., Lim, L. P., *et al.* (2007) MicroRNA targeting specificity in mammals: determinants beyond seed pairing. *Mol Cell* **27**, 91–105

Gurbuxani, S., Schmitt, E., Cande, C., Parcellier, A., Hammann, A., *et al.* (2003) Heat shock protein 70 binding inhibits the nuclear import of apoptosis–inducing factor. *Oncogene* **22**, 6669–6678

Hanahan, D. (1985) DNA Cloning: A Practical Approach (Glover, D.M., ed.), Vol. 1, 109

Hangen, E., Féraud, O., Lachkar, S., Mou, H., Doti, N., *et al.* (2015) Interaction between AIF and CHCHD4 Regulates Respiratory Chain Biogenesis. *Mol Cell* **58**, 1001–1014

Harijan, R. K., Zoi, I., Antoniou, D., Schwartz, S. D. and Schramm, V. L. (2017) Catalytic–site design for inverse heavy–enzyme isotope effects in human purine nucleoside phosphorylase. *PNAS* **114** (25), 6456–6461

Heimer, G., Eyal, E., Zhu, X., Ruzzo, E. K., Marek-Yagel, D., *et al.* (2018) Mutations in AIFM1 cause an X-linked childhood cerebellar ataxia partially responsive to riboflavin. *European Journal of Paediatric Neurology* **22**(1), 93–101

Horcas, I., Fernández, R., Gómez–Rodríguez, J. M., Colchero, J., Gómez–Herrero, J., and Baro, A. M. (2007) WSXM: a software for scanning probe microscopy and a tool for nanotechnology. *The review of scientific instruments* **78**(1), 013705

Horikoshi, N., Cong, J., Kley, N., and Shenk, T. (1999) Isolation of differentially expressed cDNAs from p53–dependent apoptotic cells: activation of the human homologue of the Drosophila peroxidasin gene. *Biochem Biophys Res Commun* **261**, 864–869

Hornus, S., Lévy, B., Larivière, D., and Fourmentin, E. (2013) Easy DNA modeling and more with GraphiteLifeExplorer. *PLoS One* **8**, e53609

Hsiao, C. P., Wang, D., Kaushal, A., and Saligan, L. (2013) Mitochondria–related gene expression changes are associated with fatigue in patients with nonmetastatic prostate cancer receiving external beam radiation therapy. *Cancer Nurs* **36**, 189–197

Humphrey, W., Dalke, A., and Schulten, K. (1996) VMD: visual molecular dynamics. *Journal of molecular graphics* **14**(1), 33–28

Jeffery, C. J. (2014) An introduction to protein moonlighting. *Biochem Soc Trans* **42**, 1679–1683

Jeong, E. G., Lee, J. W., Soung, Y. H., Nam, S. W., Kim, S. H., *et al.* (2006) Immunohistochemical and mutational analysis of apoptosis–inducing factor (AIF) in colorectal carcinomas. *APMIS* **114**, 867–873

Jiménez–García, B., Pons, C., and Fernández–Recio, J. (2013) pyDockWEB: a web server for rigid–body protein–protein docking using electrostatics and desolvation scoring. *Bioinformatics (Oxford, England)*, **29**(13), 1698–1699

Johnston, C., Martin, B., Fichant, G., Polard, P., and Claverys, J. P. (2014) Bacterial transformation: distribution, shared mechanisms and divergent control. *Nature reviews. Microbiology*, **12**(3), 181–196

Joza, N., Susin, S. A., Daugas, E., Stanford, W. L., Cho, S.K., *et al.* (2001) Essential role of the mitochondrial apoptosis–inducing factor in programmed cell death. *Nature* **410**, 549–554

Joza, N., Pospisilik, A. J., Hangen, E., Hanada, T., Modjtahedi, N., *et al.* (2009) AIF: not just an apoptosis–inducing factor. *Ann N Y Acad Sci* **1171**, 2–11

Jumper, J., Evans, R., Pritzel, A., Green, T., Figurnov, M., *et al.* (2021) Highly accurate protein structure prediction with AlphaFold. *Nature* **596**, 583–589

Kaczanowski, S. (2016) Apoptosis: its origin, history, maintenance and the medical implications for cancer and aging. *Phys Biol* **13**, 031001

Karagkouni, D., Paraskevopoulou, M. D., Chatzopoulos, S., Vlachos, I. S., Tastsoglou, S., *et al.* (2018) DIANA–TarBase v8: a decade–long collection of experimentally supported miRNA–gene interactions. *Nucleic Acids Res* **46**, 239–245

Ke, X., Yan, R., Sun, Z., Cheng, Y., Meltzer, A., *et al.* (2017) Esophageal Adenocarcinoma–Derived Extracellular Vesicle MicroRNAs Induce a Neoplastic Phenotype in Gastric Organoids. *Neoplasia* **19**, 941–949

Kettwig, M., Schubach, M., Zimmermann, F. A., Klinge, L., Mayr, J. A., *et al.* (2015) From ventriculomegaly to severe muscular atrophy: Expansion of the clinical spectrum related to mutations in AIFM1. *Mitochondrion* **21C**, 12–18

Klein, J. A., Longo-Guess, C. M., Rossmann, M. P., Seburn, K. L., Hurd, R. E., *et al.* (2002) The harlequin mouse mutation downregulates apoptosis-inducing factor. *Nature* **419**(6905), 367–374

Klim, J., Gładki, A., Kucharczyk, R., Zielenkiewicz, U., and Kaczanowski, S. (2018) Ancestral State Reconstruction of the Apoptosis Machinery in the Common Ancestor of Eukaryotes. *G3 (Bethesda)* **8**, 2121–2134

Knapp, M. J. and Klinman, J. P. (2002) Environmentally coupled hydrogen tunneling. Linking catalysis to dynamics. *Eur J Biochem* **269**(13), 3113–21

Kojima, N., Tanaka, Y., Kulkeaw, K., Nakanishi, Y., Shirasawa, S., *et al.* (2015) Apoptosis–inducing Factor, Mitochondrion–associated 2, Regulates Klf1 in a Mouse Erythroleukemia Cell Line. *Anticancer Res* **35**, 4493–4499

Kosinski, J., Feder, M., and Bujnicki, J. M. (2005) The PD–(D/E)XK superfamily revisited: identification of new members among proteins involved in DNA metabolism and functional predictions for domains of (hitherto) unknown function. *BMC Bioinformatics* **6**, 172

Laemmli U. K. (1970) Cleavage of structural proteins during the assembly of the head of bacteriophage T4. *Nature*, **227**(5259), 680–685

Lee, J. W., Jeong, E. G., Soung, Y. H., Kim, S. Y., Nam, S. W., *et al.* (2006) Immunohistochemical analysis of apoptosis–inducing factor (AIF) expression in gastric carcinomas. *Pathol Res Pract* **202**, 497–501

Lee, J. Y., Chang, J., Joseph, N., Ghirlando, R., Rao, D. N., *et al* (2005) MutH complexed with hemi– and unmethylated DNAs: coupling base recognition and DNA cleavage. *Mol Cell* **20**, 155–166

Lewis, E. M., Wilkinson, A. S., Jackson, J. S., Mehra, R., Varambally, S., *et al.* (2012) The enzymatic activity of apoptosis–inducing factor supports energy metabolism benefiting the growth and invasiveness of advanced prostate cancer cells. *J Biol Chem* **287**, 43862–43875

Li, T., Li, K., Zhang, S., Wang, Y., Xu, Y., *et al.* (2020) Overexpression of apoptosis inducing factor aggravates hypoxic–ischemic brain injury in neonatal mice. *Cell Death Dis* **11**, 77

Li, W., Sun, L., Liang, Q., Wang, J., Mo, W., *et al.* (2006) Yeast AMID homologue Ndi1p displays respiration–restricted apoptotic activity and is involved in chronological aging. *Mol Biol Cell* **17**, 1802–1811

Lienhart, W. D., Gudipati, V., and Macheroux, P. (2013) The human flavoproteome. *Arch Biochem Biophys* **535**, 150–162

Liu, B., Liu, H., Zhong, D. and Lin, C. (2010) Searching for a photocycle of the cryptochrome photoreceptors. *Current Opinion in Plant Biology* **13**(5), 578–586

Lostao, A., Peleato, M. L., Gómez–Moreno, C., and Fillat, M. F. (2010) Oligomerization properties of FurA from the cyanobacterium Anabaena sp. PCC 7120: direct visualization by in situ atomic force microscopy under different redox conditions. *Biochimica et biophysica acta* **1804**(9), 1723–1729

Lozic, M., Minarik, L., Racetin, A., Filipovic, N., Babic, M. S., and Vukojevic, K. (2021) CRKL, AIFM3, AIF, BCL2 and UBASH3A during human kidney development. *Int J Mol Sci* **22**(17), 9183

Lu, J., Chen, J., Xu, N., Wu, J., Kang, Y., *et al.* (2016) Activation of AIFM2 enhances apoptosis of human lung cancer cells undergoing toxicological stress. *Toxicol Lett* **258**, 227–236

Lu, T. and Chen, F. (2011) Multiwfn: A multifunctional wavefunction analyzer. *Journal of Computational Chemistry* **33**(5), 580–592

Ludlow, M. K., Soudackov, A. V., and Hammes–Schiffer, S. (2009). Theoretical analysis of the unusual temperature dependence of the kinetic isotope effect in quinol oxidation. *J Am Chem Soc* 131, 7094–7102

Maharjan, B., Boroujeni, M. R., Lefton, J., White, O. R., Razzaghi, M., *et al.* (2015) Steric effects on the primary isotope dependence of secondary kinetic isotope effects in hydride transfer reactions in solution: caused by the isotopically different tunneling ready state conformations? *J Am Chem Soc* **137**, 6653–6661

Mahmood, T., and Yang, P. C. (2012) Western blot: technique, theory, and trouble shooting. *North American journal of medical sciences*, **4**(9), 429–434

Maklashina, E., and Cecchini, G. (2020) Determination of flavin potential in proteins by xanthine/xanthine oxidase method. *Bio Protoc* **10**(7), e3571

Marshall, K. R., Gong, M., Wodke, L., Lamb, J. H., Jones, D. J., *et al.* (2005) The human apoptosis–inducing protein AMID is an oxidoreductase with a modified flavin cofactor and DNA binding activity. *J Biol Chem* **280**, 30735–30740

Mas, P. J., and Hart, D. J. (2017) ESPRIT: A method for defining soluble expression constructs in poorly understood gene sequences. In N. A. Burgess–Brown (Ed.). *Heterologous Gene Expression in E. coli: Methods and Protocols.* Methods in Molecular Biology, vol. 1586 (pp. 45–63). Berlin, Germany: Springer Science and Business Media

Mate, M. J., Ortiz–Lombardia, M., Boitel, B., Haouz, A., Tello, D., *et al.* (2002) The crystal structure of the mouse apoptosis–inducing factor AIF. *Nat Struct Biol* **9**, 442–446

Mei, J., Webb, S., Zhang, B., and Shu, H. B. (2006) The p53–inducible apoptotic protein AMID is not required for normal development and tumor suppression. *Oncogene* **25**, 849–856

Meyer, K., Buettner, S., Ghezzi, D., Zeviani, M., Bano, D., *et al.* (2015) Loss of apoptosis–inducing factor critically affects MIA40 function. *Cell Death Dis* **6**, e1814

Millan, A., and Huerta, S. (2009) Apoptosis–inducing factor and colon cancer. *J Surg Res* **151**, 163–170

Miramar, M. D., Costantini, P., Ravagnan, L., Saraiva, L. M., Haouzi, D., *et al.* (2001) NADH oxidase activity of mitochondrial apoptosis–inducing factor. *J Biol Chem* **276**, 16391–16398

Miriyala, S., Thippakorn, C., Chaiswing, L., Xu, Y., Noel, T., *et al.* (2016) Novel role of 4–hydroxy–2–nonenal in AIFm2–mediated mitochondrial stress signaling. *Free Radic Biol Med* **91**, 68–80

Miyake, N., Wolf, N. I., Cayami, F. K., Crawford, J., Bley, A., *et al.* (2017) X–linked hypomyelination with spondylometaphyseal dysplasia (H–SMD) associated with mutations in AIFM1. *Neurogenetics* **18**, 185–194

Modjtahedi, N., Giordanetto, F., Madeo, F., and Kroemer, G. (2006) Apoptosis–inducing factor: vital and lethal. *Trends Cell Biol* **16**, 264–272

Modjtahedi, N., Hangen, E., Gonin, P., and Kroemer, G. (2015) Metabolic epistasis among apoptosis–inducing factor and the mitochondrial import factor CHCHD4. *Cell Cycle* **14**, 2743–2747

Modjtahedi, N., Tokatlidis, K., Dessen, P., and Kroemer, G. (2016) Mitochondrial Proteins Containing Coiled–Coil–Helix–Coiled–Coil–Helix (CHCH) Domains in Health and Disease. *Trends Biochem Sci* **41**, 245–260

Montague, J. W., Hughes, F. M., Cidlowski, J. A. (1997) Native recombinant cyclophilins A, B, and C degrade DNA independently of peptidylprolyl cis–trans–isomerase activity. Potential roles of cyclophilins in apoptosis. *J Biol Chem* **272**, 6677–6684

Morton, S. U., Prabhu, S. P., Lidov, H. G., Shi, J., Anselm, I., *et al.* (2017) AIFM1 mutation presenting with fatal encephalomyopathy and mitochondrial disease in an infant. *Cold Spring Harb Mol Case Stud* **3**, a001560

Murata, Y., Furuyama, I., Oda, S., and Mitani, H. (2011) A novel Rieske–type protein derived from an apoptosis–inducing factor–like (AIFL) transcript with a retained intron 4 induces change in mitochondrial morphology and growth arrest. *Biochem Biophys Res Commun* **407**, 92–97

Nagel, Z. D. and Klinman, J. P. (2006) Tunneling and dynamics in enzymatic hydride transfer. *Chem Rev* **106**(8), 3095–118

Nakamura, M., Saeki, K. and Takahashi, Y. (1999) Hyperproduction of recombinant ferredoxins in *Escherichia coli* by coexpression of the ORF1–ORF2–iscS–iscU–iscA–hscB–hs cA–fdx–ORF3 gene cluster. *The Journal of Biochemistry* **126**, 1, 10–18

Nguyen, H. P., Villivalam, S. D., Jung, B. C., You, D., Lin, F., *et al.* (2022) AIFM2 is required for high–intensity aerobic exercise in promoting glucose utilization. *Diabetes 2022* **71**(10), 2084–2093

Nguyen, H. P., Yi, D., Lin, F., Viscarra, J. A., Tabuchi, C., *et al.* (2020) Aifm2, a NADH Oxidase, Supports Robust Glycolysis and Is Required for Cold– and Diet–Induced Thermogenesis. *Mol Cell* **77**, 600–617.e604

Novo, N. (2017) Caracterización funcional de AIFM3 mediante inactivación del gen por la técnica CRISPR–Cas9 y sobreexpresión de la proteína en bacterias y células eucariotas [Degree Research Project, University of Zaragoza]

Novo, N. (2018) Towards the molecular characterization of the human AIFM3 (apoptosis–inducing factor, mitochondrion–associated 3) [Master Research Project, University of Zaragoza]

Novo, N., Ferreira, P., Medina, M. (2021) The apoptosis–inducing factor family: Moonlighting proteins in the crosstalk between mitochondria and nuclei. *IUBMB Life* **73**, 568–581

Novo, N., Romero–Tamayo, S., Marcuello, C., Boneta, S., Blasco–Machin, I., *et al.* (2022) Beyond a platform protein for the degradosome assembly: the Apoptosis Inducing Factor as an efficient nuclease involved in chromatinolysis. *PNAS Nexus* **2**, 1–11

Ohiro, Y., Garkavtsev, I., Kobayashi, S., Sreekumar, K. R., Nantz, R., *et al.* (2002) A novel p53–inducible apoptogenic gene, PRG3, encodes a homologue of the apoptosis–inducing factor (AIF). *FEBS Lett* **524**, 163–171

Ohyama, M., Tsuchiya, A., Kaku, Y., Kanno, T., Shimizu, T., *et al.* (2015) Phosphatidylinositol Derivatives Induce Gastric Cancer Cell Apoptosis by Accumulating AIF and AMID in the Nucleus. *Anticancer Res* **35**, 6563–6571

Olsson, M. H., Søndergaard, C. R., Rostkowski, M., and Jensen, J. H. (2011) PROPKA3: Consistent Treatment of Internal and Surface Residues in Empirical pKa Predictions. *Journal of chemical theory and computation* **7**(2), 525–537

Otera, H., Ohsakaya, S., Nagaura, Z., Ishihara, N., and Mihara, K. (2005) Export of mitochondrial AIF in response to proapoptotic stimuli depends on processing at the intermembrane space. *EMBO J* **24**, 1375–1386

Paesano, L., Perotti, A., Buschini, A., Carubbi, C., Marmiroli, M., *et al.* (2016) Markers for toxicity to HepG2 exposed to cadmium sulphide quantum dots; damage to mitochondria. *Toxicology* **374**, 18–28

Pallarés, M. C., Marcuello, C., Botello–Morte, L., González, A., Fillat, M. F., and Lostao, A. (2014) Sequential binding of FurA from Anabaena sp. PCC 7120 to iron boxes: exploring regulation at the nanoscale. *Biochimica et biophysica acta* **1844**(3), 623–631

Pandolfo, M., Rai, M., Remiche, G., Desmyter, L., and Vandernoot, I. (2020) Cerebellar ataxia, neuropathy, hearing loss, and intellectual disability due to AIFM1 mutation. *Neurology. Genetics* **6**(3), e420

Pang, D., Thierry, A. R. and Dritschilo, A. (2015) DNA studies using atomic force microscopy: capabilities for measurement of short DNA fragments. *Front Mol Biosci*, 29 January 2015

Pingoud, V., Wende, W., Friedhoff, P., Reuter, M., Alves, J., *et al.* (2009) On the divalent metal ion dependence of DNA cleavage by restriction endonucleases of the EcoRI family. *J Mol Biol* **393**, 140–160

Ravagnan, L., Gurbuxani, S., Susin, S. A., Maisse, C., Daugas, E., *et al.* (2001) Heat–shock protein 70 antagonizes apoptosis–inducing factor. *Nat Cell Biol* **3**, 839–843

Rinaldi, C., Grunseich, C., Sevrioukova, I. F., Schindler, A., Horkayne–Szakaly, I., *et al.* (2012) Cowchock syndrome is associated with a mutation in apoptosis–inducing factor. *Am J Hum Genet* **91**, 1095–1102

Robinson, K. M., and Lemire, B. D. (1996) A requirement for matrix processing peptidase but not for mitochondrial chaperonin in the covalent attachment of FAD to the yeast succinate dehydrogenase flavoprotein. *J Biol Chem* **271**, 4061–4067

Romero–Tamayo, S. (2022) Insights into the conformational landscape and interaction networks in human Apoptosis Inducing Factor [PhD thesis, University of Zaragoza]

Romero–Tamayo, S. *et al.* (2021) W196 and the *β*–Hairpin Motif Modulate the Redox Switch of Conformation and the Biomolecular Interaction Network of the Apoptosis–Inducing Factor. *Oxid Med Cell Longev* **2021**, 6673661

Salscheider, S. L., Gerlich, S., Cabrera–Orefice, A., Peker, E., Rothemann, R. A., *et al.* (2022) AIFM1 is a component of the mitochondrial disulfide relay that drives complex I assembly through efficient import of NDUFS5. *The EMBO Journal* **41**, e110784

Sambrook, J., & Russell, D. W. (2006) Preparation and Transformation of Competent E. coli Using Calcium Chloride. *CSH protocols, 2006*(1), pdb.prot3932

Sanchez, A. (2013) Mecanismos catalíticos en ferredoxina–$NADP^+$ reductasas de tipo planta [PhD thesis, University of Zaragoza]

Sancho, P., Sánchez–Monteagudo, A., Collado, A., Marco–Marín, C., Domínguez–González, C., *et al.* (2017) A newly distal hereditary motor neuropathy caused by a rare AIFM1 mutation. *Neurogenetics* **18**, 245–250

Sander, O., Henß, A., Näther, C., Würtele, C., Holthausen, M. C., *et al.* (2008) Aromatic hydroxylation in a copper bis(imine) complex mediated by a μ–η^2:η^2 peroxo dicopper core: a mechanistic scenario. *Chem Eur J* **14**, 9714–9729

Scott, A. J., Walker, S. A., Krank, J. J., Wilkinson, A. S., Johnson, K. M., *et al.* (2018) AIF promotes a JNK1–mediated cadherin switch independently of respiratory chain stabilization. *J Biol Chem* **293**, 14707–14722

Scott, A. J., Wilkinson, A. S., and Wilkinson, J. C. (2016) Basal metabolic state governs AIF–dependent growth support in pancreatic cancer cells. *BMC Cancer* **16**, 286

Sevrioukova, I. F. (2009) Redox–linked conformational dynamics in apoptosis–inducing factor. *J Mol Biol* **390**, 924–938

Sevrioukova, I. F. (2016) Structure/function relations in AIFM1 variants associated with neurodegenerative disorders. *J Mol Biol* **428**(18), 3650–3665

Shelar, S. B., Kaminska, K. K., Reddy, S. A., Kumar, D., Tan, C. T., *et al.* (2015) Thioredoxin–dependent regulation of AIF–mediated DNA damage. *Free Radic Biol Med* **87**, FRBMD1500111

Shen, S. M., Guo, M., Xiong, Z., Yu, Y., Zhao, X. Y., *et al.* (2015) AIF inhibits tumor metastasis by protecting PTEN from oxidation. *EMBO Rep*

Sorrentino, L., Calogero, A. M., Pandini, V., Vanoni, M. A., Sevrioukova, I. F., *et al.* (2015) Key Role of the Adenylate Moiety and Integrity of the Adenylate–Binding Site for the NAD(+)/H Binding to Mitochondrial Apoptosis–Inducing Factor. *Biochemistry* **54**, 6996–7009

Sotres, J. *et al.* (2008) Unbinding Molecular Recognition Force Maps of Localized Single Receptor Molecules by Atomic Force Microscopy. *ChemPhysChem* **9**, 590–599

Sotres, J., Lostao, A., Gómez–Moreno, C., Baró, A. M. (2007) Jumping mode AFM imaging of biomolecules in the repulsive electrical double layer. *Ultramicroscopy* **107**, 1207–1212

Sousa da Silva, A. W., & Vranken, W. F. (2012) ACPYPE – AnteChamber PYthon Parser interfacE. *BMC research notes* **5**, 367

Sucharitakul, J., Buckel, W. and Chaiyen, P. (2020) Rapid kinetics reveal surprising flavin chemistry in bifurcating electron transfer flavoprotein form *Acidaminococcus fermentans*. *J Biol Chem* **296** (100124), 1–15

Sun, T., Aceto, N., Meerbrey, K. L., Kessler, J. D., Zhou, C., *et al.* (2011) Activation of multiple proto–oncogenic tyrosine kinases in breast cancer via loss of the PTPN12 phosphatase. *Cell* **144**, 703–718

Susin, S. A., Daugas, E., Ravagnan, L., Samejima, K., Zamzami, N., *et al.* (2000) Two distinct pathways leading to nuclear apoptosis. *J Exp Med* **192**, 571–580

Susin, S. A., Lorenzo, H. K., Zamzami, N., Marzo, I., Snow, B. E., *et al.* (1999) Molecular characterization of mitochondrial apoptosis–inducing factor. *Nature* **397**, 441–446

Susin, S. A., Zamzami, N., Castedo, M., Daugas, E., Wang, H. G., *et al.* (1997) The central executioner of apoptosis: multiple connections between protease activation and mitochondria in Fas/APO-1/CD95– and ceramide–induced apoptosis. *J Exp Med* **186** (1), 25–37

Takamitsu, E., Otsuka, M., Haebara, T., Yano, M., Matsuzaki, K., *et al.* (2015) Identification of Human N–Myristoylated Proteins from Human Complementary DNA Resources by Cell–Free and Cellular Metabolic Labeling Analyses. *PLoS One* **10**, e0136360

Tao, Y. F., Xu, L. X., Lu, J., Hu, S. Y., Fang, F., *et al.* (2015) Early B–cell factor 3 (EBF3) is a novel tumor suppressor gene with promoter hypermethylation in pediatric acute myeloid leukemia. *J Exp Clin Cancer Res* **34**, 4

Taylor, R. G., Walker, D. C., and McInnes, R. R. (1993) *E. coli* host strains significantly affect the quality of small scale plasmid DNA preparations used for sequencing. *Nucleic Acids Res* **21**, 1677–1678

Tse, E. C. M., Hoang, T. T. H., Varnell, J. A. and Gewirth, A. A. (2016) Observation of an inverse kinetic isotope effect in oxygen evolution electrochemistry. *ACS Catal* **6**, 5706–5714

Urbano, A., Lakshmanan, U., Choo, P. H., Kwan, J. C., Ng, P. Y., *et al.* (2005) AIF suppresses chemical stress–induced apoptosis and maintains the transformed state of tumor cells. *Embo J* **24**, 2815–2826

Vahsen, N., Candé, C., Dupaigne, P., Giordanetto, F., Kroemer, R. T., *et al.* (2006) Physical interaction of apoptosis–inducing factor with DNA and RNA. *Oncogene* **25**, 1763–1774

van Zundert, G. C. P., Rodrigues, J. P. G. L. M., Trellet, M., Schmitz, C., Kastritis, P. L., *et al.* (2016) The HADDOCK2.2 Web Server: User–Friendly Integrative Modeling of Biomolecular Complexes. *J Mol Biol* **428**, 720–725

Vanoni, M. A. (2021) Iron–sulfur flavoenzymes: the added value of making the most ancient redox cofactors and the versatile flavins work together. *Open Biol* **11** (5): 210010

Velazquez–Campoy, A., Goñi, G., Peregrina, J. R., and Medina, M. (2006) Exact analysis of heterotropic interactions in proteins: Characterization of cooperative ligand binding by isothermal titration calorimetry. *Biophys J* **91**, 1887–1904

Velazquez–Campoy, A., Leavitt, S. A., and Freire, E. (2004) Characterization of protein–protein interactions by isothermal titration calorimetry. *Methods in molecular biology* (Clifton, N.J.), **261**, 35–54

Villanueva, R. (2015) The reductase activity of the human Apoptosis Inducing Factor: molecular bases and implications in the enzyme apoptotic function [PhD thesis, University of Zaragoza]

Villanueva, R., Ferreira, P., Marcuello, C., Usón, A., Miramar, M. D., *et al.* (2015) Key Residues Regulating the Reductase Activity of the Human Mitochondrial Apoptosis Inducing Factor. *Biochemistry* **54**, 5175–5184

Villanueva, R., Romero–Tamayo, S., Laplaza, R., Martínez–Olivan, J., Velázquez–Campoy, A., *et al.* (2019) Redox– and Ligand Binding–Dependent Conformational Ensembles in the Human Apoptosis–Inducing Factor Regulate Its Pro–Life and Cell Death Functions. *Antioxid Redox Signal*

Wang, J., Wang, W., Kollman, P. A., and Case, D. A. (2006) Automatic atom type and bond type perception in molecular mechanical calculations. *Journal of molecular graphics & modelling* **25**(2), 247–260

Wang, J., Wolf, R. M., Caldwell, J. W., Kollman, P. A. and Case, D. A. (2004) Development and testing of a general amber force field. *Journal of computational chemistry* **25**(9), 1157–1174

Wang, J., Zhang, C., Wu, Y., He, W., and Gou, X. (2019) Identification and analysis of long non–coding RNA related miRNA sponge regulatory network in bladder urothelial carcinoma. *Cancer Cell Int* **19**, 327

Wang, L., Zhang, C., and Ye, P. (2022) The microRNA–3622b–3p contributes to tumor progression and metastasis through an miR–3622–AIFM2 axis in prostate cancer [abstract]. *Proceedings of the American Association for Cancer Research Annual Meeting 2022*. Abstract nr 89

Wang, X., Yang, C., Chai, J., Shi, Y., and Xue, D. (2002) Mechanisms of AIF–mediated apoptotic DNA degradation in Caenorhabditis elegans. *Science* **298**, 1587–1592

Wang, Y. *et al.* (2016) A nuclease that mediates cell death induced by DNA damage and poly(ADP–ribose) polymerase–1. *Science* **354**

Wei, Y., Thyparambil, A. A., and Latour, R. A. (2014) Protein helical structure determination using CD spectroscopy for solutions with strong background absorbance from 190 to 230nm. *Biochimica et biophysica acta*, **1844**(12), 2331–2337

Westheimer, F. H. (1961) The magnitude of the primary kinetic isotope effect for compounds of hydrogen and deuterium. *Chem Rev* **61** (3), 265–273

Wiseman, T., Williston, S., Brandts, J. F., and Lin, L.–N. (1989) Rapid measurement of binding constants and heats of binding using a new titration calorimeter. *Analytical Biochemistry* **179**, 131–137

Woodward, K. J., Stampalia, J., Vanyai, H., Rijhumal, H., Potts, K., *et al.* (2019) Atypical nested 22q11.2 duplications between LCR22B and LCR22D are associated with neurodevelopmental phenotypes including autism spectrum disorder with incomplete penetrance. *Mol Genet Genomic Med* **7**, e00507

Wu, M., Xu, L. G., Li, X., Zhai, Z., and Shu, H. B. (2002) AMID, an apoptosis–inducing factor–homologous mitochondrion–associated protein, induces caspase–independent apoptosis. *J Biol Chem* **277**, 25617–25623

Wu, M., Xu, L. G., Su, T., Tian, Y., Zhai, Z., *et al.* (2004) AMID is a p53–inducible gene downregulated in tumors. *Oncogene* **23**, 6815–6819

Xie, Q., Lin, T., Zhang, Y., Zheng, J., and Bonanno, J. A. (2005) Molecular cloning and characterization of a human AIF–like gene with ability to induce apoptosis. *J Biol Chem* **280**, 19673–19681

Yakovleva, L., Chen, S., Hecht, S. M., and Shuman, S. (2008) Chemical and traditional mutagenesis of vaccinia DNA topoisomerase provides insights to cleavage site recognition and transesterification chemistry. *J Biol Chem* **283**, 16093–16103

Yang, W. (2011) Nucleases: diversity of structure, function and mechanism. *Q Rev Biophys* **44**, 1–93

Ye, H., Cande, C., Stephanou, N. C., Jiang, S., Gurbuxani, S., *et al.* (2002) DNA binding is required for the apoptogenic action of apoptosis inducing factor. *Nat Struct Biol* **9**, 680–684

Yu, C. J., Jia, L. T., Meng, Y. L., Zhao, J., Zhang, Y., *et al.* (2006) Selective proapoptotic activity of a secreted recombinant antibody/AIF fusion protein in carcinomas overexpressing HER2. *Gene Ther* **13**, 313–320

Yumerefendi, H., Tarendeau, F., Mas, P. J., and Hart, D. J. (2010) ESPRIT: An automated, library–based method for mapping and soluble expression of protein domains from challenging targets. *J Struct Biol* **172**, 66–74

Zheng, A., Zhang, L., Song, X., Wang, Y., Wei, M., *et al.* (2019) Clinical implications of a novel prognostic factor AIFM3 in breast cancer patients. *BMC Cancer* **19**, 451

Zhou, H. X., and Pang, X. (2018) Electrostatic Interactions in Protein Structure, Folding, Binding, and Condensation. *Chem Rev* **118**, 1691–1741

Zhu, C., Wang, X., Deinum, J., Huang, Z., Gao, J., *et al.* (2007) Cyclophilin A participates in the nuclear translocation of apoptosis–inducing factor in neurons after cerebral hypoxia–ischemia. *J Exp Med* **204**, 1741–1748

Zhu, N., Hou, J., Wu, Y., Liu, J., Li, G., *et al.* (2018) Integrated analysis of a competing endogenous RNA network reveals key lncRNAs as potential prognostic biomarkers for human bladder cancer. *Medicine* **97**, 11887

Zong, L., Guan, J., Ealy, M., Zhang, Q., Wang, D., *et al.* (2015) Mutations in apoptosis–inducing factor cause X–linked recessive auditory neuropathy spectrum disorder. *J Med Genet* **52**, 523–531

Zuidema, E., Escorihuela, L., Eichelsheim, T., Carbó, J. J., Bo, C., *et al.* (2008) The rate–determining step in the rhodium–xantphos–catalysed hydroformylation of 1–octene. *Chem Eur J* **14**, 1843–1853

ANNEXES

ANNEX I

Table 1. Indexed miRNAs in the DIANA-TarBase v8 (http://www.microrna.gr/tarbase) that have as targets aifm1, aifm2 *and* aifm3. DIANA-TarBase v8 is a reference database devoted to the indexing of experimentally supported miRNA targets (Karagkouni *et al.*, 2018).

Target	Name	miRNA QuickGO function/s	Related disease/s	References
aifm1, aifm2	hsa-miR-1-3p	Positive regulation of protein phosphorylation, cell fate commitment, heart rate and myotube differentiation; negative regulation of cardiac muscle hypertrophy; regulation of cardiac muscle contraction by regulation of release of sequestered calcium into cytosol by sarcoplasmic reticulum; gene silencing		Eichhorn *et al.*, 2014
aifm1	hsa-miR-25-3p	Negative regulation of cardiac muscle tissue growth and hypertrophy in response to stress; and gene silencing.	Hematologic neoplasms, uterine cervical neoplasms	Xue *et al.*, 2013
aifm1	hsa-miR-26b-5p	Involved in negative regulation of defence response to virus; positive regulation of cell cycle, protein serine/threonine kinase activity, tau-protein kinase activity, and apoptotic signalling pathway; and gene silencing	Hematologic neoplasms, uterine cervical neoplasms	Gennarino *et al.*, 2009
aifm1, aifm3	hsa-miR-147a	Negative regulation of vascular endothelial growth factor production; positive regulation of cell cycle arrest and drug sensitivity; gene silencing		Lee *et al.*, 2014
aifm1	hsa-miR-155-5p	Indirectly involved in negative regulation of interleukin-1β and interleukin-6 production; positive regulation of leukocyte activation, cardiac muscle hypertrophy, and necrotic cell death;	Hematologic neoplasms, B-cell chronic lymphocytic leukaemia, uterine cervical neoplasms	Selbach *et al.*, 2008

		and regulation of cell population proliferation and cytokine production involved in immune response		
aifm1	hsa-miR-340-3p	Indirectly involved in negative regulation of translation under environmental stress	Hematologic neoplasms	Karginov *et al.*, 2013
aifm1	hsa-miR-452-5p	Negative feedback loop to a positive one to elicit cellular reprogramming to the neuronal lineage.	Hematologic neoplasms, uterine cervical neoplasms	Xue *et al.*, 2013
aifm1	hsa-miR-744-3p	Indirectly involved in negative regulation of translation under environmental stress	Hematologic neoplasms	Karginov *et al.*, 2013
aifm1	hsa-miR-766-3p	Involved in cellular response to lipopolysaccharide; negative regulation of prostaglandin biosynthetic process, inflammatory response, and interleukin-1β, interleukin-6 and interleukin-8 production; and gene silencing		Karginov *et al.*, 2013
aifm2	hsa-miR-16-5p	Negative regulation of endothelial cell proliferation, cell population proliferation, and angiogenesis; and positive regulation of cardiac muscle cell apoptotic process	Adenocarcinoma, colorectal neoplasms, hematologic neoplasms, uterine cervical neoplasms	Selbach *et al.*, 2008
aifm2	hsa-miR-27a-3p	Negative regulation of gene expression and low-density lipoprotein particle clearance; regulation of cholesterol esterification; and gene silencing	Hematologic neoplasms, uterine cervical neoplasms	Shirasaki *et al.*, 2013
aifm2	hsa-miR-93-5p	Negative regulation of gene expression and interleukin-8 production	Hematologic neoplasms, uterine cervical neoplasms	Whisnant *et al.*, 2013
aifm2	hsa-miR-129-2-3p	Positive regulation of cilia biogenesis and elongation; gene silencing	Hematologic neoplasms	Cao *et al.*, 2012
aifm2	hsa-miR-133a-3p	Negative regulation of cell population proliferation, cell migration, cardiac muscle hypertrophy, cardiac muscle cell		Grimson *et al.*, 2007

		apoptotic process, and low-density lipoprotein particle clearance; positive regulation of cell fate commitment, gene expression and myotube differentiation; and regulation of cardiac muscle contraction by regulation of release of sequestered calcium ion		
aifm2	hsa-miR-146a-5p	Negative regulation of cholesterol storage, interleukin-6 and interleukin-8 production, inflammatory response, protein kinase B signalling, intracellular signal transduction, matrix metallopeptidase secretion, and chemokine (C-X-C motif) ligand 2 production; positive regulation of apoptotic process	Hematologic neoplasms, kaposi sarcoma	Li *et al.*, 2010
aifm2	hsa-miR-186-5p	Positive regulation of apoptosis; negative regulation of cell proliferation; regulation of migration, invasion, cell cycle, intracellular metabolism, angiogenesis and lymphangiogenesis; gene silencing	Hematologic neoplasms, uterine cervical neoplasms	Wang *et al.*, 2019 ; Whisnant *et al.*, 2013
aifm2	hsa-miR-214-3p	Negative regulation of cell population proliferation, cell migration, angiogenesis, gene expression, actin filament polymerization and lamellipodium assembly; gene silencing	Hematologic neoplasms	Cho *et al.*, 2019; Fan *et al.*, 2017
aifm3	hsa-miR-151a-3p	Indirectly involved in negative regulation of translation under environmental stress	Hematologic neoplasms, uterine cervical neoplasms	Karginov *et al.*, 2013
aifm3	hsa-miR-210-3p	Negative regulation of neuron projection development; positive regulation of cell migration; tube formation; and gene silencing	Hypoxic hepatomas	Cheng *et al.*, 2020; Mutharasan *et al.*, 2011; Yang *et al.*, 2012

Cao, J., Shen, Y., Zhu, L., Xu, Y., Zhou, Y., Wu, Z., Li, Y., Yan, X. and Zhu, X. (2012) *miR-129-3p controls cilia assembly by regulating CP110 and actin dynamics*. Nat Cell Biol. 14, 697-706

Cheng, H., Chang, S., Xu, R., Chen, L., Song, X., Wu, J., Qian, J., Zou, Y. and Ma, J. (2020) *Hypoxia-challenged MSC-derived exosomes deliver miR-210 to attenuate post-infarction cardiac apoptosis*. Stem Cell Res Ther. 11, 224

Cho, J., Teshigawara, R., Kameda, M., Yamaguchi, S. and Tada, T. (2019) *Nucleus-localized adiponectin is survival gatekeeper through miR-214-mediated AIFM2 regulation*. Genes Cells. 24, 126–138

Eichhorn, S. W., Guo, H., McGeary, S. E., Rodriguez-Mias, R. A., Shin, C., Baek, D., Hsu, S. H., Ghoshal, K., Villén, J. and Bartel, D. P. (2014) *mRNA destabilization is the dominant effect of mammalian microRNAs by the time substantial repression ensues.* Mol Cell. 56, 104–115

Fan, F. Y., Deng, R., Yi, H., Sun, H. P., Zeng, Y., He, G. C. and Su, Y. (2017) *The inhibitory effect of MEG3/miR-214/AIFM2 axis on the growth of T-cell lymphoblastic lymphoma*. Int J Oncol. 51, 316–326

Gennarino, V. A., Sardiello, M., Avellino, R., Meola, N., Maselli, V., Anand, S., Cutillo, L., Ballabio, A. and Banfi, S. (2009) *MicroRNA target prediction by expression analysis of host genes.* Genome Res. 19, 481–490

Grimson, A., Farh, K. K., Johnston, W. K., Garrett-Engele, P., Lim, L. P. and Bartel, D. P. (2007) *MicroRNA targeting specificity in mammals: determinants beyond seed pairing.* Mol Cell. 27, 91–105

Karagkouni, D., Paraskevopoulou, M. D., Chatzopoulos, S., Vlachos, I. S., Tastsoglou, S., Kanellos, I., Papadimitriou, D., Kavakiotis, I., Maniou, S., Skoufos, G., Vergoulis, T., Dalamagas, T. and Hatzigeorgiou, A. G. (2018) *DIANA-TarBase v8: a decade-long collection of experimentally supported miRNA-gene interactions*. Nucleic Acids Res. 46, 239–245

Karginov, F. V. and Hannon, G. J. (2013) *Remodeling of Ago2-mRNA interactions upon cellular stress reflects miRNA complementarity and correlates with altered translation rates.* Genes Dev. 27, 1624–1632

Lee, C. G., McCarthy, S., Gruidl, M., Timme, C. and Yeatman, T. J. (2014) *MicroRNA-147 induces a mesenchymal-to-epithelial transition (MET) and reverses EGFR inhibitor resistance.* PLoS One. 9, e84597

Li, J., Wan, Y., Guo, Q., Zou, L., Zhang, J., Fang, Y., Fu, X., Liu, H., Lu, L. and Wu, Y. (2010) *Altered microRNA expression profile with miR-146a upregulation in CD4+ T cells from patients with rheumatoid arthritis*. Arthritis Res Ther. 12, R81

Mutharasan, R. K., Nagpal, V., Ichikawa, Y. and Ardehali, H. (2011) *microRNA-210 is upregulated in hypoxic cardiomyocytes through Akt- and p53-dependent pathways and exerts cytoprotective effects.* Am J Physiol Heart Circ Physiol. 301, 1519–1530

Selbach, M., Schwanhäusser, B., Thierfelder, N., Fang, Z., Khanin, R. and Rajewsky, N. (2008) *Widespread changes in protein synthesis induced by microRNAs.* Nature. 455, 58–63

Shirasaki, T., Honda, M., Shimakami, T., Horii, R., Yamashita, T., Sakai, Y., Sakai, A., Okada, H., Watanabe, R., Murakami, S., Yi, M., Lemon, S. M. and Kaneko, S. (2013) *MicroRNA-27a regulates lipid metabolism and inhibits hepatitis C virus replication in human hepatoma cells*. J Virol. 87, 5270–5286

Wang, Z., Sha, H. H. and Li, H. J. (2019) *Functions and mechanisms of miR-186 in human cancer*. Biomed Pharmacother. 119, 109428

Whisnant, A. W., Bogerd, H. P., Flores, O., Ho, P., Powers, J. G., Sharova, N., Stevenson, M., Chen, C. H. and Cullen, B. R. (2013) *In-depth analysis of the interaction of HIV-1 with cellular microRNA biogenesis and effector mechanisms*. mBio. 4, e000193

Xue, Y., Ouyang, K., Huang, J., Zhou, Y., Ouyang, H., Li, H., Wang, G., Wu, Q., Wei, C., Bi, Y., Jiang, L., Cai, Z., Sun, H., Zhang, K., Zhang, Y., Chen, J. and Fu, X. D. (2013) *Direct conversion of fibroblasts to neurons by reprogramming PTB-regulated microRNA circuits*. Cell. 152, 82–96

Yang, W., Sun, T., Cao, J., Liu, F., Tian, Y. and Zhu, W. (2012) *Downregulation of miR-210 expression inhibits proliferation, induces apoptosis and enhances radiosensitivity in hypoxic human hepatoma cells in vitro*. Exp Cell Res. 318, 944–954

ANNEX II

The following publications derived from this PhD thesis:

- Novo, N., Ferreira, P., and Medina, M. (2021) The apoptosis–inducing factor family: Moonlighting proteins in the crosstalk between mitochondria and nuclei. *IUBMB Life* **73**, 568–581
- Novo, N., Romero–Tamayo, S., Marcuello, C., Boneta, S., Blasco–Machin, I., Velázquez–Campoy, A., Villanueva, R., Moreno–Loshuertos, R., Lostao, A., Medina, M., and Ferreira, P. (2022) Beyond a platform protein for the degradosome assembly: the Apoptosis Inducing Factor as an efficient nuclease involved in chromatinolysis. *PNAS Nexus* **2**, 1–11

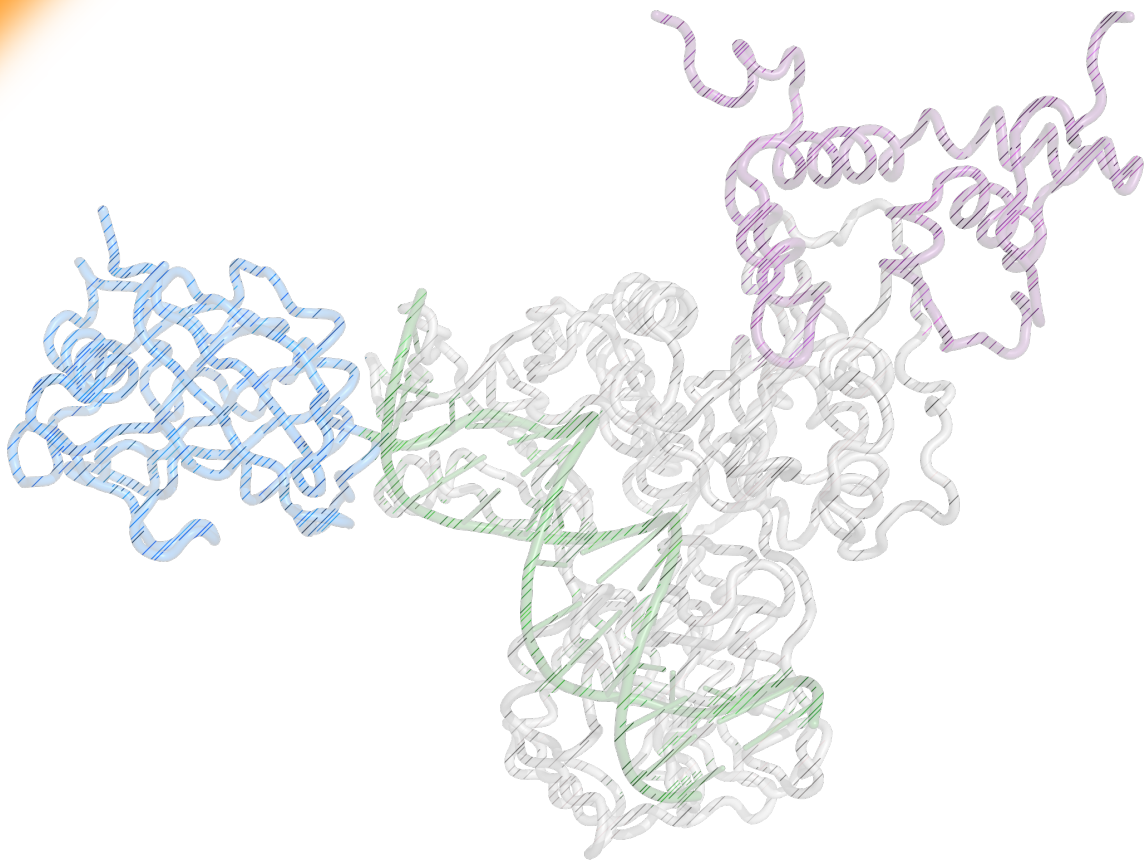

Facultad de Ciencias
Universidad Zaragoza

Instituto Universitario de Investigación
Biocomputación y Física
de Sistemas Complejos
Universidad Zaragoza